https://doi.org/10.15388/vu.thesis.209
https://orcid.org/0000-0001-5298-5217

STATE RESEARCH INSTITUTE CENTER FOR PHYSICAL SCIENCES AND TECHNOLOGY

Vilius
VERTELIS

Magnetic field diffusion in metallic and superconducting cylinders

DOCTORAL DISSERTATION

Natural sciences,
Physics (N 002)

VILNIUS 2021

This dissertation was written between 2017 and 2021 at State Research Institute Center for Physical Sciences and Technology and French-German Research Institute of Saint-Louis.

Academic supervisor:
Prof. Habil. Dr. Saulius Balevičius (State Research Institute Center for Physical Sciences and Technology, Natural scieces, Physics – N 002).

Academic consultant:
Dr. Markus, Schneider (French-German Research Institute Of Saint-Louis, Natural Sciences, Physics – N 002).

Dissertation Defence Panel:
Chairman – **prof. dr. Kęstutis Arlauskas** (Vilnius University, Natural Sciences, Physics – N 002).
Members:
Prof. Habil. Dr. Steponas Ašmontas (State Research Institute Center for Physical Sciences and Technology, Natural Sciences, Physics – N 002),
Prof. Habil. Dr. Algimantas Fedaravičius (Kaunas University of Technology, Technological Sciences, Mechanical Engineering – T 009),
prof. Dr. Jurij Novickij (Vilnius Gediminas Technical University, Technological Sciences, Eletrical and Electronic Engineering – T 001),
Prof. Habil. Dr. Sigitas Tamulevičius (Kaunas University of Technology, Natural Sciences, Physics – N 002).

The dissertation shall be defended at a public meeting of the Dissertation Defence Panel at 14:00 on 17th of september 2021 in meeting room A101 of the State Research Institute Center for Physical Sciences and Technology
Address: Saulėtekio av. 3, A101, Vilnius, Lithuania
Tel. +3702340541; e-mail: vilius.vertelis@ftmc.lt

The text of this dissertation can be accessed at the libraries of State Research Institute Center for Physical Sciences and Technology and Vilnius University, as well as on the website of Vilnius University:
www.vu.lt/lt/naujienos/ivykiu-kalendorius

https://doi.org/10.15388/vu.thesis.209
https://orcid.org/0000-0001-5298-5217

VALSTYBINIS MOKSLINIŲ TYRIMŲ INSTITUTAS FIZINIŲ IR
TECHNOLOGIJOS MOKSLŲ CENTRAS

Vilius
VERTELIS

Magnetinio lauko difuzija į metalinius ir superlaidžius cilindrus

DAKTARO DISERTACIJA

Gamtos mokslai,
Fizika (N 002)

VILNIUS 2021

Disertacija rengta 2017– 2021 metais Valstybiniame mokslinių tyrimų institute Fizinių ir technologijos mokslų centre bei Prancūzijos-Vokietijos tyrimų institute Saint-Louis′e.

Mokslinis vadovas:
Prof. habil. dr. Saulius Balevičius (Valstybinis mokslinių tyrimų institutas Fizinių ir technologijos mokslų centras, gamtos mokslai, fizika – N 002).

Mokslinis konsultantas:
Dr. Markus Schneider (Prancūzijos-Vokietijos tyrimų institutas Saint-Louis′e, gamtos mokslai, fizika – N 002).

Gynimo taryba:
Pirmininkas – **prof. dr. Kęstutis Arlauskas** (Vilniaus universitetas, gamtos mokslai, fizika – N 002).
Nariai:
Prof. habil. dr. Steponas Ašmontas (Valstybinis mokslinių tyrimų institutas Fizinių ir technologijos mokslų centras, gamtos mokslai, fizika – N 002),
Prof. habil. dr. Algimantas Fedaravičius (Kauno technologijos universitetas, technologijos mokslai, mechanikos inžinerija – T 009),
prof. dr. Jurij Novickij (Vilniaus Gedimino technikos unversitetas, technologijos mokslai, elektros ir elektronikos inžinerija – T 001),
Prof. habil. dr. Sigitas Tamulevičius (Kauno technologijos universitetas, gamtos mokslai, fizika – N 002).

Disertacija ginama viešame Gynimo tarybos posėdyje 2021 m. rugsėjo mėn. 17 d. 14 val. Valstybinio mokslinių tyrimų instituto Fizinių ir technologijos mokslų centro A101 auditorijoje. Adresas: Saulėtekio al. 3, A101, Vilnius, Lietuva, tel. +3702340541 ; el. paštas vilius.vertelis@ftmc.lt

Disertaciją galima peržiūrėti Valstybinio mokslinių tyrimų instituto Fizinių ir technologijos mokslų centro ir Vilniaus universiteto bibliotekose ir VU interneto svetainėje adresu: https://www.vu.lt/naujienos/ivykiu-kalendorius

LIST OF ABBREVIATIONS

AFM Atomic Force Microscope.

B-dot inductive magnetic field senor, pickup coil.

Bi-2223 bismuth strontium calcium copper oxide $Bi_2Sr_2Ca_2Cu_3O_{10-x}$.

BSCCO same as Bi-2223.

CMR Colossal Mangetoresistance.

DC Direct current.

EGP Elektromagnetiškai Greitinama Platforma.

EM Electromagnetic.

emf electromotive force.

EML Electromagnetic Launcher.

FEM Finite Element Method.

FFF Free Flux Flow.

HTS High Temperature Superconductor.

IV current-voltage relationship.

MF Magnetic Field.

MFD Magnetic Field Diffusion.

PFM Pulsed Field Magnetization.

PFU Pulse Forming Unit.

PI-MOCVD Pulsed Injection Metalorganic Chemical Vapor Deposition.

PIT Powder-In-Tube.

RHEED Reflection High-Energy Electron Diffraction.

S^{3}EL Superconducting Self-Supplying Electromagnetic Launcher.

SMES Superconducting Magnetic Energy Storage.

VSE Velocity Skin Effect.

YBCO or Y-123 Yttrium barium copper oxide $YBa_2Cu_3O_{7-x}$.

CONTENTS

Acknowledgments

In the four years that it took me to prepare this thesis, I have received an enormous amount of support from people I consider dear to me. I feel extremely grateful to my parents, Elena and Dainius Verteliai, for raising me the way they did and providing me with the opportunity to reach for my dreams. I also want to thank my wife Ernesta Bužavaitė-Vertelienė for being the light of my life that kept me going.

This thesis would have been impossible without the guidance and mentoring from prof. Saulius Balevičius, with whom countless hours were spent discussing. I have learned invaluable lessons from him and for that I will always be thankful. I am immensely grateful to Dr. Markus Schneider, who suggested the topic of my thesis, gave me the opportunity to carry out this PhD, trusted me to pursue it in my way and helped pursuing it. He allowed me to stay with my family in Lithuania during this pandemic, for which I am truly thankful. Under the guidance of these two scientists, I've grown both as a researcher and as a person.

I appreciate the help from Skirtmantas Keršulis, Voitech Stankevič and Grégory Vincent for helping me with my experiments and showing me around the laboratories and equipment. I thank prof. Nerija Žurauskienė for helping me with the thesis management and solving problems related to it. I want to express my gratitude to the administrative staff of both ISL and CPST.

A special thank you goes to the Liebfried family: Oliver, Rasa, Lukas and Aiden. They made me, a stranger, feel welcome so far away from home and made my stay fun and eventful.

Investigations of magnetic field diffusion (MFD) inside highly conducting materials started with the discovery of Faraday's electromagnetic induction law. During the past few decades, the interest in the magnetic diffusion significantly increased due to the development of new technologies, such as electromagnetic metal welding [1], flux compression generators [2] and electromagnetic launch [3]. In the latest case, the acceleration of MFD investigations benefited from the development of new pulsed magnetic field measurement technologies [4] and software for the calculation of the field distribution and dynamics. MFD is important for electromagnetic launch because it determines the acceleration force acting on an armature and the electromagnetic environment of the payload. Bodies with cylindrical shape are especially interesting as they represent the simplest configuration of an armature in the coilgun case and of a payload of an electromagnetic railgun. This shape of is also important not only from a technical point of view, but also due to its symmetry which allows to reduce the dimensionality of the problem that, in turn, accelerates the magnetic field distribution calculations. The MFD process during electromagnetic launch is strongly linked to the magnetic field distribution of the magnetic field source. The MFD will cause different field distribution in a simple railgun compared to an augmented railgun, a single-stage pancake coil or a synchronous multistage coilgun. MFD is also different for different types of high conductivity materials like conventional metals or superconductors. Contrary to metals, type II superconductors are nonlinear conductors. Their electrical conductivity strongly depends on the electric field, magnitude of the magnetic field and temperature. These materials, below their critical current density, show a negligible resistivity as their $E - j$ relationship shows a power-law behaviour. This makes it possible to use type II superconductors not only for armatures or for magnetic shields for payloads, but also for the development of high power fault current limiters.

Recently, a new design of a multirail railgun with a hexagonal rail arrangement [5, 6] was introduced. The main advantage of this device is its versatility as it can be set up in various arrangements, including segmented, multishot, and augmented configurations. The most convenient payload geometry for such railgun is a cylinder. For this reason, the investigation of magnetic effects in close proximity to a cylindrical conductive payload placed inside a hexagonal railgun in a serial augmented mode is very important to determine the elec-

tromagnetic environment of the payload. Usually, time-dependent magnetic field distributions are calculated using numerical techniques like finite difference or finite element methods. However, in order to obtain reliable results, the calculations have to be matched with experimental magnetic field evolution measurements. For this reason, theoretical studies of the magnetic field distribution inside a hexagonal railgun equipped with a cylindrical metallic payload during operation in a series augmented mode were compared with experimental measurements performed using a unique CMR-B-scalar sensor array [7, 8].

Hollow superconducting cylinders (tubes) are used in permanent magnets [9–11], magnetic shields [12–14], fault current limiters [15–18] and superconducting high-energy particle accelerators [19]. To operate and to test these devices, it is necessary to know how pulsed magnetic flux penetrates the cavity of the tube. Studies of this process in bulk type II superconductors (rings or hollow cylinders with thick walls) have been carried out previously [20–23]. A thin-walled tube configuration helps to reduce the high costs of superconducting material and can be used for magnetic shields or for "smart superconducting grids" [24, 25]. Long pipes made from MgB_2 by hydro-extrusion [25], paint-coating [26] and metalorganic decomposition technique [27] have been proposed. In such cases, it is important to have non-destructive means with which to evaluate the intrinsic properties of the superconducting material, such as critical current density vs. magnetic field, maximal magnetic field that can be screened and the power law index. In order to obtain these properties, experimental results need to be evaluated using an adequate theoretical model adapted to the experimental conditions. Such method was applied for a systematic investigation of the magnetic field responses of tubes with different dimensions and different magnitudes of the applied field [28]. It was based on the calculation of the electric current distribution in the bulk of the superconducting material, which, however, was the result of discrete coupled superconducting circuits carrying different currents in different regions along the radial and axial directions of the superconducting tube. Thus, for tubes with various configurations, this method requires to choose specific discretization algorithms, which makes the calculation procedure dependent on the tube geometry. Fortunately, for a geometry of a thin-walled tube, this description can be simplified without losing the accuracy of the calculation procedure. Since the walls are thin, it is possible to assume that there is no spatial variation of the current density throughout the thickness of the wall. Joule heating can also be neglected due to effective cooling of the superconducting material. Hence, measuring

the magnetic field inside a thin-walled superconducting tube should provide more accurate information about the properties of the superconducting material than in the case of thick-walled tubes. For this reason, a simple method for the analysis and determination of the main properties of a superconducting material was developed in the present thesis. The method is based on a lumped-parameter equation and the measurement of the magnetic field outside and inside a thin-walled tube. The method was validated by an experimental study of the magnetic field dynamics inside of a small diameter thin-walled Bi-2223 tube exposed to an axial pulsed magnetic field. Both CMR-B-scalar and B-dot sensors were used to measure the field dynamics.

The MFD process can generate high electrical current densities in a thin-walled superconducting tube subjected to an axial magnetic field, especially if the tube is exposed to a highly transient magnetic field. High current, together with a high external magnetic field, can significantly change the conductivity of superconducting films by bringing them into the flux flow resistive state. Joule heating and various electrical instabilities are associated. If one side of a superconducting film has no direct contact with a cooling agent, the heat flow from the superconductor decreases and makes the film more susceptible to current-induced heating. For this reason, investigations of electric and magnetic properties of superconducting films prepared on high thermal conductivity dielectric substrates are of high importance. Processes that appear in type II superconductor films carrying high electrical current densities and exposed to the magnetic field were experimentally investigated in microbridges made from submicron thick YBCO films prepared on Al_2O_3 substrates with CeO_2 sublayer by the pulsed injection MOCVD method [29]. It was demonstrated that the I-V characteristics of these films exhibit a wide range of nonlinear dissipative states and that such films can be successfully used to realize high speed fault current limiters [30–35]. The analysis and explanation of the main processes taking place when these microstrips were affected by a strong electrical current and a DC magnetic field was not yet done. This was the next objective of the investigation performed in the frame of the present thesis.

A coil accelerator or a coilgun is an electromagnetic launcher that accelerates ferromagnetic (reluctance coilgun) or conductive (induction coilgun) armatures to high velocities by employing magnetic fields. The lack of sliding electrical contact between the barrel and the launch package as well as the absence of a propellant eliminates friction and reduces the mass of the launch package, while, in turn, reducing the amount of energy needed to reach the de-

sired velocities. However, a complex modular power supply with high requirements for switches, real-time projectile tracking and control is required [36,37]. Joule heating, armature flux capture, and structural integrity are the factors which limit the performance of metal armatures [38, 39]. Type II superconductors are intriguing materials that behave very differently from normal conductors. Above the critical current, the resistivity of the superconductor increases rapidly, and the superconductor returns into its normal (resistive) state. This nonlinear behaviour makes the electric and magnetic properties of these materials attractive for various applications [40–42], one of which is electromagnetic launch. The use of these materials as armatures for electromagnetic launchers can lift some of the limitations associated with normal conductor armatures as well as cause some new unforeseen behaviour. At present, only a relatively small number of studies investigating the electromagnetic launch of such superconducting armatures have been performed in comparison to those which investigated the launch of normal metal armatures. Calculations performed in [43] demonstrated that a pre-magnetized superconducting armature (using field-cooled magnetization) can be more effectively accelerated by a pulsed magnetic field than an armature made from conventional metals. However, this method of acceleration is more complicated in comparison to using a non-magnetized superconducting armature as it adds a preparation stage that requires energy. Another drawback of using a magnetized armature is that it can be necessary to move the armature to the optimal trigger position after the premagnetization process [43]. Thus, an acceleration method that employs simple non-magnetized armatures is more preferable, however, parametric investigations of the electromagnetic launch of such armatures up to now have not been conducted. During this type of acceleration, the MFD process mainly determines the energy transfer from the coil to the armature and defines the ballistic characteristics of the armature. For this reason, the final part of this thesis was the investigation of a disc-shaped single-domain YBCO armature accelerated by a pancake coil. The acceleration studies were performed in a vertical geometry. Magnetic field dynamics measured using a CMR-B-scalar sensor an displacement measurements using optical sensors were successfully reproduced by theoretical modelling results.

Goals

There are four main goals of the present thesis:

1. The investigation of the magnetic field dynamics inside the bore of a novel versatile hexagonal multi-rail railgun in a series augmented mode equipped with a cylindrical metallic payload.
2. Experimental and theoretical investigation of the pulsed magnetic field penetration dynamics in a hollow thin-walled tube made from a type II Pb-doped Bi-2223 superconductor.
3. The evaluation of processes that appear in microbridges made from submicron thick YBCO films prepared on Al_2O_3 substrates with CeO_2 sublayer by the pulsed injection MOCVD method carrying high electrical current densities and exposed to the magnetic field.
4. The investigation of the behaviour or a disk-shaped superconducting single-domain YBCO armature cooled to 77 K under vertical electromagnetic acceleration using a single-stage pancake coil.

Tasks

Tasks to achieve these goals were the following:

- To design an experimental setup based on SR\3-60 multirail electromagnetic launch platform by configuring it in multiple augmented arrangements and installing the magnetic field measurement system containing an array of 4 CMR-B-scalar sensors.
- To build a time-dependent numerical model based on the finite element method (COMSOL Multiphysics AC/DC module) for the analysis of the magnetic field distribution inside the bore of a serial augmented hexagonal railgun.
- To calculate the magnetic field dynamics in the proximity of a cylindrical aluminium payload and to compare the results with experimental measurement results.
- To create an experimental setup for the investigation of the pulsed magnetic field penetration inside a hollow thin-walled superconducting cylinder made from $Bi_{1.8}Pb_{0.26}Sr_2Ca_2Cu_3O_{10+x}$ and to perform experiments using a B-dot and a CMR-B-scalar sensor.
- To develop a mathematical lumped-parameter model that is capable to explain the main behaviour of the magnetic field dynamics and the

trapped flux inside the hollow thin-walled cylinder. To test the validity of this approach by comparing it with the experimental measurements.

- To analyze of the magnetoresistive effect in 440 nm thick YBCO films prepared on Al_2O_3 substrates with CeO_2 sublayers by the pulsed injection MOCVD method in temperatures ranging from 20 K to 300 K.
- To explain the nature and the mechanism of the experimentally obtained S-shaped I-V characteristics and the time-changing resistance of the microbridges after they were affected by a step-like magnetic field.
- To create an experimental setup for investigating the behaviour of a disk-shaped superconducting YBCO armature cooled to 77 K under vertical electromagnetic acceleration based on an IR distance sensor and a CMR-B-scalar magnetic field sensor.
- To develop a numerical model for the nonlinear eddy current problem in the armature's frame of reference using Maxwell's equations in their H-formulation in the 2D axis-symmetric form using Comsol Multiphysics commercial software and to apply this model for the investigation of the disc armature displacement and magnetic field dynamics.
- To evaluate the effectiveness of the coilgun type electromagnetic accelerator with a type II superconducting armature using the numerical model.

Practical value and novelty

The influence of a cylindrical conductive payload on the transient magnetic field distribution during electromagnetic launch with a series augmented hexagonal railgun was investigated for the first time. The obtained magnetic field distributions can be used when designing launch packages with sensitive payloads.

A quick, nondestructive method based on a lumped parameter equation was proposed to evaluate the in-field properties of type II superconducting tubes whose wall thickness is shorter than the Bean's penetration depth.

Intrinsic current-voltage relationships of thin-film YBCO microbridges prepared on Al_2O_3 with CeO_2 sublayer that were obtained using ns duration electrical pulses were used to model electrothermal instabilities observed in DC measurements for the first time. This model can be used to predict the behaviour of fault current limiters exposed to long-lasting faults.

Numerical simulation of a single-stage coilgun with a type II superconducting armature was validated by experimental results for the first time. Numerical

simulations were later used to determine the properties of such armatures and to show in what conditions these armatures are superior to normal metal armatures.

Scientific statements

- The magnetic field diffusion causes a magnetic field disturbance in the proximity of a cylindrical conductive payload during the operation of a series augmented hexagonal railgun. This disturbance can be well modeled with quasistatic Maxwell's equations using the finite element method.

- The nonlinear magnetic field diffusion equation describing the magnetic field propagation inside a type II superconducting tube can be simplified to a lumped parameter equation when the wall thickness is considerably smaller than the Bean's penetration length. This equation, together with pulsed magnetic field measurements inside the tube, can be used to quickly and nondestructively evaluate the relation between the critical current density and the magnetic field together with the power-law index of the superconducting material.

- The magnetoresistance of 400 nm thick YBCO films prepared on Al_2O_3 substrate with CeO_2 sublayer by the PI- MOCVD method in the superconducting state is linear with respect to the magnetic field and in accordance with the flux flow model for dirty superconductors. The S-shaped I-V characteristics of microstrips made from these films observed under voltage bias as well as the time-dependent resistance under constant current bias is a result of a thermo-electrical instability caused by Joule heating due to the flux flow-induced resistive state.

- The motion and the magnetic field dynamics during electromagnetic acceleration of a disc-shaped type II superconducting armature can be explained using numerical simulations based on quasi-static Maxwell's equations in their H formulation and the assumption that the superconductor is a nonlinear conductor with a power-law E-j relationship. The type II superconductor outperforms normal metals when accelerated by magnetic pulses with smaller time derivatives and the use of superconducting armatures is advantageous in the lower pulse amplitude range.

Author's contribution

Vilius Vertelis, while consulting with Saulius Balevičius and Markus Schneider, planned and performed all of the measurements presented in sections 2.1, 2.2, and 2.4, designed and built the experimental setups used in sections 2.2 and 2.4, analyzed the results and performed all of the presented simulations and calculations. The author participated in the writing and formatting of the manuscripts of the publications included in this thesis.

List of publications

1. V. Vertelis, S. Balevicius, V. Stankevic, N. Zurauskiene, and M. Schneider, "The Application of a CMR-B-Scalar Sensor for the Investigation of the Electromagnetic Acceleration of Type II Superconductors," *Sensors*, vol. 21, no. 4, p. 1293, 2021, doi: 10.3390/s21041293.

2. V. Vertelis et al., "Superconducting protector against electromagnetic pulses based on YBCO film prepared on an Al_2O_3 substrate with a CeO_2 sublayer," *Supercond. Sci. Technol.*, vol. 34, no. 3, p. 035007, 2021, doi: 10.1088/1361-6668/abd459.

3. V. Vertelis, S. Balevicius, V. Stankevic, N. Zurauskiene, and M. Schneider, "Pulsed magnetic flux penetration dynamics inside a thin-walled superconducting tube,"*J. Appl. Phys.*, vol. 127, no. 11, p. 113901, Mar. 2020, doi: 10.1063/1.5145370.

4. V. Vertelis, G. Vincent, M. Schneider, S. Balevičius, V. Stankevič, and N. Žurauskiene, "Magnetic Field Expulsion from a Conducting Projectile in a Pulsed Serial Augmented Railgun," *IEEE Trans. Plasma Sci.*, vol. 48, no. 3, pp. 727–732, Mar. 2020, doi: 10.1109/TPS.2020.2970764.

Other publications during this PhD

1. E. Bužavaitė-Vertelienė, V. Vertelis, and Z. Balevičius, "The experimental evidence of a strong coupling regime in the hybrid Tamm plasmon-surface plasmon polariton mode," *Nanophotonics*, Feb. 2021, doi: 10.1515/nanoph-2020-0660.

2. I. Plikusiene, V. Maciulis, O. Graniel, M. Bechelany, S. Balevicius, V. Vertelis, Z. Balevicius, A. Popov, A. Ramanavicius and A. Ramanaviciene, "Total internal reflection ellipsometry for kinetics-based assessment of bovine serum albumin immobilization on ZnO nanowires," *J. Mater. Chem. C*, vol. 9, no. 4, pp. 1345–1352, 2021, doi: 10.1039/D0TC05193D.

International conferences

1. V. Vertelis, G. Vincent, V. Stankevic, S. Balevičius and M. Schneider, "Magnetic field expulsion caused by a conducting projectile in an augmented railgun" *19th International Symposium on Electromagnetic Launch Technology* (EML 2018), Saint-Louis, France.

2. V. Vertelis, S. Balevicius, V. Stankevic, N. Zurauskiene and M. Schneider, "Magnetic field dynamics inside a thin-walled superconducting tube" *14th European Conference on Applied Superconductivity* (EUCAS 2019), Glasgow, United Kingdom.

3. V.Vertelis, S.Balevicius, M. Schneider, „Numerical modelling of a type II superconducting disk electromagnetic launching using a pancake coil" *7th edition of the International Workshop on Numerical Modelling of High Temperature Superconductors* (HTS 2020), Nancy, France (online).

Structure of the thesis

The thesis is divided into two parts: literature review and original results obtained during this thesis. The literature review covers the main effects associated with magnetic field diffusion in non-magnetic conductors, magnetic and electric properties of both bulk and thin-film type II superconductors. The review also introduces to the numerical efforts in modellling the nonlinear magnetic field diffusion in bulk type II superconductors. Finally, the importance of the magnetic field diffusion to electromagnetic launchers like railgun and coilgun is analyzed.

The results section is further divided into four subsections. The first one discusses the magnetic field diffusion into an electrically isolated cylindrical aluminum payload accelerated by a hexagonal railgun in a series augmented mode. The second subsection analyses the transient response of the magnetic

field inside a high-temperature superconducting tube made from Bi-2223. Intrinsic electrical properties of thin YBCO films prepared on Al_2O_3 substrate with a CeO_2 sublayer are investigated at several temperatures in the third subsection and are used to model their DC behaviour using electrothermal model. The last subsection investigates the properties of a single-stage pancake coilgun with a disk-shaped superconducting YBCO armature. The study is expanded outside the experimental capabilities by using an experimentally validated finite element model of the system.

1.1 Magnetic field diffusion in non-magnetic metals

The distribution and time evolution of the magnetic field inside highly electrically conductive environments (metals) can be obtained using four equations developed by James C. Maxwell [44]. These equations describe interactions between electromagnetic (EM) fields, currents and charge as:

$$\nabla \cdot \mathbf{D} = q \tag{1.1}$$

$$\nabla \cdot \mathbf{B} = 0 \tag{1.2}$$

$$\nabla \times \mathbf{E} = -\frac{\partial \mathbf{B}}{\partial t} \tag{1.3}$$

$$\nabla \times \mathbf{H} = \mathbf{j} + \frac{\partial \mathbf{D}}{\partial t}, \tag{1.4}$$

where $\mathbf{D}$ is the electric displacement field, q is the density of free charge, $\mathbf{B}$ is the magnetic field induction, $\mathbf{E}$ - the electric field, $\mathbf{H}$ is the magnetic field (MF) and $\mathbf{j}$ is the free current density. These equations are used to derive equations for describing multitude of effects that range from electrostatics to optics.

An equation describing the propagation of the magnetic field inside conductive matter in quasi-stationary case (where the rate of change of $\mathbf{D}$ and the motion of the conductor can be neglected) can be derived from Maxwell's equations. Assuming that $\mathbf{E}= \rho \mathbf{j}$ and $\mathbf{B}= \mu \mathbf{H}$ (here ρ is the resistivity of the material and μ is its magnetic permeability), we can substitute (1.4) into (1.3) to get

$$\nabla \times \rho \left(\nabla \times \frac{\mathbf{B}}{\mu} \right) = -\frac{\partial \mathbf{B}}{\partial t}. \tag{1.5}$$

For isotropic nonmagnetic conductive materials ρ and μ are constants, thus, replacing the double curl according to a vector calculus identity and knowing the equation (1.2) we get

$$\frac{\rho}{\mu} \nabla^2 \mathbf{B} = \frac{\partial \mathbf{B}}{\partial t}. \tag{1.6}$$

This second order partial differential equation is equivalent to a concentration diffusion equation. In addition, the scalar term has a unit of m^2/s, that is the unit of a diffusion coefficient. Because of this similarity, the process of magnetic field penetration into conductive media is called magnetic field diffusion and governs the propagation of low frequency magnetic fields in normal con-

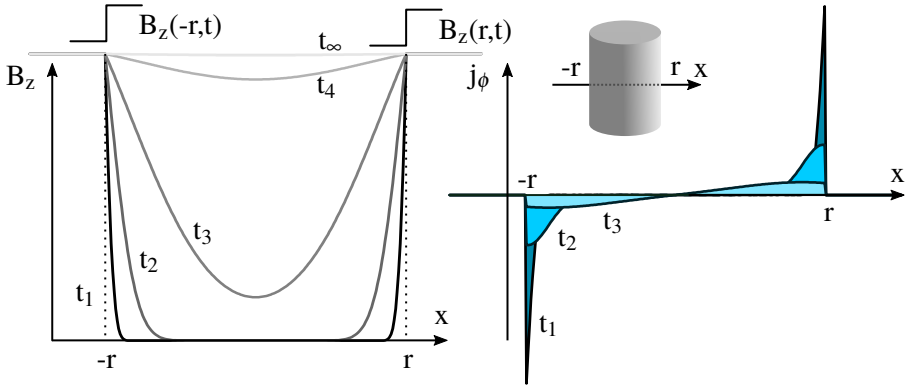

Figure 1.1.1. Magnetic field and current density distributions in a conductive cylinder at different moments after an application of an external magnetic field.

ductors. It has to be noted that the unknown is a vector quantity in contrast to that of heat or diffusion equations where the solution is a scalar field. It can be shown that the vector equation decomposes into a set of scalar equations. The number of these equations depends on the dimensions of the problem. In three dimensions using Cartesian coordinates the magnetic field is composed of three scalar components as

$$\mathbf{B}(x,y,z,t) = [B_x(x,y,z,t), B_y(x,y,z,t), B_z(x,y,z,t)] \tag{1.7}$$

and the equation for a single component becomes.

$$\frac{\rho}{\mu}\frac{\partial^2 B_i}{\partial x_i^2} = \frac{\partial B_i}{\partial t}. \tag{1.8}$$

where the subscript i denotes the component. An illustration of the magnetic field diffusion in linear conductors can be seen in Figure 1.1.1.

In cases dealing with external driving currents and moving conductors it is more convenient to derive an equation based on the magnetic vector potential $\mathbf{A}$, defined by $\mathbf{B} = \nabla \times \mathbf{A}$. The diffusion equation with contributions from the electric potential and motion under Coulomb gauge ($\nabla \cdot \mathbf{A} = 0$) becomes:

$$\nabla^2 \mathbf{A} = \mu\sigma\left(\frac{\partial \mathbf{A}}{\partial t} + \nabla\phi + \mathbf{v} \times \nabla \times \mathbf{A}\right), \tag{1.9}$$

where σ is the electrical conductivity, $\mathbf{v}$ is the velocity and ϕ is the electric potential. Here μ is assumed to be constant in space [45].

Parabolic partial differential equations of the form (1.8) have been studied

extensively in heat propagation and concentration diffusion for over a century and many techniques have been developed to solve them. For simple geometries analytic solutions exist while numerical techniques are employed for more complex geometries [46].

1.2 Magnetic field in superconductors

The magnetic field behaves very differently in type I superconductors than in regular conductors. In these materials, below their superconducting transition temperature T_c , the magnetic field is expelled from their interior by a process called Meissner effect [47]. In this Meissner state, type I superconductors are perfect diamagnets. If an external magnetic field is applied, the Meissner state exists until a critical value H_c of external field is reached. Above it, superconductivity disappears, leaving the material in its normal state. The electrodynamics of the Meissner state was described by the London brothers [48]. Based on the kinetic theory of non scattering electrons and the Meissner effect, they derived two equations:

$$\mathbf{E} = \Lambda \frac{d\mathbf{j}}{dt}, \quad \Lambda = \frac{m_e}{n_s e^2} \tag{1.10}$$

$$\Lambda \nabla \times \mathbf{j} = \mathbf{B}. \tag{1.11}$$

Here m_e is the electron mass, n_s is the density of superconducting electrons, and e is the charge of an electron. The first equation concludes that there is no electric field if the current density is stationary, allowing for persistent currents to flow without dissipation. The second equation, in combination with eq. (1.4), shows that the magnetic field exponentially decays from the surface of a superconductor in the Meissner state with a characteristic length λ_L , called the London penetration depth.

$$\lambda_L = \sqrt{\frac{\Lambda}{\mu}} \tag{1.12}$$

This decay of the field is caused by a supercurrent circulating within a λ_L depth from the surface. According to Sisbee's rule, when an external field of magnitude H_c is applied to a type I superconductor, a critical current density j_c is induced to screen it.

Type II superconductors also exhibit the Meissner state, but due to a negative energy of the superconducting/normal interface, at a field value of H_{c1}

the magnetic field is allowed into the interior of these superconductors in quantized amounts. These quanta were predicted by A. A. Abrikosov [49] and are called Abrikosov vortices or fluxons and this state is called the mixed state. Each fluxon carries within it a magnetic flux of $\Phi_0 = h/(2e)$ (h is the Plank's constant), majority of which is distributed within a cylinder of a radius λ_L. The density of superconducting electrons decreases over the coherence length ξ inside the fluxon and drops to zero at the center, therefore, vortices are considered to have normal cores. Inside the superconductor, these vortices repel each other forming a triangular lattice. The lattice constant decreases with increasing external field, decreasing the magnetization of type II superconductors. Superconductivity is destroyed at a field H_{c2} called the second or the upper critical field.

A macroscopic model explaining the irreversible magnetization of type II superconductors was proposed by C. P. Bean [50]. He argued, that due to the zero resistivity, an infinitesimal electric field would induce a critical current density, so the macroscopic current density inside type II superconductors in their mixed state is either j_c or zero. This model is called the Bean's critical state model. According to this model, the curl of the magnetic field can only have two values:

$$\nabla \times \mathbf{H} = \begin{cases} j_c, & \text{or} \\ 0. \end{cases} \tag{1.13}$$

Under this assumption, one can see from eq. (1.3) that any change of magnetic field will induce j_c and that this change will be screened in a surface layer whose depth is proportional to the absolute change of the magnetic field and inversely proportional to the magnitude of j_c. An illustration of the resulting magnetic field and the induced current density distributions in an infinitely long superconducting cylinder exposed to an external magnetic field pulse according to Bean's critical state can be seen Fig. 1.2.1.

In the general case, the current density in type II superconductors is not limited to the two discrete values. Abrikosov vortices experience Lorentz force since inside them both the magnetic field and the electric current can exist simultaneously. If the superconductor is very pure, in other words, it does not have defects that bind the magnetic field lines, called pinning centers, the vortices are free to move. Moving fluxons, in addition to Lorentz force, experience viscous drag. This drag is theorized to originate from the dissipation by normal

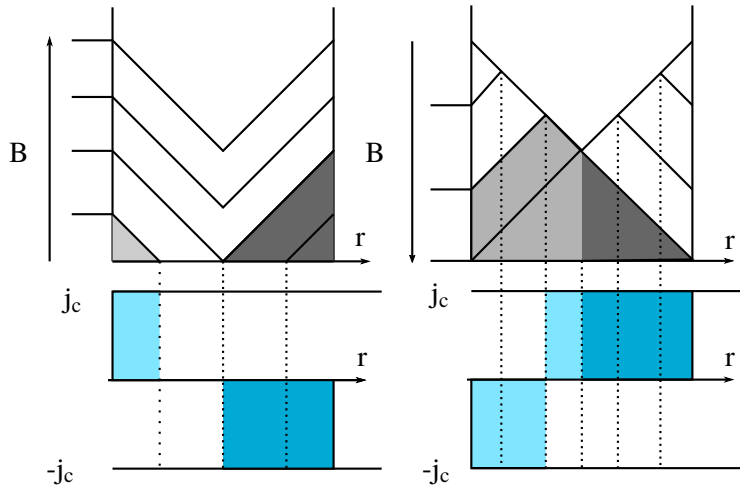

Figure 1.2.1. Magnetic field and current density distributions in a superconducting cylinder in a changing external magnetic field according to Bean's critical state model.

electrons [51]. Due to the motion of the magnetic flux line, an electric field is induced inside the normal cores and dissipative currents arise [52]. Since energy is lost, vortices move as if through a viscous medium [53,54] described by a viscous drag coefficient. This mode of conduction is called Free Flux Flow (FFF). If, however, the vortices are pinned by pinning centers, they will not move until the Lorentz force will exceed the force holding them in place, called the pinning force, and there will be no electric field induced until they detach. The resulting E-j relationship in FFF regime is:

$$E = \rho_{FFF} j, \quad \rho_{FFF} = \rho_n \frac{B}{B_{c2}} \tag{1.14}$$

where ρ_{FFF} and ρ_n are the free flux flow and the normal state resistivities, respectively.

The electric field to current density relationship (E-j) in type II superconductors at finite temperature is divided into two regions: flux creep and FFF. Flux creep is observed in the low current region where the Lorentz force is unable to depin the vortices. Some of the vortices are able to detach due to the available thermal energy $k_B T$ [55]. With increasing current density, this portion increases, leading to an exponential increase of the electric field [56]. A resulting equation for E as a function of j derived from a hopping equation of Arrhenius type is

$$E = 2Blv_0 e^{\frac{-U_0}{k_B T}} \sinh \frac{U_0 j}{j_c k_B T}, \tag{1.15}$$

where l is the distance a vortex moves in a single hop, v_0 is the hopping attempt frequency, U_0 is the average pinning barrier height [57].

From the theories of collective flux creep [58] and vortex glass [59] the current voltage relationship and the effective pinning potential is [60]:

$$E(j) = E_c e^{\frac{-U(j)}{k_B T}}, \quad U(j) = U_0 \frac{(\frac{j_c}{j})^\alpha - 1}{\alpha} \tag{1.16}$$

if $\alpha \to 0$ one gets a power law E-j relationship:

$$E = E_c \left(\frac{j}{j_c}\right)^n. \tag{1.17}$$

Here E_c is the critical electric field ($1\,\mu V/cm$ by convention), j_c is the critical current density at which the E_c is reached and n is the parameter describing the "hardness" of the superconducting/normal transition. High n values model hard, Bean-like superconductors, while low values approximate flux creep regime. This relationship has been observed in many experiments [61–64]. The power law relationship neglects the Meissner state, thus, it is valid only in situations dealing with strong magnetic fields and large currents. Using this substitution law, one can derive an equation for magnetic field diffusion in type II superconductors:

$$\nabla \times \left(\frac{E_c}{{j_c}^n} |\nabla \times \mathbf{H}|^{n-1} \nabla \times \mathbf{H} \right) = -\mu \frac{\partial \mathbf{H}}{\partial t}. \tag{1.18}$$

This equation is a nonlinear diffusion equation with a magnitude-dependent diffusion rate.

1.3 Magnetic field diffusion in railguns

The magnetic field diffusion is commonly encountered in electromagnetic launchers. An electromagnetic launcher (EML) is a device that transforms electromagnetic energy into linear kinetic energy. Railguns are promising EML platforms for many applications like space launch [65–67], materials research [68] and defence [69]. Railguns are the simplest imaginable linear motors and consist of at least two rails and a sliding armature. The working principle can be seen in Figure 1.3.1. Injection terminals at the breech of the device supply pulsed (usually) current through the rails. The current flows from one rail to

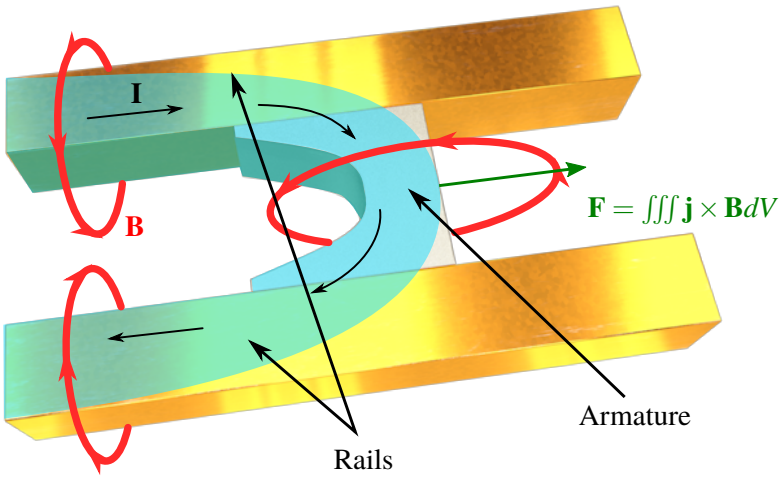

Figure 1.3.1. A conceptual view of a simple railgun and its working principle.

the other through the armature forming a closed current loop. Because of the interplay between the magnetic field and the current, a force appears on the rails, the armature and the connecting cables. This force is directed in the outward direction from the closed loop. The armature is free to slide, thus it is accelerated once the driving force overcomes friction.

There are two main types of railguns: a simple railgun and an augmented railgun. A simple railgun relies on the main rails upon which the armature slides to produce the magnetic field for the acceleration. This requires high currents to produce considerable force. The force in a simple railgun can be estimated from the railgun force equation [70]

$$\mathbf{F} = \frac{\mathbf{L}' I^2}{2}, \tag{1.19}$$

where $\mathbf{L}'$ is the inductance gradient of the coilgun.

To reach hypervelocities, simple railguns are operated using currents of hundreds of kiloamperes or even megaamperes and produce magnetic fields in the order of tens of teslas [71–73]. The simultaneous existence of large electrical current densities and friction forces damages the rails and reduces their lifetime [74, 75]. Another, more complicated railgun design, is an augmented railgun. In an augmented railgun, in addition to the magnetic field generated by the driving rails themselves, an external magnetic field is used. This additional field results in a higher propelling force acting on the projectile for the same

armature current. It allows for an operation at a lower current, meaning lower Joule heating and the ability to use a wider selection of power supplies. The augmentation can be realized in several ways e.g., permanent magnets [76], persistent mode superconducting electromagnets [77], or pulsed electromagnets [78–81]. In a case where an external parallel augmentation coil is used the equation for force becomes [82]

$$\mathbf{F} = \frac{\mathbf{L}' I^2}{2} + \mathbf{M}' I I_a, \tag{1.20}$$

where $\mathbf{M}'$ is the gradient of the mutual inductance between the railgun and the augmentation coil and I_a is the current flowing through the field augmenting coil.

The size of the power supply is, probably, the main aspect limiting the wider application of railgun systems. Currently, the most widely used power supplies are based on capacitor banks [83]. Efforts to reduce the size of the power supply lead to inductive energy storage [84–86]. A relatively new concept is the self-supplying railgun. It combines a railgun with an inductive energy storage by using the magnetic field to both supply current to the rails and to augment the field. For this purpose a Superconducting Magnetic Energy Storage (SMES) can be used and this setup is called the Superconducting Self-Supplying Electromagnetic Launcher (S^3EL) [87–90]. All of above mentioned electromagnetic railgun designs are characterized by different magnetic field configurations, thus, different field distributions under MFD are observed during their operation. The investigation of this process allows to evaluate the current distribution in the rails and the electromagnetic impact on the armature and the payload. That is especially important if the EML is used to accelerate smart electronic payloads. The bore of a railgun is a harsh environment due to high mechanical loads, temperature gradients and transient magnetic fields. It was shown, that electronics can survive being accelerated by a simple railgun and even record data live [91]. This is possible because of the rapid decrease of MF in front on the current carrying armature. It was also demonstrated that electronic components can be damaged by the transient magnetic field in the proximity of a railgun if placed carelessly [92]. In an augmented railgun magnetic fields would be present even in front of the armature. If the augmentation is pulsed, the payload would experience transient magnetic fields which can be harmful due to the induced electromotive force (emf). In launchers of this type, an addition of magnetic screening should be considered for the protection

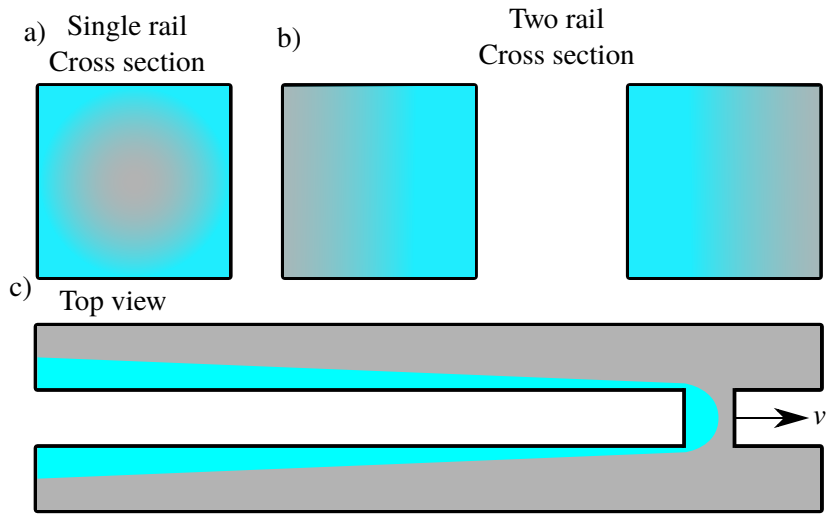

Figure 1.3.2. Illustration current density distributions affected by skin effect (a), proximity effect (b) and velocity skin effect (c). Grey represents low current density and aqua - high.

of sensitive payloads.

The operation of railguns intrinsically relies on the time dependent magnetic field. Highly conductive materials, such as copper and aluminium, are used in railguns to minimize the resistive losses. They have low magnetic diffusivities. For this reason, in a time frame that these devices operate (up to tens of milliseconds), the magnetic field does not reach an equilibrium configuration and MFD is an important aspect for the efficiency of a device. Magnetic field diffusion in railguns has been under extensive research in the past decades. Three main effects that are caused by the MFD are encountered under pulsed current operation of the railgun: skin effect, proximity effect, and velocity skin effect. The skin effect is a current concentration at the surface of a conductor caused by the pulsed current flowing through the conductor (see Figure 1.3.2 a). For a sinusoidal current, the current density decays exponentially with distance from the surface with a characteristic length called the skin depth [70]:

$$\delta = \sqrt{\frac{2}{\mu\sigma\omega}}, \tag{1.21}$$

where ω is the angular frequency of current oscillations.

The Proximity effect appears as a result of the magnetic interplay between two or more conductors. Under pulsed current conditions, rails generate time

varying MF. If the rails are close together, the generated field will be strong enough to cause current redistribution. This magnetic coupling of the rails causes the current to concentrate near the surface that is closer to the other rail (see Figure 1.3.2 b). Proximity effect in closed circuits will be accompanied by skin effect, so the observed current distribution is the superposition of both. This effect is predicted in several theoretical investigations [82, 93, 94] and has been observed experimentally by measuring currents through differently spaced brushes of a brushed armature in static [95] and low velocity [96] cases. Recently, a method to reconstruct current density distribution in a rail from a set of magnetic field measurements was proposed [97]. The reconstruction of experimental data revealed the proximity effect and was in good agreement with direct current measurements of individual filaments of a test launcher.

Velocity skin effect (VSE) is observed in railguns at high armature velocities. It was initially observed indirectly as an efficiency roll-off of a railgun when increasing the shot energy [98–100]. It was later suggested that this roll-off is caused by the velocity skin effect [3]. This conclusion was drawn from careful theoretical analysis of experimentally observed launcher efficiency vs. muzzle velocity curves. VSE causes a current concentration near the inner faces of the rail (similarly to proximity effect), in turn increasing the resistance of the system and causing local heating of the rails (see Figure 1.3.2 c). VSE is caused by the MFD in response to the changing magnetic field introduced by the motion of the armature and becomes more apparent with increasing armature velocity. In addition, current is expected to localize near the trailing edge of the armature, further increasing the resistance of the system, scaling as $v^{3/2}$ with velocity [101]. Current concentration in the rear end of a moving armature was observed experimentally in a U shaped armature by reconstructing the current density distribution from magnetic field measurements made using B-dot sensors[1] [102] (velocity range 600-1100 m/s).

A new generation of pulsed magnetic field measurement technologies that simplified the analysis of the obtained data together with rapidly increasing computing power and more sophisticated modelling software accelerated the MFD research in electromagnetic launchers. The proximity and skin effects were directly observed when measuring the magnetic field in close proximity to a rail using a CMR B-scalar sensor array [103, 104]. Later, using similar

[1] B-dot sensor is a magnetic magnetic field sensor that measures the change of the magnetic field. They are constructed from coils of conductive wire and produce voltage due to magnetic induction. The name B-dot comes from the notation of time derivatives i.e., $\partial \mathbf{B}/\partial t = \dot{\mathbf{B}}$.

sensors, the magnetic diffusion was even measured inside of a rail [7]. The measurements were in good agreement with theoretical results that take MFD into account. Detailed coupled physics models have been developed to describe the behaviour of railgun systems, e.g. electromechanical [105, 106], and electrothermal [107–109].

Payloads in a railgun can range from simple metal rods [110, 111] to complex smart projectiles [91] or even nanosatellites [67]. MFD is especially important if EML is used to accelerate smart electronic payloads. Recently, a new design of a multi-rail hexagonal railgun with hexagonal rail arrangement [5, 6] was introduced. The main advantage of this device is its versatility as the setup can be arranged in a segmented, multishot, or augmented configuration. The magnetic field diffusion, however, was not investigated in such a railgun design. Research of the magnetic effects in close proximity to a conductive cylindrical payload inside a hexagonal railgun in an augmented mode is of importance to determine the effectiveness of these payloads as conductive MF screens for the protection of smart electronic payloads. The time-dependent magnetic field distribution calculated using the finite element method combined with experimental measurements performed using a CMR-B-scalar sensor array can be used as an effective tool. This was the first main task of the present thesis.

1.4 Magnetic field diffusion in type II superconducting cylinders

Superconducting cylinders (bulk and hollow) are used in permanent magnets [9–11], magnetic shields [12–14], fault current limiters [15–18] and superconducting high-energy particle accelerators [19]. As well as conventional ferromagnets, these superconductors can be magnetized as bulk permanent magnets with current record of 17.6 T trapped into a silver containing $GaBa_2Cu_3O_{7-x}$ bulk at 26 K [112]. Also, there is a great interest in these materials to be applied like magnetic field sources [113] in magnetic bearings [114–116], electric generators [117–119] and motors [120–122]. For the operation and testing of these devices, it is very important to know how the pulsed magnetic flux penetrates into the superconductor. Due to the high price of high-temperature superconductors (HTS) and the unforgiving results of design flaws (catastrophic quenching and mechanical failure), it is preferable to model the behaviour of the device before its production.

The electrodynamics of type II superconductors is nonlinear due to their E-j relationship (eq. 1.17) and cases where analytic solutions exist are scarce and mainly exist for the critical state approximation [123]. In other cases, nu-

merical techniques are employed. Various eddy current problem formulations suited to handle different superconductor application scenarios or to improve computation times have been proposed [124–128].

An extensive study of the magnetic field diffusion and its effects in type II superconductors has been carried out by Ernst Helmut Brandt in a series of papers covering various superconductor geometries (discs and rings [23, 60, 129] and rectangular bars [130–132]). In these papers, he proposes a numerical method (sometimes called the Brandt algorithm) that solves for the current density and therefore limits the calculation to the volume of the superconductor. His method is based on an integral equation relating the temporal change of local current density to the total local magnetic field as:

$$\frac{\partial \mathbf{j}(\mathbf{r},t)}{\partial t} = \frac{1}{\mu_0} \iiint Q^{-1}(\mathbf{r},\mathbf{r}') \left[\mathbf{E}(\mathbf{j}(\mathbf{r}',t)) - \frac{\partial \mathbf{A}_a(\mathbf{r}',t)}{\partial t} \right] dV, \tag{1.22}$$

where Q^{-1} is an integration kernel that is an inverse to the Laplace equation's Green's function and $\mathbf{A}_a$ is the magnetic vector potential due to external sources. $\mathbf{E}$ here is the electric field, that is replaced by an E-j relationship. For a superconductor, the power law (eq. 1.17) is assumed to incorporate flux creep. The integral is solved by discretizing the superconducting domain into elements, forming a matrix from the integral kernel, and summing over all elements. The time-dependent current density is obtained by $\mathbf{j}(t+\Delta t) = \mathbf{j}(t) + \partial \mathbf{j}(t)/\partial t \Delta t$. Brandt's method can be interpreted as a system of magnetically coupled circuits where the kernel represents mutual inductances between them (diagonal terms correspond to self inductance) [130].

Brandt's method was successfully applied to study magnetic shielding properties of high-T_c superconducting hollow cylinders. Denis et. al. [28] measured the attenuation of axial DC and AC fields inside a bismuth strontium calcium copper oxide $Bi_2Sr_2Ca_2Cu_3O_{10-x}$ (Bi-2223) tube and compared the measurements with simulation results. The results were in good agreement and revealed the effects that tube geometry has on the shielding factor. Fagnard et. al. [133] simulated the magnetic field response inside a superconducting tube exposed to time-dependent magnetic fields in transverse and axial directions with various magnetic field ramp rates. In their simulations, they accounted for $j_c(B)$ relationship by the use of the Kim model [134]. Simulations showed that the magnetic field limit for high shielding factors depends on the ramp rate, which was confirmed by experiments carried out with Bi-2223 supercon-

ducting tubes. The influence of the ramp rate was attributed to flux creep and the exponent n that describes it as well as to the $j_c(B)$ relationship.

Another method for calculating eddy currents in type II superconductors with cylindrical symmetry in critical state was proposed by Araujo-Moreira et. al. [135] In this model, they subdivide the superconductor into rings and calculate their self and mutual inductances. In its essence, this method is a special case of Brandt's method for cylinders. It differs as Beans critical state is implemented instead of a continuous power law E-j relationship. The eddy current distribution under a given magnetic field is found by iterating the current flowing through each ring until a minimum magnetic field energy configuration is found. The total magnetic energy of one element in this description is [136]:

$$E_i = \frac{1}{2}L_i I_i^2 + I_i \sum_{\substack{j \\ j \neq i}} M_{ij} I_j - 2\pi I_i \mu_0 \int_0^{r_i} r H_z dr. \tag{1.23}$$

Here L_i is the self inductance of a ring segment, I_i is the current through an element, M_{ij} is the mutual inductance between rings i and j. In Bean's critical state, it is assumed that the current flowing in the ring can only by zero or $I_c = j_c \Delta r \Delta z$, where Δr and Δz are the discretization step sizes. This reduces the amount of iterations needed by lowering the total number of possible system configurations. Later, the magnetically coupled superconductor loop model was extended to include the $j_c(B)$ [137]. This method was applied to calculate magnetic hystereses of superconducting cylinders [135] and rings [138]. Recently, this method was applied to axial and radial arrays of superconducting rings by Liu et. al. [136]. They systematically investigated the magnetization and levitation forces and how they are affected by the geometry of the array.

The appearance of sophisticated software that uses the Finite Element Method (FEM) being capable of dealing with highly nonlinear equations attracted the attention of researchers. FEM techniques are now the most commonly used and developed methods and can be applied to superconducting material problems using a variety of formulations [139]. In addition, FEM is more flexible in that it allows more complex shapes to be discretized. A-V or A-ϕ formulation is a widely used description of eddy current problems both in normal conductors and superconductors [140, 141]. The equation governing the evolution of vector potential is (1.9) with an added constraint:

$$\nabla \cdot \left(\sigma(\mathbf{A}, \phi) \left(\frac{\partial \mathbf{A}}{\partial t} + \nabla \phi \right) \right) = 0. \tag{1.24}$$

This formulation is convenient when modelling the magnetic behaviour of devices connected to electrical circuits as both voltage and current can be imposed. In the power law description of type II superconductors, the resistivity vanishes when current density is equal to zero. Since $\sigma = 1/\rho$, conductivity becomes undefined. To avoid stability issues, a very small resistivity ρ_0 is added [142] so that:

$$\rho(E) = \frac{E_c^{\frac{1}{n}}}{j_c}|E|^{\frac{n-1}{n}} + \rho_0 \tag{1.25}$$

The A-V formulation has been successfully applied to model a magnet-superconductor interaction [143, 144] and AC losses in HTS tapes [142, 145]. This approach was compared to Brandt's method for superconducting tubes by Lousberg et. al. [146] to reveal satisfying agreement. Using the A-V formulation, Lausberg et. al. [12] numerically analyzed the shielding capabilities of hybrid ferromagnetic/superconductor hollow tubes. Their analysis revealed that the use of such hybrid systems improves magnetic shielding properties than using only superconductor or only ferromagnetic materials and that the radial order of the layers influences both the magnetic field limit of high shielding factors and its decay with increasing field. Ohsaki et. al. [147] used the A formulation. to study pulsed field magnetization (PFM) of a bulk YBCO ring. In their model, they treated the critical current density as a function of both the magnetic field and the temperature $j_c(B,T)$. Joule heating was accounted for by coupling the electromagnetic and thermal problems.

Another common group of formulations is based on the current density potential $\mathbf{T}$, defined by $\mathbf{j} = \nabla \times \mathbf{T}$. This approach is usually used for high aspect ratio problems like superconducting tapes. It is very powerful as it allows to treat the superconducting layer of the tape as a one dimensional object and to specify net current flowing through it as

$$I = (T_2 - T_1) \cdot d, \tag{1.26}$$

where T_1 and T_2 are the values of $\mathbf{T}$ at the ends of the line representing the cross section of the tape and d is the thickness of the superconducting layer. Since the magnetic field needs to be ralated to $\mathbf{T}$, coupled formulations are used. Most

common are T-Ω (Ω is the scalar magnetic field potential) [148, 149]

$$\begin{aligned} &\nabla \times \rho \nabla \times \mathbf{T} = \mu \frac{\partial}{\partial t} (\mathbf{H}_0 + \mathbf{T} - \nabla \Omega) \\ &\nabla \cdot (\mu (\mathbf{H}_0 + \mathbf{T} - \nabla \Omega)) = 0 \end{aligned} \tag{1.27}$$

and T-A formulations [126, 127, 150]

$$\begin{aligned} &\nabla \times \rho \nabla \times \mathbf{T} = \mu \frac{\partial \mathbf{B}}{\partial t} \\ &\nabla \times \frac{1}{\mu} \nabla \times \mathbf{A} = \mathbf{j}. \end{aligned} \tag{1.28}$$

T is defined in electrical current carrying parts while Ω or **A** are calculated in the entire solution domain.

Even though the 1D approximation of the tape reduces the number or elements needed, the simulation of magnets with large numbers of windings and layers remains computationally intensive. Berrospe-Juarez et. al. [127] showed how to greatly reduce computation times when using the T-A formulation. They introduced the multi-scale approach, where only a part of the windings is analysed and the current density in the rest is interpolated from them, and the homogenization approach, where the layer of tapes is treated as a bulk. The multi-scale method lowered the computation time 9 times and homogenization by 18 with 0.3% and 2% relative error in magnetization losses in comparison to the full T-A model.

The most widely used description in HTS modelling today is the H formulation (H-form) [122] (equation 1.18) which is based directly on Maxwell's equations. The implementation of this model is intuitive since the variables are physically measurable quantities. This method is also numerically accurate as no post-processing of the results is needed. On the other hand, it requires to define a dummy resistance for the air domain. This formulation has been successfully applied for the calculation of AC losses [151–154], estimation of tape DC properties [155–157], magnetization of bulk HTS [139, 158, 159] etc. Ainslie et. al. [160] performed a comprehensive study on pulsed field magnetization (PFM) of HTS bulks. In their model, they coupled the 3D eddy current problem in H-formulation with the heat equation to account for the heating of the HTS sample. Heating effects on the properties of the HTS were taken into consideration by implementing $j_c(T)$ relationship. In addition, the effects of an inhomogeneous critical current density were investigated and were revealed

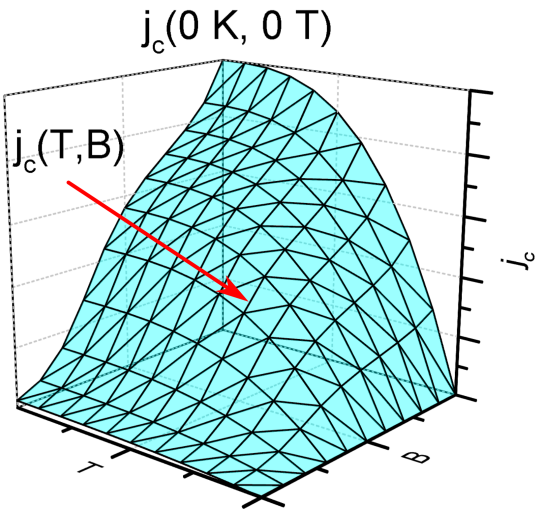

Figure 1.4.1. Critical surface of a superconductor

to distort the profile of the trapped magnetic field and to reduce its amplitude due to localized heating. Zou et. al. [161] also investigated the PFM of HTS, but in their model they also included $j_c(B)$ dependence. Sass et. al. [162] applied H-form to model the dynamic levitation forces acting between a permanent magnet and YBCO bulks and second generation (2G) HTS tape stacks as the distance between the magnet and the superconductor was changed in time. The results were in good agreement with experimental data. Later, Quéval et. al. [163] took a similar approach to model the levitation forces between permanent magnet arrays and HTS bulks and tape stacks. Their analysis covered dynamic forces in cases with both vertical and lateral movement and good agreement between simulation and experiments was achieved.

The critical current density is a function of both the magnetic field and temperature. The properties of superconductors can be illustrated by a critical surface that relates temperature, magnetic field and critical current density (see Fig. 1.4.1). These relationships need to be accounted for to accurately model processes that happen over a wide range of magnetic fields and temperatures. Probably the most often used description for $j_c(B)$ is the Kim model [164]

$$j_c(B) = \frac{j_{c0}}{1 + \frac{B}{B_c}}. \tag{1.29}$$

Here j_{c0} is the critical current density at zero field and B_c is a characteristic

magnetic field value. For $j_c(T)$, an empirical relationship is used

$$j_c(T) = j_{c0}\left(1 - \left(\frac{T}{T_c}\right)^2\right)^m . \tag{1.30}$$

j_{c0} here is the critical current density at 0 K, T_c is the characteristic transition temperature. m is a constant that is usually set to 1.5 [160, 161, 165] or 2 [147, 166].

The above presented magnetic diffusion studies were mainly performed on bulk type II superconductors (cylinders, rings and tubes). However, thin-walled superconducting tubes (or pipes) are used for many other hollow cylinder applications. This thin-walled tube configuration allows to reduce the high costs of superconducting material when it is used for magnetic shields or for "smart superconducting grids" delivering both chemical fuel (liquid H_2 that doubles as the coolant) and electricity via a superconductor [24, 25]. Long pipes made from MgB_2 by hydro-extrusion [25] or by coating paint [26] have been proposed. Pipes coated with YBCO ($YBa_2Cu_3O_{7-x}$) were also envisioned using the metalorganic decomposition technique [27]. In such cases, it is important to have non-destructive means with which to evaluate the intrinsic properties of the superconducting material. Usually the properties of interest are the maximal magnetic field (B_c) that can be screened by the superconductor (not to be mistaken with the thermodynamic critical field), the critical current density (j_c) vs. the magnetic field (B) dependence and the electric field (E) vs. the current (j) power law exponent (n).

These parameters were extracted for various cylinder configurations by employing the method described in [60]. This method was applied for a systematic investigation of the magnetic field responses of tubes with different dimensions and different magnitudes of the applied field [28]. In [133], Fagnard et. al. investigated the magnetic field inside the cavity of thin-walled superconducting hollow cylinders. In order to validate the numerical results, an experimental magnetic field penetration study was conducted using a Pb-doped B-2223 ($Bi_{1.8}Pb_{0.26}Sr_2Ca_2Cu_3O_{10+x}$) tube and different transient magnetic field sweep rates. The theoretical approach used in [28, 60] was based on the calculation of the current distribution in the bulk of the superconducting material, which, however, is the result of discrete coupled superconducting circuits carrying different currents in different regions along the radial direction of superconducting tube. Thus, for tubes with various configurations, it is necessary to choose specific discretization algorithms, which makes the calculation procedure de-

pendent on the tube geometry. Fortunately, for a geometry like the thin-walled tube, this description can be simplified without losing the accuracy of the calculation procedure. Since the walls are thin, it is, thus, possible to assume that there is no spatial variation of the current density throughout the thickness of the wall. Joule heating can also be neglected, as the superconductor is effectively cooled. Hence, measuring the magnetic field inside a thin-walled superconducting tube is particularly suited to accurately determine the properties of the superconducting material.

The next task of this thesis was the development of a non-destructive method for quick characterization of type II superconducting materials shaped as thin-walled tubes.

1.5 Properties of thin-film type II superconductors

As it was shown in section 1.2, the diffusion of a pulsed magnetic field induces electrical current at the surface of type II superconductors. A current caused by high magnetic field transients can exceed the critical current causing the superconductor to get into the flux flow dissipative state, which is associated with heating and various electrical instabilities. These phenomena were intensively studied since the discovery of HTS materials as large efforts were made to create a technology for a commercially viable lossless transfer of electrical energy. HTS materials are brittle ceramics and are not malleable like copper, so to compete with it, a technology allowing to have flexible HTS wires was needed. The first generation (1G) HTS wires are manufactured by powder-in-tube (PIT) technology using Bi-2223 superconductor and silver [167]. This method, however, is not optimal due to the large amount of silver needed which increases the cost. Furthermore, Bi-2223 quickly looses its ability to carry current in a magnetic field at the temperature of liquid nitrogen [168], which limits the application of 1G wires in magnets. The second generation (2G) HTS wires use epitaxial layers of YBCO deposited on thin metallic tapes. These tapes use significantly less silver and YBCO exhibits better in-field performance, allowing these tapes to be used in electromagnets and electric generators [169].

The most obvious difference between bulk superconductors and thin film superconductors is their geometry. This difference, however, causes various effects in thin films that are not seen in bulks. One of these effects is the dependence of the critical current density on the thickness of the YBCO film, which was first reported in [170]. It was obtained that the j_c of the tape is several times higher than that of a bulk and decreases rapidly as the thickness

of the tape increases from hundreds of nm to a few μm. Foltyn et. al. [171] presented a simple model to explain this effect. They argued that j_c is a function of tape thickness that goes from j_{cs} at the interface with the substrate to j_{cb} (bulk value) over some transitional length and that the experimentally observed j_c is the average over the tape's thickness. The reason for this, they argued, is the induced strain at the interface between the superconductor and the substrate. They showed that a thickness independent j_c can be achieved by using $NdGaO_3$, a low lattice mismatch substrate [172]. They also showed that j_c can be controlled with the thickness of a $PrBa_2Cu_3O_{7-x}$ (good lattice match) buffer layer [173], confirming the interface enhancement hypothesis. From this, they attributed the thickness effect to an excess pinning of the magnetic vortices by the misfit dislocations present at the interface between the layers. A significant improvement was observed in YBCO/CeO_2 multilayered structures where the j_c was maintained close to the j_{cs} due to the reintroduction of lattice stress [168]. Kim et. al. [174] showed that a nearly constant $j_c(t)$ can be achieved with metal-organic deposition as the deposited layers are porous and strong 3D pinning is obtained through out the entire thickness.

Just as for bulk HTS, the performance thin-film HTS decreases in stronger magnetic fields and at higher temperatures. In general, three regions are discerned. The so-called plateau region is observed in low magnetic fields and, in this region, the critical current density weakly depends on the applied field [168, 175]. The influence of the magnetic field generated by the current in the superconductor (called the self-field) dominates over the external field, so it has little effect on the measured j_c. At higher magnetic fields follows, the power-law region follows where $j_c(B) \propto B^{-\alpha}$ which ends when the field amplitude approaches the irreversibility field at which the vortices depin and a rapid decrease of j_c is observed. A phenomenological description of $j_c(B)$ that covers all three regions was provided by Aytug et. al. [176]

$$j_c(B) = j_{c0}\left(1+\frac{B}{B_0}\right)^{-\alpha}\left(1-\frac{B}{B_{irr}}\right)^{2}. \tag{1.31}$$

Here B_0 represents the crossover field between the plateau and the power-law regions and B_{irr} is the irreversibility field.

Another feature of epitaxial HTS layers is the anisotropic response to the magnetic field. The in-field critical current density varies with the direction of the applied field. $j_c(\theta)$ (θ is usually defined as the angle between the applied field and the normal vector of the tapes surface) usually has a peak when

the magnetic field is applied perpendicular to the surface of the layer [177]. This effect is observed because of the correlated flux pinning by the planar or linear defects parallel to the substrate [168]. Aytug et. al. [176, 178] investigated the effects of substrate decoration by Ir nanoparticles and obtained that such substrate treatment results in higher, more isotropic $j_c(\theta)$. Matsumoto et. al. [179] observed a broad peak centered at $\theta = 0^\circ$ (in addition to a sharp peak at 90°) in samples where the Y_2O_3 nanoislands were deposited on the substrate prior to the YBCO deposition. These nanoislands introduced linear defects perpendicular to the tapes surface and introduced collective pinning in this direction. Similar results were obtained by Goyal et. al. [180] in $BaZrO_3$ doped YBCO layers. The angular dependence of HTS films limits their performance in solenoid electromagnets due to perpendicular MF components at the solenoid ends. An isotropic $j_c(\theta)$ with high maximum value is required. Such properties were achieved by Horide et. al. by introduction of both $BaSnO_3$ nanorods oriented perpendicular to the substrate and Y_2O_3 nanoparticles [181].

Current voltage relationships (IV's) of thin film high temperature superconductors measured under current bias exhibit a discontinuous jump once the current reaches a certain value I^*, called the quench current [182]. Several mechanisms have been proposed to explain this phenomenon. In [182,183], the observed discontinuity in YBCO films was explained by a decreasing flux flow viscosity due to a nonequilibrium quasiparticle distribution within the vortex core at high vortex velocities, an effect theorized Larkin and Ovchinnikov [184]. In their theory theory, the flux flow instability is an intrinsic feature of the IV curve. Peterson et. al. [185] found that the DC current biased YBCO IV's in addition to having a "jump" are also hysteretic and do not return until the current through the sample reaches I_m. Under voltage bias, the measured IV's had an S shape with negative differential resistance region. In this work, the observed behaviour was explained by a formation of a hotspot - a normal region within the layer. The discontinuity then appears with the formation of the hotspot. In the hotspot theory, a normal region with resistivity equal to the normal state resistivity is maintained by Joule heating caused by the current flow until the heating power becomes insufficient to maintain the hotspot above T_c, explaining the observed hysteresis. Hotspot theory was developed for low-T_c superconductors by Skocpol et. al. [186] Jakob et. al. [187] showed that the observed discontinuity disappears if the measuring pulse duration is reduced (from few ms to 50 μs) and a smooth transition is achieved. Maza et. al. [188,189] argued that the discontinuous jump can be explained purely as an

electrothermal instability with uniform heating of the tape when the intrinsic IV curves are smooth and temperature dependent:

$$E(j,T) = E_0(T)\left[\frac{j}{j_0(T)} - 1\right]^n, \tag{1.32}$$

$$E_0(T) = E_1\left(1 - \frac{T}{T_c}\right)^{n_0}, \tag{1.33}$$

$$j_0(T) = j_1\left(1 - \frac{T}{T_c}\right)^{n_0}. \tag{1.34}$$

In this theory, the observed jump is caused by thermal runaway and is not an intrinsic feature of the IV curve. They obtained a good agreement between thermal theory and experiment with values of E_1 j_1 n_0 and n evaluated by fitting the low current region of the measured IV's where thermal effects are minimal. Kiss et. al. [190] investigated quench dynamics of HTS tapes using ~ 100 μs current pulses. They obtained, that a rapid rise in temperature can occur even during ~ 100 μs duration measurements for sufficiently high currents. In any case, the origin of the observed transition remains an open topic [191–194].

One way to minimize Joule heating at high electrical currents is to reduce the duration of the current pulse. Switching from superconducting to resistive states of thin film YBCO was investigated by Balevičius et. al. using 3 to 80 to ns electrical pulses. In [195], they showed that the transition to the resistive state in YBCO films is of subnanosecond duration and happens synchronously with the applied voltage impulse. This initial rise in resistance is immediately followed by a much slower rise attributed to Joule heating. Using 3-10 ns pulses with a 0.4 ns rise time showed that the IV's of these tapes are arrays of straight segments whose number and slope depend on the temperature [196]. IV's measured at different points on the sample had similar structures with segments starting at same currents indicating homogeneous voltage drop along the sample and contravening hotspot theory. Measurements using longer pulses (80 ns) showed that IV's do not depend on the pulse duration only until a certain value I_{c1}. Above this value, the response becomes time-dependent and the IV's change with the choice of time instant that they were evaluated at. IV's evaluated later after the beginning of the pulse lose the segmented linear shape (are rounded) and show higher voltages that approach the normal state resistivity [30]. IV's in the high power region were investigated in [197] using 60 ns pulses. It was found that the line array structure persists

until up to several times higher than critical currents, until the sample is irreversibly destroyed at a damage current I_d. In the presented data, the samples never their reached normal state resistance before the damage occurred. Damages to the films had a characteristic shape - one main narrow (compared to the width of the tape) streak perpendicular to the direction of the current flow and a smaller branchlike structure originating from it. Based on these results, it can be argued that thermal effects start to influence the IV's of HTS tapes <10 ns after the excitation with a high current current and that to obtain an isothermal IV voltage pulses with a short risetime (<1 ns) are needed. The IV should be evaluated right after the rise time of the voltage pulse.

Usually, the duration of magnetic field pulses that II superconductors are exposed to is in the range of milliseconds or tens of milliseconds [20, 21, 161], therefore the duration of the overcritical current pulse induced in type II superconductor is of the same order. In addition, the overcritical current regime is realized at an external magnetic field, therefore, a significant power dissipation can appear which can cause considerable Joule heating of the superconducting material. This can deteriorate the performance of superconducting magnetic field screens and inductive fault current limiters [17]. In these cases, heating could be decreased by preparing films on high thermal conductivity substrates. Among various substrates, Al_2O_3 is very attractive [198] with a low dielectric constant ε that ranges between 9.164 and 9.424, low high frequency dielectric loss that is accompanied with high thermal conductivity (≈ 20 W/m·K close to the temperature of liquid nitrogen [199]). However, specific buffer layers with matched lattice constants are needed to deposit conventional high-T_c superconductors like YBCO or BSCCO. For this reason, the third goal of this thesis was the investigation of electric properties of thin YBCO films prepared by the Pi-MOCVD technique on Al_2O_3 substrate with CeO_2 sublayer when they are influenced by DC currents, magnetic fields and short high power electrical pulses.

1.6 Magnetic field diffusion in coilguns

Coilguns, as the name suggests, use coils to accelerate objects. Depending on which projectile properties they use, two groups can be identified: reluctance coilguns and induction coilguns [200]. Reluctance coilguns use ferromagnetic projectiles and the attractive force between them and a magnetic field source. Induction coilguns employ conductive armatures. Figure 1.6.1 demonstrates the operation of a pancake coilgun. Due to the Lentz's rule, counter currents

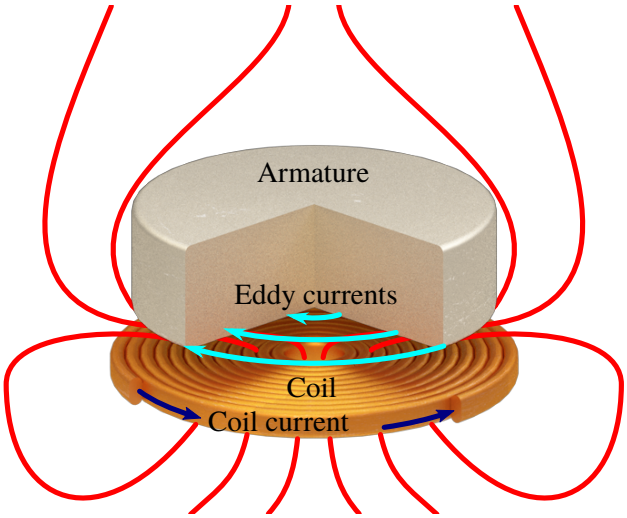

Figure 1.6.1. A conceptual view of a single-stage coilgun with a pancake coil and its working principle. The induced eddy currents interact with the applied field producing force in the opposite direction of the magnetic field gradient.

are induced inside a conductive armature to oppose the magnetic field change. These currents, in the presence of a magnetic field, accelerate the armature in the opposite direction of the magnetic field gradient. In a simplest coilgun case of two coaxial current carrying loops, the force generated between them is [38]:

$$\mathbf{F} = I_1 I_2 \mathbf{M}', \tag{1.35}$$

where I_1 and I_2 are respective currents in the loops and $\mathbf{M}'$ is the mutual inductance gradient between them. In a general case, the total force acting on an armature is determined from:

$$\mathbf{F} = \iiint_{\Omega} (\mathbf{j} \times \mathbf{B})\, dV, \tag{1.36}$$

Ω here is the volume of the armature.

A major advantage of coilgun systems is that they do not require sliding electrical contact with the projectile for current injection like in the railgun case. This cuts down on friction force, barrel erosion and electric arcing. A big drawback is scalability. Single-stage coilguns are limited in the amount of energy they can transfer [38] and multistage coilguns require a complicated power supply system that follows the motion of the armature through the barrel [39]. Nevertheless, various coilgun systems have been developed. A 45 stage coilgun

was built in Sandia National Laboratories that accelerated 340 g projectiles up to 406 m/s [201]. Lockheed Martin and Sandia National Laboratories developed a prototype electromagnetic launcher for missile preacceleration capable of accelerating a mass of 650 kg to a velocity of 12 m/s within 100 ms [202]. Kaye et. al. [37] reported on a project to adapt a coilgun system for conventional mortar rounds in order to achieve greater muzzle velocities and to reduce their variation in comparison to a conventional propellant mortar. Researchers of French-German Research Institute of Saint-Louis have developed steerable active armor system that launches an interceptor using coil accelerators [203,204]. A similar device was built and modelled by Zhang et. al. [205]. Coilguns are also being considered for either land or naval based artillery [39, 206].

Induction coil launchers generate current in the armature by magnetic induction. The applied field, with time, diffuses into the armature due to the finite resistivity of an armature material. In synchronous wave coilguns, tightly packed multistage launchers where the magnetic field follows the armature as it is accelerates, magnetic diffusion causes the effect called the armature capture [207]. The eddy currents weaken and the propelling force decreases. In the extreme case, no force is produced if the armature is completely saturated [208]. This puts a limit on how long the launch system can be if armature capture is not accounted for. To maintain the acceleration efficiency, the accelerating magnetic field wave is moved slightly faster than the armature by adjusting the coil firing times to follow the not yet saturated region of the armature. The velocity difference between the armature and the magnetic field wave is called the slip velocity. Slipping is effective until the entire length of the armature is saturated. To further accelerate the armature, the polarity of the current in the subsequent coils can be reversed with a correction in coil activation timing (equal to the slipping done) [209]. Reversing the direction of the applied field doubles the induced current and as a result - the driving force. The downside of this is that the induced current density is highly localized at the surface and causes significant heating and armature can begin to melt.

Another effect related to the magnetic field diffusion and the armature capture is magnetic braking. The armature experiences deceleration after passing a coilgun stage or when exiting the muzzle. This effect is caused by the reversal of the eddy current direction as a consequence of the decrease of the magnetic flux that has penetrated the armature. This can happen because of a decreasing current in the driving coil or in this case, due to the motion of the armature. Several studies investigating this effect have been carried out. Zhang

et. al. [39] compared the simulated performance of several armature geometries in a 4 stage coilgun. They showed that using a solenoid armature instead of a single-body tube (sleeve) reduces the braking force due to a more uniform current distribution. On the other hand, the solenoid armature did not survive experimental testing due to the decreased structural integrity. In [207], Su et. al. showed that the relative loss of velocity can be minimized by the choice of system parameters, like: armature mass, capacitance of the bank, crowbar diode resistance etc. However, the biggest improvement was observed with solenoid armatures instead of single-body tubes.

Type II superconductors, as mentioned in previous sections, are intriguing materials that behave very differently from normal conductors. The nonlinear magnetic diffusion observed in these materials could be interesting in the context of electromagnetic launch. Because of their different properties, the use of these materials as armatures for electromagnetic launchers can reduce some of the limitations encountered when using normal conductors as well as cause some new unforeseen behaviour. At present, only a relatively small number of investigations of the electromagnetic launch of such superconducting armatures have been carried out compared to those which investigated the launch of armatures made from normal metals. Costa Branco et. al. [210] investigated a 4 stage linear coil accelerator with YBCO armature. They found that describing the armature as a pure diamagnet (superconductor in Meissner state) failed to explain the experimental results and that a more detailed description for the superconductor is needed. Calculations performed by Yang et. al. [43] investigated a single-stage induction coilgun with a premagnetized type II superconducting armature described in H formulation with (1.17) E-j and (1.29) $j_c(B)$ relationships. With their simulations, they demonstrated that a pre-magnetized superconducting armature (using field-cooled magnetization) can be accelerated more effectively by a pulsed magnetic field than an armature made from conventional metals (in this case aluminum). However, this method of acceleration is more complicated in comparison to using a non-magnetized superconducting armature as it adds a preparation stage that requires energy. Another drawback when using a magnetized armature is that it can be necessary to move the armature to the optimal trigger position after the premagnetization process [43]. Thus, a simple non-magnetized armature acceleration method is more preferable. However, up to now, parametric investigations of the electromagnetic launch of such armatures have not yet been conducted. The MFD process during this type of acceleration is the main factor that determines the

energy transfer from the coil to the armature and defines the ballistic characteristics of the armature.

For this reason, the final part of this thesis was the investigation of a vertical acceleration of a disc shaped single-domain YBCO armature using a single-stage pancake coilgun . Magnetic field dynamics measured using a CMR-B-scalar sensor together with displacement measurements were compared with theoretical modelling using H formulation and FEM.

2. RESULTS

2.1 Magnetic field expulsion from a conducting projectile in a pulsed serial augmented railgun

A novel design of a multi-rail hexagonal railgun [5, 6] is advantageous due to its versatility. The setup can be arranged in a segmented, multi-shot or augmented configuration, the latter being used for the purposes of the work presented here. In this chapter, magnetic field distribution in and around a cylindrical conductive payload placed inside an SR\3-60 hexagonal railgun in an augmented mode are investigated experimentally and theoretically. Time-dependent magnetic field distributions were calculated using finite element method (COMSOL Multiphysics AC/DC module). These calculations were compared with experimental measurements performed using a CMR-B-scalar sensor array.

The results presented in the following chapter were originally published in:
V. Vertelis, G. Vincent, M. Schneider, S. Balevičius, V. Stankevič, and N. Žurauskiene, "Magnetic Field Expulsion from a Conducting Projectile in a Pulsed Serial Augmented Railgun," *IEEE Trans. Plasma Sci.*, vol. 48, no. 3, pp. 727–732, Mar. 2020, doi: 10.1109/TPS.2020.2970764

2.1.1 Theory for the calculation of dynamic magnetic field distribution

To calculate the dynamic magnetic field distribution around a conductor exposed to a pulsed magnetic field, eq. 1.6 is employed. Dynamic magnetic fields enter a conductor via a diffusive process where eddy currents induced by a temporal change of the magnetic field cause the generation of a field opposing the change of the applied field inside the conductor (Lentz's rule). Due to the superposition of these fields, the net field is now reduced inside and near the sides normal to the field lines and increased around the sides of a conductor. The induced eddy currents decay with a specific time constant determined by the conductivity of the metal. As the current decays, magnetic field penetrates further into a conductor until a stationary configuration is reached. Now, if the external field begins to decay, the process reverses and the induced currents try to maintain the flux penetrating the sample.

To describe the problem mathematically, we need a set of Maxwell's equations:

$$\nabla \times \mathbf{E} = -\frac{\partial \mathbf{B}}{\partial t}, \tag{2.1.1}$$

$$\nabla \times \mathbf{B} = \mu \mathbf{j} \tag{2.1.2}$$

For low power railguns, where Joule's heating can be neglected, the conductor can be considered linear and isotropic, then using Ohm's law $j = \sigma E$ in (2.1.1) and $\nabla \cdot B = 0$ we arrive at the magnetic diffusion equation:

$$\frac{1}{\mu\sigma}\nabla^2 \mathbf{B} = \frac{\partial \mathbf{B}}{\partial t} \tag{2.1.3}$$

where μ and σ are the magnetic permittivity and the electric conductivity, respectively. This equation describes how the magnetic flux density behaves and changes in time inside a conductor. The quantity $(\mu\sigma)^{-1}$ is called the magnetic diffusion coefficient.

Conductors moving in a magnetic field generate electromotive forces. For our calculations we will consider the payload to be electrically isolated from completing a circuit, so that only the screening current is flowing inside the payload. During the operation of a pulsed augmented railgun, the external magnetic field is dynamic, hence the boundary condition for equation (2.1.3) is time dependent. Though analytic solutions exist for some geometries and field pulse shapes, numerical methods provide more flexibility.

If magnetic shielding is the main concern, the solution to equation (2.1.3) for a geometry of interest (e.g. a hollow cylinder) gives the full temporal and spatial magnetic field distribution. Using this enables to evaluate the shielding performance of the design i.e. penetration depth and the magnetic transients.

We are generally interested in the field distribution around the conductor during the magnetic pulse, but so far we've only got the internal part. To get the full induced field we need to insert the solution of (2.1.3) into (2.1.2) to get the current density distribution. The next step is to apply the Biot-Savart law:

$$\mathbf{B}_{\text{ind}} = \frac{\mu}{4\pi} \iiint_V \frac{\mathbf{j} \times \mathbf{R}}{|\mathbf{R}|^3} dV \tag{2.1.4}$$

where R is a distance vector from the position of the integration kernel to the point of interest ($R = r - r'$) and V is the volume of the sample. Combining B_{ind} with the external field gives the magnetic field distribution around a conductor in a pulsed magnetic field environment at a given moment.

In our calculations, a homogeneous augmentation field pulse with only a

Figure 2.1.1. The SR\3-60 railgun [6].

z component $B_z(t)$ was assumed. An experimentally measured magnetic field pulse was used as a boundary condition for the equation (2.1.3). The solution for the equation (2.1.3) is a function of coordinates and time. Since the field only has a z component, the induced current density will be equal to:

$$\mathbf{j}(t,x,y,x) = \frac{1}{\mu}\langle \frac{d}{dy}B_z(t,x,y,z), -\frac{d}{dx}B_z(t,x,y,z), 0\rangle \tag{2.1.5}$$

We put this expression for the current density into the equation (2.1.4) which we integrated numerically and get the field distribution:

$$\begin{aligned} &B(t,x,y,z) = \langle 0,0,B_z(t)\rangle + \\ &+ \iiint \frac{1}{|\mathbf{R}|^3}\langle J_y R_z, -J_x R_z, J_x R_y - J_y R_x\rangle dx'dy'dz' \end{aligned} \tag{2.1.6}$$

where $R = \langle x-x', y-y', z-z'\rangle$ and the components of $\langle J_x, J_y, J_z\rangle$ are functions of the integration coordinates x', y', z'. The integral does not need to be carried out strictly over the volume of the payload. Integrating over a box around it is enough, because the current amplitude is zero outside the payload and does not contribute to the value of the integral.

2.1.2 The SR\3-60 railgun and the pulsed magnetic field measurement system

The SR\3-60 is a multi-rail electromagnetic launch platform that can be configured in multiple arrangements. This railgun has 3 pairs of 2 m long rails offset by 60°, forming a hexagonal bore with 29 mm face to face (see Fig. 2.1.1).

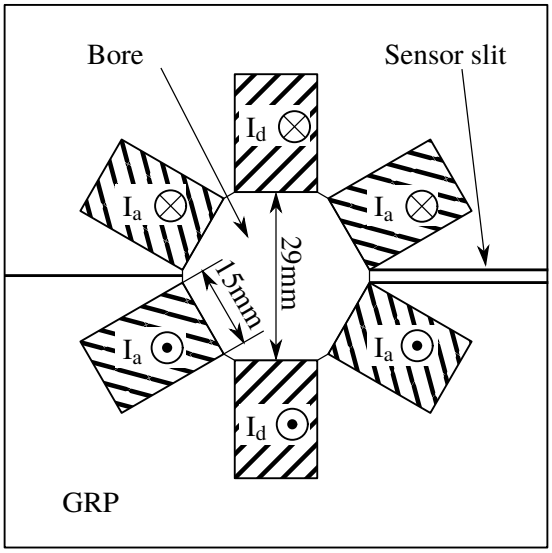

Figure 2.1.2. Cross-sectional view of SR\3-60 railgun. I_d denotes rails with driving current used to supply the armature. I_a marks augmentation rails.

Figure 2.1.3. The launch package used in the experiments of this subsection. The package contains a copper brush armature, a 3D-printed plastic housing and an aluminum disk payload.

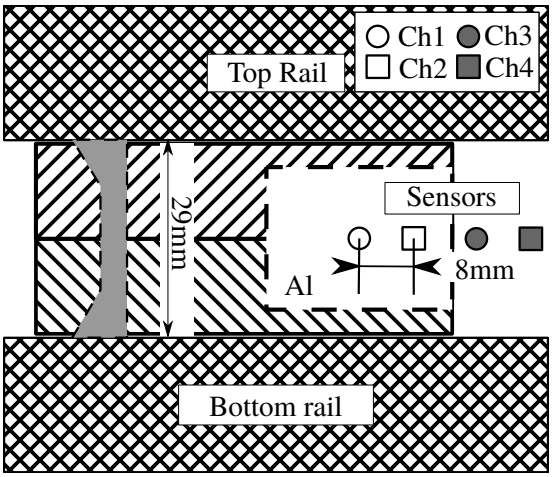

Figure 2.1.4. Side view of the SR\3-60 and sensor positioning. Side rails are not shown.

For our experiments, the SR\3-60 was operated in a serial augmented configuration. The rails were short-circuited at the breech and the muzzle in such a way that the side rails were used for field augmentation and the vertical pair for driving the projectile. All of the rails were connected in series because of concerns about magnetic coupling and the lack of protection against it. Figure 2.1.2 shows the cross-section of the SR\3-60 and current directions (looking from the breech). Static experiments were performed with the driving rails disconnected from the circuit.

For our launch package, we 3D-printed a hexagonal plastic housing (28 mm face-to-face) for a copper brush-type armature and an aluminum payload (see Fig. 2.1.3). The total length of the package was 6 cm. The payload was a cylinder with a radius of 12 mm and a height of 24 mm. The cross-section of the launch package in between the drive rails can be seen in Fig. 2.1.4. The payload was placed inside a 3D printed sabot so that is be electrically isolated from the rails and from the armature. The distance between the brush and the payload was 19 mm. The total mass of the launch package was 57 g.

Though it would be ideal to measure the magnetic field in the projectile's frame of reference during launch, this is difficult to achieve because the sensors would have to travel together with the projectile. Another way of measuring the complete magnetic field dynamics would require a large number of sensors along the bore. For simplicity, to measure the magnetic field distribution around the payload four CMR sensors were placed as depicted in Fig.

2.1.4. Four slits were milled in the glass reinforced plastic (GRP) housing in between the top and bottom side-rails with the first slit being 88 cm from the breech and others placed every 8 mm towards the muzzle. When inserted, the measuring volumes of the sensors were 18 mm from the bore's center. The relatively small active volume of the sensors (0.5 mm×50 µm×400 nm) provides a localized measurement in comparison to the scale of the experiment.

Sensors based on the colossal magnetoresistance monitor the absolute value of the magnetic field instead of its projection to the active plane. The anisotropy of their sensitivity is negligible for fields higher than a few hundred mT making them ideal to measure fields where the field direction is changing during the experiment.

For static shots (no acceleration), the launch package was placed such that the mid-point of the aluminium cylinder would coincide with the Ch1 sensor. A series of dynamic shots (with launch package acceleration) were performed with the distance between the center of the payload and the first sensor of 0 cm, 1.2 cm, 6.2 cm and 11.2 cm respectively.

2.1.3 Magnetic field dynamics inside the bore of a serial augmented hexagonal railgun

The results of static experiments are presented in Figure 2.1.5. The experiments were repeated twice for every configuration and showed perfect reproducibility. The magnetic field pulse generated by the augmentation coils alone (no payload inside the bore and the driving rails disconnected form the circuit) is depicted as a dashed line for reference. All three sensors measured identical pulses when no launch package was present.

When performing the same measurement with the aluminum payload centered around the Ch1 sensor (with driving rails still disconnected), as expected from considerations in section 2.1.1, close to the center of the projectile the magnetic flux density was reduced in comparison with the reference pulse. The difference was 300 mT (8%) at a distance of 6 mm from the projectile's surface at peak current measured by Ch1. Ch1 and Ch2 measurements are close to each other while Ch3 is visibly higher. This difference from the reference measurement was caused by the generation of eddy currents inside the payload, which in turn generate additional magnetic fields of opposing direction. The difference diminished afterwards and became unnoticeable at about 1 ms where the difference from the reference vanishes as well. At around 2 ms measurements with the payload started to diverge from the reference by decaying slower as the

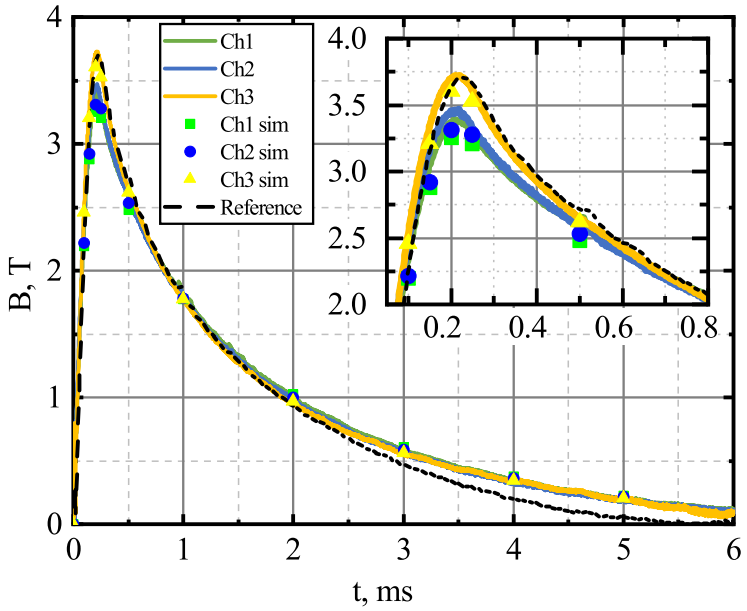

Figure 2.1.5. Absolute value of magnetic flux density in the proximity of the static payload, reference measurement without the payload and a result of simulation based on method described in section 2.1.1. The inset shows a zoomed in view of the peak.

induced currents try to maintain the already captured flux. It has to be noted that the measured current through the rails is slightly lower without than with the launch package (10% at 3 ms, 16% at 4 ms), possibly due to changes in system resistance from shot to shot. The measurements start to diverge around 1.5 ms.

The normalized curves of the measured current and magnetic field noticeably differ in shape, especially around the peak. This suggests that the current density distribution is not constant in time for this rise time. This is due to skin effect. The tail part of the curves decay with the same rate, implying that the current distribution becomes stationary though not necessarily uniform.

During the dynamic experiments, projectiles were accelerated to top speeds of about 110 m/s within 4 ms with a peak acceleration of 72 km/s^2 at peak current. Figure 2.1.6 shows the magnetic field measurements during launch with different projectile start positions with respect to the sensors.

The position of the projectile remains relatively unchanged for about 0.5 ms so the initial peak can be interpreted as static. We see that the amplitude of the

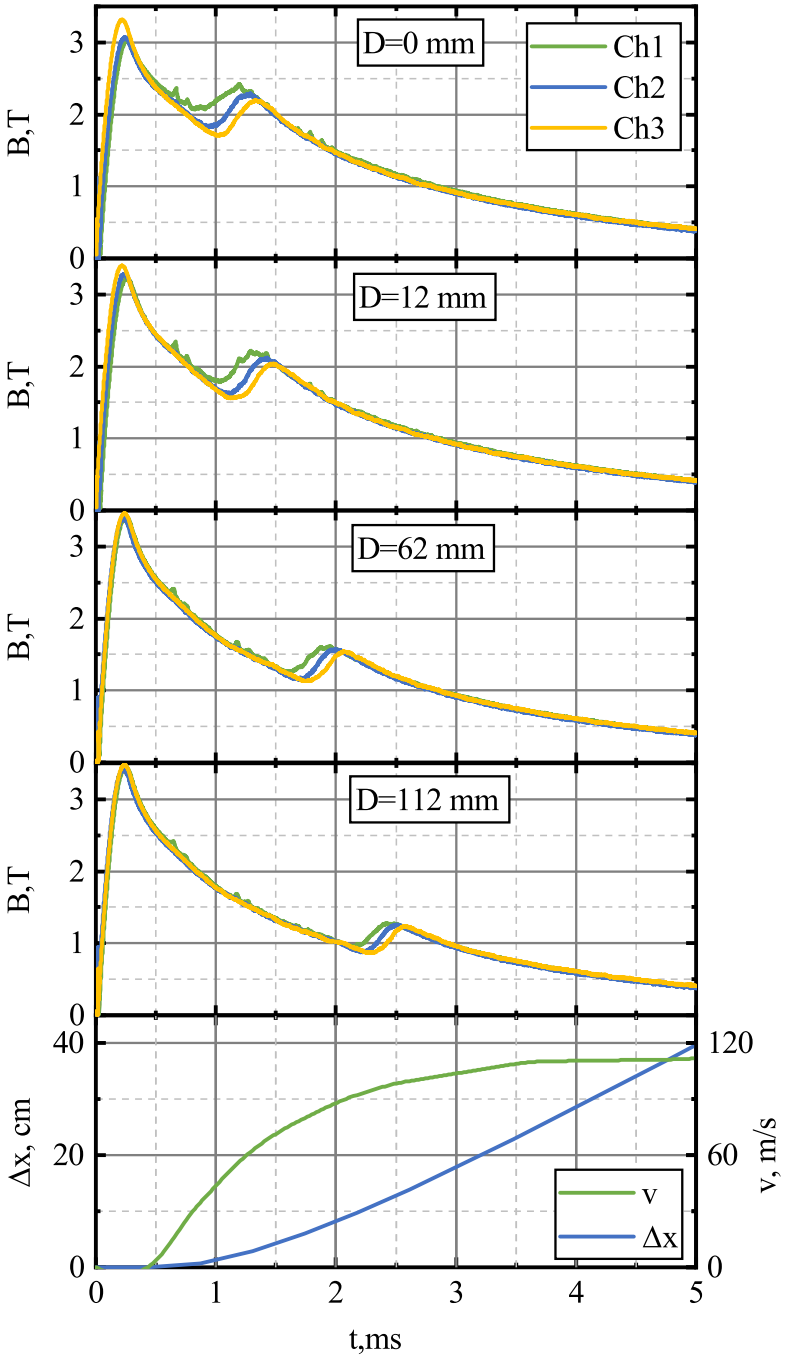

Figure 2.1.6. Absolute value of magnetic flux density measured in dynamic experiments and the dynamics of the payload. D is the start position of the projectile measured from the center of the payload to the Ch1 sensor.

measurements, again, depends on the proximity to the payload. This decrease is visible up to 28 mm from the center of the payload. Measurements at greater distances reveal identical values except for the second peak. When the projectile is centered, we can see a slightly higher field in Ch1 right after the peak current (0.5 ms-0.8 ms) that could be caused by the payload trapping some flux.

The second bump seen at different times, (offsetting the field equally for all of the sensors) is caused by the armature passing by the sensors. As the projectile moves, the current carrying portion of the driving rails increases. The different time intervals and rise angles of the second peak measured with evenly spaced sensors are a consequence of the motion of the projectile. Differences between measurements are most pronounced when the sensors are closer to the armature's starting position where acceleration of the projectile is the highest (within 5 cm). After the projectile has passed the sensors, all three pairs of rails carry the same total current instead of just the two augmenting rails, and, hence, the field is higher.

In order to quantitatively analyse the experimental results a numerical code was built following the steps described in section 2.1.1. The model assumed a pulse of spatially uniform magnetic field perpendicular to the axis of the cylinder (parallel to the z axis in the figures) being applied to a cylindrical payload with dimensions matching those of the physical one. The reference measurement was used as a time dependent boundary condition on a surface of a cylindrical domain over which the diffusion equation was solved. Eddy currents were calculated by taking a curl of the solution to the diffusion equation and the induced magnetic field was calculated with equation (2.1.4). For the total field value we took the superposition between the applied and the induced fields.

The simulation results obtained from the model at sensor positions can be seen as points in Fig. 2.1.5. Simulation results show good agreement with the experimental measurements both in absolute value and in proportion between the sensors. The simulation slightly overestimates the effect of field reduction around the peak of the pulse (focused in the inset), but is quite accurate during the tail of the pulse. The cause of this could be the fact that the augmentation field in our experimental configuration is non-uniform. The uniform field simplification is more suited for the cases where the augmentation rails are further from the payload. Our reference measurement was taken in an area of the highest field (in between the augmentation rails), meaning that the magnetic field around the sample was lower than that, hence would induce lower currents. The

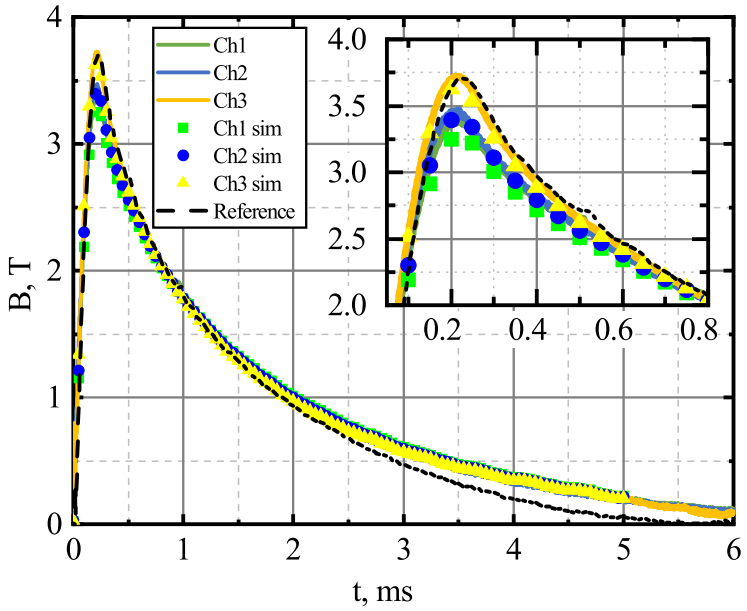

Figure 2.1.7. Comparison between experimental results and an FEM simulation. The inset shows a zoomed in view of the peak.

fact that the decaying part is accurate is related to the fact that the eddy currents are deeper inside the payload when magnetic field has diffused further into the sample, so that their distribution has lower effect on the external field.

In order to account for the inhomogeneity of the field an FEM model was built. We modelled a time dependent magnetic field response of a 10 cm long section of the rails with and without an aluminium payload at the center. The augmenting rails were supplied with a current pulse of a uniform density and a shape of the reference magnetic field measurement (peak value of 121 kA, experimentally measured - 118 kA). We are aware that this differs from the experiments, but modelling the actual time dependent current density distribution is outside of the scope of this study and would serve little purpose, since we're investigating the effects of the projectile.

The FEM simulation results corresponding to field values at the sensor positions can be seen in Fig. 2.1.7 and are in good agreement with the experiment. The measurement values are, again, slightly higher those predicted by the simulation. We believe that this could be a consequence of a lack of precision while placing the sensors or the projectile as small variations in distance have notable effects on field measurements in such a close proximity.

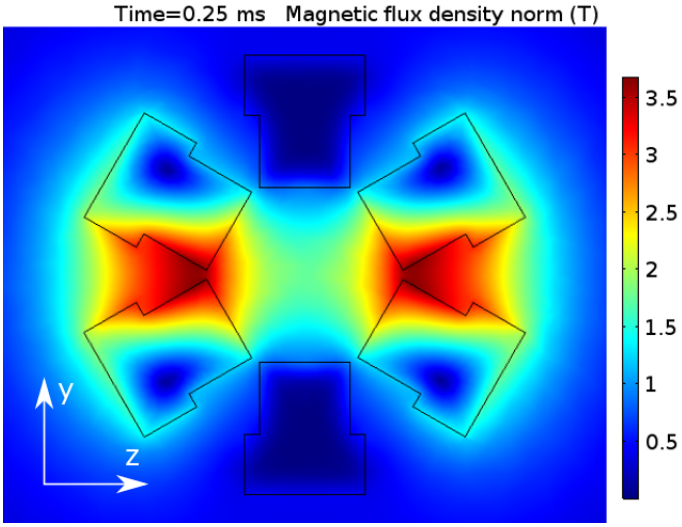

Figure 2.1.8. Distribution of magnetic flux density when the railgun bore is empty

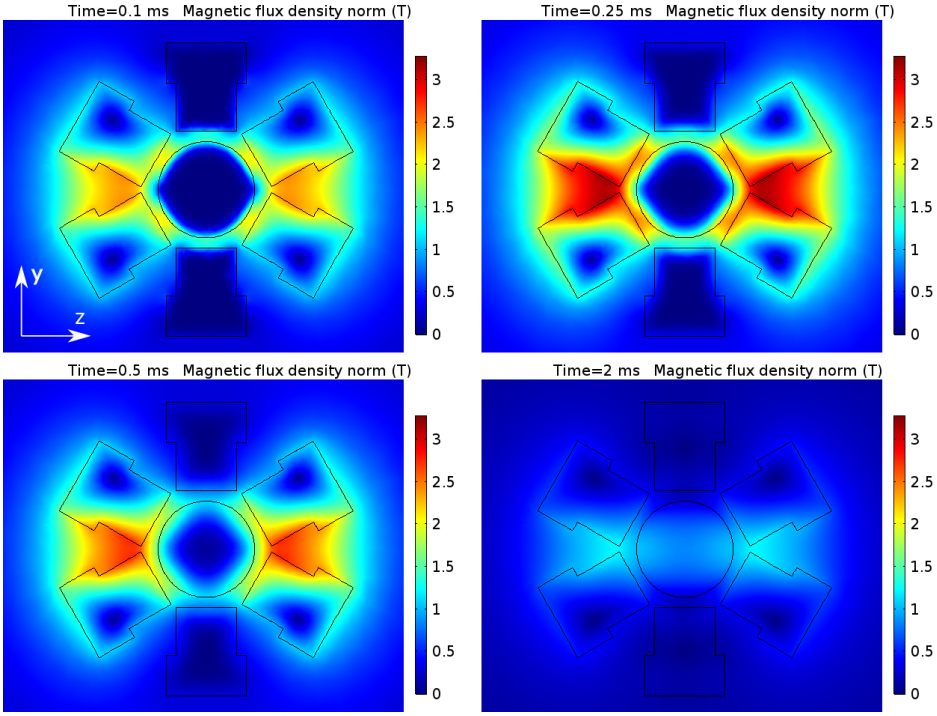

Figure 2.1.9. Magnetic flux density distribution in a yz plane intersecting the center of the payload at different times of the magnetic field pulse.

The magnetic flux density distribution calculated with an FEM solver at peak current when the bore is empty can be seen in Fig. 2.1.8. The augmentation is providing close to 2 T in the middle of the bore where it would interact with the driving current and 3.7 T in between the augmentation rails. This result is close to the one experimentally measured. It can be seen that the driving rails, which in the static case do not carry the excitation current, are subject to the transient field and are expelling it.

The Magnetic flux density distribution at different times with the payload present are shown in Fig. 2.1.9. Initially the magnetic field is expelled from the interior of both the payload and the driving rails resulting in magnetic field redistribution around them. Magnetic flux density is reduced at the poles parallel to the z axis and increased at ones parallel to the y-axis. Deviations decrease with time as the field penetrates deeper into the conductors. At around 2 ms the field fully penetrates the sample. The reversal of the effect is present but very slight and could be better seen in Fig. 2.1.7.

Initially, only thin surface sections of the payload and the rails support the magnetic field. Later on, the magnetic field can be seen diffusing deeper into the conductors with different rates. The field penetrates the payload faster than the rails because the conductivity of aluminium is almost half that of copper. Magnetic permeabilities of the materials do not play a big role because they are effectively equal to that of free space.

These results give some insight in projectile design. Using less conductive metals like tungsten for projectiles would minimize the effect because of the faster diffusion. If shielding is the main concern, then more conductive materials are to be used. The most dangerous part of the pulse for electronics in the projectile is the fast rise, because of the high induced electric field (equation (2.1.1)). Even if the field penetrates the shielding, the potential harm is reduced due to reduced amplitudes and rise times. Locations of concern would not be those with lower field, but rather the areas with higher field. Fig. 2.1.10 shows the magnetic flux density distribution in the *yx* plane going through the center of the payload. The field is increased around the edge of the conductor as it is expelled from its volume and needs to go around. The area between the armature and the conductive payload would temporarily have reduced field due to opposing field directions between the one generated by the armature and redistributed augmentation field. This would lead to net attraction between the armature and the payload.

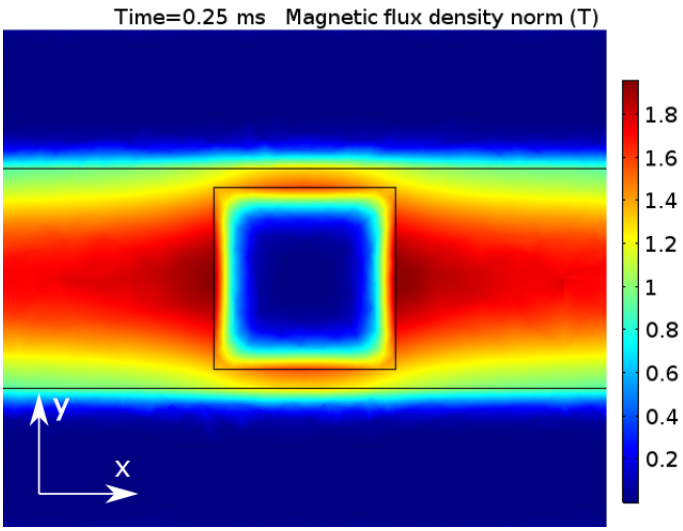

Figure 2.1.10. Magnetic field distribution in xy plane showing field concentration around the conductive payload.

2.1.4 Summary

The investigations of the magnetic field dynamics inside the bore of a serial augmented hexagonal railgun have revealed that a conductive payload noticeably alters the field configuration. We have calculated and experimentally validated the transient magnetic field distribution around a conductive cylindrical payload. The magnitude of the magnetic field disturbance decays sharply with the distance from the surface of the conducting payload and is the highest during the abrupt change of magnetic field pulse. The effect of magnetic field expulsion should be taken into consideration when designing launch packages.

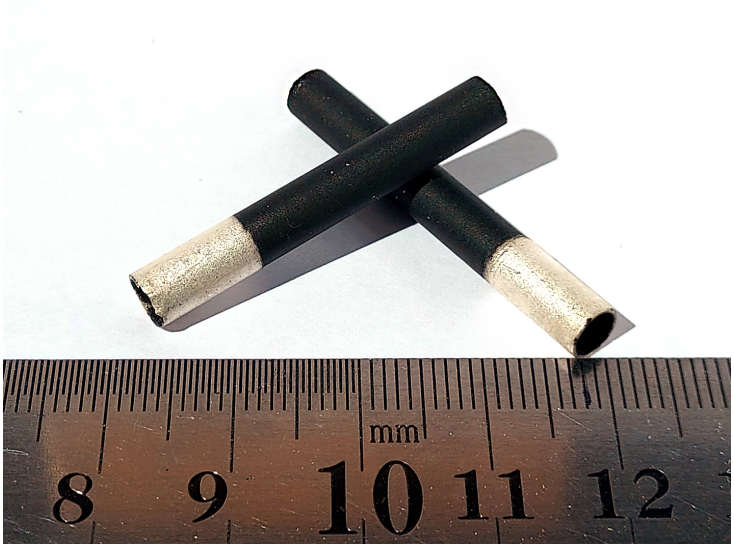

Figure 2.2.1. Bi-2223 current leads

2.2 Pulsed magnetic flux penetration dynamics inside a thin-walled superconducting Pb-doped B-2223 tube

Results presented in this subsection deal with the magnetic behaviour of thin-walled superconducting tubes in transient magnetic fields. In general, the magnetic field penetration into a type II superconductor is governed by a nonlinear diffusion equation. In the case of a thin-walled superconducting tube, where cooling is effective due to a large surface area and screening field induced in the superconducting tube is small compared to the applied field, it is possible to simplify this equation to a lumped parameter equation. The lumped parameter equation can be used to describe both the induced current flowing in the tube and the magnetic field distribution. Here it is demonstrated that a measurement of a transient magnetic field in the inner hollow part of a superconducting tube can be used to determine the critical current density vs. magnetic field and the power law index of the material when analyzed with the lumped parameter equation. The experiments were performed with a thin-walled Bi-2223 tube submerged in liquid nitrogen using a B-dot and a colossal magnetoresistance sensor.

The results presented in the following chapter were originally published in:
V. Vertelis, S. Balevicius, V. Stankevic, N. Zurauskiene, and M. Schneider, “Pulsed magnetic flux penetration dynamics inside a thin-walled supercon-

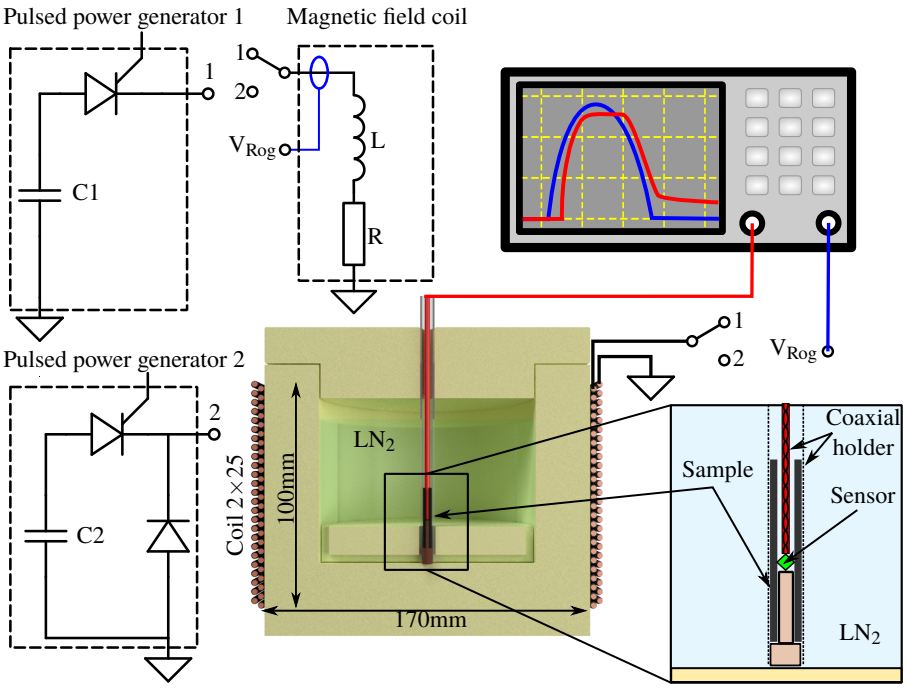

Figure 2.2.2. Schematic diagram of experimental setup.

ducting tube," *J. Appl. Phys.*, vol. 127, no. 11, p. 113901, Mar. 2020, doi: 10.1063/1.5145370.

2.2.1 Experimental setup for pulsed magnetic flux measurements

For this investigation of the penetration of a pulsed magnetic field into a thin-walled superconducting tube, a commercially available Bi-2223 superconductor tubular current lead [211] was used (photograph in Fig. 2.2.1). It was 33 mm in length and had an outer diameter of 5 mm. The tube used was made by cutting out a section of a 70 mm tube in order to avoid the influence of the silver contact layers deposited at the ends of the tube. The thickness of the tube wall was 0.5 mm. A schematic diagram of the experimental setup is presented in Figure 2.2.2. The superconducting tube was installed into a special 6 mm inner diameter coaxial holder, which was placed vertically along the longitudinal axis of a cylindrical plastic container filled with liquid nitrogen. This container was then put inside a coil made of two layers with 25 windings in each. The height of the magnetic coil was 10 cm and its inner diameter was 17 cm. The coil was made from 2.2 mm diameter copper wire and had an inductance of

395 μH. For the generation of the pulsed magnetic field, a high current pulse generator described in [212] was used. In order to measure the current and to calculate the applied magnetic field generated by the coil, a Rogowski coil was mounted on one of the current pulse generator current leads.

A textolite spacer was inserted at one end of the superconducting tube to reduce the free space inside the coaxial holder and to ensure the same spatial configuration for every measurement. A magnetic field probe (B-dot or CMR-B-scalar sensor) was inserted through the other end of the tube so that the sensor's measurement volume would touch the spacer. This put the sensor about 17 mm from the end of the superconductor and in the middle of the coil-generated magnetic field distribution plateau. The applied magnetic field was calculated using the current flowing in the magnetic coil, which was measured with the Rogowski coil.

The B-dot sensor consisted of a 2 mm diameter, 20 winding, 5 mm length search coil. The uncertainty of the integration constant of the B-dot sensor and the slow magnetic field decay at the "tail" of the magnetic field pulse were the main sources of measurement error, which in our case was no more than 5%. Additionally, for the measurement of the magnetic field inside the superconducting tube, we used a miniature (10^{-2} mm^3 effective volume, probe radius 1 mm) CMR-B-scalar sensor, which was made from a thin nanostructured La-Sr-MnO film, exhibiting the colossal magnetoresistance phenomenon. These CMR-B-scalar sensors have a non-zero response to a magnetic field independently from its orientation. This property makes them a useful measurement tool in cases of a pulsed magnetic field, where this field simultaneously changes magnitude and direction. These sensors can be successfully operated at room temperatures. However, at liquid nitrogen temperature, the La-Sr-MnO film is in a ferromagnetic state and exhibits a long-term remnant resistance relaxation process [213]. This phenomenon needs to be taken into consideration as it can induce additional measurement errors. In order to overcome this difficulty, a special experimental arrangement was used, which allowed for the insertion and removal of the superconducting tube from the cryostat without changing the sensor's remnant resistance.

Measurements of the pulsed magnetic field inside the superconducting tube using the CMR-B-scalar sensor were performed in the following way: The first step was sensor conditioning without the superconductor. For this purpose, the sensor was cooled down to 77 K and exposed to a magnetic field pulse with a peak value of 0.5 T. The superconductor tube was then slowly submerged into

the liquid nitrogen so that the CMR-B-scalar sensor would be located at the center of the tube. After a test with the superconductor tube, the tube was then removed, and the CMR-B-scalar sensor was calibrated using a magnetic field pulse of a known shape and amplitude. Before each subsequent measurement, due to the permanent magnetization of the superconducting tube, it was heated above its critical temperature T_c by withdrawing it into ambient air.

2.2.2 Theory: Lumped parameter model equation

The dynamics of the magnetic field inside a II type superconducting hollow cylinder (tube) exposed to a pulsed magnetic field can be characterised by three phases [214]. The first phase, called the "delay", manifests itself up to the point in time when the maximal field (B_c) that can be screened by the tube sample is reached. The magnetic field inside the tube during this phase is negligibly small. In the second phase, a partial penetration of the magnetic field (B_i) inside the tube when the applied field (B_a) becomes higher than B_c is observed. This field (B_i) then grows up to its peak value, which coincides in time with the maximum of B_a. In the third phase, the B_i is decaying. The decay happens in two periods: a fast and a very slow, which are related to the decay of B_a and the flux creep, respectively. The dynamics of the magnetic field density (B) at any point in space during all these phases can be calculated using the magnetic diffusion equation, which in its differential form is:

$$\nabla \times \left(\frac{\rho}{\mu} (\nabla \times \mathbf{B}) \right) = -\frac{\partial \mathbf{B}}{\partial t}, \tag{2.2.1}$$

where ρ is the resistivity of the material. For type II superconductors, ρ strongly depends on the current density j. It the Ohm's law $E = \rho j$ using an empirical power law relation (eq. 1.17):

$$E = E_c \left(\frac{j}{j_c(B)} \right)^n$$

where E_c is the critical electric field ($1\,\mu V/cm$), j and j_c are the current density and the critical current density at which the critical electric field is reached and n is an empirical parameter that represents the quality of the superconductor and its electric behaviour in the resistive state caused by the vortex motion. The critical current density j_c is a function of both the magnetic field (B) and the temperature (T). For this reason, power dissipation and cooling conditions need to be taken into consideration. The solution of equation (2.2.1), using

relation (1.17) in the general case, requires integration according to coordinates. However, a long thin-walled superconducting tube can be modelled as a solenoid wound out of a thin wire. The equation (2.2.1) can then be transformed into a relatively simple lumped parameter equation (see appendix A) for the current flowing in one winding ($I = d^2 j$) in which the geometry of the tube is represented by the inductance of the solenoid (L):

$$L\frac{dI}{dt} + \frac{2\pi R \cdot E_c}{(d^2 j_c(B))^n}|I|^{n-1}I = -\frac{l_s}{d}\pi R^2 \frac{dB_a(t)}{dt}. \tag{2.2.2}$$

Here d is the thickness of the tube wall, R is the tube radius ($R >> d$) and l_s is the tube length. This makes it possible to avoid the spatial integration of (2.2.1). The inductance L can be calculated from well-known solenoid equations assuming that the thin-walled superconducting tube is a single layer solenoid having a finite length l_s and a wire thickness of d. The main requirement for such approach is that the difference between magnetic field at the outer and inner surfaces of the wall has to be small in comparison to the absolute values of these fields. This is realized if Bean's penetration length (l_p), which is a function of B_a as $l_b = B_a/(\mu j_c)$, significantly exceeds the wall thickness (d). Thus, this "thin-wall" condition can be satisfied when B_a is several times higher than B_c.

Moreover, this thin wall also enables the realization of good cooling of the superconducting material if the tube is submerged inside a liquid cooling media. In such case, the ρ dependence on temperature is minimal and does not need to be taken into account. The assumption that a thin-walled superconducting tube can be imagined as a thin single layer solenoid in which the cross section of each turn is d^2 makes it possible to easily calculate the magnetic field (B_i) in the center of the tube. This field value is then directly proportional to the current I ($B = \beta I$) with a conversion constant (β) equal to [215]:

$$\beta = \frac{\mu l_s}{2d\sqrt{R^2 + \frac{l_s^2}{4}}}. \tag{2.2.3}$$

After the external field pulse vanishes ($B_a = 0$), an analytical solution of the trapped field decay can be obtained by solving equation (2.2.2) assuming that j_c remains constant. In this case, the expression for $B_{ic}(t)$ is:

$$B_{ic}(t) = \left[B_0^{n-1} + (1-n)\frac{\beta^{1-n} E_c l_s \cdot 2\pi R}{d^{2n+1} L j_c^n} \cdot t\right]^{\frac{1}{1-n}} \tag{2.2.4}$$

Here B_0 is the trapped magnetic field inside the superconducting tube at the end of the applied magnetic field pulse and j_c is the critical current density at this field amplitude. The analytic expression (2.2.4) can be used for a simple determination of the exponent n in the empirical power law when taking the B_0 value from the beginning of the experimentally obtained B_{ic} decay curve.

To accurately measure B_i, the axial magnetic field shouldn't vary much in the vicinity of the measurement volume. This requirement can be achieved in two ways: by using a small magnetic field sensor, or by increasing l_s, so that the influence of the tube ends would be negligible. The influence of the tube geometry was investigated using the numerical results obtained in [28] for thick-walled tubes having different l_s/R_a ratios (R_a is the average tube radius). It was demonstrated that when $l_s/R_a > 10$, the magnetic field gradient at up to 2 R_a distance along tube's longitudinal axis is negligible. Thus a tube, with a length of l_s about an order of magnitude higher than its radius R_a, can be characterized as a "long" tube and a sensor with dimensions that are smaller than R_a can be successfully used for the accurate measurements of B_i.

The results of the lumped parameter model were compared with a 2D axisymmetric finite element model (FEM) based on an H formulation [216] using the same material properties. This model was constructed using Comsol Multiphysics software. The heating effects were also neglected. A spatially uniform, time-dependent external magnetic field was applied on the solution domain boundary. An experimentally obtained applied magnetic field pulse was then used for the pulse shape so that the results could be compared directly.

2.2.3 Modelling of the dynamic magnetic field penetration

In order to investigate how the lumped parameter model equation describes the penetration of the magnetic field inside a tube made from a type II superconductor, we took into consideration the experimentally obtained relationship between j_c and B. As is typical for its low and middle field ranges, this relation at relatively low magnetic fields j_c abruptly decreases with an increase of B, while in the medium magnetic fields, the j_c vs. B tends to saturate, so that the j_c becomes approximately constant [217].

Figure 2.2.3 shows the calculation of the magnetic field inside the tube for several half-sine applied magnetic field pulses when the amplitudes are in the range where j_c is constant. In such a case, the magnetic field penetration is not well described at the low magnetic fields (i.e., at the beginning of the pulse), but when the external flux density significantly exceeds B_c and condition j_c =

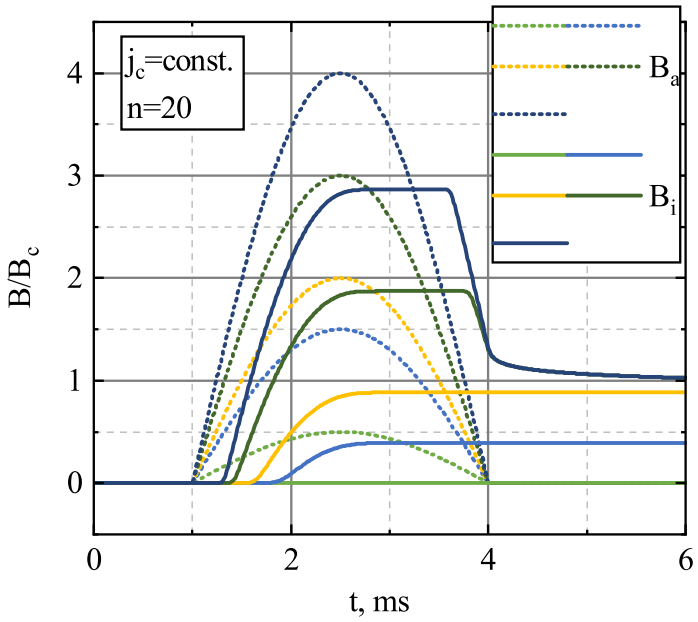

Figure 2.2.3. Simulation results illustrating the effect of a fixed duration applied magnetic field pulse (B_a) on the magnetic field (B_i) inside a thin-walled superconducting tube normalized to the maximal field (B_c) that can be screened by the sample.

const. is satisfied, the lumped parameter equation is able to accurately describe the properties of the B_c dynamics. Once the external field starts to decrease, the supercurrent changes its direction to maintain a constant flux throughout the tube. This creates a plateau region in the B_i pulse waveform. The B_i value at the plateau stays constant until the difference between B_a and B_i becomes equal to B_c. With a further decrease of B_a, the B_i begins to decrease, and the remaining trapped flux density is then B_c.

The influence of n on the B_i dynamics when j_c is constant is presented in Figure 2.2.4. The calculations were performed using equation (1.17) without the implementation of the ρ saturation when the superconductor goes into its normal state. In this case, the simulations were more accurate at the higher n values, because the low n values do not produce a sharp step, thus giving a lower resistance than one would expect from experimental observations when $j > j_c$. The results obtained using a fixed magnetic pulse having a 3 ms duration and an amplitude $B_a = 3B_c$ (see Figure 2.2.3) showed that the lower n values produce lower B_i amplitudes. However, it needs to be noted that the B_i value

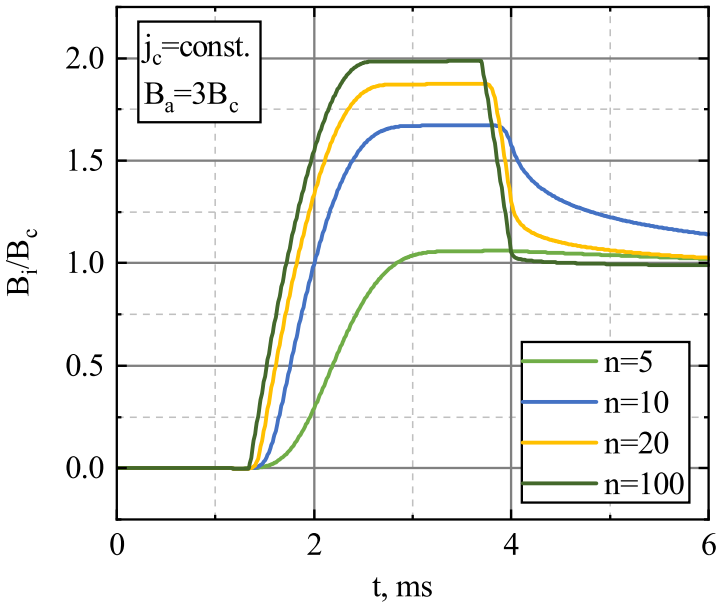

Figure 2.2.4. B_{i} (normalized to B_{c}) dynamics with different power law index values at fixed magnetic field pulse when j_{c} is constant.

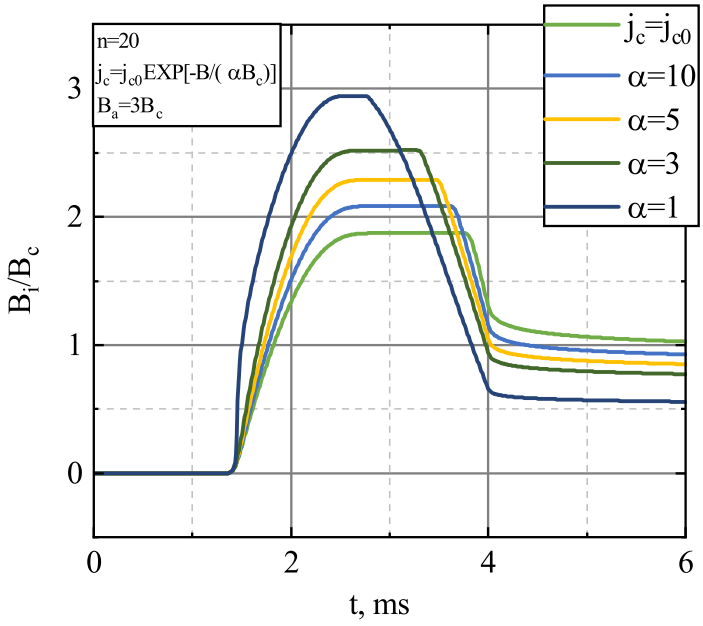

Figure 2.2.5. B_{i} (normalized to B_{c}) dynamics with different *alpha* values when the j_{c}-B dependence is approximated by the exponential function $j_{\mathrm{c}}(B) = j_{\mathrm{c0}}\exp[-B/\alpha B_{\mathrm{c}}]$.

depends on the combination of n and the time derivative of B_a. For this reason, at low B_a derivatives (long duration pulses), the B_i amplitude could increase with the lower n values, but this increase is weak at n values higher than 20.

Figure 2.2.5 illustrates the B_i dynamics at the low B_a range when j_c is a function of B. For this simulation, the j_c vs. B dependence was approximated by using the simple exponentially decaying function, where j_{c0} is the critical current density at $B = 0$ and α is the empirical coefficient, which depends on properties of the superconducting material. This shows how abrupt the j_c vs. B dependence is. As it can be seen from Figure 2.2.5, an increase of α makes the B_i penetration rate slower and increases the trapped magnetic field value. With decreasing j_c the duration of the plateau region also decreases. For very low values of j_c the plateau could become hard to measure, but a plateau is a sign that the sample remains superconducting at that field. Thus, the parameter showing the abruptness of the j_c vs. B dependence is the main variable when fitting the experimentally obtained B_i dynamic curves.

2.2.4 Experimental magnetic flux dynamics and evaluation of an in-field critical current density

Figures 2.2.6 and 2.2.7 show the experimental measurements of B_a and B_i when the superconducting tube was cooled down to 77 K. These measurements were performed using a B-dot sensor at two different magnetic field pulse durations (≈ 3 ms and 8 ms). A very similar behaviour of B_i was also recorded using the CMR-B-scalar sensor (see Figure 2.2.8), thus showing that the dimensions of the B-dot sensor are sufficiently small. The experimental B_i pulses were fitted with the simulation curves obtained from equation (2.2.2), where the fitting parameters were the $j_c(B)$ dependence and the n value. The other constant parameters used for these calculations are given in Table 1.

As an additional validation of this lumped parameter equation approach, the experimentally measured B_a and B_i time derivatives (Figure 2.2.9) were compared with the simulations using a finite element model and the lumped parameter equation (2.2.2). In the case of the B-dot, the magnetic field time derivative

Table 1. Values used to fit experimental data with the lumped parameter model.

L	l_s	R	d	$j_c(B)$
2.62 µH	33 mm	2.25 mm	0.5 mm	Fig. 2.2.11

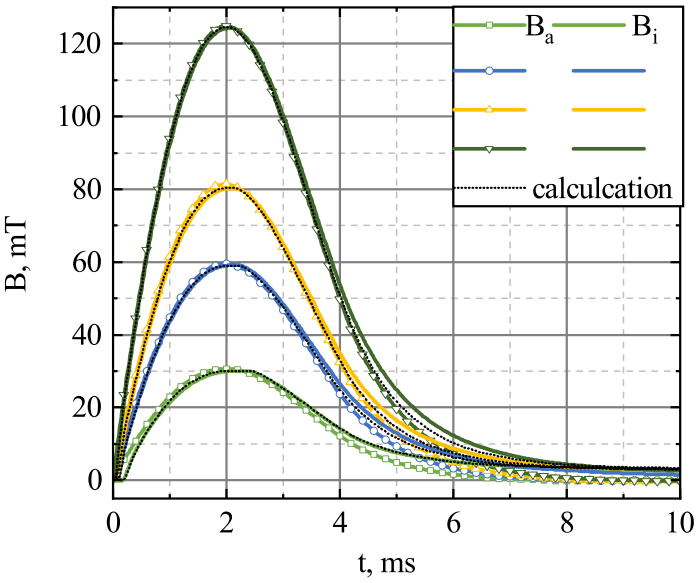

Figure 2.2.6. The B_i dynamic measured using a B-dot sensor when the B_a pulse duration was $\approx$ 8 ms. The B_a is marked with symbols and the numerical fits based on equation 2.2.2 are represented by the black dotted lines.

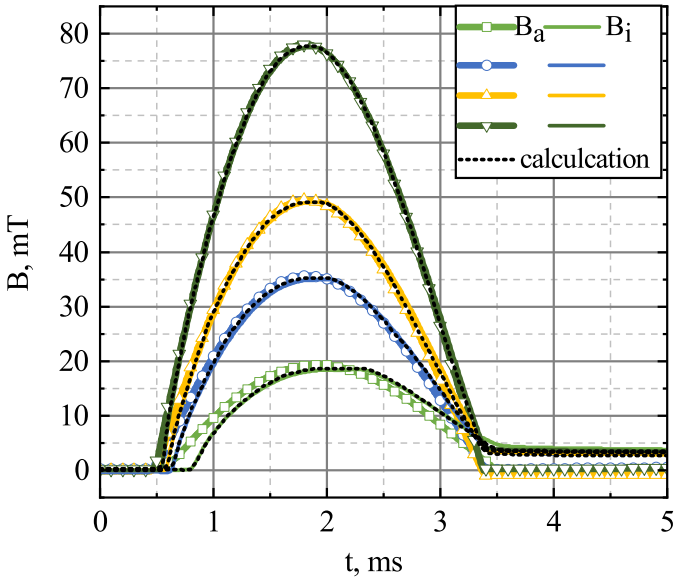

Figure 2.2.7. The B_i dynamic measured using a B-dot sensor when the B_a pulse duration was $\approx$ 3 ms. The B_a is marked with symbols and the numerical fits based on equation 2.2.2 are represented by the black dotted lines.

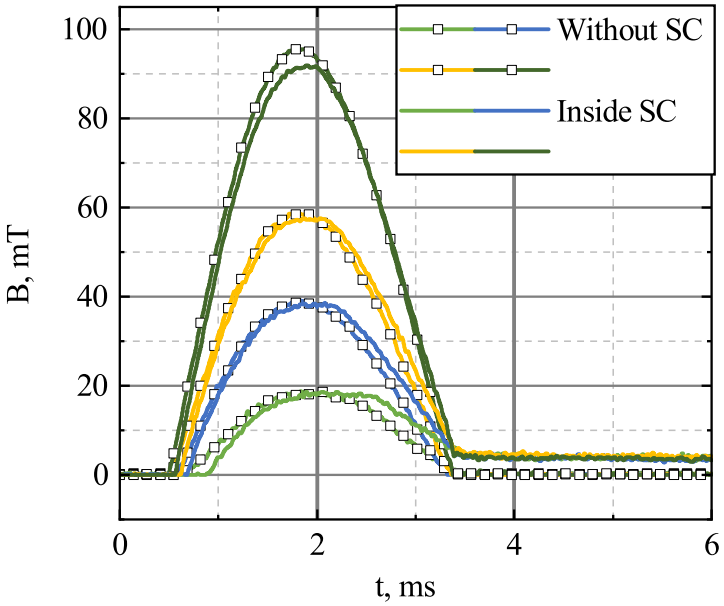

Figure 2.2.8. The B_i dynamics measured using the CMR-B-scalar sensor when the B_a pulse duration was ≈ 3 ms. The B_a is marked with symbols.

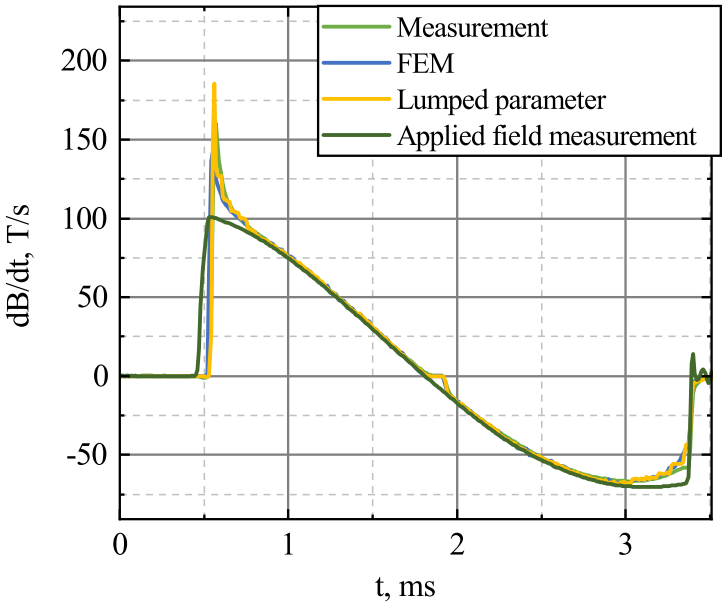

Figure 2.2.9. The time derivatives of the applied magnetic flux density (B_a) and the density inside (B_i) the superconducting tube. Experimental data, the finite element and lumped parameter models are compared.

is the directly measured quantity so the comparison between the measurement and the models is more accurate than using the integrated signal. Moreover, as it can be seen from Figure 2.2.9, the magnetic field derivative inside the superconducting tube is more sensitive to the peculiarities of the B dynamics and shows a sharp spike with a higher amplitude at the moment when the magnetic field penetrates into the superconductor than in the case of an unscreened external field. The plateau region before the field starts to decrease is also more pronounced in the derivative of the field. At around 1.8 ms, a region where the derivative is zero can be seen, indicating that the sample remains superconducting, while it is hard to tell from the integrated signal (Figure 2.2.7).

The best fit of the experimental curves was obtained at $n = 20$. This means that the flux creep is small in the sample and that the sample exhibits Bean-like behaviour. The results presented in Figures 2.2.6, 2.2.7 and 2.2.8 show that the experimentally measured B_i dynamics are in good agreement with the calculations, which confirms the validity of the application of the power law and the isothermal simplification assumed in the case of the investigated superconducting tube. The simulation results also agree well with the experimental measurements when predicting the trapped flux. The measured remaining flux density fluctuated from 2.9 mT to 3.7 mT, while the simulations predicted 2.9 mT to 3.3 mT for the short pulses and 1.5 mT to 3 mT for the experimental and 2.6 mT to 3.4 mT in the simulations for the longer ones, confirming that the lumped parameter method is capable of predicting the persistent currents and in turn, the trapped field in dynamic conditions.

The third phase of the B_i dynamics, i.e., the decay of B_i over time after the end of the applied magnetic field pulse, was investigated using the CMR-B-scalar sensor. Figure 2.2.10 shows the results of this decay measurement using an applied magnetic field pulse of 19 mT amplitude and 3 ms duration. The dashed line in Figure 2.2.10 shows the calculation using formula (2.2.4), which is in good agreement with the measurement results when the values used to fit the data are such as are given in Table 2. This confirms the validity of the assumptions made in order to get the analytical formula (2.2.4) for the B_i decay process.

Table 2. Values used to draw the theoretical curve in Figure 2.2.10.

B_0	n	j_c	β
4.82 mT	20	5.8 MA/m^2	2.5 mT/A

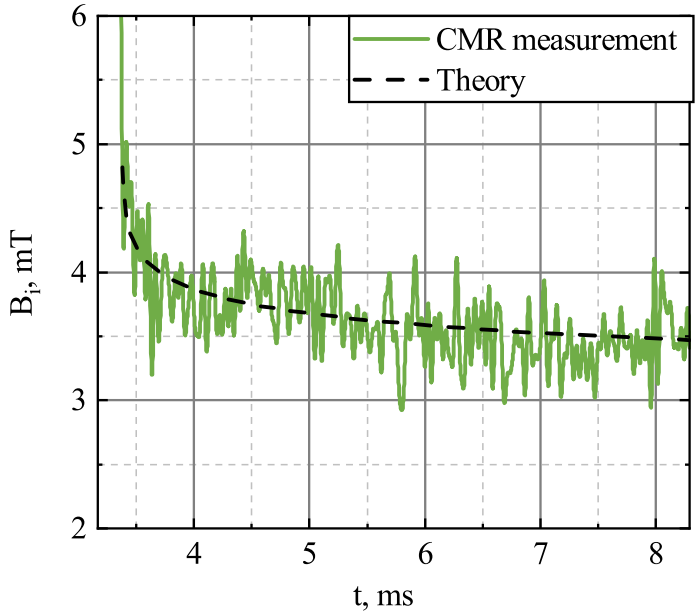

Figure 2.2.10. The B_i decay after the applied magnetic field pulse. Comparison between the CMR-B-scalar sensor measurement and the analytical expression (2.2.4).

These measurements and simulations make it possible to evaluate the power law index n and j_c vs. B dependence. Figure 2.2.11 presents this dependence as triangles, which was obtained using two applied magnetic field pulses with different pulse durations and amplitudes (3 ms, 8 ms and 77.5 mT, 125 mT respectively), when the power law index n was equal to 20. As can be seen for both pulses, the j_c vs. B dependence value and the shape is the same and does not depend on the parameters of the magnetic pulse being used. Thus, in our case, the magnetic pulse parameters (derivative and amplitude) were not critical for the investigation of the properties of the thin-walled superconducting tube material. Figure 2.2.11 also shows a comparison of the results obtained from fitting the experimental results with simulations using the lumped parameters equation and the properties provided in datasheet of the tube manufacturer (diamonds). Our investigations showed a very similar j_c vs. B dependence behaviour, but about a 20% lower j_c value, which can be explained as the different magnetic field orientation to the electrical current flowing in the superconductor. This phenomenon was demonstrated in the Bi-2223 tubular current leads when the magnetic field was applied parallel and perpendicular to the tube axis [218].

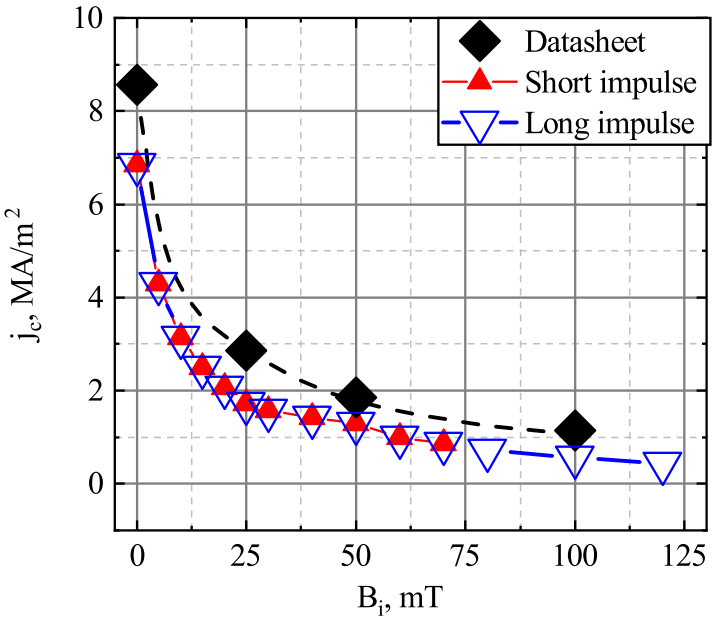

Figure 2.2.11. The j_c vs. B curves obtained from fitting the experimental data using the lumped parameter equation. The square shape dots show the $j_c(B)$ values presented in the datasheet of the superconducting tube manufacturer.

2.2.5 Summary

Experimental and theoretical investigations of the pulsed magnetic field penetration dynamics conducted on a thin-walled tube made from a type Bi-2223 superconductor have demonstrated that the lumped parameter approach is capable of describing the magnetic field dynamics and the trapped flux inside this tube. It is possible to evaluate the j_c vs. B dependence and the exponent n in power law of the tube material from a single measurement. With further development, this method could be used as a quick non-destructive way to check the quality and to characterize such superconducting tubular samples.

2.3 Effects of high current and magnetic field on thin YBCO films prepared on a Al_2O_3 substrate with a CeO_2 sublayer

The magnetic behaviour of type II superconducting bulks can be explained by the intrinsic properties of the material. However, direct nondestructive measurements of these properties in bulk samples are problematic and the measured properties are volume-averaged. In this section, thin YBCO films prepared on Al_2O_3 substrates with CeO_2 sublayers carrying overcritical current and exposed to magnetic fields were studied both in DC and pulsed current regimes. The observed behaviour is analyzed theoretically in the context of self-heating using isothermal current voltage characteristics obtained using nanosecond duration electric pulses.

The results presented in the following chapter were originally published in:
V. Vertelis et al., "Superconducting protector against electromagnetic pulses based on YBCO film prepared on an Al_2O_3 substrate with a CeO_2 sublayer," *Supercond. Sci. Technol.*, vol. 34, no. 3, p. 035007, 2021, doi: 10.1088/1361-6668/abd459.

2.3.1 Preparation technology of thin YBCO films and superconducting microbridges

The PI-MOCVD method was used for the preparation of both the CeO_2 sublayers and the YBaCuO films. The layers were deposited on a single crystal Al_2O_3 substrate. The deposition of the CeO_2 sublayer and the YBaCuO film was done in–situ at 750 °C substrate temperature. The CeO_2 sublayer thickness (h) was 140 nm or 480 nm. For the preparation of the YBaCuO film, the metal organic precursors with Y:Ba:Cu = 1:1.6:1.6 and 1:2.0:1.6 content were used. After the deposition of the YBaCuO film, thickness of which (d) was 440 nm, it was annealed in an O_2 atmosphere for 30 min. The annealing temperature was the same as for the deposition (750 °C). The analysis of the YBaCuO film performed using the reflection high-energy electron diffraction (RHEED) method showed spot-like intensive diffraction patterns (see Fig. 2.3.1 a), indicating that the films were of perfect structure and high surface roughness. An investigation of the film surfaces by an atomic force microscope (AFM) also demonstrated that the films consisted of microcrystallites oriented in mosaic-like morphologies, which were different for different thicknesses of the CeO_2 sublayers (see Fig.2.3.1 b and c).

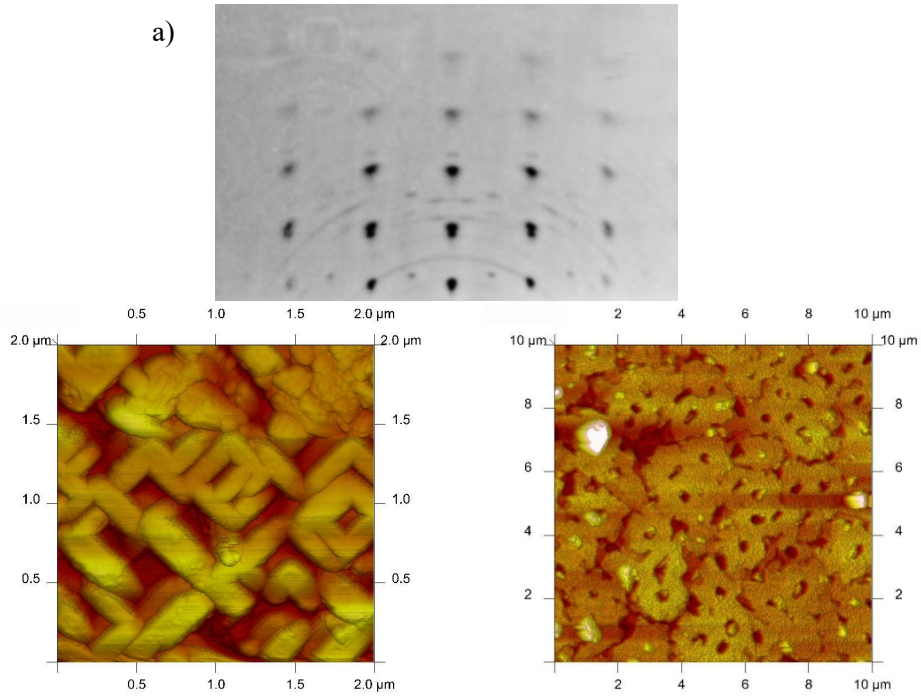

b) CeO_2; d=650 nm; S1a c) CeO_2; d=150 nm; S4a

Figure 2.3.1. a) A RHEED pattern obtained from a 440 nm thick YBCO film. It was prepared using 1:1.6:1.6 precursor ratio on a 650 nm thickness CeO_2 sublayer. b) and c) show YBCO film surface images obtained by AFM, when the height (h) of the CeO_2 sublayer was 480 nm and 140 nm for samples S1a and S4a, correspondingly.

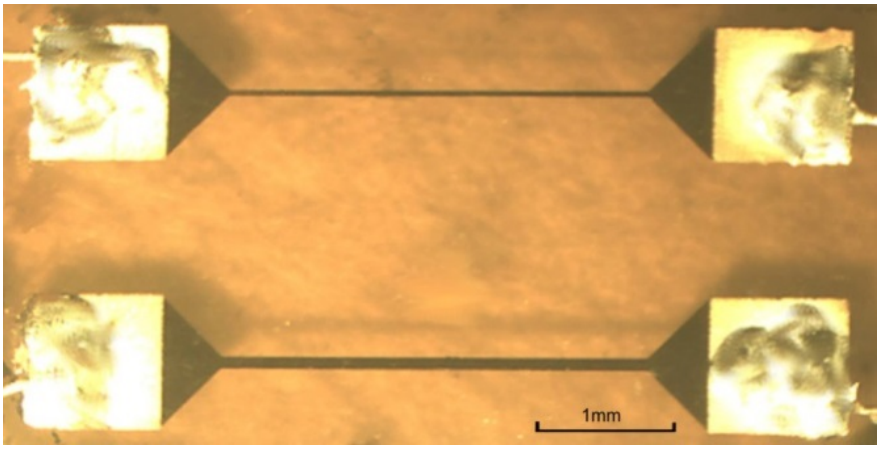

Figure 2.3.2. Top view of the YBCO strip-like microbridges used for the investigation of their electrical properties.

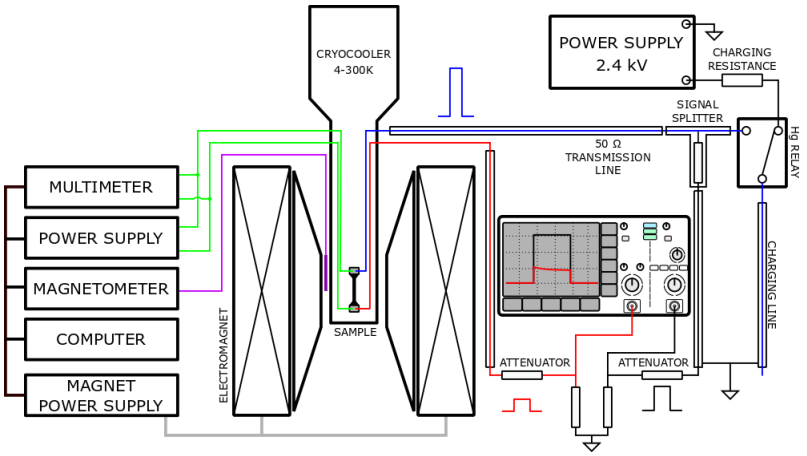

Figure 2.3.3. Schematic diagram of the setup used for the investigation of the YBCO strip-like microbridge I–V characteristics at different temperatures, low DC current, presence of a magnetic field and high voltage nanosecond duration pulses.

After deposition, the samples were shaped by conventional photolithography as 3 mm length (l) and 60 µm or 100 µm width (w) strip-like microbridges with contact sites at their ends (see Fig. 2.3.2). The contact sites (1×1 mm square) were covered with a 2 µm thick silver film deposited using thermal vacuum evaporation. After that, the samples were annealed for 20 min in an oxygen atmosphere at 420-450 °C temperature.

2.3.2 Experimental setups for investigating the electrical properties of thin YBCO films

For the characterization of the electric and magnetic properties of the YBaCuO films, the experimental setup presented in Fig. 2.3.3 was used. This setup consisted of two parts: one for the measurement of their IV characteristics using DC current and a magnetic field and the other that used high voltage nanosecond duration electrical pulses. In both of these measurement regimes, the sample was mounted inside a closed cycle He cryocooler "Janis" in order to perform the investigations at different temperatures, which could be varied from 4.2 K to 300 K.

The resistance (R) vs. temperature (T) dependences in the DC case were investigated using the two-terminal method when the applied current was 0.1 mA in a temperature range from 40 K to 150 K. The voltage drops and current through the samples were recorded by means of a multimeter. The IV charac-

Table 3. Sample parameters for YBCO films with CeO_2 sublayer. d and h are YBCO and CeO_2 thicknesses, respectively.

Sample	Y:Ba:Cu	d, nm	h, nm	w, μm	$T_{C1} - T_{C2}$, K	Δ(TS), K
S1a	1:1.6:1.6	440	650-700	100	89.8 – 72	17.8
S1b	1:1.6:1.6	440	650-700	60	89.7 – 69.5	20.2
S2a	1:1.6:1.6	440-480	650	100	88.3 – 72.1	16.2
S3a	1:2.0:1.6	440	650	100	84.2 – 73.3	10.9
S4a	1:1.6:1.6	440	140	100	90 – 83.8	6.2

teristics were measured using a slow ramp signal generated using a digitally controlled power supply. For the investigation of magnetic field influence on the electrical conductivity of the films, the microbridges were placed inside an external magnetic field (B_{ex}), which was directed perpendicular to the microbridge plane and was changed from zero up to 0.7 T (see experimental setup in Fig. 2.3.3). During these measurements, the electrical current flowing through the samples was kept constant at 0.75 mA.

Strong pulsed electric field measurements were performed using pulses with rectangular shape and durations of about 10 ns, 0.5 ns rise times and amplitudes up to 1 kV. These pulses were generated in a 50 ohm coaxial transmission line by means of an electromechanical Hg relay. For IV characteristic measurement, the samples were mounted in a special wide band (∼10 GHz) co-planar holder and connected in series with the transmission line. Measurements were performed in a temperature range from 20 K to 80 K.

In order to measure the sample resistance, the amplitudes of incident U_{in} and transmitted U_{tr} pulses were measured using a signal splitter with a 1:80 ratio and two separate channels of a high-speed Tektronix DPO 70604 oscilloscope. The voltage drops (U_s) and current (I_s) in the samples were calculated using following formulas: $U_s = 2(U_{in} - U_{tr})$ and $I_s = U_{tr}/Z$. Here Z was the impedance of coaxial transmission waveguide and was equal to 50 Ω.

2.3.3 Electrical properties at DC electric current and magnetic field

Zero external magnetic field (bias current 0.1 mA)

The typical resistance (R) vs. temperature (T) dependences measured for the investigated YBCO microbridges are presented in Fig. 2.3.4. The main parameters of the samples used for this investigation are shown in Table 3. As it

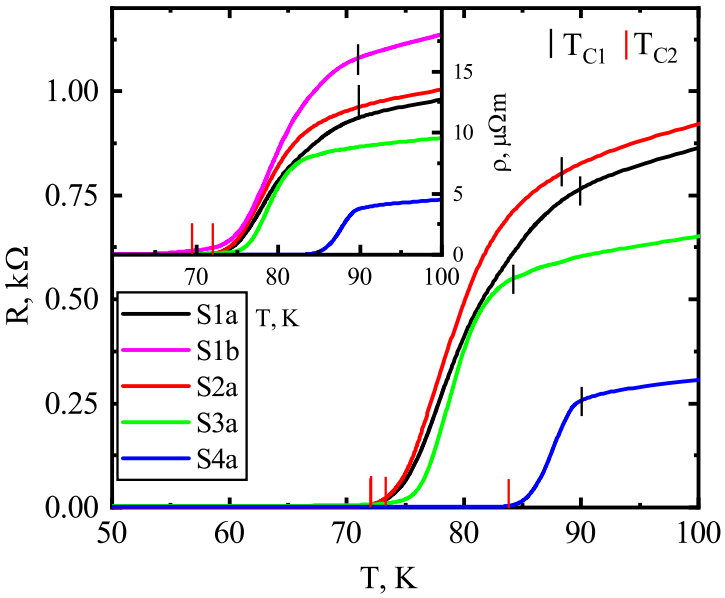

Figure 2.3.4. Dependence of electrical resistance (R) on temperature (T) of investigated microbridges (parameters are presented in Table 3) prepared on Al_2O_3 substrates with CeO_2 sublayers. The insert shows the dependence of the resistivity (ρ) on temperature (T) for the microbridges with different widths (S1a; w = 100 μm ,S1b; w = 60 μm (pink)).

can be seen from Fig. 2.3.4, the $R = f(T)$ dependences exhibit three regions: the metallic normal state (NS) obtained at temperatures higher than T_{C1} , the transient state (TS), which covers temperature range from T_{C1} to T_{C2}, and the superconducting state (SS) appearing below T_{C2}. The T_{C1} was determined as a temperature at which the linear decrease of the samples resistance with temperature in NS transforms to the abrupt decrease of this resistance down to the zero resistance SS state. The T_{C2} corresponded to the highest temperature where the sample resistance in the frame of measurement accuracy is zero.

According to the results shown in Fig. 2.3.4, the resistance and the corresponding resistivity of the films in NS was higher for films deposited on the larger thickness of the CeO_2 sublayers and prepared using 1:2.0:1.6 precursors content (samples S3a and S4a). The increase of B_a in the precursors content from 1:1.6:1.6 to 1:2.0:1.6 led to a decrease of NS resistivity by about two times, but it did not radically influence the T_{C1} and T_{C2} values. Meanwhile, films prepared on lesser (140nm) thickness CeO_2 sublayers demonstrated a

significant increase of T_{C1} and T_{C2}. As it is can be seen from Fig. 2.3.4 and Table 3, the temperature range of the TS state Δ(TS)=$T_{C1} - T_{C2}$ is smaller for samples with lower NS resistance. It was obtained that in the case of S1 type films microbridges having 60 μm width exhibit higher resistivity in comparison to that of 100 μm wide microbridges. As this parameter is important for a fault current limiter's attenuation value, it was decided to perform further investigations only on microbridges with a width equal to 100 μm. The insert in Fig. 2.3.4 shows how the resistivity (ρ) of the film depends on T for superconducting samples having different widths when the thickness of the CeO_2 sublayer h was constant.

DC external magnetic field (bias current 0.75 mA)

Fig. 2.3.5 a), b) shows the magneto-resistive effect of YBCO film manifesting as a change of microbridge resistance $\Delta R(B_{ex}) = R(B_{ex}) - R(0)$ (here $R(B)$ and $R(0)$ are the resistance of the microbridge at fixed and zero magnetic field, respectively) at external magnetic field (B_{ex}). The ΔR vs. B_{ex} dependences for the superconducting microbridge S1a were measured at two different temperatures ranges: (I) $T < T_{C2}$ and (II) $T_{C2} < T < T_{C1}$. It was obtained (see Fig. 2.3.5 a) that the ΔR vs. B_{ex} dependences of the temperature range I are well expressed in the low resistivity region (close to zero in the frame of measurement method sensitivity ($\approx 0.05\ \Omega$), which does not depend on the magnetic field values up to the critical magnetic field B_c. An increase of the temperature (T) led to a decrease of the B_c value as $B_c \approx B_{c0}[1 - (T/T_c)^2]$ (see Fig. 2.3.5 c). Here B_{c0} is a constant and T_c is the critical superconductor temperature. It is a fitting constant describing the thermal properties of B_c and should not be confused with T_{C1} or T_{C2}. At magnetic fields higher than B_c, the superconducting film was transformed into the resistive state, which starts as a linear ΔR dependence on B_{ex} and transforms at higher B_{ex} to nonlinear behaviour. The increase of T produced a more abrupt ΔR vs. B_{ex} dependence and larger range of ΔR in the linear part of ΔR vs. B_{ex} curve. At $T \approx T_{C2}$, the ΔR as a function of B_{ex} is linear in the whole B_{ex} range. In the temperature range II, a further increase of temperature showed a decrease of the magneto-resistive effect (see Fig. 2.3.5 b) and a change of the linear ΔR vs. B_{ex} dependence to $\Delta R \propto B_{ex}^{1/2}$ behaviour.

High current (up to 200mA) regime

Fig. 2.3.6 shows the voltage (V) vs. current (I) characteristics of a microbridge S1a measured at different temperatures. These characteristics were

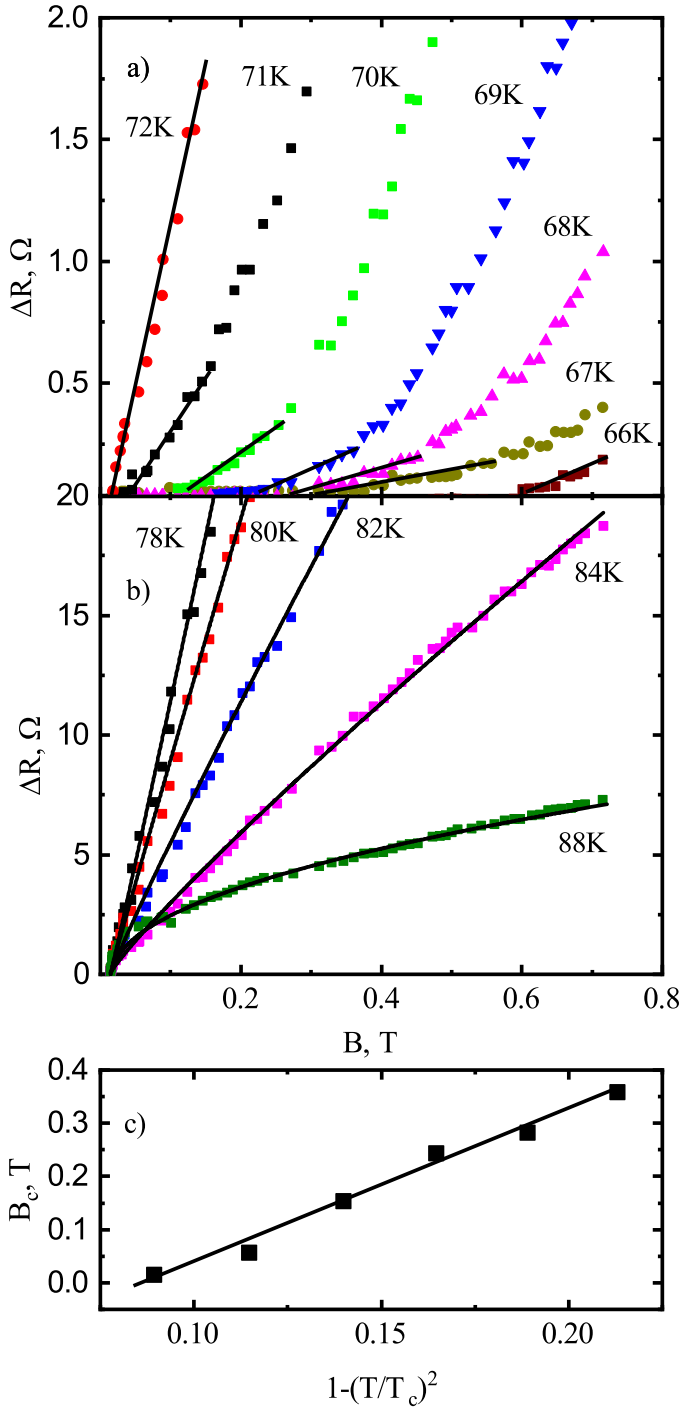

Figure 2.3.5. a), b) Resistance change (ΔR) dependence on the external magnetic field (B_{ex}) at different temperatures of a microbridge S1a. c) shows the critical magnetic field (B_c) dependence on temperature in a $1-(T/T_c)^2$ scale.

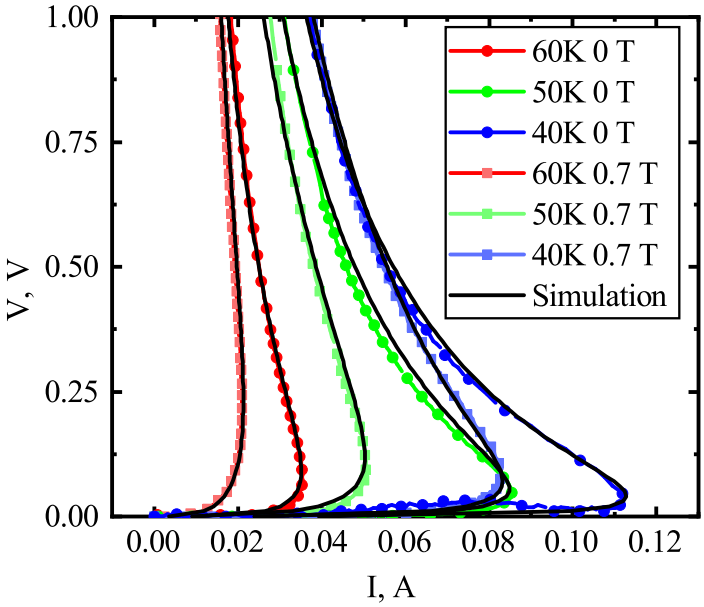

Figure 2.3.6. The IV characteristics of a microbridge S1a at different substrate temperatures. The circles correspond to measurements performed at zero magnetic field, the squares at B_{ex} = 0.7 T. Solid lines are simulations obtained using isothermal IV curves measured by ns duration pulses.

measured in a stabilized voltage source regime in two cases: at zero external magnetic field and when B_{ex} was 0.7 T. As it can be seen from Fig. 2.3.6, they were S-shaped, having a branch with negative differential resistance. The critical current (I_{ci}) at which the negative differential resistance appeared decreased with an increase of temperature T and the B_{ex} value.

Kinetics of the microbridge resistance (triggered by a B_{ex} = 0.75 T field)

When a superconducting bridge, kept at a constant current I_a that is less than I_{ci}, was affected by an external magnetic field (B_{ex}), an instability was observed as a resistance increase over time. This phenomenon is demonstrated in Fig. 2.3.7, which shows the time evolution of R when S1A microbridge was exposed to a 0.75 T DC external magnetic field for 4.45 s. Below I_a = 4 mA, the increase of the R caused by the external magnetic field did not induce any R changes over time; however for higher I_a values, the B_{ex} induced a time dependent growth of R, which started at the beginning of the B_{ex} application. This growth tends to saturate when I_a<I_{ci}. However, at I_a=I_{ci} (≈12 mA), after a relatively slow R

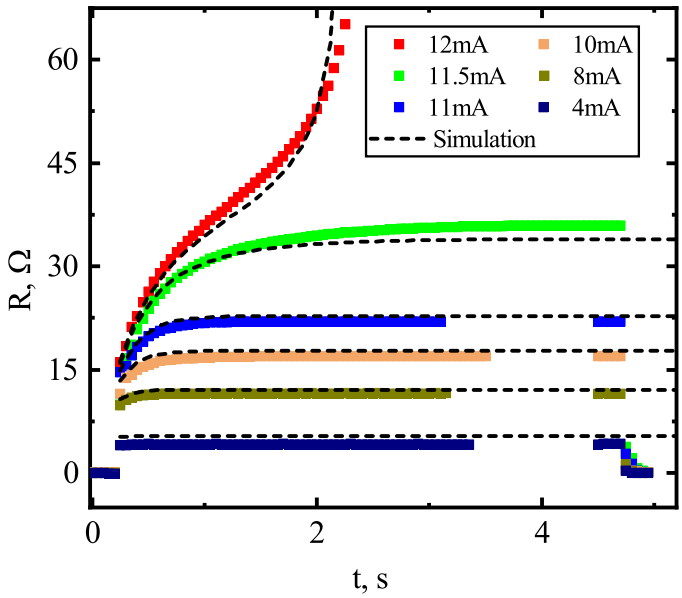

Figure 2.3.7. Time evolution of the superconducting YBCO microbridge S1a resistance after it was exposed to a 0.75 T DC external magnetic field. Dashed lines are simulation results using IV curves obtained with nanosecond electrical pulses.

increase at the beginning of the magnetic field influence, the dynamics of the R time evolution drastically changes, demonstrating a fast growth of R over time.

2.3.4 Resistive state induced by high voltage nanosecond duration electrical pulses

Fig. 2.3.8 demonstrates the typical waveforms of the incident and transmitted electrical pulses at low (Fig. 2.3.8 a) and high (Fig. 2.3.8 b)) current regimes when the microbridge is cooled down to 60 K temperature. At $I \ll I_c$, there is no difference in the waveform of these pulses; however, the amplitude of the transmitted pulse is slightly lower than the incident pulse amplitude. It corresponds to an attenuation of about 0.2 dB being introduced by the superconducting microbridge in a 50 Ω impedance transmission line. This is the result of a contact pad resistance and the small impedance change at the interconnection between coaxial cable and strip-like sample holder. When $I \gg I_c$, the difference between amplitudes of the incident and transmitted pulses strongly increases and a large attenuation (12 dB) is induced in the transmission line.

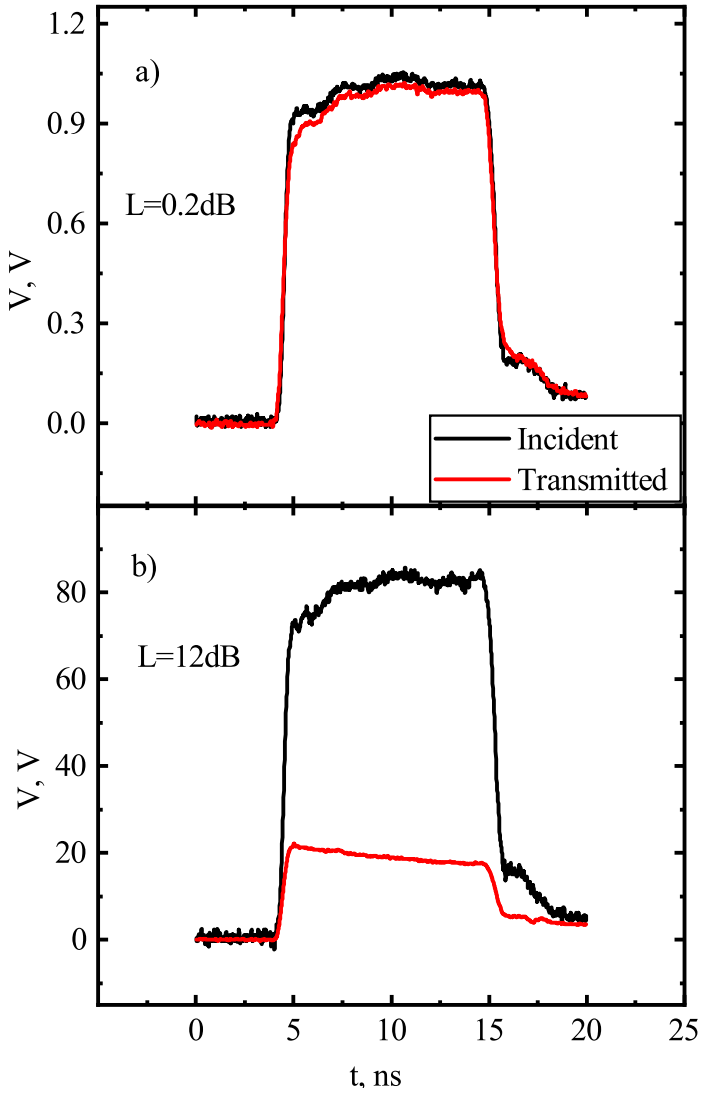

Figure 2.3.8. Waveforms of the incident and the transmitted pulse when microbridge S2a, cooled down to 60 K, was connected in series to a 50 Ohm impedance transmission line: a) low current $I \ll I_c$ regime, b) high current $I \gg I_c$ regime.

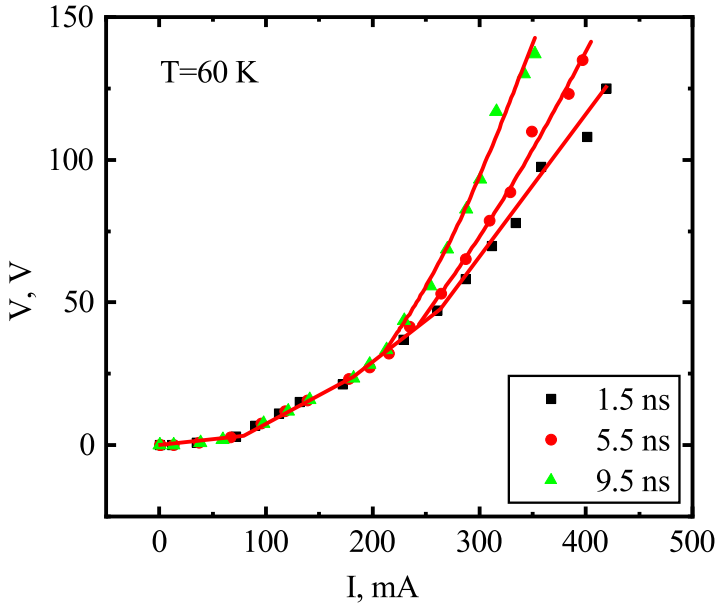

Figure 2.3.9. The IV characteristics of microbridge S2a measured at different time instances.

Moreover, the waveform of the transmitted pulse demonstrates a slow voltage decrease over time.

When $\gg I_c$, the IV characteristics are different when measured at different time instants from the beginning of the current pulse (see Fig. 2.3.9). It shows that thermal effects (Joule heating) play a significant role when the current density through the 100 μm width microbridge exceeds $\approx 4.5 \cdot 10^5$ A/cm^2 ($I \approx 200$ mA). Consequently, for the investigation of the IV characteristics in which the influence of Joule heating is negligible, measurements performed shortly after ($\approx$ 1 ns) the start of the pulse are preferable.

Fig. 2.3.10 a) shows the IV characteristics measured for the S1a sample at different temperatures when the incident electrical pulse rise time is $\approx$ 1 ns. These characteristics were typical for all investigated samples and, as it can be seen from Fig. 2.3.10 a), consisted of an assembly of straight line segments whose number and angle to the current axis increased with an increase of the microbridge temperature. Such shapes of the IV characteristics were obtained earlier in [196] for polycrystalline YBCO films prepared on $NdGaO_3$ (NGO) substrates and were explained by the motion of the vortices associated with various pinning centers having different pinning strengths, which were

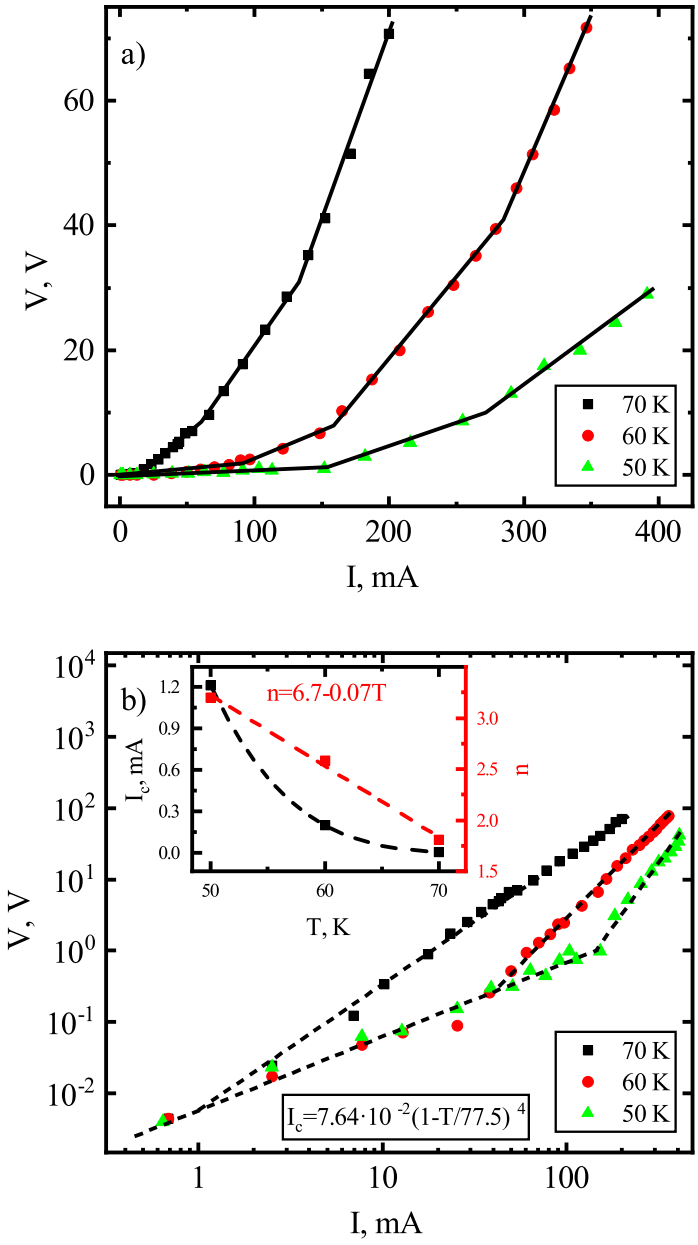

Figure 2.3.10. IV characteristics of S1a sample measured at the end of a square waveform electrical pulse rise time (≈ 1ns). b) The logarithmic plot of these IV characteristics.

uniformly distributed in the superconducting film. The number of centers that can be depinned increases when the temperature of the film approaches T_c. For this reason, at temperatures near T_c , the total IV characteristic becomes highly nonlinear and can be described with high enough accuracy by the power law $V \propto I^n$. This can be seen from the logarithmic plot of the IV characteristics presented in Fig.2.3.10 b. Moreover, this plot shows that the IV characteristic consists of two straight lines: one, which manifests itself at the beginning of the V-I curves and does not depend on the temperature and corresponds to the Ohm's law (n≈1), the other corresponding to the power-law of type II superconductors. The Ohm's law part of the IV characteristic shows initial attenuation (about 0.3-0.7 dB), which, as it was mentioned earlier, has to be associated with the microbridge's electrical contact areas and transmission line cable interconnections.

The analysis using this plot (see inclusion in Fig.2.3.10 b) showed that an increase of temperature (T) linearly decreases the power-law index n as:

$$n = n_0 - \alpha T. \tag{2.3.1}$$

Here α and n_0 are constants. Meanwhile, the critical current (I_c) depends nonlinearly on temperature as:

$$I_c = I_{c0}\left[1 - \frac{T}{T_c}\right]^4. \tag{2.3.2}$$

The I_{c0} in formula (2.3.2) is a function of magnetic field induction (B).

The results presented in Fig. 2.3.8-2.3.10 show that YBCO films prepared on Al_2O_3 substrate with CeO_2 sublayer can be used as protectors against subnanosecond rise time electrical transients. Fig. 2.3.11 demonstrates how microstrips prepared from different films are able to induce attenuation in a 50 Ω transmission line when pulsed overcurrent is produced during subnanosecond time. For comparison of the attenuation properties, microstrips S1a, S2a, and S4a were cooled down to 70 K. The attenuation using microstrip S3a is presented for two temperatures 70 K and 80 K. According to Fig. 2.3.11, larger attenuation was realized using microstrips, whose films exhibit a wider TS temperature range.

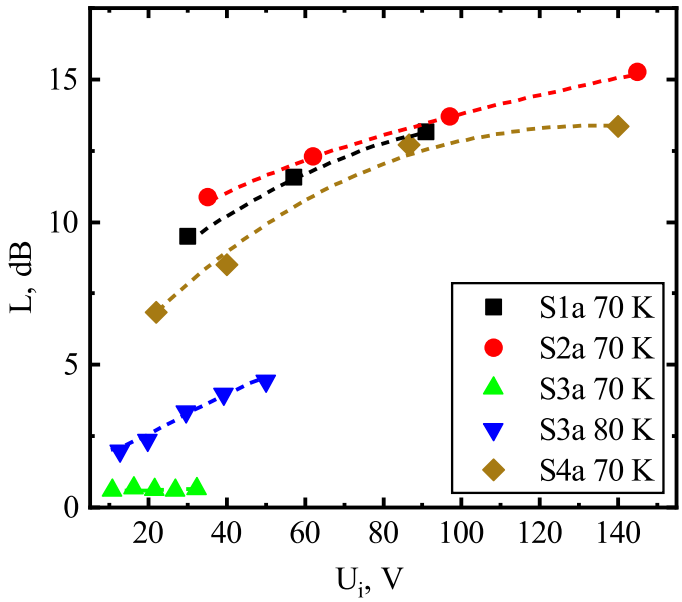

Figure 2.3.11. Attenuation of 50 ohm transmission line (L) vs. incident pulse voltage (U_i) for different microstrips prepared using films listed in Table 3.

2.3.5 Evaluation of thermal and non-thermal effects

This investigation demonstrated that thin submicron thick YBCO films prepared on Al_2O_3 substrates with CeO_2 sublayers exhibit superconducting properties below temperatures ranging from 72 K to 84 K for different content of metal organic precursors and CeO_2 thicknesses. The significantly wider temperature range of TS for films prepared on thicker (440 nm) CeO_2 sublayers in comparison to the films deposited on thinner (140 nm) CeO_2 layers show that these films contained large numbers of structural imperfections having different superconducting properties. In case of the 140 nm thick CeO_2 layer, better matching of the lattice constants between the YBCO films and this layer is thus achieved, which makes it possible to prepare more perfect films having higher critical temperatures and lower TS temperature ranges. Moreover, an insert in Fig. 2.3.4 shows that films have macroscopic inhomogeneity of the properties resulting in wider TS temperature range for lower w microbridges. Also, it has to be stated that the less perfect films are preferable for certain applications as they can provide larger protection of the electrical circuits due to their wider resistive IV characteristic state and thus be triggered more easily by an external magnetic field.

The application of an external DC magnetic field (B_{ex}) induces the resistive state (RS), the appearance of which can be well explained in terms of magnetic flux flow. When B_{ex} is applied at temperatures below T_{C2}, the critical magnetic field (B_c) obtained from the ΔR vs. B_{ex} dependences, fit the classic rule $B_c \approx B_{c0}[1-(T/T_c)^2]$. According to the data presented in the insert of Fig. 2.3.5 for sample S1a, the $T_c \approx T_{C2} = 72$ K. At $T < T_{C2}$, if B_{ex} was higher when B_c the linear increase of resistivity with B_{ex} would demonstrate the validity of the Bardeen-Stephen model typical for flux flow in dirty superconductors [51]. The nonlinear behaviour of ΔR vs. B_{ex} at higher B_{ex} was also obtained in [219] and explained by the interaction between some vortices, which start to move at the banks of the grain boundary and contribute to higher voltage along the sample. In our case, such boundaries could be related to the structural imperfections of wide TS range films.

In case when $T_{C2} < T < T_{C1}$, some part of the microstrip is in a normal state and the contribution of the magneto-resistive effect to the total resistance of the microstrip decreases. This is a result of essentially different behaviour of the magneto-resistive effect, i.e. a decrease of the ΔR value with the increase of microstrip temperature T. Moreover, because the other superconducting regions of the microstrip are close to their critical temperature of the superconducting to normal state transition, the external magnetic field is sufficiently strong and nears the critical field H_{C2} of type II superconductors. In this case as it was shown in [220], the reduction of the number of the quasiparticles participating in the energy dissipation in the d-wave vortex state produces the flux flow resistivity $\propto B_{ex}^{1/2}$ behaviour.

The electrical characteristics of the strip-like microbridges measured using DC bias exhibited strongly non-linear behaviours. We assume that the negative differential resistance region in the *V-I* curve (Fig.2.3.6) as well as the resistance instability (Fig. 2.3.7) is the product of the current-induced flux flow resistive state and the thermal heating of the film, which is uniform along the whole microbridge length. Such model was successfully used to explain the IV characteristics of similar microbridges with widths ranging from 10 to 100 μm made from 0.15 μm thick epitaxial $YBa_2Cu_3O_{7-\Delta}$ films grown on $SrTiO_3$ substrates [188,189]. We also reject the "hot spot" phenomenon during the thermoelectrical instability in our modelling, because, as it was shown in [221], there was no additional voltage jump in the V-I characteristics at the investigated temperature range.

For the numerical simulations of the microbridge behaviour, we used the

isothermal power-law relationship for type II superconductors obtained using ns duration pulses (as suggested in [189]) with the experimental critical current I_c and the power-law index n dependences on temperature (see Fig. 2.3.10 b). As the experimental curves were double valued in voltage, an equation for current was used derived from the power law equation (1.17):

$$I = I_c(T)\left(\frac{V}{V_c}\right)^{\frac{1}{n(T)}} \tag{2.3.3}$$

here V_c is the critical voltage ($E_c l$= 0.3 μV) and I_c is the current at which V_c is reached. The resistance (R_t) of the microbridge obtained from Ohm's law is the following:

$$R_t(T) = V_c I^{n(T)-1} I_c(T)^{-n(T)}. \tag{2.3.4}$$

In order to simulate the V-I characteristic and the time evolution of the microbridge resistance, we calculated the temperature change of the microbridge when it was affected by the electrical current. This was done by using a heat balance equation where the increase in heat (dQ/dt) is equal to the difference between the Joule heating (VI) and Newtonian cooling ($k\Delta T$), assuming that the specific heat (C) of the YBCO material linearly increased with the temperature as:

$$C(T) = \gamma T + C_0 \tag{2.3.5}$$

where γ and C_0 are empirical constants. Taking formulas (2.3.1) and (2.3.2) into consideration and expressing V from eq. (1.17), we obtained the following equation for the calculation of the temperature (T) vs. time (t) dependence:

$$Dd_f \frac{dT(t)}{dt}(\gamma T(t) + C_0) = \frac{V_c I^{n(T(t))+1}}{lw} I_c(T(t))^{-n(T(t))} - k(T(t) - T_s). \tag{2.3.6}$$

Here d_f is the microbridge thickness, D is the density of the YBCO material, k and T_s are the heat conductance and temperature of the substrate, correspondingly.

For the simulation of the resistance dynamics when the microbridge was triggered by a pulsed magnetic field, the equation (2.3.6) was solved numerically. The solid line curves in Fig. 2.3.7 show the modelling of the dynamic resistance response to the magnetic field pulse. At low currents ($I \leq 4$ mA), the

value of the steady state resistance did not change with the applied magnetic field. At such times, the influence of the Joule heating induced temperature increase is negligible. However, at higher currents ranging approximately from 4 mA to 11.5 mA, the value of the steady state resistance reached after several seconds is the result of both the magnetic field and the increase of the microbridge temperature.

The essential change of resistance (R) vs. time (t) dynamic behaviour observed when under the influence of a 12 mA current can also be explained on the basis of the electro-thermal instability model. The solid line curve in Fig. 2.3.7 shows the simulation results using equations (2.3.4), (2.3.5) and (2.3.6), demonstrating that the resistance grows relatively slowly at the beginning of magnetic field pulse and transforms into a rapid, avalanche-like increase of the resistance due to the heating of the tape. It has to be noted that both "saturating" and "unstable" types of R vs. t dependences shown in Fig. 2.3.7 demonstrate qualitative agreement with microbridge temperature vs. time dependences predicted in [189], which additionally confirms the electrothermal origin of the instability.

The IV curves measured using DC were calculated by substituting the empirical $I_c(T)$ and $n(T)$ laws (eq. 2.3.1 and 2.3.2) into the power law equation (2.3.3). In the DC case, each point in the IV dependence is stable because the YBCO microbridge is in thermal equilibrium. For this reason, the dT/dt term in equation (2.3.6) is zero. This makes it possible to obtain a steady state temperature of the film (T_{fs}), which depends on the power ($P = IV$) dissipated in the film as $T_{fs} = IV/(wlk) + T_s$. The final equation for the current voltage relationship was obtained using 2.3.3 and replacing T in (2.3.1) and (2.3.2) by T_{fs}.

$$I - \sqrt[n_0 - \alpha\left(\frac{VI}{klw} + T_s\right)]{\frac{V}{V_c}} I_{c0} \left(1 - \frac{1}{T_c}\left[\frac{VI}{klw} + T_s\right]\right)^4 = 0 \qquad (2.3.7)$$

This equation was solved numerically with respect to I for V values that ranged from 0 to 2 V while looking for the smallest positive root using Newton's iteration method. Experimental coefficient values were used for these calculations. The results are presented in Fig. 2.3.6 (black lines) and show good agreement with the measurements. This demonstrates that the IV curve peculiarities in the DC mode can be well explained by Joule heating due to the induced flux flow resistance.

2.3.6 Summary

The properties of thin YBCO films prepared on Al_2O_3 substrates with CeO_2 layers by the PI-MOCVD method strongly depend on the content of the MOCVD precursors and the thicknesses of the CeO_2 sublayers. These factors influence the film's morphology, resistivity in their normal state, the critical temperature of superconductivity and the temperature range of the transition from normal to the superconducting state.

The exposure of a YBCO film cooled down to a superconducting state to an external DC magnetic field slightly higher than the critical one causes a linear magneto-resistive effect, which is in accordance with the Bardeen-Stephen model typical for flux flow in superconductors. If the film is in the temperature range of superconducting to normal state transition, this corresponds to the condition where the external magnetic field is close to the upper critical field of type II superconductors and the resistance change due to the magnetic field is proportional to the square root of this field. That is typical for d-wave vortices appearing due to the reduction of the number of the quasiparticles participating in the energy dissipation.

The current-voltage (IV) characteristics of microbridges made from these films obtained using DC electrical current have demonstrated S-shaped behaviours, which can be triggered by an external magnetic field and be well explained by the thermo-electrical instability appearing as a result of the uniform Joule heating of the flux flow-induced resistive state of the superconducting film. Meanwhile, the resistive part of the IV characteristics measured using high voltage nanosecond duration electrical pulses consists of several straight lines and is a result of the heating free flux flow. This resistive state is wider for films with large temperature ranges of superconducting to normal state transition. These films are preferable for the design of fault current limiters as they exhibit low voltage thresholds and higher possibilities of transmission line attenuation.

The low dielectric constant and the high thermal conductivity of Al_2O_3 substrates with submicron thick CeO_2 layers make it possible to design multiuse superconducting protectors based on YBCO microbridges, which are able to protect high frequency "front-door" transmission lines against ultra-fast high voltage transients and low DC currents faults.

2.4 Electromagnetic launch of cylindrical type II superconducting armatures using single stage pancake coilgun

This subsection introduces to the behaviour of a type II superconducting armature when accelerated vertically by a pulsed magnetic field generated by a single-stage pancake coil. This study is performed using a numerical MFD finite element simulation and an experimental study of the magnetic field dynamics at the center of the pancake coil when the payload was a superconducting disc made from YBCO, cooled down to 77 K. The dynamic magnetic field measurements were performed using a CMR-B-scalar sensor, which was specifically manufactured in order to increase the sensor's sensitivity in the range up to 500 mT. The experimental results are used to validate the numerical model and to extend the study outside the experimental capability range. The effects of driving current amplitude, pulse duration and pulse shape are investigated and compared between both normal metal and superconducting armatures.

The results presented in the following chapter were originally published in:
V. Vertelis, S. Balevicius, V. Stankevic, N. Zurauskiene, and M. Schneider, "The Application of a CMR-B-Scalar Sensor for the Investigation of the Electromagnetic Acceleration of Type II Superconductors," *Sensors*, vol. 21, no. 4, p. 1293, 2021, doi: 10.3390/s21041293.

2.4.1 Single stage pancake coilgun with a disk-shaped YBCO armature: Experimental setup

The electromagnetic acceleration of the superconducting armature was performed in a vertical arrangement. This allowed for easy cooling and did not require any mechanical guides for the armature. Moreover, by measuring the highest altitude reached by the armature and its time of flight, it was possible to easily evaluate the mechanical energy applied to the armature by the electromagnetic acceleration. The schematic diagram of the experimental setup used for these investigations is presented in Figure 2.4.1a. The magnetic field source used was a 13-turn pancake coil, made from an enameled copper wire (2×4 mm). The coil had an inner diameter of 1 cm, an outer diameter of 6.2 cm and was glued to a textolite housing, which was hollowed out to accommodate the pancake (the housing is not shown in Figure 2.4.1a). The distance from the top of the pancake coil to the top of the housing was 2 mm. The isolation gap

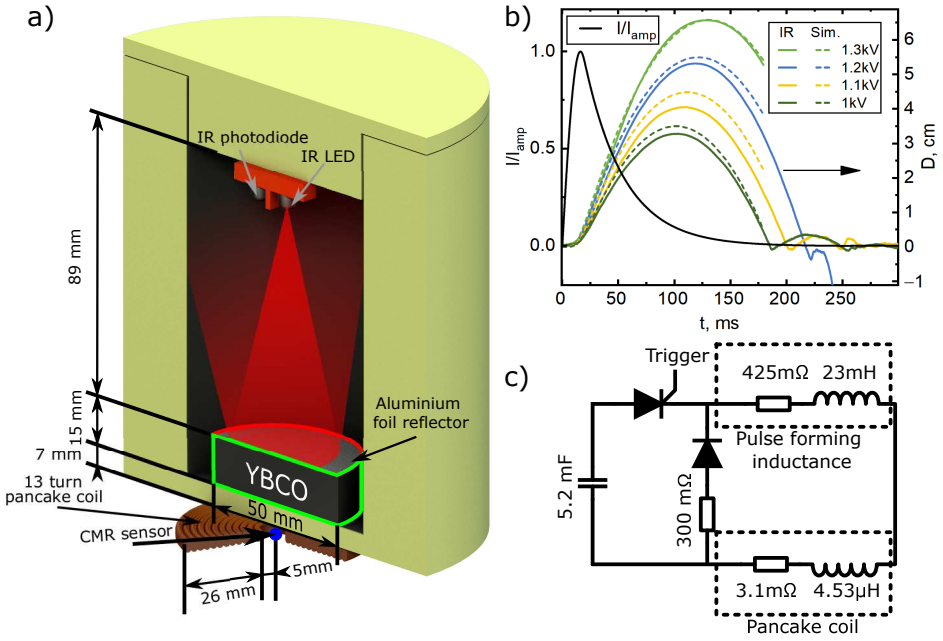

Figure 2.4.1. Experimental setup: schematic diagram and geometry of the coil-gun (a), normalized current pulse produced by the pulse forming unit (black curve) and typical displacement measurements (b). An electrical diagram of the pulse forming unit is presented in (c).

between coil windings was about 0.1 mm. The container for the liquid nitrogen, which served as a cryostat, was made from polystyrene and was mounted on top of the housing. The base of the cryostat on which the YBCO sample rested had a thickness of 5 mm; thus, the total distance between the surface of pancake coil and the superconducting armature was l_{cd} = 7 mm. The cryostat was closed with a lid, leaving an 8.5 cm distance for the projectile to travel vertically inside it.

For the superconductor launch experiments, a commercially available bulk single domain seed melt grown YBCO sample with a critical temperature of ∼90 K [222] was used (seen in fig. 2.4.2). The sample had a disc geometry with a diameter of d_D = 50 mm, a height of h_D = 15 mm and a mass (m) of 171 g. The disc was cooled down by slowly dripping liquid nitrogen onto it until the nitrogen began to wet the YBCO surface, after which the nitrogen was poured onto it until it was submerged. The experiments were performed once the nitrogen boiled off and was no longer visible at the bottom of the container in order to avoid any drag caused by the residual nitrogen.

Figure 2.4.2. Bulk single domain seed melt grown YBCO samples. One on the bottom has an aluminum reflector attached.

Power to the pancake coil was delivered from a pulse forming unit (PFU). A schematic electrical circuit of the PFU is presented in Figure 2.4.1c. The PFU generated a single, tooth-shaped current pulse with a ∼16 ms rise time and a ∼150 ms decay ("tail") (see black curve in Figure 2.4.1b). The PFU capacitor bank was rated for 5 kV charging voltage and was able to produce about a 2.5 T amplitude magnetic field pulse at the center of the pancake coil. The PFU was equipped with a large (23 mH) pulse forming inductance (compared with the 4.53 μH of the pancake coil) in order to reduce the superconductor's influence on the total inductance of the circuit. This allowed the use of a standard pulse shape, regardless of the amplitude of the pulse or the presence of the superconducting armature. To minimize the influence of the mechanical stress on the superconductor created by the transient magnetic field, the amplitude of the magnetic field pulse used for the EM acceleration was no more than 0.35 T. This magnetic pulse amplitude was able to launch the superconductor to the upper limits of our measuring range.

The CMR-B-scalar sensor used for the pulsed magnetic field measurements was made from a 0.4 μm thick La-Sr-Mn-O (LSMO) film grown onto a polycrystalline Al_2O_3 substrate by the pulsed injection metal–organic chemical vapor deposition technique [223]. For the relatively low magnetic field values (up to 0.3 T) used in our experiments, it was necessary to have an extremely

sensitive sensor. This was achieved by using a special chemical content of the film, i.e., $La_{0.82}Sr_{0.18}Mn_{1.15}O_3$ with Mn excess. According to [224], the magnetoresistance of films with this content at room temperature is about 30 % higher compared to films with stoichiometric Mn content. Another specific feature of our experiment was the highly inhomogeneous distribution of the magnetic field in the space between pancake coil and the superconducting armature where the sensor was placed. In such case, the accurate measurement of the local magnetic field requires a sensor with an extremely small active volume. For this reason, we used a CMR-B-scalar sensor with the following dimensions: 400 μm width, a 50 μm gap between electrodes and a 0.4 μm thickness. The effective volume of such sensor, estimated by using its highest dimension as its diameter, was $\approx 10^{-2}$ mm^3.

Manganites (LSMO) below the temperature of the transition from the paramagnetic to the ferromagnetic states (T_m) exhibit remnant magnetization [213]. Therefore, special procedures of calibration were required to avoid memory effects when the sensor was used at cryogenic temperatures [225]. This complicated the use of the CMR-B-scalar sensor in the vicinity of a superconductor cooled down to a liquid nitrogen temperature. To circumvent this, the CMR-B-scalar sensor was placed on the central axis of the pancake coil outside the cold zone, so that only the sensor's encapsulation touched the base of the cryostat. Thus, the active volume of the sensor was at a 7.5 mm distance from the bottom of the superconducting disc-shaped armature. As the temperature of the CMR-B-scalar sensor did not get much lower than room temperature, the sensor demonstrated no memory effects.

It should be noted that the magnetoresistance effect in such thin manganite films has a very low anisotropy (less than 2%) to the direction of the magnetic field when the value of this field is higher than 1 T [226]. However, for lower fields, this anisotropy increases with the decreasing magnitude of the field, and in our case was about ± 10%. In order to decrease the measurement error due to this anisotropy, we placed the sensor so that the thin film plane was perpendicular to the symmetry axis of the pancake coil. We estimated that a ten degree change in the field direction produces about a 0.3% measurement deviation from the real value.

For measurements of the vertical displacement of the superconducting armature, an analogue IR distance sensor was placed in the middle of the cryostat lid. This sensor measured the intensity of the reflected infrared light, which is a distance-dependent quantity. The bore of the cryostat was covered with an

IR absorbing coating to reduce the background signal of the distance sensor. A reflector made from thin aluminum foil was mounted on the top surface of the YBCO disc to increase the reflectance and in turn, the signal at greater distances.

Our experiments began with the cooling procedure described above. Once the liquid nitrogen had mostly boiled off, the capacitor bank was charged to the desired voltage. After the liquid nitrogen was no longer visible at the bottom of the cryostat, the cryostat was carefully closed with the lid. The estimated disk temperature based on a measurement made using a resistive thermometer Pt-1000 placed at the bottom of the disk was $\sim$76.6 K. Then, the capacitor bank was discharged through the pulse-forming inductance connected in series with the pancake coil. Typical disc trajectories can be seen in the top right of Figure 2.4.1b (colored solid curves). Artifacts seen in the trajectory after armature touchdown were caused by a physical rebound from the bottom of the container. After the experiment, the sample was repositioned and resubmerged in nitrogen for a consecutive test.

2.4.2 Motion of the superconducting armature and magnetic field dynamics

Disk displacement (D) studies were performed in the free flight regime when the drag force caused by the surrounding nitrogen gas was negligible. To avoid any rotational motion of the disk-shaped superconducting armature that could lead to an unreliable signal from the IR sensor, the disk center, the pancake coil center and the magnetic field sensor were placed along the same axis. The experimental armature displacement vs. time curves are presented in the top right of Figure 2.4.1b. They consisted of several peaks, the first of which shows the armature movement due to the electromagnetic acceleration, while the others are the result of the disk bouncing from the bottom of the cryostat. As it can be seen, the front of the first peak exhibits two phases: a relatively slow (delay) altitude change that lasts approximately 15 ms after the beginning of the current pulse and corresponds to the current pulse rise time, and a fast phase, which lasts up to the time instant when the armature reaches its highest altitude. The displacement growth during the delay phase was more abrupt at higher capacitor bank charge voltages. The fast phase of the displacement curve can be well approximated by a parabolic law that is typical for free fall at the surface of the Earth.

Maximum displacements (D_m) in addition to direct readings of the IR sensor (labelled "Voltage" in Figure 2.4.3) were also estimated from the flight du-

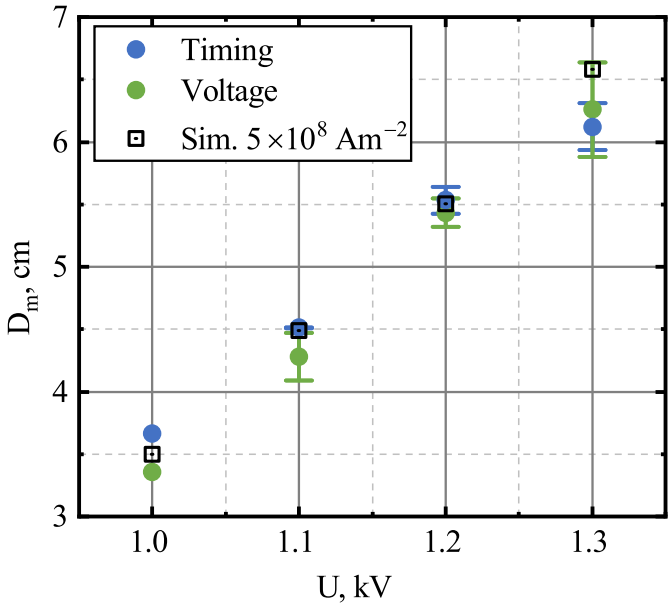

Figure 2.4.3. Maximum displacement (D_m) reached by the superconductor for different capacitor voltages. The height calculated from the flight duration is labelled "Timing". "Voltage" corresponds to the height measured by the sensor, and "Simulation" shows the results obtained from modelling with j_c=5 · 10^8 A/m^2.

rations (labelled "Timing" in Figure 2.4.3) as the lift-off and touchdown events could be clearly identified from the displacement curves. The values of D_m for different capacitor charge voltages (from 1 to 1.3 kV) are presented in Figure 2.4.3. The experimentally used capacitor voltages corresponded to the 450, 490, 530 and 570 A current amplitudes I_{amp} flowing through the pancake coil. At higher charging voltages, the armature rose past the distance sensor calibration range, which covered nearly the whole cryostat. For voltages below 1 kV, the displacement readings were too small to be reliable, and no displacement was observed for voltages below 700 V when the Lorentz force was smaller than the weight of the YBCO disc. "Timing" and "Voltage" approaches gave similar results. D_m appeared to follow a nearly linear trend with increasing capacitor voltage within the investigated voltage range.

Figure 2.4.4 shows the results of the magnetic field measurements using a CMR sensor placed, as shown in Figure 2.4.1a, during experiments with and without the superconductor. In the case of an empty cryostat experiments (la-

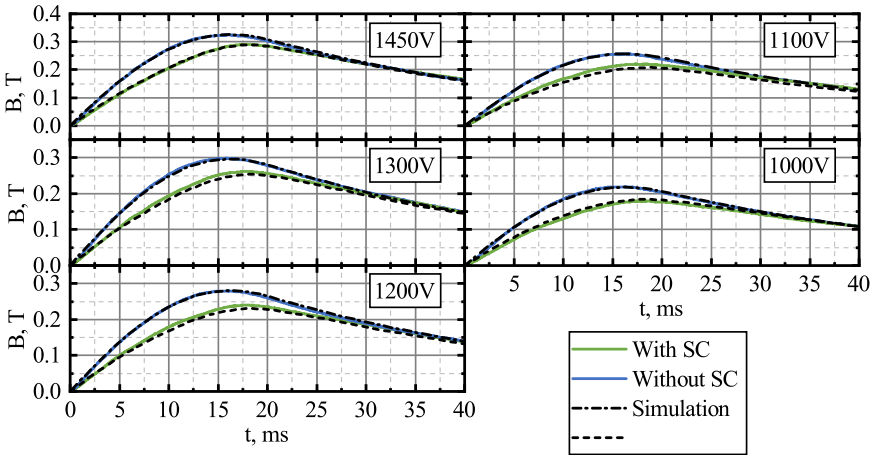

Figure 2.4.4. Magnetic field dynamics: the blue curves show the measured field with the empty cryostat. The green curves represent the measurements during the acceleration of the superconductor. The dashed lines are the simulation results of the reference field and the field during superconductor acceleration (j_c=5 · 10^8 A/m^2) for the corresponding capacitor charge voltages.

belled "Without SC"), the magnetic field pulses had the same waveforms as the current pulses flowing through the pancake coil. Introducing the superconductor significantly changed the magnetic pulse waveforms coming from the empty cryostat case. The superconducting disk caused a decrease in the magnetic field magnitude. This decrease was strongly expressed in the beginning of the magnetic field pulse and partially covered the pulse decay period. The difference between the reference field magnitude ("Without SC") and the one during launch ("With SC") gradually disappeared as the superconducting armature moved away from the pancake coil and its influence on the field in the sensor position diminished. The time until the magnetic field value for "Without SC" and "With SC" became the same, decreased with the increasing capacitor bank charging voltage and was approximately equal to the delay time visible in the displacement vs. time curve (see Figure 2.4.1b). This shows that the electromagnetic interaction between the coil and the superconducting disk mainly took place during this time period.

2.4.3 Modelling the superconducting armature using H formulation

The behaviour of our experimental setup was also investigated numerically. Figure 2.4.5 shows the principal geometry used in our modelling. The dimen-

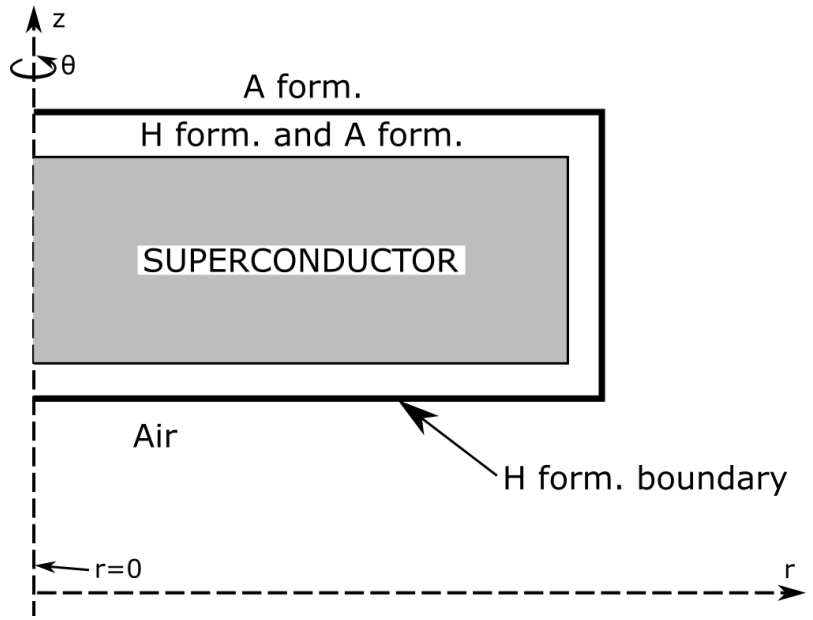

Figure 2.4.5. Model geometry: the superconductor domain is represented by the grey square, and the air domain is left white.

sions of the superconducting domain used for simulation were the same as that of the sample's used in the experiments. The nonlinear eddy current problem was solved in the armature's frame of reference using Maxwell's equations in their H-formulation (H-form) in 2D axis-symmetric form using Comsol Multiphysics commercial software:

$$\nabla \times \mathbf{E} + \mu \frac{\partial \mathbf{H}}{\partial t} = 0 \tag{2.4.1}$$

$$\nabla \times \mathbf{H} = \mathbf{j} \tag{2.4.2}$$

Here, $\mathbf{E}$ is the electric field (bold symbols represent vectors), μ- the magnetic permeability, $\mathbf{H}$ - the magnetic field and $\mathbf{j}$ - the current density. Different E substitution laws were used for the air and superconductor domains. The air was described as having linear resistivity $E = \rho j$, while a power–law relationship was used for the superconducting domain.

$$\mathbf{E} = E_{\mathrm{c}} \left(\frac{|\mathbf{j}|}{j_{\mathrm{c}}} \right)^{n} \frac{\mathbf{j}}{|\mathbf{j}|} \tag{2.4.3}$$

Here, E_{c} is the critical electric field (by convention 1 μV/cm), j_{c} is the cur-

rent density at which the critical electric field is reached and n is a parameter that describes the "hardness" of the superconductor and models the "steepness" of the superconducting-normal transition. Generally, j_c depends on the magnetic field and the temperature. These dependencies were neglected in our model, and a constant j_c was assumed. This is physically accurate when the sample does not heat up, and a slowly varying region of the j_c-H curve is reached.

The H-form problem is a boundary value problem with a boundary condition [162]:

$$\mathbf{H}(r,z,t) = \mathbf{H}_{SC} + \mathbf{H}_{PC} \tag{2.4.4}$$

Here, $\mathbf{H}_{SC}$ is the magnetic field generated by the eddy currents inside the superconductor and $\mathbf{H}_{PC}$ is the field generated by the pancake coil. $\mathbf{H}_{PC}$ is the product of the current pulse $I_{amp}G(d \cdot t)$ (I_{amp} is the amplitude of the pulse, G represents the pulse waveform seen in Figure 2.4.1b, t is the time and d is the pulse duration multiplier. d = 1 corresponds to the experimental pulse). The magnetic field generated by the coil thus was:

$$\mathbf{H}_{PC} = \mathbf{F}(r, z + l_{cd} + D(t)) \cdot I_{amp}G(d \cdot t) \tag{2.4.5}$$

Here, the $\mathbf{F}(r,z)$ is the spatial magnetic field map of the pancake coil, which was calculated separately. $\mathbf{H}_{SC}$ was calculated in a separate A formulation module (magnetic fields in AC/DC module) using the current density calculated in the H-form module as an input and treating the entire model domain as air to avoid a secondary generation of eddy currents.

The electrodynamic problem was solved in the superconductor's frame of reference, offsetting the magnetic field map by the solution of the mechanical problem $D(t)$ for each time step. The displacement, velocity and acceleration were calculated from the Lorentz force, taking gravity into account. Since the problem is axially symmetric, the dynamic equation for the vertical displacement (D) was:

$$m\frac{d^2D(t)}{dt^2} = \int (j_\theta \cdot \mu H_r) dV - mg \tag{2.4.6}$$

Here, m is the disk mass (in our calculations 171 g), and j_θ and H_r are current density and magnetic field components in θ and r directions. V is the disk volume, and g is the standard gravity (9.8 m/s^2).

2.4.4 Analysis of mechanical energy transfer to the superconducting armature

For the analysis of the experimental results presented in Figures 2.4.1–2.4.4 (D vs.t, D_m vs. capacitor bank voltage U and B vs. t at sensors position), we performed calculations using the mathematical procedures presented in section 2.4.3. In our model, the superconductor was described by two parameters: j_c and n. The value of the parameter n was chosen to be 20, because at that value, it describes a hard super-conductor with a flux-creep regime [130], which is the most common kind supported by the literature [43, 216, 227]. The dashed curves in Figure 2.4.1b show the modelling results of the D vs. t dependence. As it can be seen, it well demonstrates all the features of the disc movement obtained experimentally (delay and parabolic phases). Good quantitative agreement (in the frame of experimental error) between the experiments and the calculations was achieved using $j_c = 5 \cdot 10^8$ A/m^2. In order to estimate how reasonable this value was, we calculated the j_c using the trapped magnetic field (B_t = 1.2-1.3 T) measured at 77 K temperature 1 mm above the superconductor's surface, which was included in the data sheet provided by the disk manufacturer [222]. This estimation was performed using an analytical formula (2.4.8) derived from the Biot–Savart law by its direct integration over a cylindrical domain populated by a constant current density directed azimuthally:

$$\mathbf{B}(0,z) = \frac{\mu j_c}{4\pi} \int_0^a \int_0^{2\pi} \int_{-d}^{d} \frac{1}{\sqrt{r'^2 + (z-z')^2}^3} \begin{Bmatrix} -cos\theta(z-z') \\ -sin\theta(z-z') \\ r' \end{Bmatrix} r' dr' d\theta' dz', \tag{2.4.7}$$

$$j_c = \frac{2B_t}{\mu} \left((z-d) \ln \left| \frac{\sqrt{a^2 + (z-d)^2} + a}{z-d} \right| - (z+d) \ln \left| \frac{\sqrt{a^2 + (z+d)^2} + a}{z+d} \right| \right)^{-1} \tag{2.4.8}$$

Here B_t is the trapped field, a is the radius of the disk, d is its half height and z is the distance between the center of the disk and the point at which the trapped field was measured (on the central axis of the disk). A j_c in the range 1.2–1.3·10^8 A/m^2 was obtained. A four times higher j_c value that was satisfactory to match our modelling with the experiments can be easily explained by the significantly lower magnetic field (0.35 T) in our experiments than the

one generated by the magnetized sample according to the datasheet. Such bulk superconductor j_c behaviour was provided by the disc manufacturers in [228].

Using fixed j_c and n values ($5 \cdot 10^8$ A/m^2 and 20, respectively), the obtained simulations were in good agreement with the experimental data (maximal displacement D_m for different U) that is presented in Figure 2.4.3. D_m was evaluated from the calculated D vs. t curves, taking the peak value. Modelling based on equations presented in section 2.4.3 allowed the simulation of the magnetic field dynamics measured by a CMR-B-scalar sensor (see Figure 2.4.4) in both the "Without SC" (dashed–dotted curves) and "With SC" (dashed curves) cases. As it can be seen from Figure 2.4.4, the B vs. t dependences measured during the launch of the superconducting disk can be well described by simulations using the same j_c and n parameters that were used for the simulation of D vs. t and D_m vs. U.

Good agreement between the simulation and the experimental results demonstrated that the modelling method in the armature's frame of reference, neglecting Joule heating, is suitable for the study of the behaviour of type II superconductors during an electromagnetic launch. In the following sections, we present theoretical studies of this configuration, which were outside the limits of our experimental capabilities. We investigated different scenarios with different pancake current waveforms: "step-like" (1 ms rise time) and "experimental" (Figure 2.4.1b). In addition, we investigated the effects of critical current density, armature starting distance from the driving coil and pulse duration using the experimental current pulse waveform. The performance of the superconducting armatures was compared with Cu and Al armatures of the same geometry, cooled to 77 K.

Influence of j_c on Energy Conversion

In a vertical acceleration arrangement, the total mechanical energy is the sum of its kinetic energy and potential energy. During acceleration, this energy evolves over time until a steady value W_{tot} is reached. This energy value depends on the electromagnetic energy generated in the pancake coil and the electromagnetic interaction between the superconducting armature and the coil. With a fixed coil current pulse waveform, the amplitude I_{amp} and the armature geometry W_{tot} depends only on the magnitude of j_c. Calculations of the j_c influence on W_{tot} transferred to the armature at different coil current amplitudes were performed using experimental armature geometry at two starting distances from the surface of the pancake coil and the superconducting armature: 7 (our

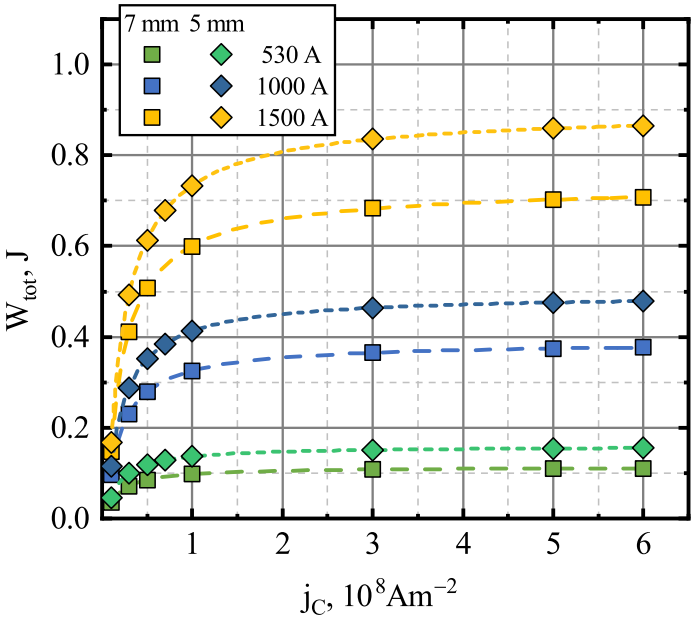

Figure 2.4.6. The influence of the critical current density on the total mechanical energy transferred to the superconductor for different current pulse amplitudes and starting heights. The symbols represent the simulation data. The lines are the logistic function fits ($y(x) = (c_1 - c_2)/(1 + (x/x_0)^p) + c_2$).

experimental condition) and 5 mm, presented in Figure 2.4.6. Initially, as can be seen in Figure 2.4.6, an increase in the j_c leads to an increase in W_{tot} transferred to the superconductor, but with sufficiently high j_c, this transfer tends to saturate. This can be explained by the decrease of the magnetic field penetration depth, which becomes shallower and approaches a surface field limit due to the increase in the j_c. This depth then again increases with the field amplitude and the surface current limit is pushed to higher j_c values. As can be seen in Figure 2.4.6, under otherwise identical launch conditions (pulse waveform and amplitude), a decrease in the distance between the pancake coil and the superconducting armature l_{cd} increases the W_{tot} value. Lowering the l_{cd} by 2 mm causes increases in the W_{tot} of about 40%, 27% and 22% for pulse amplitudes of 0.53, 1 and 1.5 kA, respectively. These results indicate a way of making more economical launch systems. Relatively high launch efficiency can be reached using a superconductor with a relatively low j_c.Thus expensive, high j_c armature material could be replaced by materials with a lower j_c without a significant decrease in the launch efficiency.

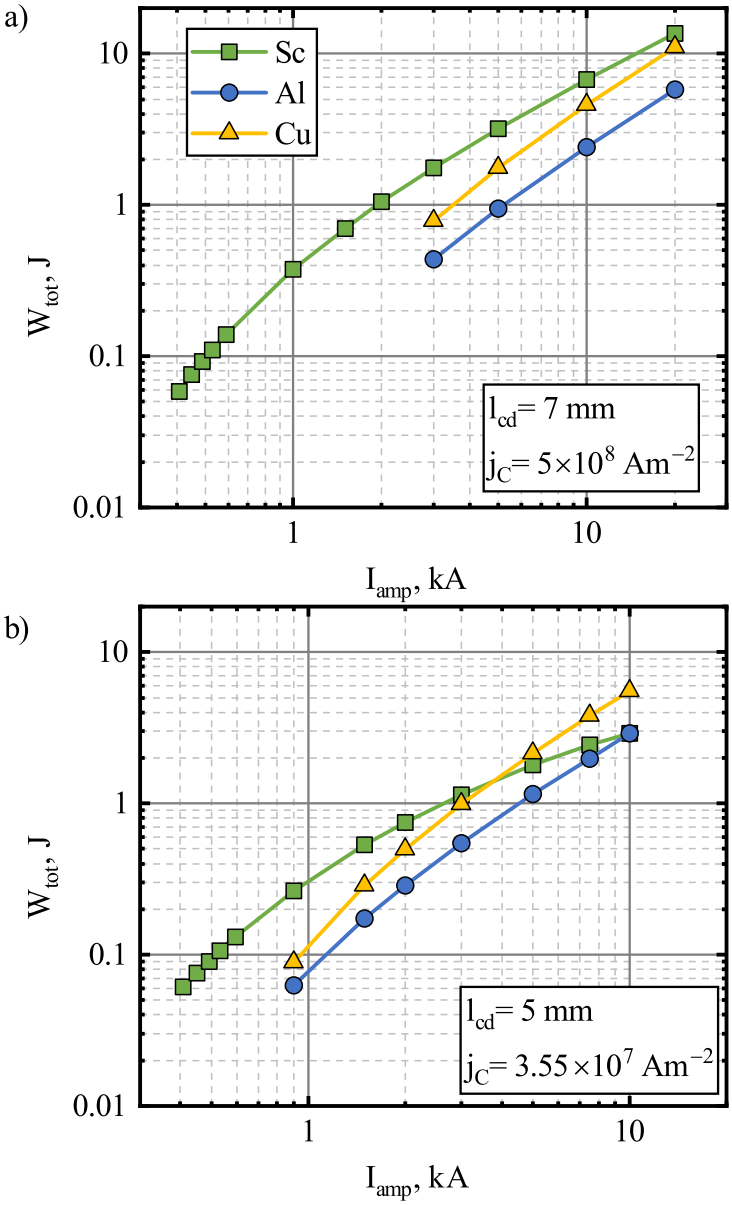

Figure 2.4.7. The influence of the current pulse amplitude on the total mechanical energy transferred to an armature made from a type II superconductor, copper or aluminum for the experimental pulse shape and duration. l_{cd}=7 mm, j_c=5 · 10^8 A/m^2 (a) and l_{cd}=5 mm, j_c=3.55 · 10^7 A/m^2 (b).

Effects of Pulse Amplitude

To investigate the behaviour of an electromagnetic superconductor launch in a broader range, we performed numerical calculations outside the current amplitude range that our experimental setup could withstand. Two sets of l_{cd} and j_c were investigated (7 mm with $5 \cdot 10^8$ A/m^2 and 5 mm with $3.55 \cdot 10^7$ A/m^2). The first one corresponded to the experimental conditions. The second set produced values of W_{tot}, which were close to those obtained in the experimentally investigated scenarios, only with a 2 mm shorter starting distance l_{cd}. This set illustrates the worst case that could be justified by experimental error. The performance of the superconductors was also compared with armatures of the same geometry, which were made from copper and aluminum, the materials most commonly used today. We assumed the temperature of liquid nitrogen for all of the materials to make the comparisons fair. Masses and resistivities of the armatures used in the simulations were m= 264 g and $\rho = 2.65 \cdot 10^{-9}$ Ωm for copper and m= 79.5 g and $\rho = 4.44 \cdot 10^{-9}$ Ωm for aluminum. The results obtained from the simulations are presented in Figure 2.4.7 (points up to 600 A correspond to the experimental values). As can be seen, an increase in the current amplitude resulted in a higher energy being transferred to all the armatures. For the superconducting armatures, this increase is larger in the lower amplitude range ($W_{tot} \propto I_{amp}^{\sim 2}$) and reduces to a nearly linear relationship for the first parameter set and a sublinear one for the second set. Superconducting armatures performed better than the normal metal ones at these lower current pulse amplitudes in both cases. This advantage decreased with the current pulse amplitude, and in the second parameter set case, copper overtook the superconductor at $I_{amp} \approx 3.7$ kA. By extrapolating the data, copper is expected to overcome the superconductor at 43 kA in the first parameter set case.

The Influence of Pulse Duration

The energy obtained by the superconducting armature due to electromagnetic acceleration depends on the duration of the coil current pulse. In addition, the launch process is complicated by the large magnetic field gradient through which the armature passes during acceleration. To investigate how W_{tot} depends on pulse duration (d), we performed calculations using pulses with a fixed current pulse amplitude (1.5 kA) and the waveform shown in Figure 2.4.1b, scaled in time by a factor of d. d is the relative pulse time duration, and its value represents how many times the pulse duration is shorter. The experimental pulse duration was taken to be $d = 1$.

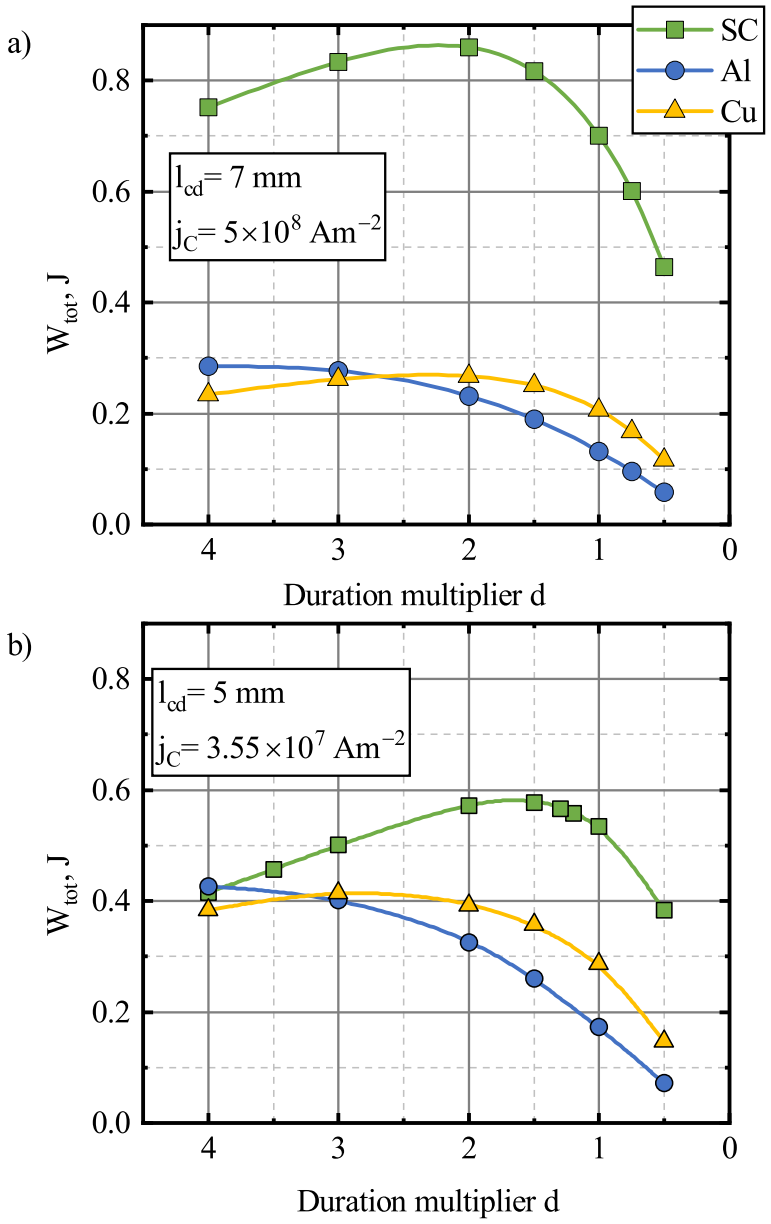

Figure 2.4.8. The influence of pulse duration on the total mechanical energy transferred to armatures made from type II superconductor, copper or aluminum. The pulse amplitude was 1.5 kA. l_{cd}=7 mm, j_c=5 · 10^8 A/m^2 (a) and l_{cd}=5 mm, j_c=3.55 · 10^7 A/m^2 (b).

Figure 2.4.8 illustrates the effects of the d value on W_{tot} in each of the parameter sets. In the case of the first parameter set, the superconductor outperformed the metal armatures within the entire investigated duration range. However, this advantage of the superconducting armature was lower in the case of the second set of values and disappeared when the pulse duration was four times shorter. The metal armatures also showed improvement when brought close to the field source due to the increased magnetic coupling. All of the materials exhibited a peak in their W_{tot} vs. d dependence. The superconductor peaked at a $\sim$2 times shorter pulse for the first set and $\sim$1.5 times shorter for the second one and was $\sim$3 and $\sim$1.5 times more effective than the Cu armature at the same pulse length. Such behaviour can be explained by examining both the very long and the very short pulses. At the very short magnetic field pulses, the armature can be considered stationary throughout the pulse. In such cases, the force applied to the armature is proportional to the amplitude of the field for both the metal and superconducting armatures. When the pulse amplitude is kept constant, an increase in the pulse duration acts only by increasing the interaction time between the coil and the armature, which increases the energy transferred to the armature. However, under the action of a long pulse, the position of the armature cannot be considered static. At a certain moment, the driving force overcomes gravity, and the armature starts to move away from the coil. As it does so, the coupling to the coil decreases and the utilization of the remaining part of the magnetic field pulse for the energy transfer becomes smaller. In the metal armature cases, this increase in the pulse duration also reduces the driving force as the eddy currents decay over time and the field penetrates deeply into the armatures. This explains why metal armatures peaked at higher values of d. The results obtained show that the superconductor can be effectively accelerated using slower magnetic pulses. This opens up possibilities of using cheaper power sources, which do not require fast, high power switching to drive the coil.

Step-Like Field Pulses

The effects of pulse duration showed that the superconducting armature is better than the metal ones at longer pulses. For this reason, we investigated the effects of step-like (rise time of 1 ms) current pulses and their amplitude. This pulse shape has both a high magnetic field transient in the beginning of the pulse and a constant field afterwards. The results for this scenario can be seen in Figure 2.4.9. Initially, the energy transferred to the armature increased with

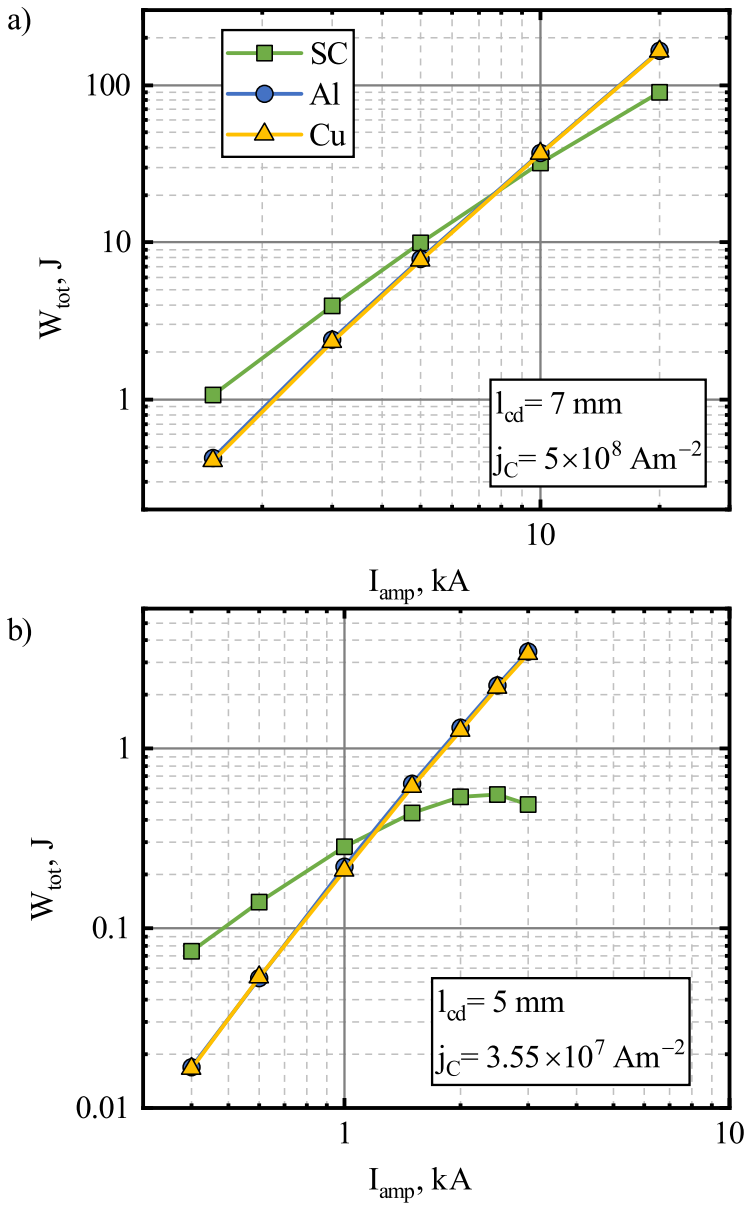

Figure 2.4.9. The influence of step-like current pulse amplitude on the total mechanical energy transferred to an armature made from type II superconductor, copper or aluminum. l_{cd}=7 mm, j_c=5 · 10^8 A/m^2 (a) and l_{cd}=5 mm, j_c=3.55 · 10^7 A/m^2 (b).

the increasing magnitude of the applied field. For the first set of parameters, W_{tot} for the superconductor increased with I_{amp} by a power of 1.7, while for the metals, this power was 2.3. In case of the second set of parameters, the power index of this relationship for metals did not change much and stayed at about 2.5. For the superconducting armature, the initial growth power of $\sim$1.5 decreased with I_{amp} and W_{tot} and began to decrease for the higher values of I_{amp}. The superconductor outperformed the metals until the amplitude of the step reached $\sim$7.5 and $\sim$1.15 kA for the first and second parameter sets, respectively. This relatively low current crossover point was in part caused by the strong braking of the superconducting armature (see analysis presented in the next section).

Magnetic Braking

The magnetic braking phenomenon is important for the operation effectiveness of inductive electromagnetic launchers. It is caused by the interaction between an armature and the magnetic field source when the flux that has already penetrated the armature begins to decrease. Magnetic field penetration into the armature is called armature capture [207]. At a certain acceleration stage, it decreases the armature driving force and, consequently, the efficiency of the synchronous wave induction coilguns, which use metal as the material for the projectile. During electromagnetic acceleration, the flux through an armature can decrease due to the decrease in the external field when the driving current begins to fall or due to its motion in a large magnetic field gradient. When this flux starts to decrease, a counter current is induced. This current then flows in the same direction as the current in the coil, and an attractive force component is introduced. In some cases, this attractive force can overcome the propelling force, and the armature is decelerated.

We obtained that this breaking phenomenon in the case of the superconducting armature is well expressed in the case of step-like pulses. Figure 2.4.10 illustrates the evolution of the mechanical energy ($W_{me}(t) = W_{kinetic}(t) + W_{potential}(t)$) over time when a superconducting armature is being accelerated by a step-like pulse, using the second set of parameters. It depicts the transition between no braking and the considerable braking regimes. For low current amplitudes, the W_{me} steadily approaches a constant value (W_{tot}). The W_{me} vs. t dependences at higher current amplitudes have a maximum (W_{max}) that is reached in the beginning of the acceleration, after which they decay to a steady value of W_{tot}, which we consider to be the total energy transferred to the armature. The

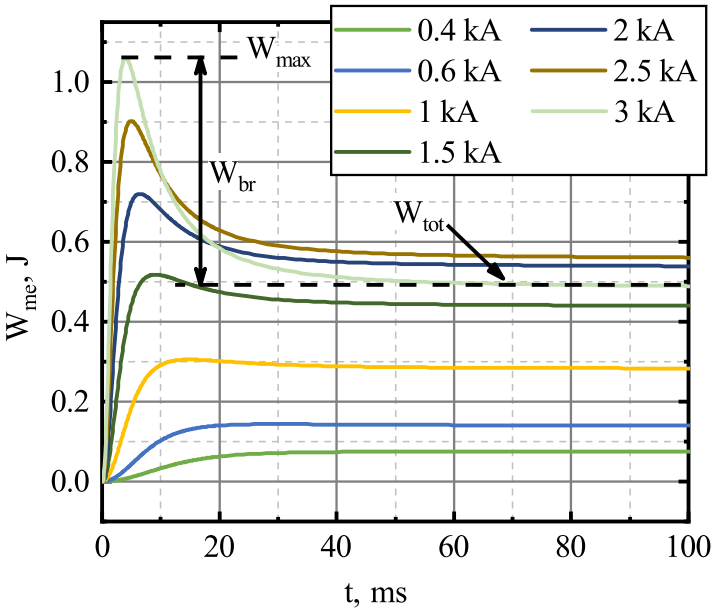

Figure 2.4.10. Evolution of the mechanical energy of the superconducting armature over time when the armature was accelerated by a step-like driving current pulse. l_{cd}=5 mm, j_c=3.55 · 10^7 A/m^2.

energy lost to magnetic braking or the braking energy is the difference between the W_{max} and W_{tot}.

No magnetic braking was observed in the critical current density parametric sweep. The values of W_{br} for all the other investigated scenarios can be seen in Figure 2.4.11. The strongest braking was observed using step-like pulses when W_{br} increased with I_{amp} by the power of ∼3.5 and ∼3 for the first and second sets, respectively, for the superconducting armature. This strong dependence was the reason why W_{tot} started to decrease with the higher values of I_{amp} when using the second set. Meanwhile, metals showed a nearly linear behaviour. It needs to be noted that even though the power of the relationship was higher for the superconducting armatures, they lost less energy than the metals along a wide range of I_{amp}. Magnetic braking could be minimized by rapidly switching the driving current off when the acceleration of the superconducting armature approached zero.

No braking occurred using the first set of j_c and l_{cd} for the superconducting armature when the simulations were performed using the experimental pulse waveform. It was, however, observed when using the second set of parameters.

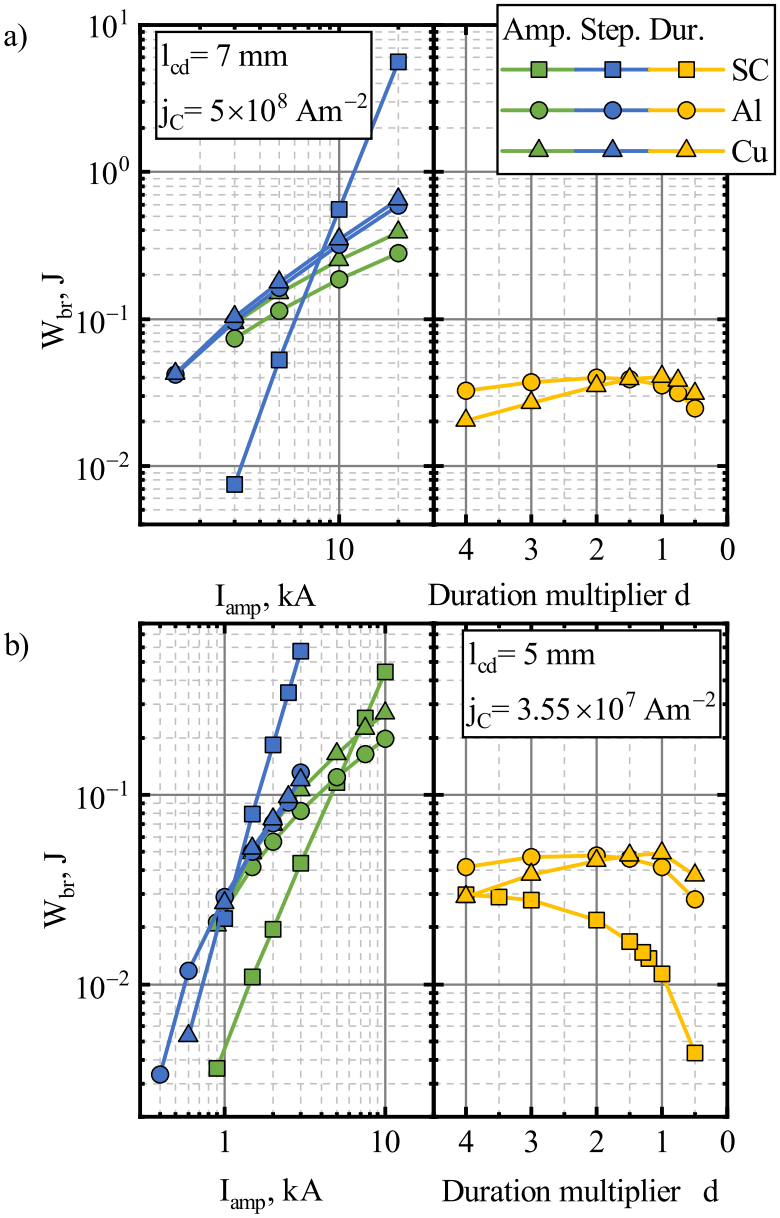

Figure 2.4.11. Total mechanical energy lost to magnetic braking. The green line (left) illustrates the effect of the experimental pulse shape amplitude, the blue line, the step-like current pulse amplitude. The yellow line(right) depicts the effects of the pulse duration. l_{cd}=7 mm, j_c=5 · 10^8 A/m^2 (a) and l_{cd}=5 mm, j_c=3.55 · 10^7 A/m^2 (b).

In this case, the W_{br} followed a parabolic behaviour ($\propto I_{amp}^{\sim 2}$). Meanwhile, the braking energy for the metals again satisfied a nearly linear trend.

For the pulse duration sweep, the W_{br} of the metal armatures was similar for both starting distances. The superconductor did not show braking with the first set of parameters. The W_{br} seemed to approach a maximum for high d and decreased as d approached 0 with the second set. This behaviour of W_{br} can be explained in the same manner as in the case of W_{tot}. At short pulses, the braking energy is mainly dependent on the interaction time and increases with the increasing pulse length. For long pulses, the armature moves away from the coil, thus reducing the magnetic coupling and thereby reducing the energy transfer between the coil and the armature.

Figure 2.4.12 shows the induced current density distributions along a vertical line at r = 1 cm at different time instances when armatures were accelerated by an experimental pulse with an amplitude of 3 kA. The current density in the Cu armature (as well as in all other normal conductors) decays both in time and along the line, going deeper into the sample. This results in the current density being strongest near the bottom of the sample, where the magnetic coupling to the driving coil is the strongest. In the superconducting armature case, the current density distribution is rectangular and close to j_c in magnitude. A high dB/dt induces an overcritical current density that is highest near the driving coil. This current also decays in time, but the decay rate is negligible below j_c. The result of this is the generation of two opposite currents circulating within the superconductor, which are located near the surface when the magnetic pulse begins to decrease. For this reason, there is always a non-negligible accelerating force component that mitigates the braking, and superconductors lose less W_{br} than the metals. It follows that larger W_{br} should be expected in situations where the magnetic field penetration depth is large, as the accelerating current would then be situated further away from the coil. This argument agrees well with the braking results discussed earlier (note W_{br} vs. I_{amp} dependences for experimental and step-like current pulses).

Overcritical current densities have to produce substantial Joule heating in the superconductors due to the power-law E-j relationship. For this reason, rapidly changing magnetic field pulses should be avoided, as it increases the armature temperature and lowers the j_c. This could damage the armature due to thermal shock. A reasonably slow magnetic field ramp-up to a constant value would mitigate this problem. This field should move synchronously with the superconductor to produce constant acceleration.

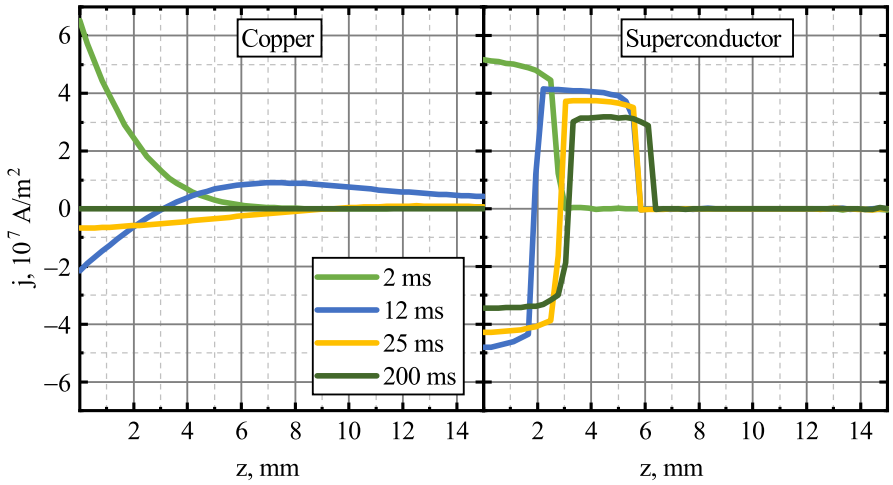

Figure 2.4.12. Current density distributions in the copper and superconducting armatures (second set of parameters) along a vertical line 1 cm from the center at different times when accelerated by an experimental current pulse of 3 kA amplitude. l_{cd}=5 mm, j_c=3.55 · 10^7 A/m^2.

The nonhomogeneous current distribution in the armature is important not only for the magnetic braking phenomenon but also for the optimal armature geometry design. Figure 2.4.13 shows the current density distribution within a superconducting armature (j_c=3.55 · 10^7 A/m^2) 200 ms after a 3 kA experimental pulse. The regions carrying no current only contribute to the total mass of the projectile and are not utilized for its acceleration. The magnetic field did not fully penetrate the superconductor in any of the regimes tested. This suggests that an armature geometry optimization is required to achieve efficient and cost-effective launch setups. The optimized shape will depend on the magnetic field distribution, its amplitude as well as the critical current density of the superconductor.

The examples discussed in this paper illustrate the main differences between normal metals and type II superconductors in coil accelerator applications. When normal metals are used, the induced current density is proportional to the magnetic field derivative and the resistivity of the material. Due to resistive losses, the field diffuses into the normal metals. When superconductors are used, the eddy currents are limited near the value of j_c by the highly nonlinear E-j relationship (equation 2.4.3). For these reasons, these two kinds of materials behave differently in coilgun scenarios. Normal metals require the

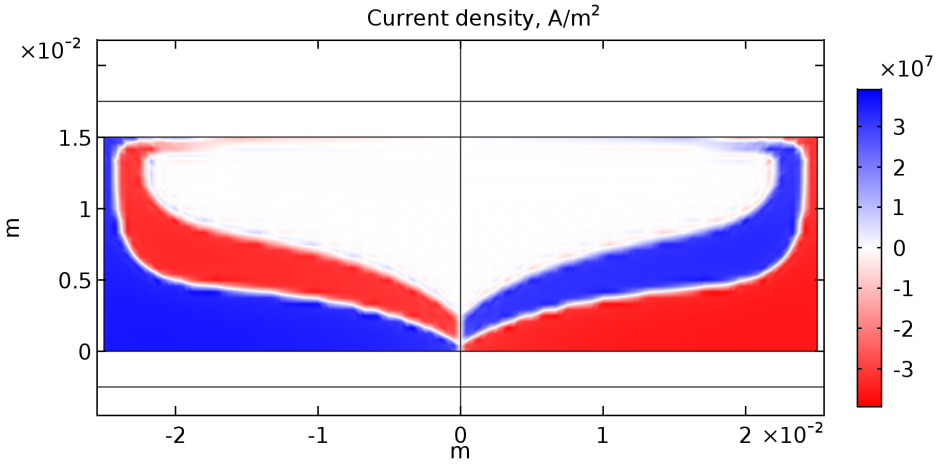

Figure 2.4.13. Current density distribution within the superconducting armature for an experimental current pulse with an amplitude I_{amp}=1.5 kA, l_{cd}=5 mm, j_c=3.55 · 10^7 A/m^2, at t=0.2 s after the beginning of the pulse.

transient magnetic field to be accelerated, while superconductors can be accelerated by a time constant field (provided it has a gradient). This modifies the requirements for coilgun design and the design of its power supply. A slow field ramp-up is desired to avoid armature heating. A magnetic field wave of a constant amplitude travelling synchronously with the superconducting armature would provide constant acceleration without a time limit in contrast to normal metals where the acceleration decreases due to the armature capture.

2.4.5 Summary

In this subsection, we investigated the behaviour of an electromagnetically accelerated disk-shaped superconducting YBCO armature cooled to 77 K. The acceleration was performed in a vertical arrangement using a single-stage pancake coil. The vertical displacement of the disk was measured using an IR distance sensor, and the magnetic field was measured using a CMR-B-Scalar sensor with small dimensions, which was able to measure the local magnitude of the magnetic field independent of its direction. It was observed that the motion and the magnetic field dynamics agreed well with the numerical simulations based on Maxwell's equations in their H-formulation, assuming that the superconductor is a nonlinear conductor with a power-law E-j relationship using realistic values of j_c. The numerical investigations showed that a higher critical current density of the superconductor increased the mechanical energy

transferred to the superconducting armature. This energy, however, had a limit for a given accelerating coil current pulse and armature starting position. The performance of the superconducting armature was numerically compared to normal metal armatures, cooled to liquid nitrogen temperature. This comparison showed that an increase in the current amplitude resulted in higher energy being transferred to all these armatures. For the superconducting armature, this increase was larger in the lower amplitude range and then was reduced to a nearly linear or sublinear relationship depending on the parameter set used for the calculations. Thus, the use of superconducting armatures was advantageous in the lower pulse amplitude range. Investigations of the influence of the pulse duration performed using pulses with a fixed current pulse amplitude and an experimental waveform demonstrated that the superconductor outperforms normal metals when accelerated by magnetic pulses with smaller time derivatives. Simulations using a step-like driving current pulse also revealed that superconductors again outperform normal metals using lower current amplitudes. The range in which they did so was, however, reduced by the strong magnetic braking caused by persistent currents. The mechanical energy lost to the magnetic braking had the strongest dependence on the pulse amplitude for step-like pulses, where the interaction was not mitigated by the reduction in the driving current. As eddy currents in type II superconductors do not decay past the critical current density, the use of superconducting armatures reduces the armature capture limitation and can increase the effectiveness of synchronous induction coilgun launchers.

- A Cylindrical aluminum payload causes a noticeable disturbance of the magnetic field dynamics inside the bore of a serial augmented hexagonal railgun that is the highest during the abrupt change of magnetic field pulse and decays sharply with the distance from the surface of the payload. This should be considered when designing launch packages.
- The lumped parameter approach is capable of describing the magnetic field dynamics and the trapped flux inside a thin-walled superconducting tube. The critical current density - magnetic field relationship and the power law exponent can be evaluated using a single magnetic pulse measurement inside a tube.
- Thin YBCO films prepared by the PI-MOCVD on Al_2O_3 substrates with CeO_2 layers below their $T_c$exposed to a DC magnetic field slightly higher than B_c display a linear magneto-resistive effect in accordance to Bardeen-Stephen model.
- Thin YBCO films prepared by the PI-MOCVD on Al_2O_3 substrates with CeO_2 layers exposed to DC voltage exhibit S-shaped current-voltage characteristics. Under constant current these films show dynamic resistance triggered by an external DC magnetic field. These phenomena can be well explained by uniform Joule heating caused by the flux flow-induced resistive state of the superconducting film.
- Motion of a superconducting disk-shaped YBCO armature cooled to 77 K electromagnetically accelerated by a pancake coil and magnetic field dynamics between them can be well described numerically with simulations based on Maxwell's equations in their H-formulation, assuming a power-law electric field-current density relationship for the superconductor.
- The mechanical energy transferred to a superconducting armature from a pulsed magnetic field source increases with the increasing critical current density of the superconducting armature. This increase has a limit for a given accelerating coil current pulse and armature starting position.
- Energy transferred to a type II superconducting armature in a coilgun depends on the shape, amplitude and duration of the coil current pulse. Superconducting armatures outperform normal metal armatures in the lower current amplitude range and when pulses with lower time derivatives are used.
- Type II superconducting armatures exhibit strong magnetic braking when step-like current pulses are used for their acceleration, however, they outperform normal metal armatures in the lower step amplitude range.

SANTRAUKA LIETUVIŲ KALBA

MOTYVACIJA

Magnetinio lauko difuzijos (MFD) didelio elektrino laidumo medžiagose tyrimai prasidėjo nuo Faraday'aus elektromagnetinės indukcijos atradimo. Per pastaruosius dešimtmečius susidomėjimas magnetinio lauko difuzija ženkliai padidėjo dėl naujų technologijų, tokių kaip: elektromagnetinis metalų suvirinimas [1], magnetokumuliaciniai generatoriai [2] ir elektromagnetinis greitinimas [3], atsiradimo. Pastaruoju atveju, domėjimosi MFD įsibėgėjimą lėmė naujos impulsinio magnetinio lauko matavimo technologijos [4] bei kompiuterinių modeliavimo programų, skirtų magnetinio lauko pasiskirstymams skaičiuoti, sukūrimas. MFD yra aktuali elektromagnetinio greitinimo kontekste, nes nulemia tiek greitinančią jėgą, tiek elektromagnetinę sviedinio aplinką. Ypatingas dėmesys skiriamas cilindrinės formos kūnams, nes tokia forma yra paprasčiausia ritės tipo elektromagnetinių svaidyklių (EML) elektromagnetiškai greitinamai platformai (EGP) bei bėgių tipo svaidyklės sviediniui. Ši forma patogi ne tik techniškai, bet ir atliekant lauko skaičiavimus, nes dėl formos simetrijos galima sumažinti uždavinio dimensiją taip pagreitinant skaičiavimus. MFD yra stipriai susieta su magnetinio lauko šaltinio kuriamo lauko forma, todėl skirtingose elektromagnetinio greitinimo sistemose, pvz.: paprastose ar sustiprinto lauko bėgių tipo elektromagnetinėse svaidyklėse, vienpakopėse ar daugiapakopėse ritės tipo elektromagnetinėse svaidyklėse, MFD nulemti magnetinio lauko pasiskirstymai yra skirtingi. MFD taip pat skiriasi ir didelio elektrinio laidumo medžiagose: metaluose ir superlaidininkuose. Skirtingai nei metalai, antro tipo superlaidininkai yra netiesiniai laidininkai, kurių savitoji varža yra nykstamai maža, jais tekant mažesniam už kritinį srovės tankiui. Ši jų savybė antro tipo superlaidininkus daro patraukliais ne tik EML EGP ar magnetinio lauko ekranavimui jose, bet ir viršsrovio ribotuvams.

Neseniai buvo pristatytas naujas daugiabėgės elektromagnetinės svaidyklės dizainas, kuriame bėgiai išdėstyti šešiakampiu [5, 6]. Pagrindinis šios EML privalumas yra jos universalumas, nes ją galima naudoti įvairiais rėžimais, įskaitant: segmentinį, daugiašūvį ir sustiprinto lauko rėžimus. Patogiausia tokios bėginės EML sviedinio geometrija yra cilindras. Dėl šios priežasties, norint nustatyti sviedinio elektromagnetinę aplinką, labai svarbu tirti magnetinį MFD poveikį šalia laidaus cilindrinio sviedinio, įdėto į šešiakampę bėginę EML, veikiančią nuoseklaus sustiprinto lauko režime. Dažniausiai laike kintantys magnetinio lauko pasiskirstymai skaičiuojami naudojant skaitmeninius

metodus, tokius kaip baigtinių skirtumų ar baigtinių elementų metodai, tačiau norint gauti patikimus rezultatus, skaičiavimai turi būti suderinti su eksperimentiniu magnetinio lauko evoliucijos matavimu. Dėl šios priežasties šiame darbe teoriniai magnetinio lauko pasiskirstymai heksagonalinėje bėgių tipo EML nuoseklaus sustiprinto lauko rėžime su cilindriniu aliuminio sviediniu buvo lyginami su eksperimentiniais matavimais, atliktais naudojant unikalią CMR-B skaliarinių magnetinio lauko jutiklių matricą [7, 8].

Tuščiaviduriai superlaidūs cilindrai (vamzdžiai) naudojami kaip nuolatiniai magnetai [9–11], magnetinio lauko ekranai [9–11], viršsrovio ribotuvai [12–14] bei didelės energijos dalelių greitintuvuose [19]. Norint valdyti ir testuoti šiuos prietaisus būtina žinoti, kaip impulsinis magnetinis srautas prasiskverbia į vamzdžio ertmę. Šis procesas buvo tyrinėtas antro tipo superlaidininkų žieduose ir storasieniuose vamzdžiuose [20–23]. Plonasienio vamzdžio konfigūracija sumažina kitais atvejais dideles superlaidžių medžiagų sąnaudas ir gali būti naudojama magnetiniams ekranams arba „išmaniesiems superlaidiems tinklams“ [24, 25]. Ilgus superlaidžius vamzdžius elektros perdavimui buvo pasiūlyta gaminti įvairiais būdais [25–27]. Praktiniams taikymams yra svarbu nedestruktyviai įvertinti superlaidaus vamzdžio savybes, tokias kaip: kritinės srovės priklausomybę nuo magnetinio lauko, didžiausią ekranuojamą lauką bei laipsninio dėsnio rodiklį. Šiems parametrams gauti eksperimentiniai rezultatai turi būti analizuojami naudojant tikslius teorinius modelius, adaptuotus pagal eksperimentines sąlygas. Tokie metodai buvo pritaikyti superlaidžių cilindrų ir vamzdžių tyrimams [28] ir rėmėsi srovės tankio skaičiavimu superlaidininko tūryje, todėl šie metodai yra priklausomi nuo geometrijos ir reikalauja specifinių diskretizacijos algoritmų. Plonasienio vamzdžio konfigūracija leidžia supaprastinti uždavinį darant prielaidą, kad srovės tankis per sienelės storį nekinta. Taip pat, dėl didelio paviršiaus ploto nulemto gero šilumos nuvedimo galima neįskaityti Joule'io šilimo. Dėl šių priežasčių, impulsinio magnetinio lauko matavimas superlaidžiame plonasieniame vamzdyje yra informatyvesnis nei storasienių vamzdžių atveju. Šioje disertacijoje pasiūlytas metodas, paremtas sutelktų parametrų lygtimi, superlaidžios medžiagos parametrams įvertinti, matuojant impulsinį magnetinį lauką plonasienio superlaidaus vamzdžio viduje bei išorėje. Metodas patvirtintas eksperimentiškai, matuojant magnetinį lauką Bi-2223 vamzdyje naudojant induktyvinį bei CMR magnetinio lauko jutiklius.

Magnetinio lauko difuzija plonasieniuose superlaidžiuose vamzdžiuose, veikiamuose ašinio magnetinio lauko, gali indukuoti didelius srovės tankius,

ypač kai magnetinis laukas greitai kinta. Dideli srovės tankiai ir magnetinis laukas gali stipriai pakeisti plonų superlaidžių sluoksnių savybes, iššaukti magnetinio srauto judėjimo nulemtą varžinę būseną, Joule'io šilimą bei įvairius elektrinius nestabilumus. Efektai pasireiškiantys antros rūšies superlaidininkuose, kuriais teka dideli srovės tankiai, buvo tyrinėti YBCO sluoksniuose, MOCVD būdu nusodintų ant mažos dielektrinės skvarbos ir didelio šiluminio laidumo Al_2O_3 padėklo su CeO_2 pasluoknsiu [29]. Buvo nustatyta, kad šie sluoksniai pasižymi plačiomis netiesinėmis disipatyviomis būsenomis ir gali būti naudojami kaip greitaveikiai viršrovės ribotuvai [30–35]. Tačiau, vyksmai pasireiškiantys, kai sluoksniai veikiami didele elektrine srove ir magnetiniu lauku, nebuvo detaliai išanalizuoti bei paaiškinti. Jų analizė bei modeliavimas yra kitas šios disertacijos objektas.

Ritės tipo EML yra įrenginys, kuris pasitelkdamas magnetinius laukus, pagreitina feromagnetines arba elektriškai laidžias EGP iki didelių greičių. Šių EML privalumai yra fizinio kontakto tarp vamzdžio ir šaudmens bei cheminio kuro nebuvimas, kas pašalina trintį ir sumažina šaudmens masę, taip sumažinant energijos kiekį, reikalingą pasiekti norimą greitį. Iš kitos pusės, šioms svaidyklėms reikalingos: sudėtinga modulinė energijos perdavimo sistema su aukštais reikalavimais elektriniams raktams, šaudmens sekimo bei kontroliavimo sistemos [36, 37]. Joule'io šilimas, EGP srauto pagavimas bei EGP mechaninis atsparumas yra faktoriai ribojantys metalines EGP [38, 39]. Antros rūšies superlaidininkų elektromagnetinės savybės stipriai skiriasi nuo normalios būsenos metalų. Jie yra netiesiniai laidininkai, kurių savitoji varža yra nykstamai maža žemiau kritinio srovės tankio. Ši savybė yra patraukli įvairiems taikymams [40–42], kurių viena yra elektromagnetinis greitinimas. Šių medžiagų naudojimas EGP gali praplėsti ritės tipo EML taikymo ribas, taip pat gali iššaukti netikėtą sistemos elgesį. Literatūroje gana mažai darbų tyrinėjančių ritės tipo EML su II tipo superlaidžiomis EGP. Skaičiavimai pateikti [43] parodė, kad įmagnetintos antros rūšies EGP gali būti pranašesnės už tradicines metalines, tačiau EGP įmagnetinimas sukuria papildomą paruošimo žingsnį, kas ne visada yra praktiška. Todėl svarbu ištirti kaip elgiasi neįmagnetinta EGP iš antros rūšies superlaidininko, kas iki šiol nebuvo atlikta. Dėl šios priežasties, paskutinėje šios disertacijos dalyje tyrinėjama vienpakopė ritės tipo EML su plokščiąja rite ir disko formos EGP iš YBCO superlaidininko. Eksperimentiniai tyrimai, atlikti naudojant CMR magnetinį lauko jutiklį bei IR atstumo matuoklį, yra lyginami su teoriniais skaičiavimais.

Tikslai

1. Ištirti magnetinio lauko dinamiką heksagonalinės bėgių tipo elektromagnetinės svaidyklės vamzdyje su cilindriniu metaliniu sviediniu nuoseklaus jungimo sustiprinto lauko režime.
2. Teoriškai ir eksperimentiškai ištirti impulsinio magnetinio lauko skverbimąsi į superlaidų plonasienį Pb legiruotą Bi-2223 cilindrą.
3. Įvertinti procesus stebimus submikroninio storio YBCO sluoksnių mikrotilteliuose, MOCVD būdu užaugintuose ant Al_2O_3 su CeO_2 pasluoksniu, juos veikiant dideliu elektrinės srovės tankiu ir išoriniu magnetiniu lauku.
4. Ištirti vienpakope ritės tipo elektromagnetine svaidykle vertikaliai greitinamo viendomenio YBCO disko, atšaldyto iki 77 K temperatūros, elgseną.

Užduotys

- Suprojektuoti eksperimentą magnetinio lauko matavimui, SR\3-60 heksagonalinėje elektromagnetinėje svaidyklėje, konfigūruojant jos bėgių jungimą bei įdiegiant keturių kolosalios magnetovaržos jutiklių sistemą.
- Sukurti skaitmeninį modelį paremtą baigtinių elementų metodu (COMSOL Multiphysics AC/DC module), aprašantį laike kintantį magnetinio lauko pasiskirstymą heksagonalinės elektromagnetinės svaidyklės vamzdyje.
- Suskaičiuoti magnetinio lauko dinamiką cilindrinio aliuminio sviedinio aplinkoje ir palyginti ją su eksperimentiniais matavimų duomenimis.
- Sukurti eksperimentinį stendą impulsinio magnetinio lauko skverbimuisi į plonasienį $Bi_{1.8}Pb_{0.26}Sr_2Ca_2Cu_3O_{10+x}$ vamzdį tirti ir atlikti tyrimus naudojant induktyvinį bei kolosalios magnetovaržos magnetinio lauko matuoklius.
- Sukurti matematinį sutelktų parametrų modelį galintį paaiškinti bendrą magnetinio lauko dinamikos elgseną plonasienio superlaidaus vamzdžio viduje bei jo pagautą magnetinį lauką ir patikrinti šį modelį lyginant jį su eksperimentiniais duomenimis.

- Ištirti magnetovaržos efektą 440 nm storio YBCO sluoksniuose, MOCVD būdu užaugintuose ant Al_2O_3 su CeO_2 pasluoksniu, 20-300 K temperatūrų ruože.
- Paaiškinti eksperimentiškai stebimų S formos voltamperinių charakteristikų bei laike kintančios mikrotiltelio varžos, jį veikiant pastoviu magnetiniu lauku, prigimtį.
- Sukurti eksperimentinį stendą superlaidaus YBCO disko, elektromagnetiškai greitinamo vertikaliai, atšaldyto iki 77 K, elgsenai tirti paremtą IR atstumo bei CMR-B skaliariniu magnetinio lauko matuokliais.
- Skaitmeniškai sumodeliuoti netiesinį sūkurinių srovių uždavinį cilindrinio sviedinio atskaitos sistemoje, paremtą Maxwell'o lygtimis jų H-formuluotėje 2D ašiai simetrinėje formoje, naudojant komercinį Comsol Multiphysics programinį paketą ir pritaikyti šį modelį sviedinio poslinkio bei magnetinio lauko dinamikos tyrimams.
- Įvertinti ritės tipo elektromagnetinės svaidyklės su antro tipo superlaidžiu sviediniu, našumą naudojant skaitmeninį modelį.

Praktinė vertė ir naujumas

Laidaus cilindrinio sviedinio įtaka dinaminiam magnetinio lauko pasiskirstymui elektromagnetinio greitinimo heksagonaline bėgių tipo elektromagnetine svaidykle nuoseklaus jungimo sustiprinto lauko režime metu tyrinėta pirmą kartą. Nustatyti magnetinio lauko pasiskirstymo profiliai gali būti naudingi kuriant sviedinius su magnetiniam laukui jautriais komponentais.

Pasiūlytas greitas, nedestruktyvus metodas, paremtas sutelktų parametrų lygtimi, superlaidžių vamzdžių, kurių sienos storis mažesnis nei Bean'o prasiskverbimo gylis, superlaidumo savybėms magnetiniame lauke nustatyti.

Savitosios YBCO sluoksnių mikrotiltelių, MOCVD būdu užaugintų ant Al_2O_3 su CeO_2 pasluoksniu, voltamperinės charakteristikos, pamatuotos naudojant ns trukmės impulsus, pirmą kartą panaudotos elektroterminių nestabilumų, stebimų nuolatinės įtampos režime, modeliavimui. Šis modelis gali būti naudojamas superlaidžių srovės ribotuvų, veikiamų ilgų viršsrovių, atsako aprašymui.

Skaitmeninis vienpakopės ritės tipo elektromagnetinės svaidyklės su antro tipo superlaidžiu sviediniu modelis pirmą kartą patvirtintas eksperimentu. Remiantis šiuo modeliu, skaitmeniniai skaičiavimai buvo panaudoti tokio tipo

sviedinių savybių ir sąlygų, kuriomis tokie sviediniai pranašesni už konvencinius, tyrimams.

Ginamieji teiginiai

- Magnetinio lauko difuzija iškraipo magnetinį lauką cilindrinio laidaus sviedinio aplinkoje, kai sviedinys greitinamas heksagonaline bėgių tipo elektromagnetine svaidykle, veikiančia nuoseklaus jungimo sustiprinto lauko režimu. Šiuo atveju magnetinio lauko pasiskirstymą galima gerai modeliuoti naudojant kvazistatines Maxwell'o lygtis ir baigtinių elementų metodą.

- Netiesinę magnetinio lauko difuzijos lygtį, aprašančią magnetinio lauko sklidimą vamzdyje iš II tipo superlaidininko, galima supaprastinti į sutelktų parametrų lygtį, kai vamzdžio sienelės storis yra žymiai mažesnis nei Bean'o įsiskverbimo gylis. Ši lygtis, kartu su impulsinio magnetinio lauko matavimu vamzdžio viduje, gali būti naudojama greitam ir nedestruktyviam superlaidžios medžiagos kritinio srovės tankio priklausomybės nuo magnetinio lauko bei laipsninio dėsnio rodiklio įvertinimui.

- Plonų YBCO sluoksnių, nusodintų ant Al_2O_3 padėklo su CeO_2 pasluoksniu PI-MOCVD metodu, magnetovarža superlaidumo būsenoje yra tiesinė magnetinio lauko atžvilgiu ir atitinka magnetinio srauto judėjimo modelį. Mikrotiltelių, pagamintų iš šių sluoksnių, S formos I-V charakteristikos, stebimos stabilizuotos įtampos režime, o taip pat laike kintančios varžos reiškinys stabilizuotos srovės režime, yra iššauktos termoelektrinio nestabilumo, kurį sukelia Joule'io šilimas magnetinio srauto judėjimo indukuotoje varžinėje būsenoje.

- Disko formos elektromagnetinės greitinimo platformos, pagamintos iš II tipo superlaidininko, vertikalų judėjimą ir magnetinio lauko dinamiką elektromagnetinio greitinimo plokščiąja rite metu galima gerai paaiškinti naudojant skaitmeninius metodus, paremtus kvazistatinėmis Maxwell'o lygtimis jų H lauko formuluotėje su prielaida, kad superlaidininkas yra netiesinis laidininkas, kurio E-j charakteristika yra laipsninė funkcija. Sviediniai iš II tipo superlaidininkų yra pranašesni už sviedinius iš normalių metalų esant mažesnėms greitinimui naudojamų magnetinio lauko impulsų kitimo spartoms bei amplitudėms.

Autoriaus indėlis

Vilius Vertelis, konsultuodamasis su Sauliumi Balevičiumi ir Markus Schneider, suplanavo ir atliko visus eksperimentinius matavimus pristatomus 2.1, 2.2 ir 2.4 poskyriuose, suprojektavo ir sukūrė 2.2 ir 2.4 poskyrių eksperimentinius stendus, išanalizavo rezultatus bei atliko visus pristatomus modeliavimus bei skaičiavimus. Autorius prisidėjo prie į disertaciją įtrauktų publikacijų rankraščių rašymo bei formatavimo.

Pirmajame disertacijos skyriuje pateikta mokslinės literatūros apžvalga su darbo tikslais bei uždaviniais susijusiomis temomis. Šiame skyriuje apžvelgiama magnetinio lauko difuzija ir jos įtaka elektromagnetinėms svaidyklėms. Aptariamos superlaidininkų savybės bei antros rūšies superlaidininkų elektrodinaminių reiškinių modeliavimas magnetinio lauko difuzijos kontekste.

1.1 poskyryje supažindinama su magnetinio lauko difuzija (MFD) elektriškai laidžiose nemagnetinėse medžiagose. Išvedama MFD lygtis kvazistatiniame Maxwell'o lygčių artinyje.

1.2 poskyryje apžvelgiamos superlaidininkų magnetinės savybės bei ypatumai. Supažindinama su Meissner'io būsena bei magnetinio lauko ekranavimu pirmos rūšies superlaidininkuose. Pateikiamos antros rūšies superlaidininkų savybės, supažindinama su Abricosov'o sūkuriais. Aprašomas Bean'o kritinės būsenos modelis antros rūšies superlaidininkų įmagnetėjimui aprašyti. Pateikiami elektrinio lauko priklausomybės nuo superlaidininkais tekančio srovės tankio dėsniai. Aprašomi laisvo srauto judėjimo bei judėjimo esant sūkurių gaudyklėms režimai.

1.3 poskyryje pateikiamas bėgių tipo svaidyklės aprašymas. Aprašomos paprastosios bei sustiprinto lauko konfigūracijos. Supažindinama su galios šaltiniais naudojamais su šiomis svaidyklėmis. Aptariami MFD sukelti paviršinis, artumo bei paviršinis greičio efektai bėgių tipo EML bei juos nagrinėjantys tyrimai.

1.4 poskyryje apžvelgiamos įvairios MFD problemos formuluotės taikomos II tipo superlaidininkų įmagnetėjimui modeliuoti. Aptariami: integralinis Brandt'o metodas, magnetinių grandinių metodas, A-V, T-A, bei H formuluotės. Pateikiami šių formuluočių taikymo pavyzdžiai. Pateikiami dažniausiai naudojami kritinės srovės priklausomybių nuo magnetinio lauko bei temperatūros dėsniai.

1.5 poskyryje kalbama apie plonų II tipo superlaidininkų sluoksnių savybes ir jų skirtumus nuo tūrinių superlaidininkų. Aprašomas kritinio srovės tankio priklausomybės nuo sluoksnio storio efektas, atlikti jo tyrimai ir aptariamos efekto priežastys. Aptariami kritinio srovės tankio priklausomybės nuo magnetinio lauko stiprio ir kampo ypatumai. Pristatomi sluoksnių voltamperinių charakteristikų tyrimai bei skirtingi modeliai aiškinantys stebimus nestabilumus. Pateikiami rezultatai, gauti voltamperines charakteristikas matuojant ultratrumpais ns trukmės impulsais.

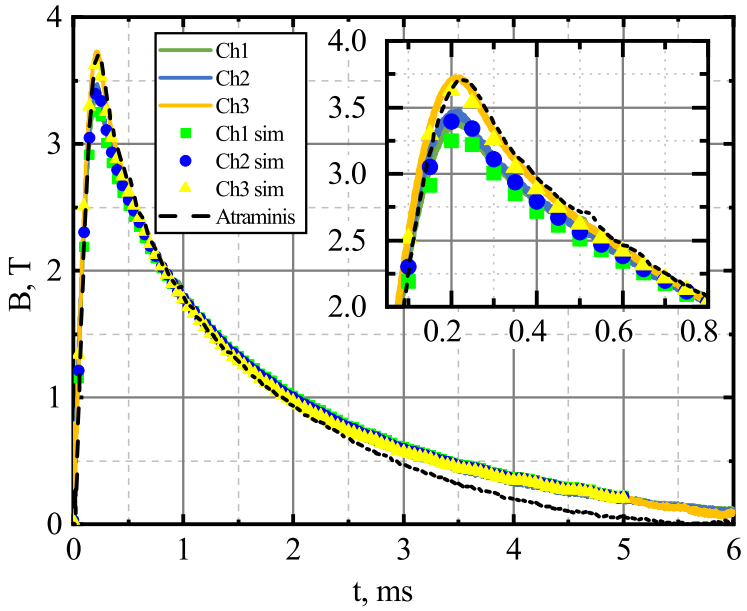

1 pav. Magnetinio srauto tankio SR\3-60 svaidyklėje matavimai aliuminio cilindrinio sviedinio aplinkoje bei lauko modeliavimas baigtinių elementų metodu.

Paskutiniame literatūros apžvalgos poskyryje (1.6) pristatomos ritės tipo elektromagnetinės svaidyklės ir praktiniai jų pritaikymai aprašyti literatūroje. Apžvelgiamos problemos su kuriomis susiduria šios svaidyklės, kai naudojamos normalaus metalo EGP, ir kokie sprendimai daromi joms spręsti. Aptariamos EGP srauto pagavimo ir magnetinio stabdymo problemos. Pristatomi aktyvavimo laiko slydimo bei lauko krypties apsukimo metodai joms spręsti. Taip pat supažindinama su tyrimais kuriuose naudojamos II tipo superlaidininkų EGP.

REZULTATAI

Antrajame skyriuje aprašomi disertacijoje naudoti eksperimentai bei jų eiga, taip pat pateikiama rezultatų analizė ir susiję skaičiavimai.

2.1 poskyryje nagrinėjamas magnetinio lauko difuzijos nulemtas magnetinio lauko iškraipymas laidaus sviedinio aplinkoje heksagonalinėje bėgių tipo elektromagnetinėje svaidyklėje, veikiančioje nuoseklaus sustiprinto lauko režime. 2.1.1 skiltyje aprašomas metodas magnetinio lauko konfigūracijai laidaus

sviedinio aplinkoje gauti homogeniško išorinio lauko atveju. 2.1.2 skiltyje yra aprašoma SR\3-60 heksagonalinė elektromagnetinė svaidyklė, tyrimo tikslais jai atliktos modifikacijos bei eksperimento schema. 2.1.3 skiltyje pristatomi ir analizuojami eksperimentiniai bei modeliavimo rezultatai, kurie yra apibendrinami 2.1.4 skiltyje.

Tyrinėjant magnetinio lauko dinamiką cilindrinio aliuminio sviedinio aplinkoje SR\3-60 svaidyklėje, veikiančioje nuoseklaus sustiprinto lauko režime, buvo pamatuotas magnetinio lauko sumažėjimas tuščios svaidyklės atžvilgiu. Matavimų rezultatai pateikti 1 paveiksle. Matavimai atlikti naudojant 3 CMR-B skaliarinių magnetinio lauko jutiklių sistemą, leidžiančią matuoti magnetinio lauko vektoriaus amplitudę, taip palengvinant eksperimento rezultatų analizę. Magnetinio lauko sumažėjimas buvo stebimas tiek statiniame režime, kai sviedinys nebuvo greitinamas, o magnetinis laukas generuotas tik lauką stiprinančiais bėgiais, tiek dinaminiame režime, kurio metu magnetinis laukas generuojamas visų bėgių. Didžiausias lauko sumažėjimas fiksuotas ties sviedinio centru, nuo kurio tolstant magnetinis laukas greitai grįžo į vertę pamatuotą tuščios svaidyklės atveju.

Šis magnetinio lauko iškraipymas paaiškintas magnetinio lauko difuzijos nulemtu magnetino lauko išstūmimu iš elektriškai laidaus aliuminio sviedinio. Buvo atlikti du magnetinio lauko dinamikos skaičiavimai sviedinio aplinkoje naudojant kvazistatines Maxwell'o lygtis: homogeniško išorinio lauko bei lauko kuriamo SR\3-60 svaidyklės nuoseklaus sustiprinto lauko režime atvejais. Modeliuoto magnetinio lauko palyginimas su eksperimentiniais matavimais pateiktas 1 paveiksle. Gautas geras kiekybinis sutapimas patvirtino modelį. Remiantis suskaičiuotomis lauko pasiskirstymo dinamikomis nustatytos zonos su didesniu ir mažesniu už atraminį magnetinio srauto tankiu. Magnetinio lauko pasiskirstymas, kuriamas lauką stiprinančių bėgių, pateiktas 2 paveiksle, o magnetinio lauko dinamika sviedinio aplinkoje pavaizduota 3 paveiksle. Magnetinio lauko iškraipymas didžiausias staigiai besikeičiant magnetiniam laukui ir greitai slopsta tolstant nuo sviedinio paviršiaus. Tai gali būti svaru kuriant šaudmenis šioms svaidyklėms su magnetiniam laukui jautriais sviediniais.

2.2 poskyryje aprašyti magnetinio lauko skverbimosi į plonasienį superlaidų vamzdį tyrimai. 2.2.1 skiltyje aprašoma eksperimente naudota įranga, matavimo metodai bei eksperimento veiksmų seka. 2.2.2 skiltyje užrašoma sutelktų parametrų lygtis į plonasienį superlaidų vamzdį indukuotą srovę ir iš jos išplaukiantį magnetinį lauką vamzdžio viduje. Užrašoma lygtis pagauto magnetinio srauto gesimui šiuo artiniu aprašyti. 2.2.3 skiltyje teo-

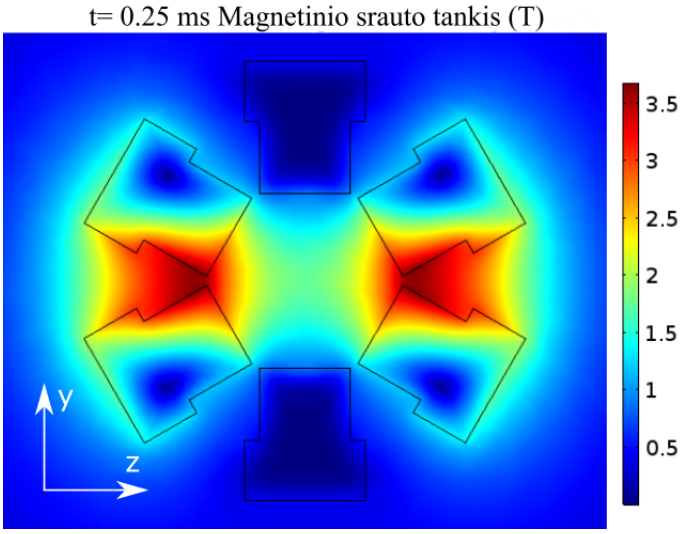

2 pav. Sumodeliuotas magnetinio srauto tankis tuščioje SR\3-60 svaidyklėje, kuriamas lauką stiprinančių bėgių.

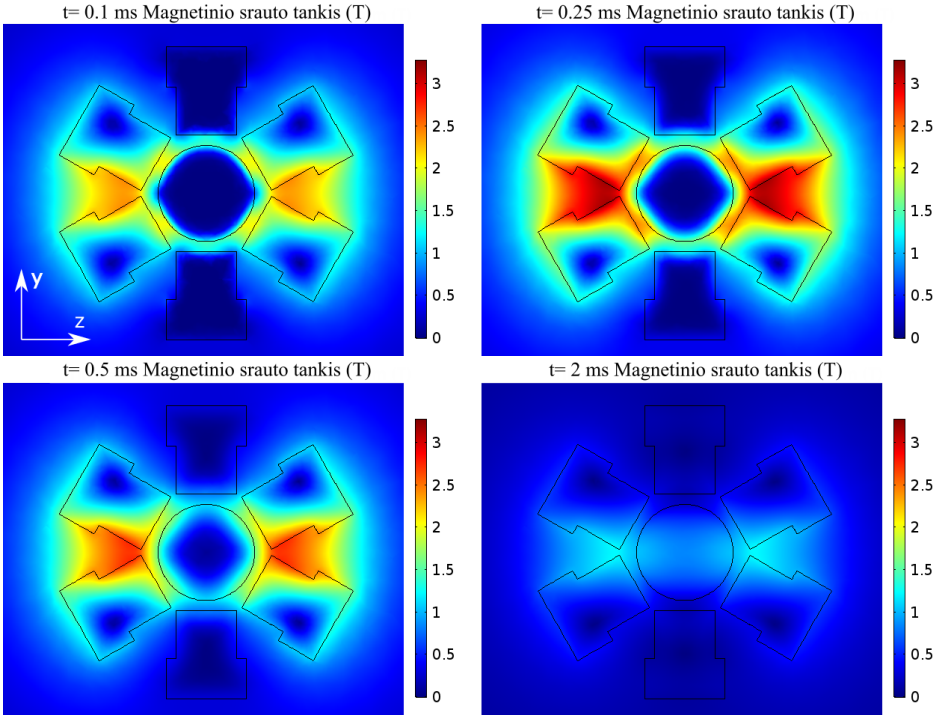

3 pav. Sumodeliuotas magnetinio srauto tankis yz plokštumoje, kertančioje aliuminio cilindrinio sviedinio centrą, skirtingais laiko mementais.

riškai analizuojamos magnetinio lauko vamzdžio viduje dinamikos, iššauktos išorinio magnetinio lauko impulso, ir įvairių parametrų įtaka joms. 2.2.4 skiltyje pristatomi eksperimentiniai rezultatai gauti B-dot bei CMR-B skaliariniais magnetinio lauko jutikliais. Šie rezultatai lyginami su teoriniais modeliavimais. Tyrimo išvados apibendrinamos 2.2.5 skiltyje.

Sudėtingą netiesinės magnetinio lauko difuzijos lygtį, kuri aprašo magnetinio lauko sklidimą bei indukuotą srovę antro tipo superlaidininkuose, plonasienio vamzdžio geometrijos atveju galima supaprastinti į sutelktų parametrų lygtį darant prielaidą, kad superlaidininkas yra netiesinis laidininkas su laipsnine elektrinio lauko priklausomybe nuo magnetinio lauko. Sutelktų parametrų lygties rėmuose tyrinėta kaip keičiasi magnetinio srauto tankio atsakas B_{i} keičiant išorinio magnetinio lauko amplitudę bei laipsninės priklausomybės parametrų: laipsnio rodiklio ir kritinės srovės priklausomybės nuo magnetinio lauko, įtaka lauko dinamikai.

Eksperimentiniai magnetinio srauto tankio atsako tyrimai atlikti naudojant Pb legiruotą Bi-2223 plonasienį vamzdelį. Buvo naudoti dvejų trukmių bei formų magnetiniai impulsai. B-dot jutikliu pamatuotos magnetinio lauko dinamikos įvairioms išorinio magnetinio lauko amplitudėms pavaizduotos 4 paveiksle. Eksperimentinės dinamikos pasižymi visomis teoriniuose skaičiavimuose stebėtomis savybėmis: impulso pradžios uždelsimu, sekamu greito magnetinio lauko augimo, pastoviu lauku išoriniam magnetiniam laukui pradedant kristi bei magnetinio lauko pagavimu išoriniam impulsui pasibaigus.

CMR-B skaliariniu magnetinio lauko jutikliu užregistruoti vamzdyje pagauto magnetinio srauto gesimai buvo palyginti su teoriniu gesimo dėsniu. Nustatyta, kad laipsninio dėsnio rodiklis tirtame vamzdyje $n \approx 20$. Naudojant šią n vertę ir derinant suskaičiuotas kreives prie eksperimentinių rezultatų buvo nustatyta kritinio srovės tankio priklausomybė nuo magnetinio lauko $j_{\mathrm{c}}(B)$ (žiūrėti 5 pav.). Šiuo būdu nustatytos $j_{\mathrm{c}}(B)$ nesiskyrė trumpiems ir ilgiems impulsams ir buvo artimos vamzdelio gamintojų pateikiamoms vertėms. Magnetinio lauko superlaidaus plonasienio vamzdelio viduje matavimas gali būti panaudotas greitam ir nedestruktyviam superlaidžios medžiagos parametrų įvertinimui jį analizuojant sutelktų parametrų lygtimi paremtu algoritmu.

2.3 poskyryje nagrinėjamos plonų YBCO sluoksnių, paruoštų MOCVD būdu ant Al_2O_3 padėklų naudojant CeO_2 pasluoknį, savybės. 2.3.1 skiltyje aprašoma sluoksnių gamyba, CeO_2 pasluoksnio storio įtaka. 2.3.2 skiltyje supažindinama su eksperimentams atlikti naudota įranga bei elektrinių savybių tyrimų metodikomis. 2.3.3 skiltyje pristatomi matavimų rezultatai. Pateikiama

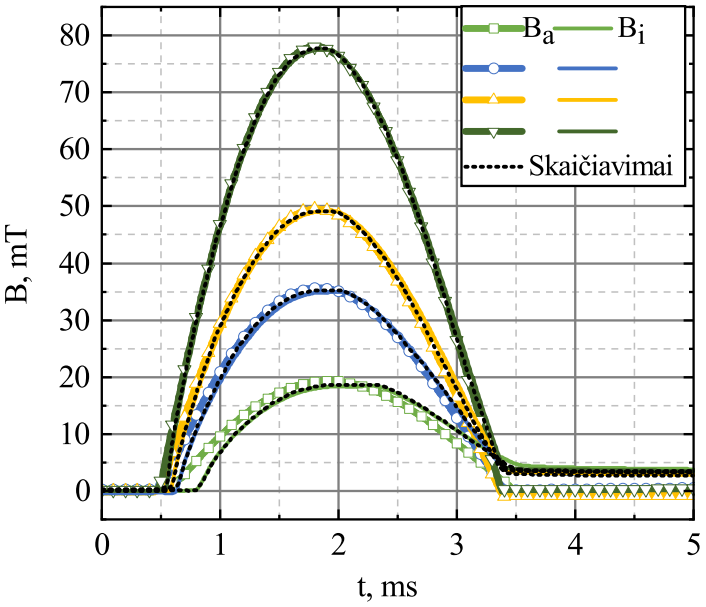

4 pav. Magnetinio stauto tankio B_{i} dinamika pamatuota Bi-2223 vamzdžio viduje naudojant B-dot jutiklį, išorinis magnetinio srauto tankis B_{a} ir magnetinio lauko vamzdžio viduje dinamikos skaičiavimai.

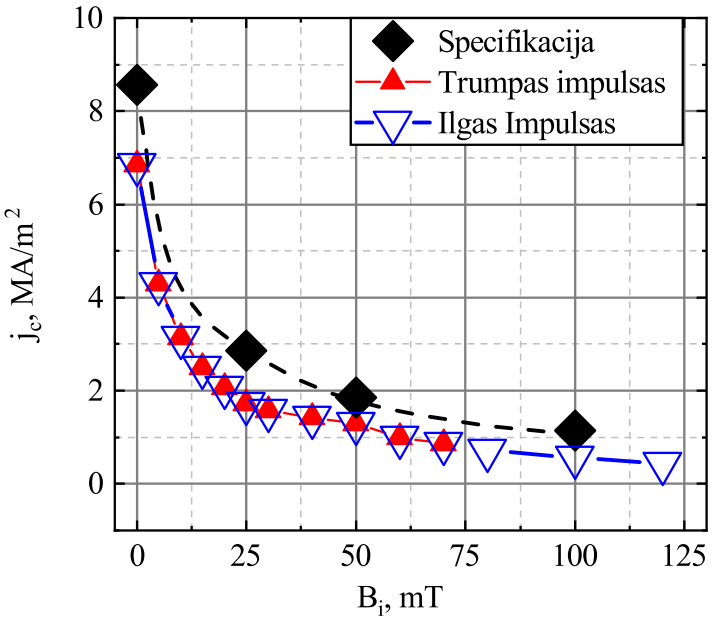

5 pav. $j_{\mathrm{c}}(B)$ priklausomybės gautos lyginant eksperimentinius rezultatus su skaičiavimais paremtais sutelktų parametrų lygtimi. Palyginimui pateiktos gamintojo nurodomos vertės (specifikacija).

sluoksnio varžos temperatūrinė priklausomybė, varžos pokytis nuo magnetinio lauko, voltamperinės charakteristikos stabilizuotos įtampos režime bei sluoksnio varžos dinamika po 0,7 T magnetinio lauko įjungimo. Sluoksnių atsakas į ns trukmės elektrinius impulsus nagrinėjamas 2.3.4 skiltyje. Aptariama trumpo elektrinio matavimo svarba ir pateikiamos izoterminės voltamperinės charakteristikos pamatuotos naudojant ns trukmės impulsus. 2.3.5 skiltyje atliekama rezultatų analizė. Pristatomi modeliai S formos voltamperinėms charakteristikoms bei varžos dinamikai aiškinti. 2.3.6 skiltyje pateikiamas rezultatų apibendrinimas.

Tyrinėjant magnetinio lauko skverbimąsi į plonasienį vamzdį Joule'io šilimas nebuvo įskaitytas dėl efektyvaus šaldymo, nulemto didelio vamzdžio geometrijos paviršiaus ploto. Siekiant ištirti kaip temperatūra ir Joule'io šilimas veikia superlaidžių sluoksnių savybes, buvo tyrinėjamos 400 nm YBCO sluoksnių MOCVD būdu užaugintų ant Al_2O_3 su CeO_2 pasluoksniu elektrinės savybės įvairiose temperatūrose ir magnetiniuose laukuose. Varžos pokyčio priklausomybės matavimai atskleidė, kad žemose temperatūrose virš kritinio magnetinio lauko varžos pokytis yra tiesinė magnetinio lauko funkcija, kaip prognozuoja Bardeen'o-Stephen'o magnetinio srauto tėkmės modelis (6 paveikslas). Kritinis magnetinis laukas, nuo kurio stebimas varžos atsiradimas, kinta žinomu $B_c \approx B_{c0}[1-(T/T_c)^2]$ dėsniu.

Dinaminės sluoksnio varžos atsiradusios po 0,75 T išorinio magnetinio srauto tankio įjungimo matavimai pavaizduoti 7 paveiksle. Tekant mažoms srovėms, įjungus magnetinį lauką sluoksnio varža pasikeičia greitai lyginant su matavimo sparta. Didinant sluoksniu tekančią elektrinę srovę, po staigaus varžos šuolio lauko įjungimo momentu seka lėtesnis varžos kilimas link soties vertės. Laikas per kurį pasiekiama soties varža ilgėja su didėjančia srove. Peržengus ribinę srovę, sluoksnio varžos dinamika pakinta - stebimas nestabilumas, kai varžos augimas iš pradžių lėtėja, o po to staigiai pagreitėja. Eksperimentinės sluoksnių voltamperinės charakteristikos stabilizuotos įtampos režime buvo S formos (žiūrėti 8 paveikslą). Šių charakteristikų forma ir lūžio srovė priklausė nuo sluoksnio temperatūros bei išorinio magnetinio lauko.

Norint paaiškinti dinaminę sluoksnio varžą buvo remtasi elektroterminiu modeliu. Sluoksnio elektrinėms savybėms nustatyti buvo panaudotos ns trukmės impulsais pamatuotos sluoksnių voltamperinės charakteristikos. Charakteristikos buvo aproksimuotos laipsniniu dėsniu su nuo temperatūros priklausančiais laipsnio rodikliu ir kritine srove. Sluoksnio savitoji šiluma aproksimuota tiese. Sluoksnio varžos dinamika gauta iš suskaičiuotos sluoksnio

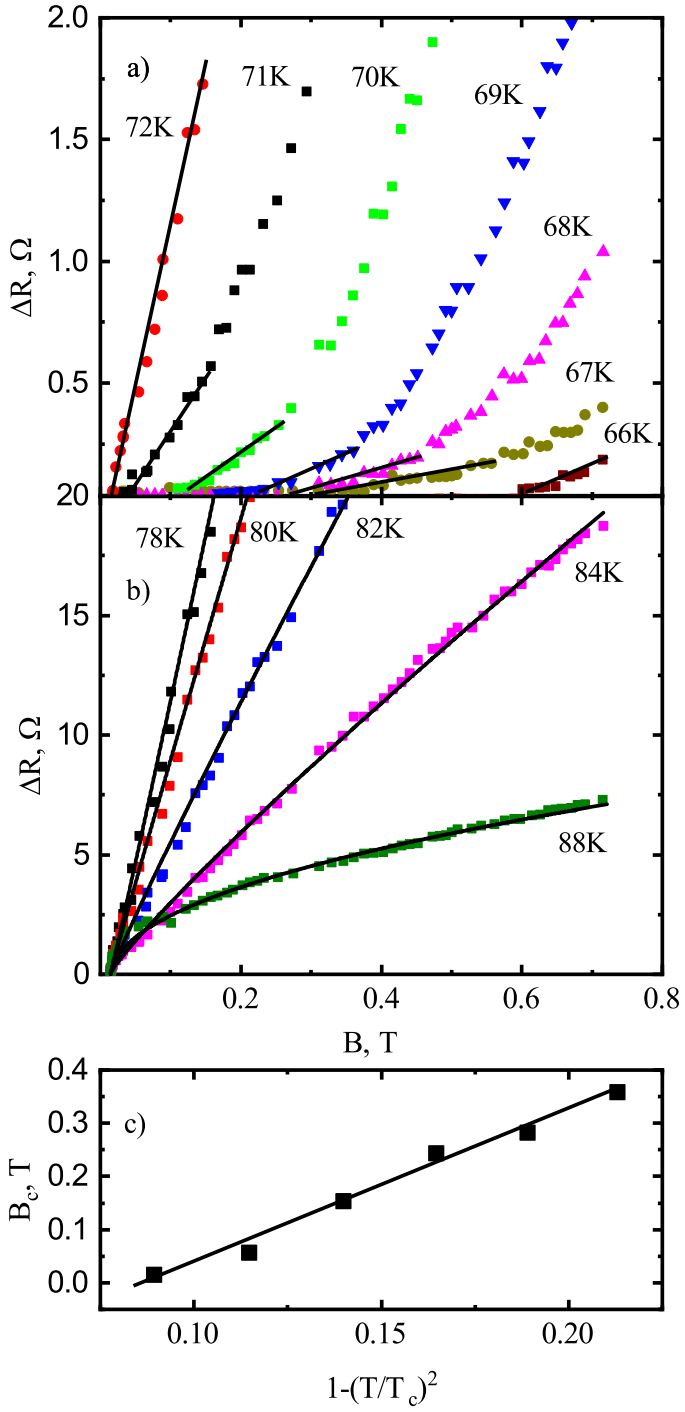

6 pav. a), b) S1a sluoksnio varžos (ΔR) priklausomybės nuo išorinio magnetinio lauko (B_{ex}) įvairiose temperatūrose. c) Kritinio magnetinio srauto tankio priklausomybė nuo temperatūros $1-(T/T_c)^2$ skalėje.

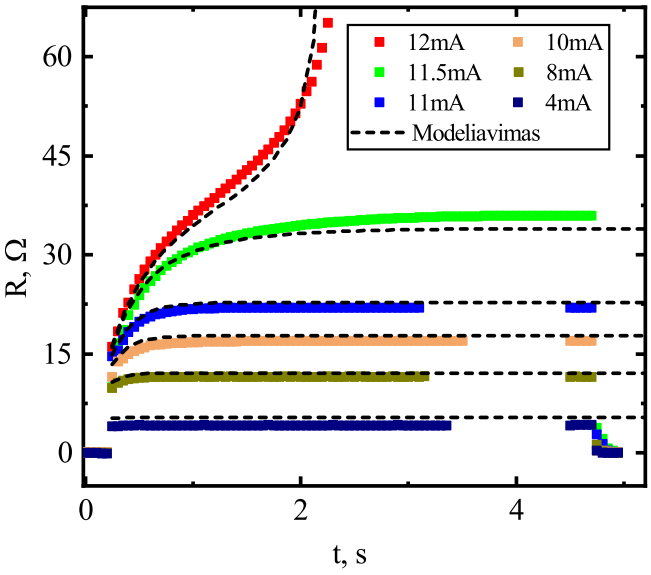

7 pav. S1a mikrotiltelio varžos evoliucija po 0,75 T magnetinio srauto tankio įjungimo. Punktyrinės linijos yra modeliuotos varžos evoliucijos naudojant voltamperines charakteristikas pamatuotas ns trukmės impulsais.

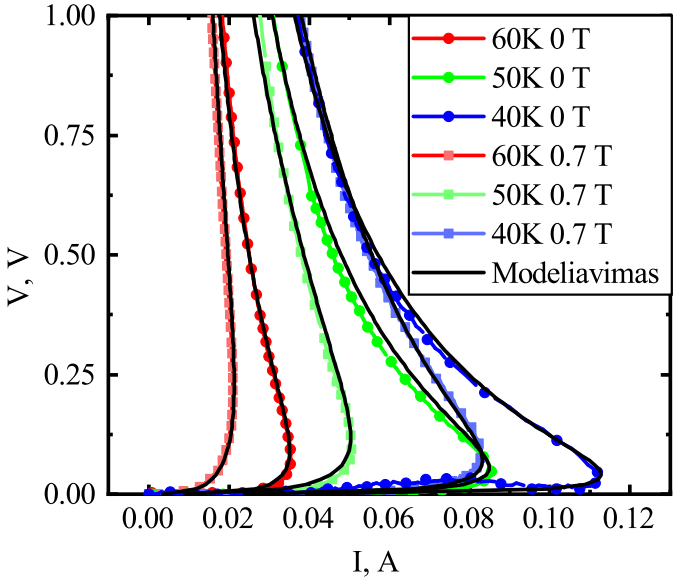

8 pav. S1a mikrotiltelio voltamperinės charakteristikos skirtingose temperatūrose. Apskritimai žymi matavimus be magnetinio lauko, kvadratai - matavimus su B_{ex} = 0,7 T. Juodos linijos vaizduoja sumodeliuotas voltamperines charakteristikas naudojant izotermines voltamperines charakteristikas pamatuotas ns trukmės impulsais.

temperatūros kitimo dinamikos naudojant šilumos pusiausvyros lygtį. Tokiu būdu suskaičiuotos YBCO sluoksnių varžos dinamikos kiekybiškai sutapo su eksperimentinėmis kreivėmis (7 paveikslas), taip patvirtindamos elektroterminę nestabilumo prigimtį.

S formos charakteristikų paaiškinimui taip pat naudotas elektroterminis modelis ir identiškos izoterminių voltamperinių charakteristikų aproksimacijos. Eksperimente stebima srovė nekito, todėl padaryta prielaida, kad stabilizuotos įtampos režime tarp sluoksnio ir šaldomo padėklo nusistovi termodinaminė pusiausvyra. Termodinaminės pusiausvyros atveju šilumos pusiausvyros lygtis gali būti išreikšta kaip algebrinė lygtis, kurios šaknys atitinka voltamperinės charakteristikos taškus. Ši lygtis spręsta Newton'o iteracijų būdu skirtingoms įtampoms, padėklo temperatūroms bei magnetinio srauto tankiams. Taip suskaičiuotos sluoksnių voltamperinės charakteristikos, įskaitant Joule'io šilimą, gerai atitiko eksperimente registruotas kreives, taip dar labiau sustiprindamos elektroterminę stebimų efektų prigimtį.

2.4 poskyryje tiriamas antro tipo superlaidžios EGP, greitinamos vienpakope ritės tipo elektromagnetine svaidykle su plokščiąja rite, elgesys. 2.4.1 skiltyje aprašoma elektromagnetinė svaidyklė, matavimo schema bei metodika. 2.4.2 skiltyje aprašomi eksperimentų rezultatai, pateikiamos EGP trajektorijos bei magnetinio lauko dinamikos. 2.4.3 aprašo matematinį svaidyklės su superlaidžiu sviediniu modelį naudotą teoriniam sistemos tyrimui. 2.4.4 atliekamas teorinis tokios sistemos tyrimas. Analogiškų sąlygų skaičiavimai lyginami su eksperimentiniais. Vėliau atliekama sistemos analizė sąlygoms už eksperimentinių galimybių ribos. II tipo EGP simuliacijos lyginamos su EGP iš vario bei aliuminio. 2.4.5 skiltyje apibendrinami tyrimo rezultatai.

Antros rūšies superlaidininkų elektrinės savybės stipriai skiriasi nuo laidininkų savybių, todėl nutarta ištirti kaip EGP iš antros rūšies superlaidininko elgsis elektromagnetinio greitinimo metu. Tyrimams naudota vienpakopė elektromagnetinė svaidyklė su plokščiąja rite vertikalioje konfigūracijoje ir iki azoto atšaldyta disko formos EGP iš YBCO superlaidininko. Eksperimentų metu buvo fiksuojama EGP trajektorija bei magnetinio lauko dinamika greitinančios ritės centre. Eksperimentai atliki keičiant kondensatorių baterijos įkrovimo įtampą nuo 1 kV iki 1,45 kV.

Šios EML sistemos elgesys taip pat buvo tiriamas teoriškai, darant prielaidą, kad superlaidininkas yra netiesinis laidininkas su laipsniniu elektrinio lauko priklausomybės nuo srovės tankio dėsniu. Modeliavimas atliktas Comsol Multiphysics baigtinių elementų programiniu paketu. Sistema modeliuota

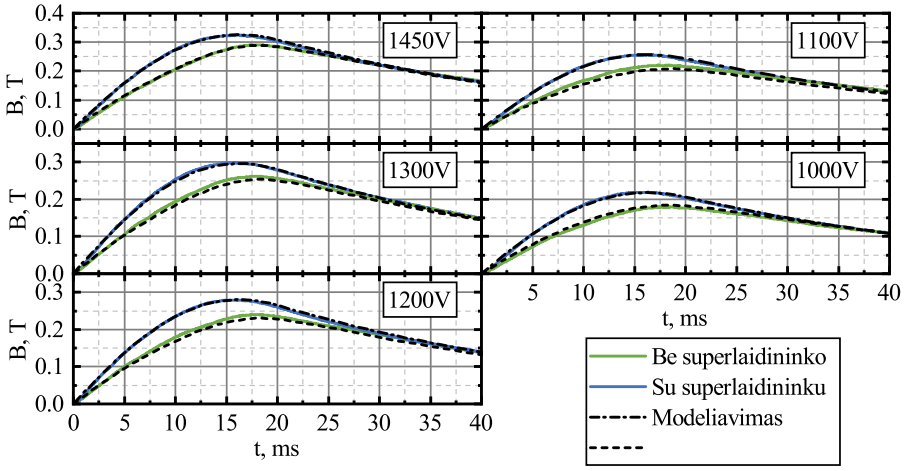

9 pav. Magnetinio srauto tankio dinamika įvairioms kondensatoriaus įkrovimo įtampoms: mėlynos kreivės rodo magnetino srauto tankį pamatuotą tuščiame kriostate, žalios kreivės vaizduoja magnetinio srauto tankio kitimą superlaidžios EGP greitinimo metu. Sumodeliuotos lauko dinamikos pavaizduotos juodomis punktyrinėmis linijomis (j_c=5 · 10^8 A/m^2).

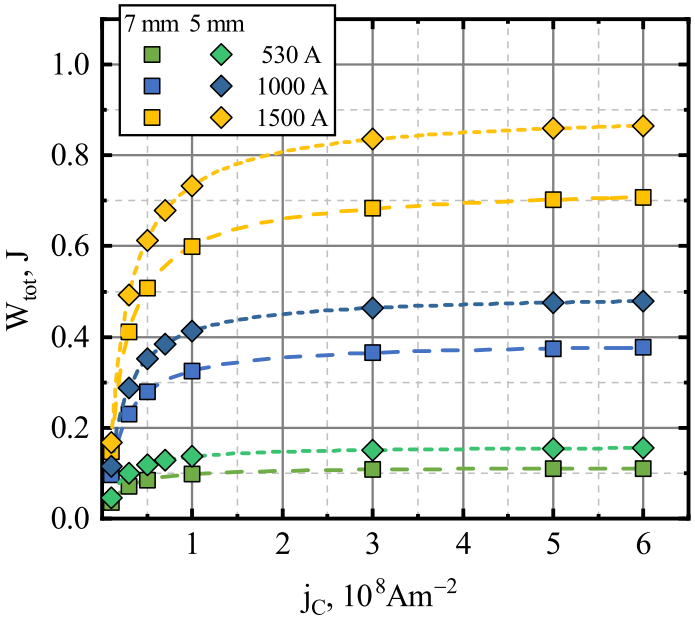

10 pav. Kritinio srovės tankio įtaka mechaninei energijai, suteiktai superlaidžiai EGP, skirtingoms srovės ritėje amplitudėms bei pradiniams EGP atstumams. Linijos - interpoliacija naudojant logistinę funkciją ($y(x) = (c_1 - c_2)/(1 + (x/x_0)^p) + c_2$).

kvazistatinėmis Maxwell'o lygtimis jų H lauko formuluotėje 2D aksisimetrinėje koordinačių sistemoje. Uždavinys spręstas EGP atskaitos sistemoje. Sumodeliuota sistemos elgsena: trajektorija bei magnetinio lauko dinamika, kiekybiškai sutapo su eksperimentiniais rezultatais, kai kritinis srovės tankis bei laipsninio dėsnio rodiklis buvo $5 \cdot 10^8$ A/m^2 ir $n = 20$. Eksperimentinių bei teorinių magnetinio srauto tankių palyginimas pavaizduotas 9 paveiksle. Gautos superlaidininko parametrų vertės nežymiai skyrėsi nuo verčių, įvertintų iš YBCO disko gamintojų pateiktų pagauto magnetinio lauko verčių.

Eksperimentu patvirtintas modelis buvo naudojamas tirti sistemos elgseną sąlygomis už eksperimentinių galimybių ribos. Tiriant kritinio srovės tankio įtaką buvo nustatyta, kad mechaninė energija, perduota superlaidžiai EGP, auga didėjant kritiniam stovės tankiui, tačiau ši energija turi viršutinę ribą fiksuotam startiniam atstumui tarp EGP ir greitinančios ritės bei srovės impulso, tekančio rite, amplitudei. Mechaninės energijos priklausomybės nuo kritinio srovės tankio trims skirtingoms ritės srovės amplitudėms bei dviems startiniams atstumams pavaizduotos 10 paveiksle.

Superlaidžios EGP elgesys taip pat buvo tirtas keičiant elektromagnetinės svaidyklės parametrus: rite tekančios srovės amplitudę, srovės impulso trukmę bei formą. Mechaninė energija suteikta superlaidžiai EGP lyginta su energija suteikta identiškos geometrijos varinei ir aliumininei EGP naudojant metalų savitąsias varžas 77 K temperatūroje. Tyrimui naudoti du parametrų rinkiniai: $j_c = 5 \cdot 10^8$ A/m^2, l_{cd}=7 mm ir $j_c = 3.55 \cdot 10^7$ A/m^2, l_{cd}=5 mm. Pirmasis atitinka eksperimentines sąlygas, o antruoju gaunamos panašios mechaninės energijos vertės 2 mm trumpesniu startiniu EGP atstumu. Tiriant eksperimentinės formos srovės impulso amplitudės įtaką nustatyta, kad abiejų parametrų rinkinių atveju superlaidžios EGP yra pranašesnės mažesnių impulso amplitudžių riboje.

Tiriant greitinančio impuso trukmės įtaką buvo naudojamas eksperimentinės formos srovės impulsas ir keičiama jo trukmė. Nustatyta, kad fiksuotai impulso amplitudei ir startinei pozicijai, egzistuoja optimali impulso trukmė energijos perdavimui. Superlaidžių EGP optimumo trukmė yra ilgų impulsų pusėje lyginant su metalinėmis.

Tiriant srovės impulso, tekančio plokščiąja rite, įtaką sistemos elgsenai buvo naudojamas laiptelio formos impulsas su 1 ms trukmės frontu. Ši forma yra ypatinga, nes turi tiek greitą kitimą impulso pradžioje, tiek pastovią dedamąją po to. Buvo tiriama, kaip laiptelio formos impulso amplitudė keičia EGP perduotą energiją. Buvo nustatyta, kad superlaidžios EGP vėl yra pra-

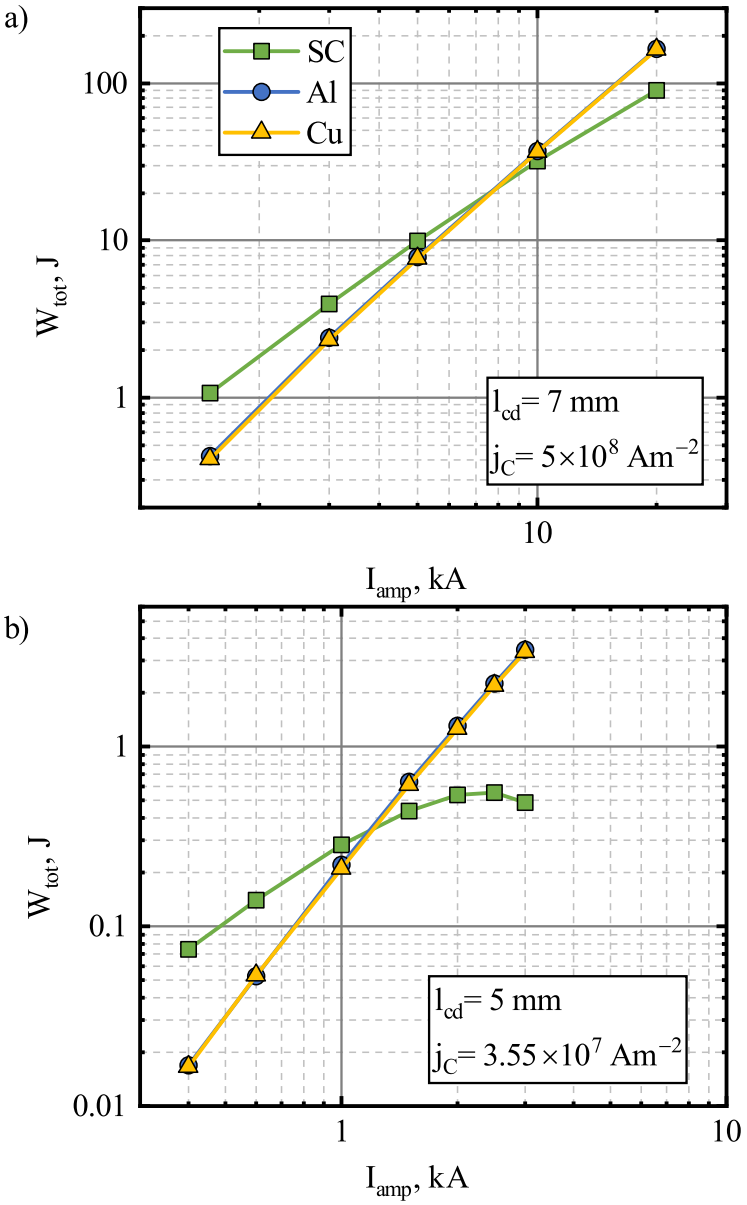

11 pav. Laiptelio formos srovės impulso amplitudės įtaka mechaninei energijai perduotai EGP iš II tipo superlaidininko, vario ar aliuminio. l_{cd}=7 mm, j_c=5 · 10^8 A/m^2 (a) ir l_{cd}=5 mm, j_c=3.55 · 10^7 A/m^2 (b).

našesnės mažesnių amplitudžių riboje. Amplitudžių diapazonas kur superlaidžios EGP pranašesnės buvo susiaurintas stipraus magnetinio stabdymo. Naudojant $j_c = 3.55 \cdot 10^7$ A/m^2, l_{cd}=5 mm parametrus, dėl stipraus stabdymo energija, perduota superlaidžiai EGP, ima mažėti viršijus ribinę srovės laiptelio amplitudę. Mechaninės energijos suteiktos įvairioms EGP dviejų startinių atstumų atveju priklausomybės nuo srovės laiptelio amplitudės pateiktos 11 paveiksle.

- Cilindrinis aliuminio sviedinys heksagonalinės bėgių tipo elektromagnetinės svaidyklės, veikiančios nuoseklaus jungimo sustiprinto lauko režime, vamzdyje ženkliai paveikia magnetinio lauko dinamiką savo aplinkoje. Magnetinio lauko iškraipymas slopsta tolstant nuo sviedinio paviršiaus ir yra stipriausias magnetiniam laukui staigiai kintant. Į tai turi būti atsižvelgta kuriant tokių svaidyklių šaudmenis.
- Sutelktų elektrinių parametrų lygtis gerai aprašo magnetinio lauko dinamiką ir pagautą magnetinį srautą plonasieniame superlaidžiame vamzdyje. Kritinį srovės tankio ir magnetinio lauko sąryšį bei laipsninio dėsnio rodiklį galima įvertinti iš magnetinio impulso matavimo vamzdžio viduje.
- Ploni YBCO sluoksniai, pagaminti PI-MOCVD būdu ant Al_2O_3 padėklų su CeO_2 pasluoksniu, temperatūrose žemesnėse nei krizinė superlaidumo temperatūra T_c, nuolatiniame magnetiniame lauke, didesniame už slenkstinį lauką B_c, pasižymi tiesine magnetovarža, aprašoma Bardeen-Stephen'o modeliu.
- Šių sluoksnių mikrotilteliai nuolatinės įtampos režime pasižymi S formos voltamperinėmis charakteristikomis. Esant pastovios srovės režimui, išorinis magnetinis laukas juose iššaukia laike augančios varžos nestabilumą. Šiuos reiškinius galima gerai paaiškinti homogenišku mikrotiltelio Joule'io šilimu dėl magnetinio srauto tėkmės nulemtos varžinės būsenos.
- Superlaidaus YBCO disko, atšaldyto iki 77 K, greitinamo elektromagnetiniu būdu plokščiąja rite, vertikalų judėjimą ir magnetinio lauko dinamiką tarp ritės ir disko galima gerai sumodeliuoti baigtinių elementų metodu, remiantis Maxwell'o lygtimis jų H formuluotėje, darant prielaidą, kad superlaidininko elektrinio lauko priklausomybė nuo srovės tankio yra laipsninė funkcija.
- Mechaninė energija, perduodama superlaidžiai disko formos elektromagnetiškai greitinamai platformai (EGP) iš impulsinio magnetinio lauko šaltinio, didėja augant EGP medžiagos kritiniam srovės tankiui, tačiau turi ribą, kuri priklauso nuo magnetinio impulso amplitudės ir pradinio EGP atstumo nuo magnetinio lauko šaltinio.
- Energija, perduota disko formos EGP iš II rūšies superlaidininkų, ritės tipo svaidyklėse priklauso nuo rite tekančios srovės impulso formos, amplitudės ir trukmės. Superlaidžios EGP yra pranašesnės už meta-

lines mažesnių impulso amplitudžių ruože ir greitinant impulsais su mažesnėmis laikinėmis išvestinėmis.
- Naudojant laiptelio formos srovės impulsus II tipo superlaidžioms EGP greitinti stebimas stiprus magnetinis stabdymas, tačiau superlaidžios EGP išlieka pranašesnės už metalines mažesnių laiptelio amplitudžių ruože.

Publikacijų disertacijos tema sąrašas

1. V. Vertelis, S. Balevicius, V. Stankevic, N. Zurauskiene, and M. Schneider, "The Application of a CMR-B-Scalar Sensor for the Investigation of the Electromagnetic Acceleration of Type II Superconductors," *Sensors*, vol. 21, no. 4, p. 1293, 2021, doi: 10.3390/s21041293.

2. V. Vertelis et al., "Superconducting protector against electromagnetic pulses based on YBCO film prepared on an Al_2O_3 substrate with a CeO_2 sublayer," *Supercond. Sci. Technol.*, vol. 34, no. 3, p. 035007, 2021, doi: 10.1088/1361-6668/abd459.

3. V. Vertelis, S. Balevicius, V. Stankevic, N. Zurauskiene, and M. Schneider, "Pulsed magnetic flux penetration dynamics inside a thin-walled superconducting tube,"*J. Appl. Phys.*, vol. 127, no. 11, p. 113901, Mar. 2020, doi: 10.1063/1.5145370.

4. V. Vertelis, G. Vincent, M. Schneider, S. Balevičius, V. Stankevič, and N. Žurauskiene, "Magnetic Field Expulsion from a Conducting Projectile in a Pulsed Serial Augmented Railgun," *IEEE Trans. Plasma Sci.*, vol. 48, no. 3, pp. 727–732, Mar. 2020, doi: 10.1109/TPS.2020.2970764.

Kitos publikacijos doktorantūros studijų metu

1. E. Bužavaitė-Vertelienė, V. Vertelis, and Z. Balevičius, "The experimental evidence of a strong coupling regime in the hybrid Tamm plasmon-surface plasmon polariton mode," *Nanophotonics*, Feb. 2021, doi: 10.1515/nanoph-2020-0660.

2. I. Plikusiene, V. Maciulis, O. Graniel, M. Bechelany, S. Balevicius, V. Vertelis, Z. Balevicius, A. Popov, A. Ramanavicius and A. Ramanaviciene, "Total internal reflection ellipsometry for kinetics-based as-

sessment of bovine serum albumin immobilization on ZnO nanowires," *J. Mater. Chem. C*, vol. 9, no. 4, pp. 1345–1352, 2021, doi: 10.1039/D0TC05193D.

Tarptautinės konferencijos

1. V. Vertelis, G. Vincent, V. Stankevic, S. Balevičius and M. Schneider, "Magnetic field expulsion caused by a conducting projectile in an augmented railgun" *19th International Symposium on Electromagnetic Launch Technology (EML 2018)*

2. V. Vertelis, S. Balevicius, V. Stankevic, N. Zurauskiene and M. Schneider, "Magnetic field dynamics inside a thin-walled superconducting tube" *14th European Conference on Applied Superconductivity (EUCAS 2019)*.

3. V.Vertelis, S.Balevicius, M. Schneider, „Numerical modelling of a type II superconducting disk electromagnetic launching using a pancake coil" *7th edition of the International Workshop on Numerical Modelling of High Temperature Superconductors* (HTS 2020), Nancy, France (online).

[1] V. Stankevic, J. Lueg-Althoff, M. Hahn, A. E. Tekkaya, N. Zurauskiene, J. Dilys, J. Klimantavicius, S. Kersulis, C. Simkevicius, and S. Balevicius, "Magnetic Field Measurements during Magnetic Pulse Welding Using CMR-B-Scalar Sensors," *Sensors*, vol. 20, p. 5925, oct 2020.

[2] S. I. Shkuratov, J. Baird, E. F. Talantsev, and L. L. Altgilbers, "Electric discharge caused by expanding armatures in flux compression generators," *Appl. Phys. Lett.*, vol. 94, no. 17, p. 171502, 2009.

[3] T. G. Engel, J. M. Neri, and M. J. Veracka, "The Velocity and Efficiency Limiting Effects of Magnetic Diffusion in Railgun Sliding Contacts," in *2008 14th Symp. Electromagn. Launch Technol.*, pp. 1–5, 2008.

[4] O. Liebfried, M. Loffler, M. Schneider, S. Balevicius, V. Stankevic, N. Zurauskiene, A. Abrutis, and V. Plausinaitiene, "B-scalar measurements by CMR-based sensors of highly inhomogeneous transient magnetic fields," *IEEE Trans. Magn.*, vol. 45, no. 12, pp. 5301–5306, 2009.

[5] G. Vincent and S. Hundertmark, "Using the hexagonal segmented railgun in multishot mode with three projectiles," *IEEE Trans. Plasma Sci.*, vol. 41, no. 5, pp. 1431–1435, 2013.

[6] G. Vincent and S. Hundertmark, "Using the SR\3-60 railgun in augmented mode," in *2014 17th Int. Symp. Electromagn. Launch Technol.*, pp. 1–4, IEEE, 2014.

[7] T. Stankevič, M. Schneider, and S. Balevičius, "Magnetic diffusion inside the rails of an electromagnetic launcher: Experimental and numerical studies," *IEEE Trans. Plasma Sci.*, vol. 41, no. 10, pp. 2790–2795, 2013.

[8] O. Liebfried, M. Schneider, M. J. Loeffler, S. Balevicius, N. Zurauskiene, and V. Stankevic, "Measurement of the magnetic field distribution in railguns using CMR-B-scalar sensors," *Acta Phys. Pol. A Gen. Phys.*, vol. 115, no. 6, p. 1125, 2009.

[9] A. Morandi, E. Perini, G. Giunchi, and M. Fabbri, "Numerical Analysis and Experimental Measurements of Magnetic Bearings Based on MgB_2 Hollow Cylinders," *IEEE Trans. Appl. Supercond.*, vol. 21, no. 3, pp. 1460–1463, 2010.

[10] A. Patel, G. Giunchi, A. F. Albisetti, Y. Shi, S. C. Hopkins, R. Palka, D. A. Cardwell, and B. A. Glowacki, "High force magnetic levitation using magnetized superconducting bulks as a field source for bearing applications," *Phys. Procedia*, vol. 36, pp. 937–942, 2012.

[11] M. K. Alqadi, F. Y. Alzoubi, S. M. Saadeh, H. M. Al-Khateeb, and N. Y. Ayoub, "Force analysis of a permanent magnet and a superconducting hollow cylinder," *J. Supercond. Nov. Magn.*, vol. 25, no. 5, pp. 1469–1473, 2012.

[12] G. P. Lousberg, J.-F. Fagnard, M. Ausloos, P. Vanderbemden, and B. Vanderheyden, "Numerical Study of the Shielding Properties of Macroscopic Hybrid Ferromagnetic/Superconductor Hollow Cylinders," *IEEE Trans. Appl. Supercond.*, vol. 20, no. 1, pp. 33–41, 2010.

[13] J. J. Rabbers, M. P. Oomen, E. Bassani, G. Ripamonti, and G. Giunchi, "Magnetic shielding capability of MgB2 cylinders," *Supercond. Sci. Technol.*, vol. 23, no. 12, p. 125003, 2010.

[14] J.-F. Fagnard, S. Elschner, A. Hobl, J. Bock, B. Vanderheyden, and P. Vanderbemden, "Magnetic shielding properties of a superconducting hollow cylinder containing slits: modelling and experiment," *Supercond. Sci. Technol.*, vol. 25, no. 10, p. 104006, 2012.

[15] F. Sirois, J. R. Cave, and Y. Basile-Bellavance, "Nonlinear magnetic diffusion in a Bi2212 hollow cylinder: Measurements and numerical simulations," *IEEE Trans. Appl. Supercond.*, vol. 17, no. 2, pp. 3652–3655, 2007.
[16] I. Vajda, A. Gyore, S. Semperger, A. E. Baker, E. F. H. Chong, F. J. Mumford, V. Meerovich, and V. Sokolovsky, "Investigation of high temperature superconducting self-limiting transformer with YBCO cylinder," *IEEE Trans. Appl. Supercond.*, vol. 17, no. 2, pp. 1887–1890, 2007.
[17] M. Dione, F. Sirois, F. Grilli, and J. Mahseredjian, "New EMTP-RV equivalent circuit model of core-shielding superconducting fault current limiter taking into account the flux diffusion phenomenon," *IEEE Trans. Appl. Supercond.*, vol. 19, no. 3, pp. 1913–1917, 2009.
[18] J. Bock, S. Elschner, and F. Breuer, "Compact superconducting current limiting component in coil configuration with low inductance," 2010.
[19] G. Ciovati, J. Anderson, B. Coriton, J. Guo, F. Hannon, L. Holland, M. LeSher, F. Marhauser, J. Rathke, R. Rimmer, and Others, "Design of a cw, low-energy, high-power superconducting linac for environmental applications," *Phys. Rev. Accel. Beams*, vol. 21, no. 9, p. 91601, 2018.
[20] Y. Itoh and U. Mizutani, "Pulsed field magnetization of melt-processed Y–Ba–Cu–O superconducting bulk magnet," *Jpn. J. Appl. Phys.*, vol. 35, no. 4R, p. 2114, 1996.
[21] U. Mizutani, T. Oka, Y. Itoh, Y. Yanagi, M. Yoshikawa, and H. Ikuta, "Pulsed-field magnetization applied to high-Tc superconductors," *Appl. Supercond.*, vol. 6, no. 2-5, pp. 235–246, 1998.
[22] T. Kono, M. Tomita, M. Murakami, and T. Takizawa, "Flux motion in bulk YBCO induced by pulsed magnetic fields," *Supercond. Sci. Technol.*, vol. 13, no. 6, p. 794, 2000.
[23] E. H. Brandt, "Susceptibility of superconductor disks and rings with and without flux creep," *Phys. Rev. B*, vol. 55, no. 21, p. 14513, 1997.
[24] P. M. Grant, "Will MgB2 Work?," *Ind. Phys.*, pp. 22–23, oct 2001.
[25] P. Mikheenko and T. H. Johansen, "Smart superconducting grid," *Energy Procedia*, vol. 58, pp. 73–78, 2014.
[26] P. Mikheenko, "Superconductivity for hydrogen economy," in *J. Phys. Conf. Ser.*, vol. 286, p. 12014, IOP Publishing, 2011.
[27] Y. Zhao, T. Qureishy, P. Mikheenko, and J.-C. Grivel, "Characterization of $YBa_2Cu3O_{7-\delta}$ Films With Various Porous Structures Grown by Metalorganic Decomposition Route," *IEEE Trans. Appl. Supercond.*, vol. 26, no. 3, pp. 1–4, 2016.
[28] S. Denis, L. Dusoulier, M. Dirickx, P. Vanderbemden, R. Cloots, M. Ausloos, and B. Vanderheyden, "Magnetic shielding properties of high-temperature superconducting tubes subjected to axial fields," *Supercond. Sci. Technol.*, vol. 20, no. 3, p. 192, 2007.
[29] T. Stankevič, "Juostelių iš plonųjų superlaidžių YBaCuO sluoksnių, išaugintų ant Al_2O_3 padėklo su CeO_2 pasluoksniu, elektrinės savybės," 2010.
[30] S. Balevičius, F. Anisimovas, V. Balčiūnas, R. Butkut, B. Vengalis, and A. S. Flodström, "The electrical instabilities during ultra-fast SN switching in high-Tc thin film microstrip," *Phys. C Supercond.*, vol. 235, pp. 3377–3378, 1994.
[31] L. L. Altgilbers, S. Baleviciusa, N. Zurauskiene, V. Stankevic, P. Cimmperman, and F. Anisimovas, "Hybrid superconducting-magnetic fault current limiter," in *Dig. Tech. Pap. Int. Pulsed Power Conf.*, vol. 2, pp. 1040–1043, 2003.
[32] L. Liang, Y. Wang, Y. Hu, W. Chen, and Z. Yan, "Protection of Elect-

ronic Circuit Based on YBCO Superconducting Thin Film Against the Induced Current Interference," *IEEE Trans. Appl. Supercond.*, vol. 29, no. 6, 2019.
[33] L. Liang, Y. Wang, Z. Yan, Z. He, P. Wang, and W. Chen, "Application of high-temperature superconducting small current limiting against overcurrent in low-noise amplifier electronic circuit," *Phys. C Supercond. its Appl.*, vol. 563, no. November 2018, pp. 28–32, 2019.
[34] B. A. Belyaev, I. V. Govorun, A. A. Leksikov, and A. M. Serzhantov, "Receiver protecting device based on microstrip structure with high-temperature superconductor film," *Tech. Phys. Lett.*, vol. 38, no. 3, pp. 211–214, 2012.
[35] M. Noe and M. Steurer, "High-temperature superconductor fault current limiters: Concepts, applications, and development status," *Supercond. Sci. Technol.*, vol. 20, no. 3, p. R15, 2007.
[36] R. J. Kaye, "Operational requirements and issues for coilgun EM launchers," *2004 12th Symp. Electromagn. Launch Technol.*, vol. 41, no. 1, pp. 59–64, 2004.
[37] R. Kaye, B. Turman, M. Aubuchon, D. Lamppa, G. Mann, E. Van Reuth, K. Fulton, G. Malejko, P. Magnotti, D. Nguyen, D. Borgwarth, A. Johnson, R. Poppe, and Others, "Induction coilgun for EM mortar," *PPPS-2007 - Pulsed Power Plasma Sci. 2007*, vol. 2, pp. 1810–1813, 2007.
[38] S. Williamson and A. Smith, "Pulsed coilgun limits," *IEEE Trans. Magn.*, vol. 33, no. 1 PART 1, pp. 201–207, 1997.
[39] T. Zhang, W. Guo, F. Lin, B. Cao, Z. Dong, R. Ren, K. Huang, and Z. Su, "Experimental results from a 4-stage synchronous induction coilgun," *IEEE Trans. Plasma Sci.*, vol. 41, no. 5, pp. 1084–1088, 2013.
[40] Z. Deng, W. Zhang, J. Zheng, B. Wang, Y. Ren, X. Zheng, and J. Zhang, "A High-Temperature Superconducting Maglev-Evacuated Tube Transport (HTS Maglev-ETT) Test System," *IEEE Trans. Appl. Supercond.*, vol. 27, pp. 1–8, sep 2017.
[41] J. H. Durrell, M. D. Ainslie, D. Zhou, P. Vanderbemden, T. Bradshaw, S. Speller, M. Filipenko, and D. A. Cardwell, "Bulk superconductors: A roadmap to applications," *Supercond. Sci. Technol.*, vol. 31, no. 10, 2018.
[42] L. Wera, J. F. Fagnard, K. Hogan, B. Vanderheyden, D. K. Namburi, Y. Shi, D. A. Cardwell, and P. Vanderbemden, "Magnetic shielding of open and semi-closed bulk superconductor tubes: The role of a cap," *IEEE Trans. Appl. Supercond.*, vol. 29, no. 3, 2019.
[43] W. Yang, L. Yao, and Z. Fu, "Simulation of Dynamic and Electromagnetic Characteristics of a Superconductor Bulk in a Single-Stage Induction Coilgun," *IEEE Trans. Plasma Sci.*, vol. 47, pp. 821–827, jan 2019.
[44] J. C. Maxwell, *A treatise on electricity and magnetism*, vol. 1. Oxford: Clarendon Press, 1873.
[45] Heinz E. Knoepfel, "Magnetic diffusion," in *Magn. Fields A Compr. Theor. Treatise Pract. Use*, pp. 442–450, John Wiley & Sons, 1999.
[46] H. E. Knoepfel, "Numerical and analog solution methods," in *Magn. Fields A Compr. Theor. Treatise Pract. Use*, pp. 513–540, John Wiley & Sons, 1999.
[47] W. Meissner and R. Ochsenfeld, "Ein neuer Effekt bei Eintritt der Supraleitfähigkeit," *Naturwissenschaften*, vol. 21, no. 44, pp. 787–788, 1933.
[48] F. London and H. London, "The electromagnetic equations of the supraconductor," *Proc. R. Soc. London. Ser. A-Mathematical Phys. Sci.*, vol. 149, no. 866, pp. 71–88, 1935.
[49] A. A. Abrikosov, "The magnetic properties of superconducting alloys,"

J. Phys. Chem. Solids, vol. 2, no. 3, pp. 199–208, 1957.
[50] C. P. Bean, "Magnetization of Hard Superconductors," *Phys. Rev. Lett.*, vol. 8, pp. 250–253, mar 1962.
[51] J. Bardeen and M. J. Stephen, "Theory of the motion of vortices in superconductors," *Phys. Rev.*, vol. 140, no. 4A, 1965.
[52] Y. B. Kim, C. F. Hempstead, and A. R. Strnad, "Flux-Flow Resistance in Type-II Superconductors," *Phys. Rev.*, vol. 139, pp. A1163—-A1172, aug 1965.
[53] A. K. Pradhan, M. Muralidhar, M. Murakami, and N. Koshizuka, "Studies of flux pinning behaviour in melt-processed ternary (Nd-Eu-Gd) Ba2Cu3Oy superconductors," *Supercond. Sci. Technol.*, vol. 13, no. 6, p. 761, 2000.
[54] M. Tinkham, "Viscous flow of flux in type-II superconductors," *Phys. Rev. Lett.*, vol. 13, no. 26, p. 804, 1964.
[55] P. W. Anderson, "Theory of Flux Creep in Hard Superconductors," *Phys. Rev. Lett.*, vol. 9, no. 7, pp. 309–311, 1962.
[56] K. Fossheim and A. Sudbø, *Superconductivity: physics and applications*. John Wiley & Sons, 2005.
[57] M. Tinkham, *Introduction to Superconductivity*. Dover Publications, 2 ed., 2004.
[58] D. S. Fisher, M. P. A. Fisher, and D. A. Huse, "Thermal fluctuations, quenched disorder, phase transitions, and transport in type-II superconductors," *Phys. Rev. B*, vol. 43, no. 1, pp. 130–159, 1991.
[59] G. Blatter, M. V. Feigel'man, V. B. Geshkenbein, A. I. Larkin, and V. M. Vinokur, "Vortices in high-temperature superconductors," *Rev. Mod. Phys.*, vol. 66, no. 4, pp. 1125–1388, 1994.
[60] E. H. Brandt, "Superconductor disks and cylinders in an axial magnetic field. I. Flux penetration and magnetization curves," *Phys. Rev. B*, vol. 58, no. 10, p. 6506, 1998.
[61] M. Ban, T. Ichiguchi, and T. Onogi, "Power laws in the resistive state in high-Tc superconductors," *Phys. Rev. B*, vol. 40, no. 7, pp. 4419–4422, 1989.
[62] Y. Ando, N. Motohira, K. Kitazawa, J.-i. Takeya, and S. Akita, "Mechanism of the Lorentz-force-independent dissipation in $Bi_2Sr_2CaCu_2O_y$," *Phys. Rev. Lett.*, vol. 67, no. 19, pp. 2737–2740, 1991.
[63] S. K. Gupta, P. Berdahl, R. E. Russo, G. Briceño, and A. Zettl, "Pulse I-V characteristics measurement to study the dissipation mechanism in epitaxial YBa2Cu3Ox thin films at high current densities," *Phys. C Supercond.*, vol. 206, no. 3, pp. 335–344, 1993.
[64] C. Peroz, J. C. Villégier, A. F. Dégardin, B. Guillet, and A. J. Kreisler, "High critical current densities observed in PrBa2Cu3O7-δ\ YBa2Cu3O7-δ\PrBa2Cu3O7-δ ultrathin film constrictions," *Appl. Phys. Lett.*, vol. 89, no. 14, p. 142502, 2006.
[65] S. Hundertmark and D. Lancelle, "A scenario for a future European shipboard railgun," *IEEE Trans. Plasma Sci.*, vol. 43, no. 5, pp. 1194–1197, 2015.
[66] I. R. McNab, "Launch to space with an electromagnetic railgun," *IEEE Trans. Magn.*, vol. 39, no. 1, pp. 295–304, 2003.
[67] S. Hundertmark, "Applying railgun technology to small satellite launch," in *Proc. 5th Int. Conf. Recent Adv. Sp. Technol.*, pp. 747–751, IEEE, IEEE, 2011.
[68] P. A. Gores, G. Vincent, M. Schneider, and J. G. Spray, "Appraisal of Rapid-Fire Electromagnetic Launch Effects on Ceramic Targets," *IEEE Trans. Plasma Sci.*, vol. 47, no. 8, pp. 4175–4180, 2019.

[69] R. O'Rourke, "Navy Lasers, Railgun, and Hypervelocity Projectile: Background and Issues for Congress," tech. rep., Congressional Research Service Washington United States, 2017.
[70] W. Ying, R. A. Marshall, and C. Shukang, *PHYSICS OF ELECTRIC LAUNCH*. Beijing: Science Press, 2004.
[71] M. Schneider, C. Schuppler, and F. Alouahabi, "Single shot performance of RAFIRA," in *2014 17th Int. Symp. Electromagn. Launch Technol.*, pp. 1–4, IEEE, 2014.
[72] S. Hundertmark, G. Vincent, F. Schubert, and J. Urban, "The NGL-60 railgun," *IEEE Trans. Plasma Sci.*, vol. 47, no. 7, pp. 3327–3330, 2019.
[73] R. A. Meger, B. M. Huhman, J. M. Neri, T. H. Brintlinger, H. N. Jones, R. L. Cairns, S. R. Douglass, T. R. Lockner, and J. A. Sprague, "NRL materials testing facility," *IEEE Trans. Plasma Sci.*, vol. 41, no. 5, pp. 1538–1541, 2013.
[74] R. A. Meger, R. L. Cairns, S. R. Douglass, B. Huhman, J. M. Neri, C. J. Carney, H. N. Jones, K. Cooper, J. Feng, T. H. Brintlinger, and Others, "EM gun bore life experiments at naval research laboratory," *IEEE Trans. Plasma Sci.*, vol. 41, no. 5, pp. 1533–1537, 2013.
[75] B. I. Machado, L. E. Murr, E. Martinez, S. M. Gaytan, and S. Satapathy, "Materials characterization of railgun erosion phenomena," *Mater. Sci. Eng. A*, vol. 528, no. 25-26, pp. 7552–7559, 2011.
[76] S. Katsuki, H. Akiyama, N. Eguchi, T. Sueda, M. Soejima, S. Maeda, and K. N. Sato, "Augmented railgun using a permanent magnet," *Rev. Sci. Instrum.*, vol. 66, no. 8, pp. 4227–4232, 1995.
[77] S. Z. Liang, Y. T. Fang, and X. Y. Huang, "Dynamic simulation of a superconducting augmented linear propulsion system," in *2015 IEEE Int. Conf. Appl. Supercond. Electromagn. Devices*, pp. 175–176, IEEE, 2015.
[78] R. L. Fuller, J. R. Kitzmiller, and M. W. Ingram, "Design and testing of a 0.60 caliber, augmented railgun," *IEEE Trans. Magn.*, vol. 27, no. 1, pp. 45–49, 1991.
[79] I. R. McNab, "The STAR railgun concept," *IEEE Trans. Magn.*, vol. 35, no. 1, pp. 432–436, 1999.
[80] J. M. Neri and J. S. Kim, "Initial operation, modeling and optimization of a low-velocity augmented railgun," in *Dig. Tech. Pap. PPC-2003. 14th IEEE Int. Pulsed Power Conf. (IEEE Cat. No. 03CH37472)*, vol. 2, pp. 1103–1106, IEEE, 2003.
[81] J. Gallant and P. Lehmann, "Experiments with brush projectiles in a parallel augmented railgun," in *2004 12th Symp. Electromagn. Launch Technol.*, pp. 53–58, IEEE, 2004.
[82] J. Gallant, "Parametric study of an augmented railgun," *IEEE Trans. Magn.*, vol. 39, no. 1, pp. 451–455, 2003.
[83] I. R. McNab, "Pulsed power options for large EM launchers," in *2014 17th Int. Symp. Electromagn. Launch Technol.*, pp. 1–11, 2014.
[84] O. Liebfried, "Review of inductive pulsed power generators for railguns," *IEEE Trans. Plasma Sci.*, vol. 45, no. 7, pp. 1108–1114, 2017.
[85] S. Hundertmark and O. Liebfried, "Power supply options for a naval railgun," *IEEE Trans. Plasma Sci.*, vol. 46, no. 10, pp. 3599–3605, 2018.
[86] O. Liebfried, V. Brommer, H. Scharf, M. Schacherer, and P. Frings, "Modular Toroidal Copper Coil for the Investigation of Inductive Pulsed Power in the MJ-RangeGenerators," *IEEE Trans. Appl. Supercond.*, vol. 30, no. 4, pp. 1–6, 2020.
[87] J. Ciceron, A. Badel, and P. Tixador, "Superconducting magnetic energy storage and superconducting self-supplied electromagnetic launcher,"

Eur. Phys. J. Appl. Phys., vol. 80, no. 2, p. 20901, 2017.
[88] A. B. Arnaud, J. Ciceron, R. Pasquet, E. Voisin, F. Forest, M. Schneider, and P. Tixador, "Design of a Superconducting Self-Supplied Electromagnetic Launcher Proof of Concept Using HTS REBCO Conductor," *IEEE Trans. Appl. Supercond.*, vol. 27, no. 4, pp. 1–5, 2016.
[89] A. Badel, P. Tixador, M. Amiet, and V. Brommer, "SMES to supply an electromagnetic launcher," *IEEE Trans. Appl. Supercond.*, vol. 22, no. 3, p. 5700204, 2011.
[90] A. Badel, P. Tixador, and M. Arniet, "Optimized use of superconducting magnetic energy storage for electromagnetic rail launcher powering," *Supercond. Sci. Technol.*, vol. 25, no. 1, p. 14006, 2011.
[91] S. Hundertmark and G. Vincent, "Investigating a radio data link to a railgun projectile—The active projectile," *IEEE Trans. Plasma Sci.*, vol. 39, no. 1, pp. 422–425, 2010.
[92] R. Ciolini, M. Schneider, and B. Tellini, "The Use of Electronic Components in Railgun Projectiles," *IEEE Trans. Magn.*, vol. 1, no. 45, pp. 578–583, 2009.
[93] Y.-t. Lou, H.-y. Li, and B.-m. Li, "Research on proximity effect of electromagnetic railgun," *Def. Technol.*, vol. 12, no. 3, pp. 223–226, 2016.
[94] J. H. Beno and W. F. Weldon, "An investigation into the potential for multiple rail railguns," *IEEE Trans. Magn.*, vol. 25, no. 1, pp. 92–96, 1989.
[95] M. Koops, T. Huijser, and W. Karthaus, "Design and evaluation of carbon fibre-reinforced launch packages with segmented, copper and molybdenum fibre armatures," *IEEE Trans. Magn.*, vol. 33, no. 1, pp. 119–124, 1997.
[96] J. Wey, P. Lehmann, R. Charon, D. Eckenfels, and C. Gauthier, "First measurements of current distribution in moving fiber-armatures in railguns," *IEEE Trans. Magn.*, vol. 35, no. 1, pp. 107–111, 1999.
[97] G. Bandini, M. Marracci, G. Caposciutti, and B. Tellini, "Pulsed-Current Distribution in Electromagnetic Rail Launchers," *IEEE Trans. Instrum. Meas.*, vol. 69, no. 12, pp. 9381–9388, 2020.
[98] A. Yamori, N. Kawashima, and M. Kohno, "Characteristics of high efficiency 300 kJ railgun," *IEEE Trans. Magn.*, vol. 31, no. 1, pp. 377–381, 1995.
[99] R. Hawke, W. Nellis, G. Newman, J. Rego, and A. Susoeff, "Summary of EM launcher experiments performed at LLNL," *IEEE Trans. Magn.*, vol. 22, no. 6, pp. 1510–1515, 1986.
[100] T. G. Engel, J. M. Neri, and W. C. Nunnally, "Efficiency and scaling of constant inductance gradient DC electromagnetic launchers," *IEEE Trans. Magn.*, vol. 42, no. 8, pp. 2043–2051, 2006.
[101] T. G. Engel, J. M. Neri, and M. J. Veracka, "Characterization of the Velocity Skin Effect in the Surface Layer of a Railgun Sliding Contact," *IEEE Trans. Magn.*, vol. 44, no. 7, pp. 1837–1844, 2008.
[102] A. K. Kondratenko, M. A. Bykov, B. S. Schastnykh, A. P. Glinov, and A. E. Poltanov, "The study of sliding contact in railgun with metal armature," *IEEE Trans. Magn.*, vol. 33, no. 1, pp. 576–581, 1997.
[103] M. Schneider, R. Schneider, V. Stankevic, S. Balevicius, and N. Zurauskiene, "Highly Local Measurements of Strong Transient Magnetic Fields During Railgun Experiments Using CMR-Based Sensors," *IEEE Trans. Magn.*, vol. 43, no. 1, pp. 370–375, 2007.
[104] M. Schneider, O. Liebfried, V. Stankevic, S. Balevicius, and N. Zurauskiene, "Magnetic Diffusion in Railguns: Measurements Using CMR-Based Sensors," *IEEE Trans. Magn.*, vol. 45, no. 1, pp. 430–435, 2009.

[105] M. Schneider, J. Rackauskas, and M. J. Löffler, "Electromechanical Modeling of Components of a Linear Electromagnetic Accelerator," *IEEE Trans. Plasma Sci.*, vol. 41, no. 10, pp. 2796–2799, 2013.
[106] J. Račkauskas, R. Kačianauskas, and M. Schneider, "Investigation of armature-rail interaction in linear electromagnetic launcher," *J. Vibroengineering*, vol. 20, no. 2, pp. 1234–1239, 2018.
[107] B. Tang, Q. Lin, and B. Li, "Research on Thermal Stress by Current Skin Effect in a Railgun," *IEEE Trans. Plasma Sci.*, vol. 45, no. 7, pp. 1689–1694, 2017.
[108] G. A. Shvetsov and S. V. Stankevich, "Three-Dimensional Numerical Simulation of the Joule Heating of Various Shapes of Armatures in Railguns," *IEEE Trans. Plasma Sci.*, vol. 39, no. 1, pp. 456–460, 2011.
[109] M. Coffo and J. Gallant, "Simulation of the current distribution and the heat load of a brush projectile in a railgun with the finite element code ANSYS," *Acta Phys. Pol. a Gen. Phys.*, vol. 115, no. 6, p. 1112, 2009.
[110] B. Reck, P. Lehmann, W. Wenning, and M. D. Vo, "Projectiles with rod-shaped payloads for the PEGASUS railgun," *IEEE Trans. Magn.*, vol. 43, no. 1, pp. 397–401, 2006.
[111] A. P. Noel, A. Challita, and D. P. Bauer, "A novel railgun launch package concept," *IEEE Trans. Magn.*, vol. 37, no. 1, pp. 97–100, 2001.
[112] J. H. Durrell, A. R. Dennis, J. Jaroszynski, M. D. Ainslie, K. G. B. Palmer, Y. H. Shi, A. M. Campbell, J. Hull, M. Strasik, E. E. Hellstrom, and Others, "A trapped field of 17.6 T in melt-processed, bulk Gd-Ba-Cu-O reinforced with shrink-fit steel," *Supercond. Sci. Technol.*, vol. 27, no. 8, p. 82001, 2014.
[113] H. Maeda and Y. Yanagisawa, "Recent Developments in High-Temperature Superconducting Magnet Technology (Review)," *IEEE Trans. Appl. Supercond.*, vol. 24, no. 3, pp. 1–12, 2014.
[114] S. Mukoyama, K. Nakao, H. Sakamoto, T. Matsuoka, K. Nagashima, M. Ogata, T. Yamashita, Y. Miyazaki, K. Miyazaki, T. Maeda, and H. Shimizu, "Development of Superconducting Magnetic Bearing for 300 kW Flywheel Energy Storage System," *IEEE Trans. Appl. Supercond.*, vol. 27, no. 4, pp. 1–4, 2017.
[115] D. H. N. Dias, G. G. Sotelo, F. Sass, E. S. Motta, R. de Andrade Jr, and R. M. Stephan, "Dynamical Tests in a Linear Superconducting Magnetic Bearing," *Phys. Procedia*, vol. 36, pp. 1049–1054, 2012.
[116] M. Sparing, M. Hossain, D. Berger, A. Berger, A. Abdkader, G. Fuchs, C. Cherif, and L. Schultz, "Superconducting Magnetic Bearing as Twist Element in Textile Machines," *IEEE Trans. Appl. Supercond.*, vol. 25, no. 3, pp. 1–4, 2015.
[117] X. Song, C. Bührer, P. Brutsaert, J. Krause, A. Ammar, J. Wiezoreck, J. Hansen, A. V. Rebsdorf, M. Dhalle, A. Bergen, T. Winkler, S. Wessel, M. t. Brake, J. Kellers, H. Pütz, M. Bauer, H. Kyling, H. Boy, and E. Seitz, "Designing and Basic Experimental Validation of the World's First MW-Class Direct-Drive Superconducting Wind Turbine Generator," *IEEE Trans. Energy Convers.*, vol. 34, no. 4, pp. 2218–2225, 2019.
[118] Y. Xu, N. Maki, and M. Izumi, "Overview Study on Electrical Design of Large-Scale Wind Turbine HTS Generators," *IEEE Trans. Appl. Supercond.*, vol. 28, no. 5, pp. 1–5, 2018.
[119] K. Sivasubramaniam, T. Zhang, M. Lokhandwalla, E. T. Laskaris, J. W. Bray, B. Gerstler, M. R. Shah, and J. P. Alexander, "Development of a High Speed HTS Generator for Airborne Applications," *IEEE Trans. Appl. Supercond.*, vol. 19, no. 3, pp. 1656–1661, 2009.
[120] B. Gamble, G. Snitchler, and T. MacDonald, "Full Power Test of a 36.5

MW HTS Propulsion Motor," *IEEE Trans. Appl. Supercond.*, vol. 21, no. 3, pp. 1083–1088, 2011.
[121] Z. Huang, M. Zhang, W. Wang, and T. A. Coombs, "Trial Test of a Bulk-Type Fully HTS Synchronous Motor," *IEEE Trans. Appl. Supercond.*, vol. 24, no. 3, pp. 1–5, 2014.
[122] H. Moon, Y. Kim, H. Park, M. Park, and I. Yu, "Development of a MW-Class 2G HTS Ship Propulsion Motor," *IEEE Trans. Appl. Supercond.*, vol. 26, no. 4, pp. 1–5, 2016.
[123] G. P. Mikitik, Y. Mawatari, A. T. S. Wan, and F. Sirois, "Analytical methods and formulas for modeling high temperature superconductors," *IEEE Trans. Appl. Supercond.*, vol. 23, no. 2, p. 8001920, 2013.
[124] M. Ainslie, F. Grilli, L. Quéval, E. Pardo, F. Perez-Mendez, R. Mataira, A. Morandi, A. Ghabeli, C. Bumby, and R. Brambilla, "A new benchmark problem for electromagnetic modelling of superconductors: the high- T c superconducting dynamo," *Supercond. Sci. Technol.*, vol. 33, p. 105009, oct 2020.
[125] F. Grilli, S. Stavrev, Y. LeFloch, M. Costa-Bouzo, E. Vinot, I. Klutsch, G. Meunier, P. Tixador, and B. Dutoit, "Finite-Element Method Modeling of Superconductors: From 2-D to 3-D," *IEEE Trans. Appiled Supercond.*, vol. 15, pp. 17–25, mar 2005.
[126] F. Liang, S. Venuturumilli, H. Zhang, M. Zhang, J. Kvitkovic, S. Pamidi, Y. Wang, and W. Yuan, "A finite element model for simulating second generation high temperature superconducting coils/stacks with large number of turns," *J. Appl. Phys.*, vol. 122, p. 43903, jul 2017.
[127] E. Berrospe-Juarez, V. M. R. Zermeño, F. Trillaud, and F. Grilli, "Real-time simulation of large-scale HTS systems: multi-scale and homogeneous models using the T–A formulation," *Supercond. Sci. Technol.*, vol. 32, p. 065003, jun 2019.
[128] E. Berrospe-Juarez, F. Trillaud, V. M. R. Zermeno, F. Grilli, H. W. Weijers, and M. D. Bird, "Screening Currents and Hysteresis Losses in the REBCO Insert of the 32 T All-Superconducting Magnet Using T-A Homogenous Model," *IEEE Trans. Appl. Supercond.*, vol. 30, pp. 1–5, jun 2020.
[129] E. H. Brandt and J. R. Clem, "Superconducting thin rings with finite penetration depth," *Phys. Rev. B*, vol. 69, no. 18, p. 184509, 2004.
[130] E. H. Brandt, "Superconductors of finite thickness in a perpendicular magnetic field: Strips and slabs," *Phys. Rev. B - Condens. Matter Mater. Phys.*, vol. 54, no. 6, pp. 4246–4264, 1996.
[131] E. H. Brandt, "Square and Rectangular Thin Superconductors in a Transverse Magnetic Field," *Phys. Rev. Lett.*, vol. 74, no. 15, pp. 3025–3028, 1995.
[132] E. H. Brandt, "Electric field in superconductors with rectangular cross section," *Phys. Rev. B*, vol. 52, no. 21, pp. 15442–15457, 1995.
[133] J.-F. Fagnard, M. Dirickx, M. Ausloos, G. Lousberg, B. Vanderheyden, and P. Vanderbemden, "Magnetic shielding properties of high-Tc superconducting hollow cylinders: model combining experimental data for axial and transverse magnetic field configurations," *Supercond. Sci. Technol.*, vol. 22, no. 10, p. 105002, 2009.
[134] Y. B. Kim, C. F. Hempstead, and A. R. Strnad, "Critical Persistent Currents in Hard Superconductors," *Phys. Rev. Lett.*, vol. 9, no. 7, pp. 306–309, 1962.
[135] F. M. Araujo-Moreira, C. Navau, and A. Sanchez, "Meissner state in finite superconducting cylinders with uniform applied magnetic field," *Phys. Rev. B*, vol. 61, no. 1, pp. 634–639, 2000.

[136] J. Liu, C. Huang, H. Yong, and Y. Zhou, "Simulation of magnetization and levitation properties of arrays of ring-shaped type-II superconductors," *Phys. C Supercond. its Appl.*, vol. 534, pp. 55–60, mar 2017.
[137] A. Sanchez and C. Navau, "Critical-current density from magnetization loops of finite high-Tc superconductors," *Supercond. Sci. Technol.*, vol. 14, no. 7, p. 444, 2001.
[138] C. Navau, A. Sanchez, E. Pardo, D.-X. Chen, E. Bartolomé, X. Granados, T. Puig, and X. Obradors, "Critical state in finite type-II superconducting rings," *Phys. Rev. B*, vol. 71, no. 21, p. 214507, 2005.
[139] M. D. Ainslie and H. Fujishiro, "Modelling of bulk superconductor magnetization," *Supercond. Sci. Technol.*, vol. 28, no. 5, p. 53002, 2015.
[140] S. Stavrev, F. Grilli, B. Dutoit, N. Nibbio, E. Vinot, I. Klutsch, G. Meunier, P. Tixador, Yifeng Yang, and E. Martinez, "Comparison of numerical methods for modeling of superconductors," *IEEE Trans. Magn.*, vol. 38, no. 2, pp. 849–852, 2002.
[141] F. Gömöry, M. Vojenčiak, E. Pardo, and J. Šouc, "Magnetic flux penetration and AC loss in a composite superconducting wire with ferromagnetic parts," *Supercond. Sci. Technol.*, vol. 22, p. 034017, mar 2009.
[142] N. Nibbio, S. Stavrev, and B. Dutoit, "Finite element method simulation of AC loss in HTS tapes with B-dependent E-J power law," *IEEE Trans. Appl. Supercond.*, vol. 11, no. 1, pp. 2631–2634, 2001.
[143] D. Ruiz-Alonso, T. Coombs, and A. M. Campbell, "Computer modelling of high-temperature superconductors using an A–V formulation," *Supercond. Sci. Technol.*, vol. 17, no. 5, p. S305, 2004.
[144] F. Sass, D. H. N. Dias, G. G. Sotelo, and R. de Andrade Junior, "Superconducting magnetic bearings with bulks and 2G HTS stacks: Comparison between simulations using H and A-V formulations with measurements," *Supercond. Sci. Technol.*, vol. 31, no. 2, p. 25006, 2018.
[145] A. Musso, M. Breschi, P. L. Ribani, and F. Grilli, "Analysis of AC Loss Contributions From Different Layers of HTS Tapes Using the A-V Formulation Model," *IEEE Trans. Appl. Supercond.*, vol. 31, no. 2, pp. 1–11, 2021.
[146] G. P. Lousberg, M. Ausloos, C. Geuzaine, P. Dular, P. Vanderbemden, and B. Vanderheyden, "Numerical simulation of the magnetization of high-temperature superconductors: a 3D finite element method using a single time-step iteration," *Supercond. Sci. Technol.*, vol. 22, p. 055005, may 2009.
[147] H. Ohsaki, T. Shimosaki, and N. Nozawa, "Pulse field magnetization of a ring-shaped bulk superconductor," *Supercond. Sci. Technol.*, vol. 15, no. 5, p. 754, 2002.
[148] N. Amemiya, S.-i. Murasawa, N. Banno, and K. Miyamoto, "Numerical modelings of superconducting wires for AC loss calculations," *Phys. C Supercond.*, vol. 310, no. 1, pp. 16–29, 1998.
[149] N. Enomoto and N. Amemiya, "Electromagnetic field analysis of rectangular high Tc superconductor with large aspect ratio," *Phys. C Supercond.*, vol. 412-414, pp. 1050–1055, 2004.
[150] H. Zhang, M. Zhang, and W. Yuan, "An efficient 3D finite element method model based on the T–A formulation for superconducting coated conductors," *Supercond. Sci. Technol.*, vol. 30, no. 2, p. 24005, 2016.
[151] F. Grilli, E. Pardo, A. Stenvall, D. N. Nguyen, W. Yuan, and F. Gömöry, "Computation of Losses in HTS Under the Action of Varying Magnetic Fields and Currents," *IEEE Trans. Appl. Supercond.*, vol. 24, no. 1, pp. 78–110, 2014.
[152] Z. Xu and F. Grilli, "Modelling ac ripple currents in HTS coated con-

ductors," *Supercond. Sci. Technol.*, vol. 28, no. 10, p. 104002, 2015.
[153] B. Shen, F. Grilli, and T. Coombs, "Overview of H-Formulation: A Versatile Tool for Modeling Electromagnetics in High-Temperature Superconductor Applications," *IEEE Access*, vol. 8, pp. 100403–100414, 2020.
[154] M. Yazdani-Asrami, S. Asghar Gholamian, S. M. Mirimani, and J. Adabi, "Influence of field-dependent critical current on harmonic AC loss analysis in HTS coils for superconducting transformers supplying nonlinear loads," *Cryogenics (Guildf).*, vol. 113, p. 103234, 2021.
[155] F. Grilli, M. Vojenčiak, A. Kario, and V. Zermeño, "HTS Roebel Cables: Self-Field Critical Current and AC Losses Under Simultaneous Application of Transport Current and Magnetic Field," *IEEE Trans. Appl. Supercond.*, vol. 26, no. 4, pp. 1–5, 2016.
[156] D. Hu, M. D. Ainslie, J. Zou, and D. A. Cardwell, "Numerical Analysis of Non-Uniformities and Anisotropy in High-Temperature Superconducting Coils," *IEEE Trans. Appl. Supercond.*, vol. 25, no. 3, pp. 1–5, 2015.
[157] K. P. Thakur, A. Raj, E. H. Brandt, J. Kvitkovic, and S. V. Pamidi, "Frequency-dependent critical current and transport ac loss of superconductor strip and Roebel cable," *Supercond. Sci. Technol.*, vol. 24, no. 6, p. 65024, 2011.
[158] M. Zhang and T. A. Coombs, "3D modeling of high-Tc superconductors by finite element software," *Supercond. Sci. Technol.*, vol. 25, no. 1, p. 15009, 2011.
[159] Z. Hong, A. M. Campbell, and T. A. Coombs, "Numerical solution of critical state in superconductivity by finite element software," *Supercond. Sci. Technol.*, vol. 19, no. 12, p. 1246, 2006.
[160] M. D. Ainslie, H. Fujishiro, T. Ujiie, J. Zou, A. R. Dennis, Y. H. Shi, and D. A. Cardwell, "Modelling and comparison of trapped fields in (RE) BCO bulk superconductors for activation using pulsed field magnetization," *Supercond. Sci. Technol.*, vol. 27, no. 6, p. 65008, 2014.
[161] S. Zou, V. M. R. Zermeño, and F. Grilli, "Influence of Parameters on the Simulation of HTS Bulks Magnetized by Pulsed Field Magnetization," *IEEE Trans. Appl. Supercond.*, vol. 26, no. 4, pp. 1–5, 2016.
[162] F. Sass, G. G. Sotelo, R. De Andrade, and F. Sirois, "H-formulation for simulating levitation forces acting on HTS bulks and stacks of 2G coated conductors," *Supercond. Sci. Technol.*, vol. 28, no. 12, p. 125012, 2015.
[163] L. Quéval, K. Liu, W. Yang, V. M. Zermeño, and G. Ma, "Superconducting magnetic bearings simulation using an H-formulation finite element model," *Supercond. Sci. Technol.*, vol. 31, no. 8, 2018.
[164] Y. B. Kim, C. F. Hempstead, and A. R. Strnad, "Magnetization and Critical Supercurrents," *Phys. Rev.*, vol. 129, no. 2, pp. 528–535, 1963.
[165] A. Patel and B. A. Glowacki, "Enhanced trapped field achieved in a superconducting bulk using high thermal conductivity structures following simulated pulsed field magnetization," *Supercond. Sci. Technol.*, vol. 25, no. 12, p. 125015, 2012.
[166] T. Matsushita, E. S. Otabe, T. Fukunaga, K. Kuga, K. Yamafuji, K. Kimura, and M. Hashimoto, "Weak link property in superconducting Y-Ba-Cu-O prepared by QMG process," *IEEE Trans. Appl. Supercond.*, vol. 3, no. 1, pp. 1045–1048, 1993.
[167] K. Sato, "3 - Bismuth-based oxide (BSCCO) high-temperature superconducting wires for power grid applications: Properties and fabrication," in *Supercond. Power Grid* (C. Rey, ed.), Woodhead Publishing Series in Energy, pp. 75–95, Woodhead Publishing, 2015.
[168] S. R. Foltyn, L. Civale, J. L. MacManus-Driscoll, Q. X. Jia, B. Mai-

orov, H. Wang, and M. Maley, "Materials science challenges for high-temperature superconducting wire," *Nat. Mater.*, vol. 6, no. 9, pp. 631–642, 2007.
[169] R. Shafaie and M. Kalantar, "Design of a 10-MW-Class Wind Turbine HTS Synchronous Generator With Optimized Field Winding," *IEEE Trans. Appl. Supercond.*, vol. 23, no. 4, p. 5202307, 2013.
[170] F. E. Luborsky, R. F. Kwasnick, K. Borst, M. F. Garbauskas, E. L. Hall, and M. J. Curran, "Reproducible sputtering and properties of Y-Ba-Cu-O films of various thicknesses," *J. Appl. Phys.*, vol. 64, no. 11, pp. 6388–6391, 1988.
[171] S. R. Foltyn, H. Wang, L. Civale, Q. X. Jia, P. N. Arendt, B. Maiorov, Y. Li, M. P. Maley, and J. L. l. MacManus-Driscoll, "Overcoming the barrier to 1000 A/ cm width superconducting coatings," *Appl. Phys. Lett.*, vol. 87, no. 16, p. 162505, 2005.
[172] S. R. Foltyn, H. Wang, L. Civale, B. Maiorov, and Q. X. Jia, "The role of interfacial defects in enhancing the critical current density of YBa2Cu3O7- δ coatings," *Supercond. Sci. Technol.*, vol. 22, no. 12, p. 125002, 2009.
[173] H. Wang, S. R. Foltyn, L. Civale, B. Maiorov, and Q. X. Jia, "Attenuation of interfacial pinning enhancement in YBCO using a PrBCO buffer layer," *Phys. C Supercond.*, vol. 469, no. 23, pp. 2033–2036, 2009.
[174] S. I. Kim, A. Gurevich, X. Song, X. Li, W. Zhang, T. Kodenkandath, M. W. Rupich, T. G. Holesinger, and D. C. Larbalestier, "Mechanisms of weak thickness dependence of the critical current density in strong-pinning ex situ metal–organic-deposition-route YBa2Cu3O7- x coated conductors," *Supercond. Sci. Technol.*, vol. 19, no. 9, p. 968, 2006.
[175] Ö. Polat, J. W. Sinclair, Y. L. Zuev, J. R. Thompson, D. K. Christen, S. W. Cook, D. Kumar, Y. Chen, and V. Selvamanickam, "Thickness dependence of magnetic relaxation and *E-J* characteristics in superconducting (Gd-Y)-Ba-Cu-O films with strong vortex pinning," *Phys. Rev. B*, vol. 84, no. 2, p. 24519, 2011.
[176] T. Aytug, M. Paranthaman, A. A. Gapud, S. Kang, H. M. Christen, K. J. Leonard, P. M. Martin, J. R. Thompson, D. K. Christen, R. Meng, and Others, "Enhancement of flux pinning and critical currents in YBa 2 Cu 3 O 7- δ films by nanoscale iridium pretreatment of substrate surfaces," *J. Appl. Phys.*, vol. 98, no. 11, p. 114309, 2005.
[177] M. W. Rupich, D. T. Verebelyi, W. Zhang, T. Kodenkandath, and X. Li, "Metalorganic deposition of YBCO films for second-generation high-temperature superconductor wires," *MRS Bull.*, vol. 29, no. 8, pp. 572–578, 2004.
[178] T. Aytug, M. Paranthaman, K. J. Leonard, S. Kang, P. M. Martin, L. Heatherly, A. Goyal, A. O. Ijaduola, J. R. Thompson, D. K. Christen, R. Meng, I. Rusakova, and C. W. Chu, "Analysis of flux pinning in $YBa_2Cu_3O_{7-\delta}$ films by nanoparticle-modified substrate surfaces," *Phys. Rev. B*, vol. 74, no. 18, p. 184505, 2006.
[179] K. Matsumoto, T. Horide, A. Ichinose, S. Horii, Y. Yoshida, and M. Mukaida, "Critical current control in YBa2Cu3O7-δ films using artificial pinning centers," *Jpn. J. Appl. Phys.*, vol. 44, no. 1L, p. L246, 2005.
[180] A. Goyal, S. Kang, K. J. Leonard, P. M. Martin, A. A. Gapud, M. Varela, M. Paranthaman, A. O. Ijaduola, E. D. Specht, J. R. Thompson, and Others, "Irradiation-free, columnar defects comprised of self-assembled nanodots and nanorods resulting in strongly enhanced flux-pinning in YBa2Cu3O7- δ films," *Supercond. Sci. Technol.*, vol. 18,

no. 11, p. 1533, 2005.
[181] T. Horide, T. Kawamura, K. Matsumoto, A. Ichinose, M. Yoshizumi, T. Izumi, and Y. Shiohara, "Jc improvement by double artificial pinning centers of BaSnO3 nanorods and Y2O3 nanoparticles in YBa2Cu3O7 coated conductors," *Supercond. Sci. Technol.*, vol. 26, no. 7, p. 75019, 2013.
[182] S. G. Doettinger, R. P. Huebener, R. Gerdemann, A. Kühle, S. Anders, T. G. Träuble, and J. C. Villégier, "Electronic Instability at High Flux-Flow Velocities in High-T_c Superconducting Films," *Phys. Rev. Lett.*, vol. 73, no. 12, pp. 1691–1694, 1994.
[183] Z. L. Xiao and P. Ziemann, "Vortex dynamics in $YBa_2Cu_3O_{7-\delta}$ superconducting films: Experimental evidence for an instability in the vortex system at high current densities," *Phys. Rev. B*, vol. 53, no. 22, pp. 15265–15271, 1996.
[184] A. I. Larkin and Y. U. N. Ovchinnikov, "Nonlinear conductivity of superconductors in the mixed state," *Sov. Phys. JETP*, vol. 41, no. 5, pp. 960–965, 1975.
[185] T. L. Peterson, I. Maartense, and R. R. Biggers, "Self-heating hotspot effects in HTS thin films," *IEEE Trans. Appl. Supercond.*, vol. 5, no. 2, pp. 1436–1439, 1995.
[186] W. J. Skocpol, M. R. Beasley, and M. Tinkham, "Self-heating hotspots in superconducting thin-film microbridges," *J. Appl. Phys.*, vol. 45, no. 9, pp. 4054–4066, 1974.
[187] G. Jakob, P. V.-d. Haan, M. Wagner, Z. Xiao, and H. Adrian, "Flux-flow instability and heating effects in Bi2Sr2CaCu2O8 and YBa2Cu3O7 thin films," *Phys. B Condens. Matter*, vol. 284-288, pp. 897–898, 2000.
[188] J. Maza, G. Ferro, J. A. Veira, and F. Vidal, "Transition to the normal state induced by high current densities in $YBa_2Cu3O_{7-\delta}$ thin films: a thermal runaway account," *Phys. Rev. B*, vol. 78, no. 9, p. 94512, 2008.
[189] J. Maza, G. Ferro, M. R. Osorio, J. A. Veira, and F. Vidal, "Analytical approach to the thermal instability of superconducting films under high current densities," *Phys. Rev. B*, vol. 84, no. 21, p. 214530, 2011.
[190] T. Kiss, M. Inoue, K. Hasegawa, K. Ogata, V. S. Vysotsky, Y. Ilyin, M. Takeo, H. Okamoto, and E. Irie, "Quench characteristics in HTSC devices," *IEEE Trans. Appl. Supercond.*, vol. 9, no. 2, pp. 1073–1076, 1999.
[191] J. M. Doval, A. Ramos-Álvarez, D. Sóñora, J. C. Verde, M. Ruibal, J. A. Veira, J. Maza, and F. Vidal, "Transition to the Normal State Induced by High Current Densities in High-Tc Superconductor Microbridges Under Applied Magnetic Fields," *IEEE Trans. Appl. Supercond.*, vol. 26, no. 3, pp. 1–5, 2016.
[192] A. Leo, P. Marra, G. Grimaldi, R. Citro, S. Kawale, E. Bellingeri, C. Ferdeghini, S. Pace, and A. Nigro, "Competition between intrinsic and extrinsic effects in the quenching of the superconducting state in Fe(Se,Te) thin films," *Phys. Rev. B*, vol. 93, no. 5, p. 54503, 2016.
[193] G. Grimaldi, A. Leo, A. Nigro, S. Pace, V. Braccini, E. Bellingeri, and C. Ferdeghini, "Angular dependence of vortex instability in a layered superconductor: the case study of Fe(Se,Te) material," *Sci. Rep.*, vol. 8, no. 1, p. 4150, 2018.
[194] V. Rouco, D. Massarotti, D. Stornaiuolo, G. P. Papari, X. Obradors, T. Puig, F. Tafuri, and A. Palau, "Vortex Lattice Instabilities in YBa2Cu3O7-x Nanowires," *Materials (Basel).*, vol. 11, no. 2, 2018.
[195] S. Balevičius, A. Bičūnas, R. Butkute, V. Jasutis, V. Lisauskas, A. Vailionis, A. Flodström, and B. Vengalis, "Ultrafast Electrical Supercon-

ducting to Normal States Switching in Y-Ba-Cu-O and Bi-Sr-Ca-Cu-O Microstrips," *MRS Proc.*, vol. 275, p. 589, 1992.
[196] S. Balevicius, A. Biciunas, R. Butkute, V. Lisauskas, B. Vengalis, A. Brazdeikis, and A. Flodstrom, "Flux flow during high power nanosecond SN switching in thin high-T_c films," *IEEE Trans. Magn.*, vol. 29, no. 6, pp. 3589–3591, 1993.
[197] S. Balevicius, F. Anisimovas, R. Butkute, V. Jasutis, A. Jukna, B. Vengalis, A. Cenys, O. Kiprijanovic, and V. Lisauskas, "Fast S-N switching in wide tapes of thin high-Tc superconducting films," *Liet. Fiz. Z.*, vol. 36, no. 3, pp. 233–235, 1996.
[198] S. Suzuki, H. Shimakage, A. Kawakami, A. Saito, and M. Takeda, "Characteristics of MOD Bi-2212 thin films on r-cut sapphire with CeO 2 buffer layer," *IEEE Trans. Appl. Supercond.*, vol. 23, no. 3, pp. 3–6, 2013.
[199] Z. Xie, W. Xue, H. Chen, and Y. Huang, "Mechanical and thermal properties of 99% and 92% alumina at cryogenic temperatures," *Ceram. Int.*, vol. 37, no. 7, pp. 2165–2168, 2011.
[200] Y. Orbach, M. Oren, A. Golan, and M. Einat, "Reluctance launcher coil-gun simulations and experiment," *IEEE Trans. Plasma Sci.*, vol. 47, no. 2, pp. 1358–1363, 2018.
[201] R. J. Kaye, E. C. Cnare, M. Cowan, B. W. Duggin, R. J. Lipinski, B. M. Marder, G. M. Douglas, and K. J. Shimp, "Design and performance of Sandia's contactless coilgun for 50 mm projectiles," *IEEE Trans. Magn.*, vol. 29, no. 1, pp. 680–685, 1993.
[202] M. S. Aubuchon, T. R. Lockner, B. N. Turman, G. Root, L. Basak, R. Gaigler, B. Skurdal, and M. Floyd, "Results from sandia national laboratories/lockheed martin electromagnetic missile launcher (EMML)," in *2005 IEEE Pulsed Power Conf.*, pp. 75–78, IEEE, 2005.
[203] K. Sterzelmeier, V. Brommer, and L. Sinniger, "Active armor protection-conception and design of steerable launcher systems fed by modular pulsed-power supply units," *IEEE Trans. Magn.*, vol. 37, no. 1, pp. 238–241, 2001.
[204] E. Spahn, K. Sterzelmeier, C. Gauthier-Blum, V. Brommer, L. Sinniger, and B. Grasser, "50-kJ Ultracompact Pulsed-Power Supply Unit for Active Protection Launcher Systems," *IEEE Trans. Magn.*, vol. 45, no. 1, pp. 462–466, 2009.
[205] T. Zhang, W. Dong, W. Guo, B. Cao, Z. Su, X. Sun, M. Li, and W. Fan, "Spatial movement analysis on the intercepting projectile in the active electromagnetic armor," *IEEE Trans. Plasma Sci.*, vol. 45, no. 7, pp. 1302–1307, 2017.
[206] T. Zhang, W. Guo, F. Lin, Z. Su, H. Zhang, Y. Chen, M. Li, and X. Sun, "Design and testing of 15-stage synchronous induction coilgun," *IEEE Trans. Plasma Sci.*, vol. 41, no. 5, pp. 1089–1093, 2013.
[207] Z. Su, T. Zhang, W. Guo, J. Yue, H. Zhang, W. Fan, X. Sun, and K. Huang, "Investigation of armature capture effect on synchronous induction coilgun," *IEEE Trans. Plasma Sci.*, vol. 43, no. 5, pp. 1215–1219, 2015.
[208] B. Marder, "A coilgun design primer," *IEEE Trans. Magn.*, vol. 29, no. 1, pp. 701–705, 1993.
[209] I. R. Shokair, M. Cowan, R. J. Kaye, and B. M. Marder, "Performance of an induction coil launcher," *IEEE Trans. Magn.*, vol. 31, no. 1, pp. 510–515, 1995.
[210] P. J. Costa Branco, R. Almeida, and J. A. Dente, "On Using Meissner Effect to Conceive a New Linear Electromagnetic Launcher by Zero-Field-Cooling YBCO Bulk Superconductors," *IEEE Trans. Ind. Electron.*, vol. 61, no. 11, pp. 5894–5902, 2014.

[211] CAN, "SUPERCONDUCTING CURRENT LEADS datasheetv2." https://www.can-superconductors.com/uploads/2/1/2/9/21298520/csl_datasheetv2.pdf, jul 2015.

[212] J. Novickij, S. Balevičius, N. Žurauskienė, R. Kačianauskas, V. Stankevič, Č. Šimkevičius, S. Keršulis, and S. Bartkevičius, "Vilnius high magnetic field centre facilities," *J. Low Temp. Phys.*, vol. 159, no. 1-2, pp. 406–409, 2010.

[213] N. Žurauskiene, S. Balevičius, D. Pavilonis, V. Stankevič, V. Plaušinaitiene, S. Zherlitsyn, T. Herrmannsdörfer, J. M. Law, J. Wosnitza, N. Žurauskienė, S. Balevičius, D. Pavilonis, V. Stankevič, V. Plaušinaitienė, S. Zherlitsyn, T. Herrmannsdörfer, J. M. Law, and J. Wosnitza, "Magnetoresistance and resistance relaxation of nanostructured La-Ca-MnO films in pulsed magnetic fields," *IEEE Trans. Magn.*, vol. 50, no. 11, pp. 1–4, 2014.

[214] Y. S. Cha and T. R. Askew, "Transient response of a high-temperature superconductor tube to pulsed magnetic fields," *Phys. C Supercond.*, vol. 302, no. 1, pp. 57–66, 1998.

[215] Q. L. Peng, S. M. McMurry, and J. M. D. Coey, "Axial magnetic field produced by axially and radially magnetized permanent rings," *J. Magn. Magn. Mater.*, vol. 268, no. 1-2, pp. 165–169, 2004.

[216] J. Zou, M. D. Ainslie, H. Fujishiro, A. G. Bhagurkar, T. Naito, N. Hari Babu, J.-F. F. Fagnard, P. Vanderbemden, A. Yamamoto, N. H. Babu, J.-F. F. Fagnard, P. Vanderbemden, and A. Yamamoto, "Numerical modelling and comparison of MgB2 bulks fabricated by HIP and infiltration growth," *Supercond. Sci. Technol.*, vol. 28, no. 7, p. 75009, 2015.

[217] K. Zmorayova, V. Antal, M. Radusovska, S. Piovarci, D. Volochova, and P. Diko, "Microstructure and Properties of Y-123/Y-211 Bulk Superconductors with BaCeO3 and BaO2 Addition," *Acta Phys. Pol. A*, vol. 126, no. 1, pp. 366–367, 2014.

[218] V. Plechacek and J. Hejtmanek, "Properties of superconducting Bi-2223 tubular current leads," *Phys. C Supercond. its Appl.*, vol. 282, pp. 2577–2578, 1997.

[219] A. Diaz, L. Mechin, P. Berghuis, and J. E. Evetts, "Evidence for vortex pinning by dislocations in $YBa_2Cu_3O_{7-\delta}$low-angle grain boundaries," *Phys. Rev. Lett.*, vol. 80, no. 17, p. 3855, 1998.

[220] S. Kambe, A. D. Huxley, P. Rodière, and J. Flouquet, "Low field scaling of the flux–flow resistivity in the unconventional superconductor UPt3," *Phys. Rev. Lett.*, vol. 83, no. 9, pp. 1842–1845, 1999.

[221] Z. Xiao, E. Andrei, and P. Ziemann, "Coexistence of the hot-spot effect and flux-flow instability in high superconducting films," *Phys. Rev. B - Condens. Matter Mater. Phys.*, vol. 58, no. 17, pp. 11185–11188, 1998.

[222] Can Superconductors s.r.o., "Superconducting YBCO Levitation Bulk," 2018.

[223] R. Lukose, V. Plausinaitiene, M. Vagner, N. Zurauskiene, S. Kersulis, V. Kubilius, K. Motiejuitis, B. Knasiene, V. Stankevic, Z. Saltyte, M. Skapas, A. Selskis, and E. Naujalis, "Relation between thickness, crystallite size and magnetoresistance of nanostructured La 1- x Sr x Mn y O 3±δ films for magnetic field sensors," *Beilstein J. Nanotechnol.*, vol. 10, pp. 256–261, jan 2019.

[224] N. Žurauskienė, V. Stankevič, S. Keršulis, J. Klimantavičius, Č. Šimkevičius, V. Plaušinaitienė, M. Vagner, S. Balevičius, N. Žurauskienė, V. Stankevič, S. Keršulis, J. Klimantavičius, Č. Šimkevičius, V. Plaušinaitienė, M. Vagner, and S. Balevičius, "Increase of operating tempe-

rature of magnetic field sensors based on La–Sr–Mn–O films with Mn excess," *IEEE Trans. Plasma Sci.*, vol. 47, no. 10, pp. 4530–4535, 2019.
[225] V. Vertelis, S. Balevicius, V. Stankevic, N. Zurauskiene, and M. Schneider, "Pulsed magnetic flux penetration dynamics inside a thin-walled superconducting tube," *J. Appl. Phys.*, vol. 127, p. 113901, mar 2020.
[226] S. Balevicius, N. Zurauskiene, V. Stankevic, S. Kersulis, A. Baskys, V. Bleizgys, J. Dilys, A. Lucinskis, A. Tyshko, and S. Brazil, "Hand-Held Magnetic Field Meter Based on Colossal Magnetoresistance-B-Scalar Sensor," *IEEE Trans. Instrum. Meas.*, vol. 69, pp. 2808–2816, jun 2020.
[227] H. Yamasaki and Y. Mawatari, "Current-voltage characteristics and flux creep in melt-textured YBa2Cu3O7-δ," *Supercond. Sci. Technol.*, vol. 13, no. 2, pp. 202–208, 2000.
[228] V. Plechacek, M. Jirsa, M. Rames, and M. Muralidhar, "Batch Production of YBCO Disks for Levitation Applications," *Phys. Procedia*, vol. 36, pp. 538–543, 2012.

APPENDIX A: LUMPED PARAMETER EQUATION

To arrive at the lumped parameter equation (2.2.2), we start by integrating eq. (1.3) over the cross-section of the the tube:

$$\iint_{\Omega} \nabla \times \mathbf{E} \cdot d\mathbf{S} = \iint_{\Omega} -\frac{\partial \mathbf{B}}{\partial t} \cdot d\mathbf{S}. \tag{A.1}$$

Applying Stoke's theorem and separating the magnetic field the into the induced and the external components we arrive at:

$$\oint \mathbf{E} \cdot d\mathbf{l} = -\frac{\partial \Phi_s}{\partial t} - \frac{\partial \Phi_a}{\partial t}. \tag{A.2}$$

Using the definition of inductance and evaluating the integral we get:

$$2\pi RE = -L\frac{dI}{dt} - \frac{\partial \Phi_a}{\partial t}. \tag{A.3}$$

We expect a uniform current distribution along the length of the tube, so we assume that the tube is comprised out of $n = l_s/d$ ring elements that carry identical current. Under this assumption, current in one ring is $I = d^2 j$. The inductance L can be estimated under the same assumption using well known equations for solenoids. Φ_a is n times larger than flux through one ring. Using power-law eq. (1.17) for E we arrive at the lumped parameter equation:

$$L\frac{dI}{dt} + \frac{2\pi R \cdot E_{\mathrm{c}}}{(d^2 j_{\mathrm{c}}(B))^n}|I|^{n-1}I = -\frac{l_{\mathrm{s}}}{d}\pi R^2 \frac{dB_{\mathrm{a}}(t)}{dt}.$$

1st publication / 1 publikacija

Magnetic Field Expulsion From a Conducting Projectile in a Pulsed Serial Augmented Railgun

V. Vertelis, G. Vincent, M. Schneider, S. Balevičius, V. Stankevič and N. Žurauskiene

IEEE Transactions on Plasma Science, vol. **48**, no. 3, pp. 727-732 (2020)

DOI: 10.1109/TPS.2020.2970764

Magnetic Field Expulsion From a Conducting Projectile in a Pulsed Serial Augmented Railgun

Vilius Vertelis, Gregory Vincent, Markus Schneider, Saulius Balevičius, Voitech Stankevič, and Nerija Žurauskiene

***Abstract*— The bore of a railgun is a harsh environment with high transient magnetic fields, temperature gradients, and forces. Most common payloads in railgun launch are made from conductive materials. In this article, we consider the effects of the transient magnetic field on a conducting payload during an electromagnetic launch by a serial augmented hexagonal railgun. The magnetic field distribution in the proximity of a solid aluminum payload was investigated by numerical calculations and experimentally by using a CMR-B-scalar sensor array.**

***Index Terms*— Augmented railgun, magnetic field diffusion, pulsed magnetic field.**

I. Introduction

ELECTROMAGNETIC railgun is a promising device for military applications and space launching [1], [2]. During the past decade, the augmented electromagnetic railgun was an object of intensive research and development [3]. An augmented railgun is an arrangement where an external magnetic field is used in addition to the magnetic field generated by the driving rails themselves. This additional magnetic field results in a higher propelling force on the projectile for the same armature current. It allows for operating at a lower current, meaning lower Joule heating and the ability to use a wider selection of power supplies. The augmentation can be realized in several ways, e.g., permanent magnets [4], persistent mode superconducting electromagnets [5], or pulsed electromagnets [6]–[9].

Large efforts were directed at the studies and design of various types of multiturn augmented railguns [10]–[13]. These devices differ from one another by their magnetic field configuration, which affects the efficiency of the augmentation. It also significantly differs from the conventional one-turn railgun by having the magnetic field in front of the armature as well. This magnetic field can significantly affect the launch payloads, which range from simple metal rods [14], [15] to complex smart projectiles [16] or even nanosatellites [17]. In all of these cases, the launch package contains conductive parts, which in a transient magnetic field will, for a short time, expel a portion of the field from its interior due to an induced current, thus changing the magnetic field configuration around and inside the conducting payload.

Recently, a new design of a multirail hexagonal railgun with hexagonal rail arrangement [18], [19] was introduced. The main advantage of this device is its versatility. The setup can be arranged in a segmented, multishot, or augmented configuration, the latter being used for the purpose of this article. In this article, we present the magnetic effects in close proximity to a cylindrical conductive payload placed inside an augmented mode hexagonal railgun. Time-dependent magnetic field distribution was calculated using the finite-element method (COMSOL Multiphysics AC/DC module). These calculations were compared with experimental measurements performed using CMR-B-scalar sensor array [20], [21].

II. Theory

To calculate the dynamic magnetic field, distribution around a conductor exposed to a pulsed magnetic field diffusion can be employed. Dynamic magnetic fields enter a conductor via a diffusive process where eddy currents induced by a temporal change of the magnetic field cause the generation of a field opposing the change in the applied field inside the conductor (Lentz's rule). Due to the superposition of these fields, the net field is now reduced inside and near the sides normal to the field lines and increased around the sides of a conductor. The induced eddy currents decay with a specific time constant determined by the conductivity of the metal. As the current decays, the magnetic field penetrates further into a conductor until a stationary configuration is reached. Now, if the external field begins to decay, the process reverses and the induced currents try to maintain the flux penetrating the sample.

To describe the problem mathematically, we need a set of Maxwell's equations

$$\nabla \times E = -\frac{\partial B}{\partial t} \tag{1}$$

$$\nabla \times B = \mu J. \tag{2}$$

Manuscript received September 17, 2019; revised January 15, 2020; accepted January 27, 2020. Date of publication February 13, 2020; date of current version March 10, 2020. The review of this article was arranged by Senior Editor F. Hegeler. *(Corresponding author: Vilius Vertelis.)*

Vilius Vertelis is with the French-German Research Institute of Saint-Louis (ISL), FR-68301 Saint-Louis, France, and also with the Center for Physical Sciences and Technology, LT-10257 Vilnius, Lithuania (e-mail: viliusvertelis@gmail.com).

Gregory Vincent and Markus Schneider are with the French-German Research Institute of Saint-Louis (ISL), FR-68301 Saint-Louis, France.

Saulius Balevičius is with the Center for Physical Sciences and Technology, LT-10257 Vilnius, Lithuania.

Voitech Stankevič and Nerija Žurauskiene are with the Center for Physical Sciences and Technology, LT-10257 Vilnius, Lithuania, and also with the Department of Electrical Engineering, Faculty of Electronics, Vilnius Gediminas Technical University, LT-10223 Vilnius, Lithuania.

Color versions of one or more of the figures in this article are available online at http://ieeexplore.ieee.org.

Digital Object Identifier 10.1109/TPS.2020.2970764

For low power railguns, where Joule's heating can be neglected, the conductor can be considered linear and isotropic, and then using Ohm's law $J = \sigma E$ in (1) and $\nabla \cdot B = 0$, we arrive at magnetic diffusion equation

$$\frac{1}{\mu\sigma}\nabla^2 B = \frac{\partial B}{\partial t} \tag{3}$$

where μ and σ are magnetic permittivity and electric conductivity, respectively. This equation describes how magnetic flux density behaves and changes in time inside a conductor. The quantity $(\mu\sigma)^{-1}$ is called the magnetic diffusion coefficient.

Conductors moving in a magnetic field generate an electromotive force. For our calculations, we will consider the payload to be electrically isolated from completing a circuit, so that only the screening current is flowing inside the payload. During the operation of a pulsed augmented railgun, the external magnetic field is dynamic, hence the boundary condition for (3) is time-dependent. Although analytical solutions might exist for some geometries and field pulse shapes, numerical methods provide more flexibility.

If magnetic shielding is the main concern, the solution to (3) for a geometry of interest (e.g., a hollow cylinder) gives full temporal and spatial magnetic field distribution. With this, it is possible to evaluate the shielding performance of the design, i.e., penetration depth and the magnetic transients.

We are generally interested in the field distribution around the conductor during the magnetic pulse, but so far we have only got the internal part. To get the full induced field, we need to insert the solution of (3) into (2) to get the current density distribution. The next step is to apply Biot–Savart law

$$B_{\text{ind}} = \iiint_V \frac{J \times R}{|R|^3} dV \tag{4}$$

where R is a vector from the position of integration kernel to the point of interest ($R = r - r'$) and V is the volume of the sample. Combining the B_{ind} with the external field, we arrive at the magnetic field distribution around a conductor in a pulsed magnetic field environment at a given moment.

In our calculations, a homogeneous augmentation field pulse with only a z component $B_z(t)$ was assumed. An experimentally measured magnetic field pulse was used as a boundary condition for (3). The solution for (3) is a function of coordinates and time. Since the field only has z component, then the induced current density will be equal to

$$J(t, x, y, x) = \frac{1}{\mu}\left\langle \frac{d}{dy}B_z(t, x, y, z), -\frac{d}{dx}B_z(t, x, y, z), 0 \right\rangle. \tag{5}$$

We put this expression for current density into (4) which we integrated numerically and got the field distribution

$$B(t, x, y, z) = \langle 0, 0, B_z(t)\rangle + \iiint \frac{1}{|R|^3}\langle J_y R_z, -J_x R_z, J_x R_y - J_y R_x\rangle dx' dy' dz' \tag{6}$$

where $R = \langle x - x', y - y', z - z'\rangle$ and the components of $\langle J_x, J_y, J_z\rangle$ are functions of the integration coordinates x', y', z'. The integral does not need to be carried out strictly over the volume of the payload. Integrating over a box around it is enough, because the amplitude current is zero outside the payload and does not contribute to the value of the integral.

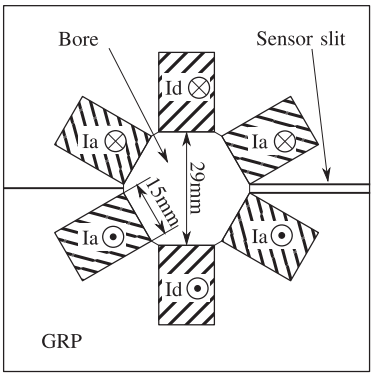

Fig. 1. Cross-sectional view of SR\3-60 railgun. I_d denotes rails with driving current used to supply the armature. I_a marks augmentation rails.

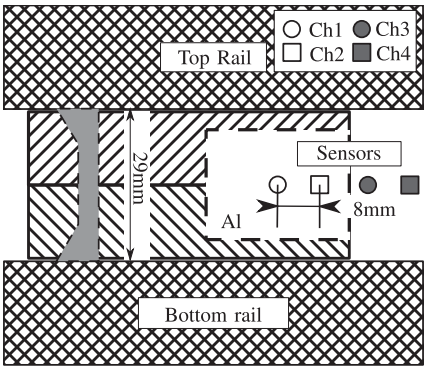

Fig. 2. Side view of the SR\3-60 and sensor positioning. Side rails are not shown.

III. Experimental Setup

The SR\3-60 is a multirail electromagnetic launch platform that can be configured in multiple arrangements. This railgun has 3 pairs of 2 m long rails offset by 60°, forming a hexagonal bore with 29 mm face to face. For our experiments, the SR\3-60 was operated in a serial augmented configuration. The rails were short-circuited at the breach and the muzzle in such a way that the side rails were used for field augmentation and the vertical pair for driving the projectile. All the rails were connected in series because of concerns about magnetic coupling and the lack of protection against it. Fig. 1 shows the cross section of the SR\3-60 and current directions (looking from the breach). Static experiments were performed with the driving rails disconnected from the circuit.

For our launch package, we 3-D printed a hexagonal plastic housing (28 mm face-to-face) for a copper brush type armature and an aluminum payload. The total length of the package was 6 cm. The payload was a cylinder with a radius of a 12 mm and a height of 24 mm. The cross section of the launch package in between the drive rails can be seen in Fig. 2. The payload was placed inside a 3-D printed sabot so that it would be

electrically isolated from the rails and from the armature. The distance between the brush and the payload was 19 mm. The total mass of the launch package was 57 g.

Although it would be ideal to measure the magnetic field in the projectile's frame of reference during launch, it is difficult to achieve because the sensors would have to travel with the projectile. Another way of measuring the complete magnetic field dynamic would require a large number of sensors along the bore. For simplicity, to measure the magnetic field distribution around the payload, four CMR sensors were placed as shown in Fig. 2. Four slits were milled in the glass-reinforced plastic (GRP) housing in between top and bottom side rails with the first slit being 88 cm from the breach and others every 8 mm toward the muzzle. When inserted, the measuring volumes of the sensors were 18 mm from the bore's center. The relatively small active volume of the sensors (0.5 mm × 50 μm × 400 nm) provides a localized measurement in comparison with the scale of the experiment.

Sensors based on colossal magnetoresistance record the absolute value of the magnetic field instead of its projection to the active plane. The anisotropy of sensitivity is negligible for fields higher than a few hundred mT making them ideal to measure fields where the field direction is changing during the experiment.

For static shots (no acceleration), the launch package was placed such that the mid-point of the aluminum cylinder would coincide with the Ch1 sensor. A series of dynamic shots (with launch package acceleration) was performed with the distance between the center of the payload and the first sensor of 0, 1:2, 6:2, and 11:2 cm, respectively.

IV. Results and Discussion

A. Experimental

The results of static experiments are presented in Fig. 3. The experiments were repeated twice for every configuration and showed perfect reproducibility. The magnetic field pulse generated by the augmentation coils alone (no payload inside the bore and the driving rails disconnected form the circuit) is depicted as a dashed line for reference. All three sensors measured identical pulses when no launch package was present.

When performing the same measurement with the aluminum payload centered around the Ch1 sensor (with driving rails still disconnected), as expected from considerations in Section II, close to the center of the projectile the magnetic flux density was reduced in comparison with the reference pulse. The difference was 300 mT (8%) at a distance of 6 mm from the projectile's surface at peak current measured by Ch1. Ch1 and Ch2 measurements are close to each other while Ch3 is visibly higher. This difference from the reference measurement was caused by the generation of eddy currents inside the payload, which in turn generates an additional magnetic field of opposing direction. The difference diminished afterward and became unnoticeable at about 1 ms where the difference from the reference vanishes as well. At around 2 ms, measurements with the payload started to diverge from the reference by decaying slower as the induced currents try to maintain the already captured flux. It has to be noted that the measured

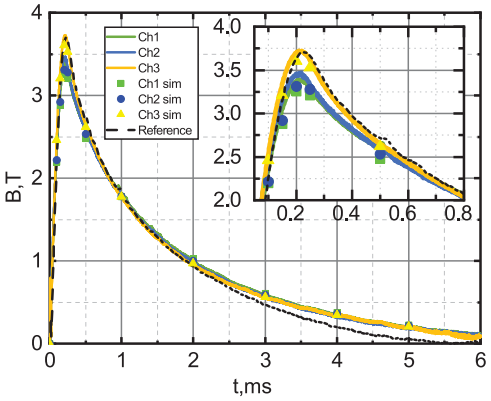

Fig. 3. Absolute value of magnetic flux density in the proximity of the static payload, reference measurement without the payload and a result of simulation based on method described in Section II.

current through the rails is slightly lower without than with the launch package (10% at 3 ms, 16% at 4 ms), possibly due to changes in system resistance from shot to shot. The measurements start to diverge around 1.5 ms.

The normalized curves of the measured current and magnetic field noticeably differ in shape, especially around the peak. This suggests that the current density distribution is not constant in time for this rise time. This is of no surprise and happens because of the skin effect. The tail part of the curves decays with the same rate, implying that the current distribution becomes constant though not necessarily uniform.

During the dynamic experiments, projectiles were accelerated to top speeds of about 110 m/s within 4 ms with peak acceleration of 72 km/s^2 at peak current. Fig. 4 shows the magnetic field measurements during launch with different projectile start positions from the sensors.

The position of the projectile remains relatively unchanged for about 0.5 ms so the initial peak can be interpreted as static. We see that the amplitude of the measurements again depends on the proximity to the payload. This decrease is visible up to 28 mm from the center of the payload. Measurements at greater distances reveal identical values except for the second peak. When the projectile is centered, we can see a slightly higher field in Ch1 right after the peak (0.5 ms–0.8 ms) current that could be caused by the payload trapping some flux.

The second bump seen at different times (offsetting the field equally for all of the sensors) is caused by the armature passing by the sensors. As the projectile moves, the current-carrying portion of the driving rails increases. The different time intervals and rise angles between evenly spaced sensors speak about acceleration and are more pronounced in closer distances where acceleration is the highest (within 5 cm). After passing the sensors, all three pairs of rails carry the same total current instead of two, and hence the increase in the field.

B. Modeling

In order to quantitatively analyze the experimental results, a numerical code was built following the steps described

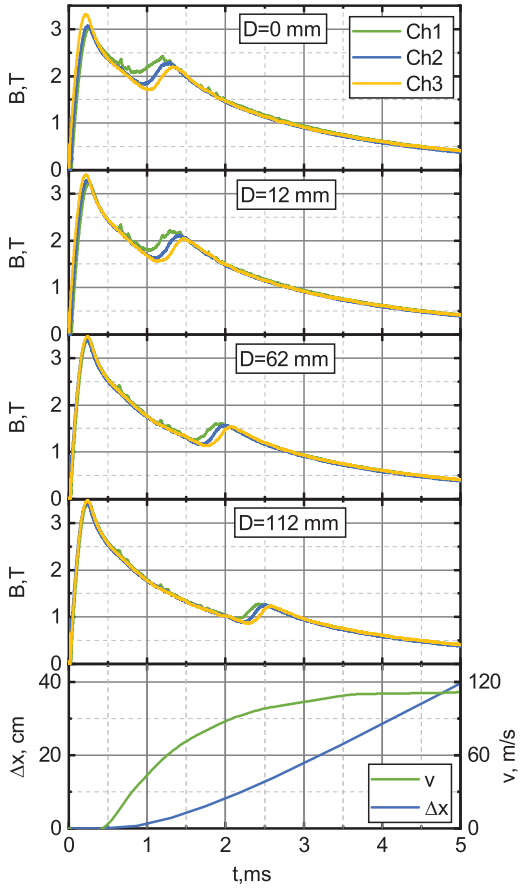

Fig. 4. Absolute value of magnetic flux density measured in dynamic experiments and the dynamics of the payload. D is the start position measured from the center of the payload to the Ch1 sensor.

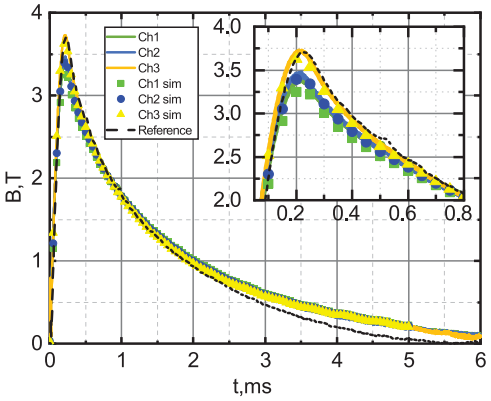

Fig. 5. Comparison between experimental results and an FEM simulation.

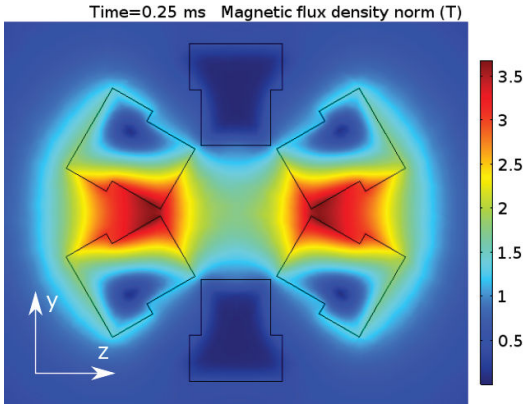

Fig. 6. Distribution of magnetic flux density when the railgun bore is empty.

in Section II. The model assumed a pulse of a spatially uniform magnetic field perpendicular to the axis the cylinder (parallel to the z-axis in the figures) being applied to a cylindrical payload with dimensions matching those of the physical one. The reference measurement was used as a time-dependent boundary condition on a surface of a cylindrical domain over which the diffusion equation was solved. Eddy currents were calculated by taking a curl of the solution to the diffusion equation, and the induced magnetic field was calculated with (4). For the total field value, we took the superposition between the applied and the induced fields.

The simulation results obtained from the model at sensor positions can be seen as points in Fig. 3. Simulation results show good agreement with the experimental measurements both in absolute value and in proportion between the sensors. The simulation slightly overestimates the effect of field reduction around the peak of the pulse (focused in the inset) but is quite accurate during the tail of the pulse. The cause of this could be the fact that the augmentation field in our experimental configuration is nonuniform. The uniform field simplification is more suitable for the cases where the augmentation rails are further from the payload. Our reference measurement was taken in an area of the highest field (in between the augmentation rails), meaning that the magnetic field around the sample was lower than that, hence would induce lower currents. The fact that the decaying part is accurate has to do with the fact that the eddy currents are deeper inside the payload when the magnetic field has diffused further into the sample, so that their distribution has a lower effect on the external field.

In order to account for the inhomogeneity of the field, a finite-element method (FEM) model was built. We modeled a time-dependent magnetic field response of a 10 cm long section of the rails with and without an aluminum payload at the center. The augmenting rails were supplied with a current pulse of uniform density and a shape of the reference magnetic field measurement (peak value of 121 kA,

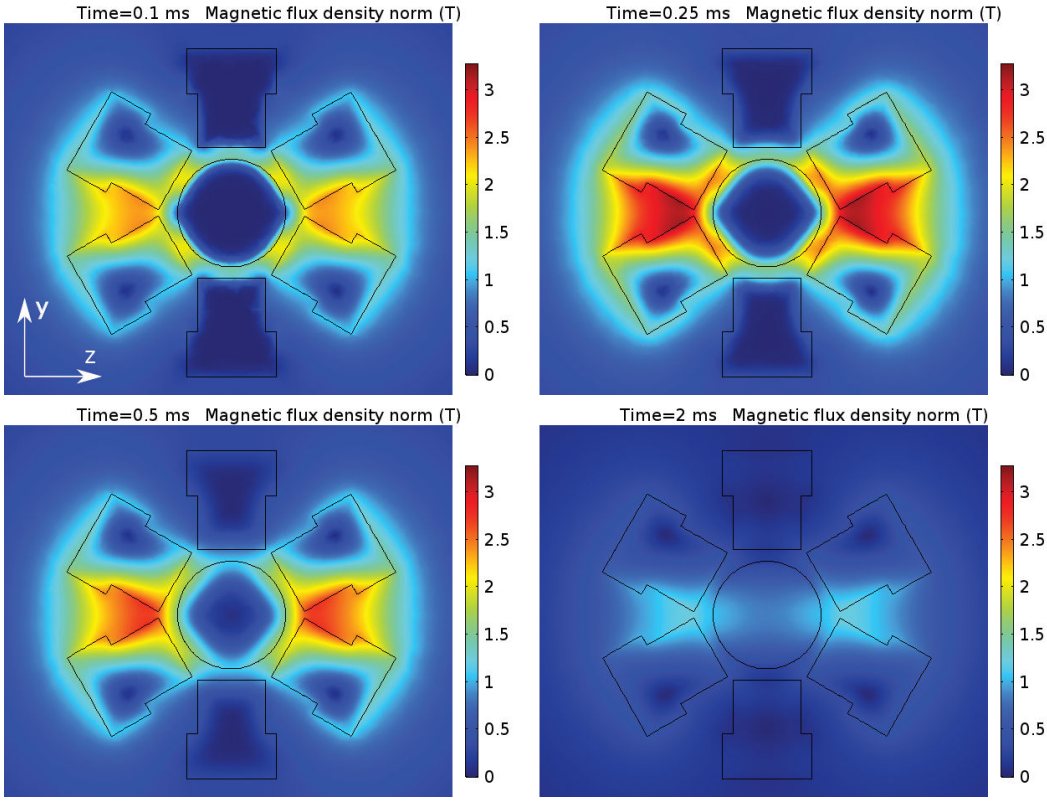

Fig. 7. Magnetic flux density distribution in a yz plane intersecting the center of the payload at different times of the magnetic field pulse.

experimentally measured −118 kA). We are aware that this is not true, but modeling the actual time-dependent current density distribution is outside of the scope of this article and would serve little purpose, since we are investigating the effects of the projectile.

The FEM simulation results corresponding to the field values at the sensor positions can be seen in Fig. 5 and are in good agreement with the experiment. Experimental measurements are, again, slightly higher than the values predicted by the simulation. We believe that this could be a consequence of a lack of precision while placing the sensors or the projectile as small variations in the distance have notable effects on field measurements in such close proximity.

The magnetic flux density distribution calculated with an FEM solver at peak current when the bore is empty can be seen in Fig. 6. The augmentation is providing close to 2 T in the middle of the bore where it would interact with the driving current and 3.7 T in between the augmentation rails. This result is close to the one experimentally measured. It can be seen that the driving rails, which in the static case do not carry the excitation current, are subject to the transient field and are expelling it.

The magnetic flux density distribution at different times with the payload present are shown in Fig. 7. Initially, the magnetic field is expelled from the interior of both the payload and the driving rails resulting in magnetic field redistribution around them. Magnetic flux density is reduced at the poles parallel to the z-axis and increased at ones parallel to the y-axis. Deviations decrease with time as the field penetrates deeper into the conductors. At around 2 ms, the field fully penetrates the sample. The reversal of the effect is present but very slight and could be better seen in Fig. 5.

Initially, only the thin surface sections of the payload and the rails support the magnetic field. With time, the magnetic field can be seen diffusing deeper into the conductors with different rates. The field penetrates the payload faster than the rail because the conductivity of aluminum is almost half that of copper. Magnetic permeabilities of the materials do not play a big role because they are effectively equal to that of free space.

These results give some insight into projectile design. Using less conductive metals like tungsten for projectiles would minimize the effect because of the faster diffusion. If shielding is the main concern, then more conductive materials are to

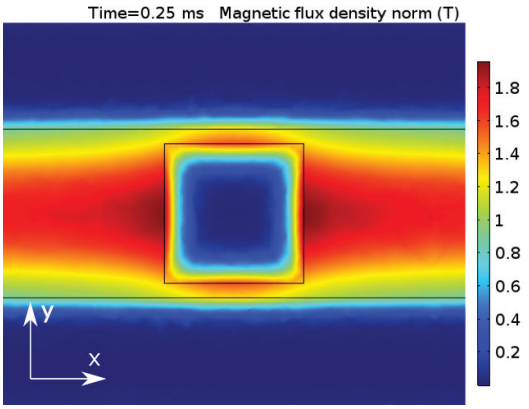

Fig. 8. Magnetic field distribution in xy plane showing field concentration around the conductive payload.

be used. The most dangerous part of the pulse for electronics is the fast rise because of the high induced electric field (1). Even if the field penetrates the shielding, the potential harm is reduced due to reduced amplitude and rise time. Areas to take more care about would not be the ones with the lower field, but rather the areas with the higher field. Fig. 8 shows the magnetic flux density distribution in the yx plane going through the center of the payload. The field is increased around the edge of the conductor as it is expelled from its volume and needs to go around. The area between the armature and the conductive payload would temporarily have reduced field due to opposing field directions between the one generated by the armature and redistributed augmentation field. This would lead to net attraction between the armature and the payload.

V. Conclusion

The investigations of the magnetic field dynamics inside the bore of a serial augmented hexagonal railgun have revealed that a conductive payload noticeably alters the field configuration. We have calculated and experimentally validated the transient magnetic field distribution around a conductive cylindrical payload. The magnitude of the magnetic field disturbance decays sharply with the distance from the surface of the conducting payload and is the highest during the abrupt change of magnetic field pulse. The effect of magnetic field expulsion should be taken into consideration when designing launch packages.

References

[1] S. Hundertmark and D. Lancelle, "A scenario for a future European shipboard railgun," *IEEE Trans. Plasma Sci.*, vol. 43, no. 5, pp. 1194–1197, May 2015.
[2] I. Mcnab, "Launch to space with an electromagnetic railgun," *IEEE Trans. Magn.*, vol. 39, no. 1, pp. 295–304, Jan. 2003.
[3] J. Gallant, "Parametric study of an augmented railgun," *IEEE Trans. Magn.*, vol. 39, no. 1, pp. 451–455, Jan. 2003.
[4] S. Katsuki *et al.*, "Augmented railgun using a permanent magnet," *Rev. Sci. Instrum.*, vol. 66, no. 8, pp. 4227–4232, Aug. 1995.
[5] S. Z. Liang, Y. T. Fang, and X. Y. Huang, "Dynamic simulation of a superconducting augmented linear propulsion system," in *Proc. IEEE Int. Conf. Appl. Supercond. Electromagn. Devices (ASEMD)*, Nov. 2015, pp. 175–176.
[6] R. Fuller, J. Kitzmiller, and M. Ingram, "Design and testing of a 0.60 caliber, augmented railgun," *IEEE Trans. Magn.*, vol. 27, no. 1, pp. 45–49, Jan. 1991.
[7] I. Mcnab, "The STAR railgun concept," *IEEE Trans. Magn.*, vol. 35, no. 1, pp. 432–436, Jan. 1999.
[8] J. Neri and J. Sung Kim, "Initial operation, modeling and optimization of a low-velocity augmented railgun," in *Proc. 14th IEEE Int. Pulsed Power Conf. Dig. Tech. Papers. (PPC)*, Jul. 2004, pp. 1103–1106.
[9] J. Gallant and P. Lehmann, "Experiments with brush projectiles in a parallel augmented railgun," *IEEE Trans. Magn.*, vol. 41, no. 1, pp. 188–193, Jan. 2005.
[10] T. Watt and M. Crawford, "Experimental results from a two-turn 40 mm railgun," in *Proc. 14th Symp. Electromagn. Launch Technol.*, Jun. 2008, pp. 1–6.
[11] A. Keshtkar, S. Mozaffari, and A. Keshtkar, "Effect of rail tapering on the inductance gradient versus armature position by 3D-FEM," *IEEE Trans. Plasma Sci.*, vol. 39, no. 1, pp. 71–74, Jan. 2011.
[12] Y. Zhang, J. Ruan, J. Liao, Y. Wang, Y. Zhang, and T. Huang, "Salvo performance analysis of triple-projectile railgun," *IEEE Trans. Plasma Sci.*, vol. 41, no. 5, pp. 1421–1425, May 2013.
[13] Z. Su *et al.*, "Design and simulation of a large muzzle kinetic energy railgun," *IEEE Trans. Plasma Sci.*, vol. 41, no. 5, pp. 1416–1420, May 2013.
[14] B. Reck, P. Lehmann, W. Wenning, and M. D. Vo, "Projectiles with rod-shaped payloads for the PEGASUS railgun," *IEEE Trans. Magn.*, vol. 43, no. 1, pp. 397–401, Jan. 2007.
[15] A. Noel, A. Challita, and D. Bauer, "A novel railgun launch package concept," *IEEE Trans. Magn.*, vol. 37, no. 1, pp. 97–100, Jan. 2001.
[16] S. Hundertmark and G. Vincent, "Investigating a radio data link to a railgun projectile—The active projectile," *IEEE Trans. Plasma Sci.*, vol. 39, no. 1, pp. 422–425, Aug. 2010.
[17] S. Hundertmark, "Applying railgun technology to small satellite launch," in *Proc. 5th Int. Conf. Recent Adv. Space Technol. (RAST)*, Jun. 2011, pp. 747–751.
[18] G. Vincent and S. Hundertmark, "Using the hexagonal segmented railgun in multishot mode with three projectiles," *IEEE Trans. Plasma Sci.*, vol. 41, no. 5, pp. 1431–1435, May 2013.
[19] G. Vincent and S. Hundertmark, "Using the sr\3-60 railgun in augmented mode," in *Proc. 17th Int. Symp. Electromagn. Launch Technol.*, Jul. 2014, pp. 1–4.
[20] T. Stankevic, M. Schneider, and S. Balevicius, "Magnetic diffusion inside the rails of an electromagnetic launcher: Experimental and numerical studies," *IEEE Trans. Plasma Sci.*, vol. 41, no. 10, pp. 2790–2795, Oct. 2013.
[21] O. Liebfried, M. Schneider, M. Loeffler, S. Balevičius, N. Žurauskienė, and V. Stankevič, "Measurement of the Magnetic Field Distribution in Railguns Using CMR-B-Scalar Sensors," *Acta Phys. Pol. A*, vol. 115, no. 6, pp. 1125–1127, Jun. 2009.

2nd publication / 2 publikacija

Pulsed magnetic flux penetration dynamics inside a thin-walled superconducting tube

V. Vertelis, S. Balevicius, V. Stankevic, N. Zurauskiene, and M. Schneider

J. Appl. Phys., vol. **127**, no. 11, p. 113901 (2020)

DOI: 10.1063/1.5145370

Journal of Applied Physics ARTICLE scitation.org/journal/jap

Pulsed magnetic flux penetration dynamics inside a thin-walled superconducting tube

Cite as: J. Appl. Phys. **127**, 113901 (2020); doi: 10.1063/1.5145370
Submitted: 17 January 2020 · Accepted: 28 February 2020 ·
Published Online: 16 March 2020

Vilius Vertelis,[1,2,a)] Saulius Balevicius,[2] Voitech Stankevic,[2,3] Nerija Zurauskiene,[2,3] and Markus Schneider[1]

AFFILIATIONS

[1]French-German Research Institute of Saint-Louis, 68300 Saint-Louis, France
[2]Center for Physical Sciences and Technology, 01108 Vilnius, Lithuania
[3]Faculty of Electronics, Vilnius Gediminas Technical University, 10223 Vilnius, Lithuania

[a)]**Author to whom correspondence should be addressed:** vilius.VERTELIS@isl.eu

ABSTRACT

In this work, we present an investigation of transient magnetic field behavior in thin-walled superconducting tubes. It has been determined that if the thickness of the tube wall is significantly less than Bean's penetration length, the non-linear magnetic field diffusion equation describing the field propagation process inside the tube can be replaced by a simplified lumped-parameter equation. This makes it possible to quickly calculate the current induced in the tube wall and the magnetic field penetrated in the tube cavity. In order to validate this theory, an experimental study of transient magnetic field penetration into a Pb-doped B-2223 ($Bi_{1.8}Pb_{0.26}Sr_2Ca_2Cu_3O_{10+x}$) tube was conducted. This was done at the temperature of liquid nitrogen using a search coil (B-dot) and a miniature colossal magnetoresistance (CMR)-B-scalar magnetic field sensor made from manganite films, which exhibit a CMR phenomenon. The experimental results were then compared with the datasheet of the superconducting tube manufacturer and the 2D axisymmetric finite element model. It was demonstrated that combining the measurements of the magnetic field outside and inside the tube with the lumped-parameter description allows one to obtain the following information: the screened and trapped magnetic field, the critical current density vs the magnetic field dependence, and the power law index of the superconducting tube material. This enables the development of a fast, non-destructive method for testing the quality of superconducting tubular current leads.

I. INTRODUCTION

Hollow superconducting cylinders are used in permanent magnets,[1–3] magnetic shields,[4–6] fault current limiters,[7–10] and superconducting high-energy particle accelerators.[11] For operating and testing these devices, it is very important to know how the pulsed magnetic field flux penetrates the cavity of the cylinder. Studies of this process within bulk type II superconductors (rings or thick wall hollow cylinders) exposed to pulsed magnetic fields have been carried out previously.[12–15]

However, thin-walled superconducting tubes or pipes are used for many other hollow cylinder applications. This thin-walled tube configuration helps reduce the high costs of superconducting material when it is used for magnetic shields or for "smart superconducting grids" such as those delivering both chemical fuel (liquid H_2) as the coolant and electricity via a superconductor.[16,17] Long pipes made from MgB_2 by hydro-extrusion[17] or by coating paint[18] have been proposed. Pipes coated with YBCO ($YBa_2Cu_3O_{7-x}$) were also envisioned using the metalorganic decomposition technique.[19] In such cases, it is important to have a non-destructive means with which to evaluate the intrinsic parameters of the superconducting material. Usually, the properties of interest are the maximal magnetic field (B_c) that can be screened by the superconductor (not to be mistaken with the thermodynamic critical field), the critical current density (j_c) vs the magnetic field (B) dependence, and the electric field (E) vsthe current (j) power law exponent (n).

In order to obtain these parameters, the experimental results need to be evaluated using an adequate theoretical model adapted to the experimental conditions. Such results were achieved quantitatively for various cylinder configurations by employing the method described in Ref. 20. This method was also applied for the systematic investigation of the magnetic field responses of tubes with different dimensions and different magnitudes of the applied field.[21] In Ref. 22, thin-walled superconducting hollow cylinders made from polycrystalline current were induced in the tube wall,

and the magnetic field was penetrated in the tube cavity. In order to validate this theory, an experimental study of transient magnetic field penetration into a Pb-doped B-2223 ($Bi_{1.8}Pb_{0.26}Sr_2Ca_2Cu_3O_{10+x}$) material was investigated, using different transient magnetic field sweep rates. The theoretical approach used in Refs. 20 and 21 was based on the calculation of the current distribution in the bulk of the superconducting material, which, however, is the result of discrete coupled superconducting circuits carrying different currents in different regions along the radial direction of the superconducting tube. Thus, for tubes with various configurations, it is necessary to choose specific discretization algorithms, which makes the calculation procedure dependent on the tube geometry. Fortunately, for a geometry-like thin-walled tube, this description can be simplified without losing the validity of the calculation procedure. Since the walls are thin, it is thus possible to assume that there is no spatial variation in the current density throughout the thickness of the wall. Joule heating can also be neglected due to the effective cooling of the superconductor material. Hence, measuring the magnetic field inside a thin-walled superconducting tube should provide more accurate information about its superconducting material properties than in the case of thick-walled tubes.

In this paper, we present an experimental study of the magnetic field dynamics inside a small diameter (5 mm outer), a thin-walled Bi-2223 tube, exposed to an axial pulsed magnetic field of several milliseconds duration, by using both an inductive (B-dot) and a novel miniature (10^{-2} mm^3 effective volume) resistive B-scalar sensor based on a colossal magnetoresistance phenomenon (CMR). We propose a simple method for the analysis and determination of the main parameters of the superconducting material, based on a lumped-parameter equation and the measurement of the magnetic field outside and inside a thin-walled tube. This non-destructive method can be used for the quick characterization of type II superconducting materials having the shapes of thin-walled tubes. This method also makes it possible to predict the screening and trapping of the magnetic fields in tubes with known parameters.

II. EXPERIMENTAL

For this investigation of the penetration of a pulsed magnetic field into a thin-walled superconducting tube, a commercially available Bi-2223 superconductor tubular current lead[23] was used. It was 33 mm in length and had an outer diameter of 5 mm. The tube used was made by cutting out a section of a 70 mm tube in order to avoid the influence of the silver contact layers deposited at the ends of the tube. The thickness of the tube wall was 0.5 mm. A schematic diagram of the experimental setup is presented in Fig. 1. This superconducting tube was installed into a special 6 mm inner diameter coaxial holder, which was placed vertically along the

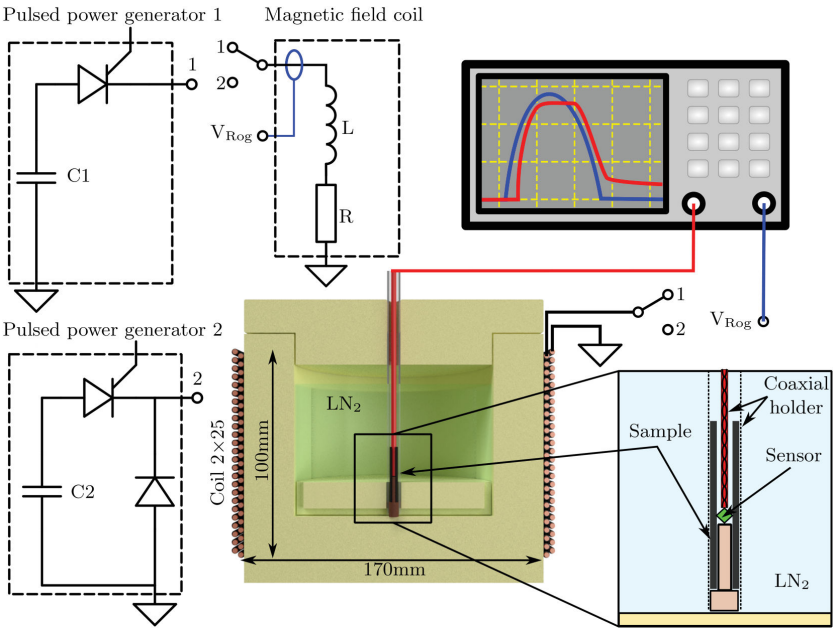

FIG. 1. Schematic diagram of an experimental setup.

longitudinal axis of a cylindrical plastic container filled with liquid nitrogen. This container was then put inside a coil made of two layers with 25 windings in each. The height of the magnetic coil was 10 cm and its inner diameter was 18 cm. The coil was made from a 2.2 mm diameter copper wire and had an inductance of 395 μH. For the generation of the pulsed magnetic field, a high current pulse generator described in Ref. 24 was used. In order to measure the current and to calculate the applied magnetic field generated by the coil, a Rogowski coil was mounted on one of the current pulse generator current leads.

A textolite spacer was inserted at one end of the superconducting tube to reduce the free space inside the coaxial holder and to ensure the same spatial configuration on every measurement. A magnetic field probe (B-dot or CMR-B-scalar sensor) was inserted through the other end of the tube so that the sensor measurement volume would touch the spacer. This puts the sensor about 17 mm from the end of the superconductor and in the middle of the coil-generated magnetic field distribution plateau. The applied magnetic field was calculated using the current flowing in the magnetic coil, which was measured with the Rogowski coil.

The B-dot sensor consisted of a 2 mm diameter, 20 windings, 5 mm length search coil. The uncertainty of the integration constant of the B-dot sensor and the slow magnetic field decay at the "tail" of the magnetic field pulse were the main sources of measurement error, which in our case was no more than 5%. Additionally, for the measurement of the magnetic field inside the superconducting tube, we used a miniature (active volume 10^{-2} mm^3 effective volume, probe radius 1 mm) CMR-B-scalar sensor, which was made from thin nanostructured La–Sr–MnO films, exhibiting the colossal magnetoresistance phenomenon. These CMR-B-scalar sensors have a non-zero response to a magnetic field running in all directions. This property makes them a useful measurement tool in the case of a pulsed magnetic field, where this field simultaneously changes magnitude and direction. These sensors can successfully operate at room temperatures. However, at liquid nitrogen temperature, the La–Sr–MnO film is in a ferromagnetic state and exhibits a long-term remnant resistance relaxation process.[25] This phenomenon needs to be taken into consideration as it can induce additional measurement errors. In order to overcome this difficulty, a special experimental arrangement was used, which allowed for the insertion and removal of the superconducting tube from the cryostat without changing the sensor's remnant resistance.

Measurements of the pulsed magnetic field inside the superconducting tube using the CMR-B-scalar sensor were performed in the following way: The first step was sensor conditioning without the superconductor. For this purpose, the sensor was cooled down to 77 K and exposed to a magnetic field pulse with a peak value of 0.5 T. The superconductor tube was then slowly submerged into the liquid nitrogen so that the CMR-B-scalar sensor would be located at the center of the tube. After a test with the superconductor tube, the tube was then removed, and the CMR-B-scalar sensor was calibrated using a magnetic field pulse of a known shape and amplitude. Before each subsequent measurement, due to the permanent magnetization of the superconducting tube, it was heated above its critical temperature Tc by withdrawing it into ambient air.

III. THEORY

A. Lumped-parameter model equation

The dynamics of the magnetic field inside a II type superconducting hollow cylinder (tube) exposed to a pulsed magnetic field exhibits three phases.[26] The first phase, called the "delay," manifests itself up to the time instant when the maximal field (B_c) that can be screened by the tube sample is reached. The magnetic field inside the tube during this phase is negligibly small. The second phase shows a partial penetration of the magnetic field (B_i) inside the tube when the applied field (B_a) becomes higher than B_c. This field (B_i) then grows up to its peak value, which coincides in time with the maximum of B_a. The third phase is the decay of the B_i value over time. This contains two periods: the fast and the very slow, which are related to the decay of B_a and the flux creep, correspondingly. The dynamics of the magnetic field density (B) at any point in space during all these phases can be calculated using the magnetic diffusion equation, which in its differential form is

$$\nabla \times \left(\frac{\rho}{\mu}(\nabla \times B)\right) = -\frac{\partial B}{\partial t}, \tag{1}$$

where ρ is the resistivity of the material. For type II superconductors, ρ strongly depends on the current density j. This can be obtained from Ohm's law $E = \rho j$ using an empirical power law relation,

$$E = E_c\left(\frac{j}{j_c(B)}\right)^n, \tag{2}$$

where E_c is the critical electric field (1 μV/cm), j and j_c are the current density and the critical current density at which the critical electrical field is reached, and n is an empirical parameter that represents the quality of the superconductor and its electric behavior in the resistive state caused by vortex motion. The critical current density j_c is a function of both the magnetic field (B) and the temperature (T). For this reason, power dissipation and the cooling conditions need to be taken into consideration. The solution of Eq. (1), using relation (2) in the general case, requires integration according to coordinates. However, a long thin-walled superconducting tube can be modeled as a solenoid wound out of a thin wire. Equation (1) can then be transformed into a relatively simple lumped-parameter equation for the current flowing in one winding ($I = d^2 j$) in which the geometry of the tube is represented by the inductance of the solenoid (L),

$$L\frac{dI}{dt} + \frac{2\pi R \cdot E_c}{(d^2 j_c(B))^n}|I|^{n-1}I = -\frac{l_s}{d}\pi R^2 \frac{dB_a(t)}{dt}. \tag{3}$$

Here, d is the thickness of the tube wall, R is the tube radius ($R \gg d$), and l_s is the tube length. This makes it possible to avoid the spatial integration of (1). The inductance L can be calculated from well-known solenoid equations assuming that the thin-walled superconducting tube is a single layer solenoid having a finite length l_s and a wire thickness of d. The main requirement for such an approach is that the difference between the magnetic field at the outer and inner sides of the wall be small in

comparison with the absolute values of these fields. This appears that Bean's penetration length (l_p), which is a function of B_a as $l_s = B_a/(\mu j_c)$ (here, μ is the magnetic permeability), significantly exceeds the wall thickness (d). Thus, this "thin-walled" condition can be satisfied when B_a is several times higher than B_c.

Moreover, this thin wall also enables the realization of good cooling of the superconducting material if the tube is submerged inside the liquid cooling media. In such a case, the ρ dependence on temperature is minimal and does not need to be taken into account. The assumption that a thin-walled superconducting tube can be imagined as a thin single layer solenoid in which the cross section of each turn is d^2 makes it possible to easily calculate the magnetic field (B_i) in the center of the tube. This field value is then directly proportional to the current I ($B = \beta I$) with a conversion constant (β) equal to Ref. 27,

$$\beta = \frac{\mu l_s}{2d\sqrt{R^2 + \frac{l_s^2}{4}}}. \quad (4)$$

After the external field pulse vanishes ($B_a = 0$), an analytical solution of the trapped field decay can be obtained by solving Eq. (3) assuming that j_c remains constant. In this case, the expression for $B_{ic}(t)$ is

$$B_{ic}(t) = \left[B_0^{n-1} + (1-n)\frac{\beta^{1-n}E_c l_s \cdot 2\pi R}{d^{2n+1}L j_c^n} \cdot t\right]^{\frac{1}{1-n}}. \quad (5)$$

Here, B_0 is the trapped magnetic field inside the superconducting tube at the end of the applied magnetic field pulse and j_c is the critical current density at this field amplitude. The analytical expression (5) can be used for a simple determination of the exponent n in the empirical power law when taking the B_0 value from the beginning of the experimentally obtained B_{ic} decay curve.

To accurately measure B_i, the axial magnetic field should not vary much in the vicinity of the measurement volume. This requirement can be achieved in two ways: by using a small magnetic field sensor or by increasing the length l_s of the tube so that the influence of the tube ends would be negligible. The influence of the tube geometry was investigated using the numerical results obtained in Ref. 21 for thick-walled tubes having different l_s/R_a ratios (R_a is the average tube radius). It was demonstrated that when $l_s/R_a > 10$, the magnetic field gradient up to 2 R_a distance along the tube longitudinal axis is negligible. Thus, a tube, with a length of l_s about an order of magnitude higher than its radius R_a, can be characterized as a "long" tube, and a sensor with dimensions that are smaller than R_a can be successfully used for the accurate measurements of B_i.

The results of the lumped-parameter model were compared with a 2D axisymmetric finite element model (FEM) based on an H formulation[28] using the same material properties. This model was constructed using Comsol multi-physics software. The heating effects were also neglected. A spatially uniform, time-dependent external magnetic field was applied on the solution domain boundary. An experimentally obtained applied magnetic field pulse was then used for the pulse shape so that the results could be compared directly.

B. Modeling of the dynamic magnetic field penetration

In order to investigate how the lumped-parameter model equation describes the penetration of the magnetic field inside a tube made from a type II superconductor, we took into consideration the experimentally obtained relationship between j_c and B. As is typical for its low and middle field ranges, this relation at relatively low magnetic fields j_c abruptly decreases with an increase of B, while in the medium magnetic fields, the j_c vs B tends to saturate so that j_c becomes approximately constant.[29]

Figure 2 shows the calculation of the magnetic field inside the tube for several half-sine applied magnetic field pulses when the amplitudes are in the range where j_c is constant. In such a case, the magnetic field penetration is not well described at the low magnetic fields (i.e., at the beginning of the pulse), but when the external flux density significantly exceeds B_c and condition j_c = const. is satisfied, the lumped parameter equation is able to accurately describe the properties of the B_c dynamics. Once the external field starts to decrease, the supercurrent changes its direction to maintain a constant flux throughout the tube. This creates a plateau region in the B_i pulse waveform. The B_i value at the plateau stays constant until the difference between B_a and B_i becomes equal to B_c. With a further decrease of B_a, the B_i begins to decrease, and the remaining trapped flux density is then B_c.

The influence of n on the B_i dynamics when j_c is constant is presented in Fig. 3. The calculations were performed using Eq. (2) without the implementation of the ρ saturation when the superconductor goes into its normal state. In this case, the simulations were

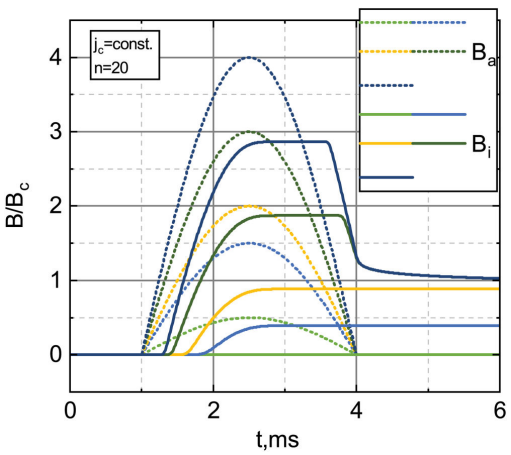

FIG. 2. Simulation results illustrating the effect of a fixed duration applied magnetic field pulse (B_a) on the magnetic field (B_i) inside a superconducting thin-walled tube normalized to the maximal field (B_c) that can be screened by the sample.

more accurate at the higher n values because the low n values do not produce a sharp step, thus giving a lower resistance than one would expect from such experimental observations when $j > j_c$. The results obtained using a fixed magnetic pulse, having a 3 ms duration and an amplitude $B_a = 3B_c$ (see Fig. 2), showed that the lower n values produce lower B_i amplitudes. However, it needs to be noted that the B_i value depends on the combination of n and the time derivative of B_a. For this reason, at low B_a derivatives (long duration pulses), the B_i amplitude could increase with the lower n values, but this increase is weak at n values higher than 20.

Figure 4 illustrates the B_i dynamics at the low B_a range when j_c is a function of B. For this simulation, the j_c vs B dependence was approximated by using the simple exponentially decaying function, where j_{c0} is the critical current density at $B = 0$ and α is the empirical coefficient, which depends on properties of the superconducting material. This shows how abrupt the j_c vs B dependence is. As it can be seen from Fig. 4, an increase of α makes the B_i penetration rate slower and increases the trapped magnetic field value. With decreasing j_c, the duration of the plateau region also decreases. For very low values of j_c, the plateau could become hard to measure, but a plateau is a sign that the sample remains superconducting at that field. Thus, the parameter showing the abruptness of the j_c vs B dependence is the main variable when fitting the experimentally obtained B_i dynamic curves.

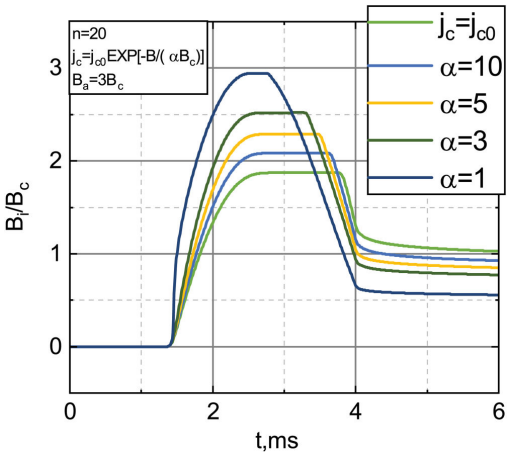

FIG. 4. B_i (normalized to B_c) dynamics with different *alpha* values when j_c-B dependence is approximated by the exponential function $j_c(B) = j_{c0}\exp[-B/\alpha B_c]$.

IV. RESULTS AND DISCUSSION

Figures 5 and 6 show the experimental measurements of B_a and B_i when the superconducting tube was cooled down to 76 K. These measurements were performed using a B-dot sensor at two different magnetic field pulse durations (≈3 ms and 8 ms). A very similar behavior of B_i was also recorded using the CMR-B-scalar sensor (see Fig. 7), thus showing that the dimensions of the B-dot sensor are sufficiently small. The experimental B_i pulses were fitted with the simulation curves obtained from Eq. (3), where the fitting parameters were the $j_c(B)$ dependence and the n value. The other constant parameters used for these calculations are given in Table I.

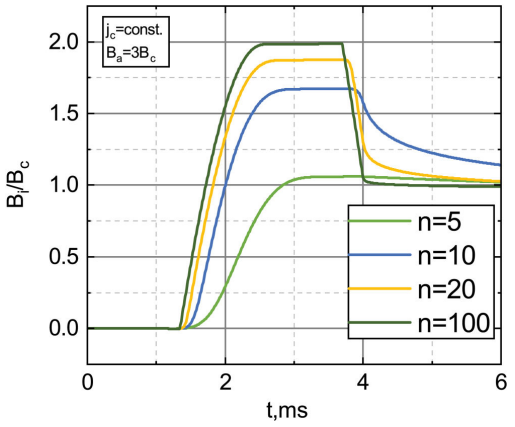

FIG. 3. B_i (normalized to B_c) dynamics with different power law values at a fixed magnetic field pulse when j_c is constant.

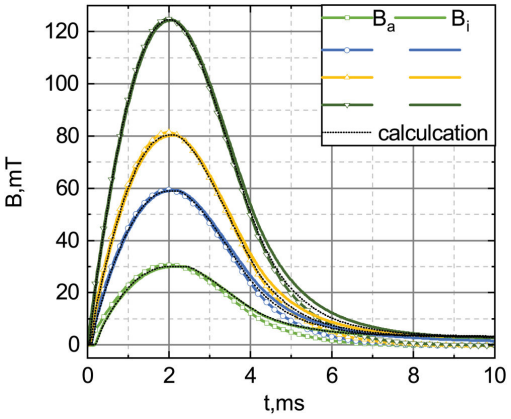

FIG. 5. The B_i dynamic measured using a B-dot sensor when the B_a pulse duration was ≈8 ms. The B_a is marked with symbols, and the numerical fits based on Eq. (3) are represented by the black dotted lines.

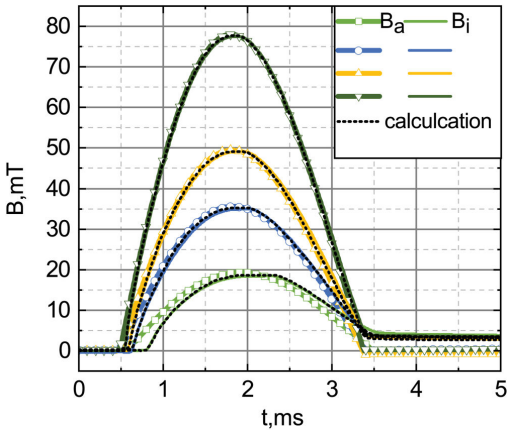

FIG. 6. The B_i dynamic measured using a B-dot sensor when the B_a pulse duration was ≈3 ms. The B_a is marked with symbols, and the numerical fits based on Eq. (3) are represented by the black dotted lines.

As an additional validation of this lumped-parameter equation approach, the experimentally measured B_a and B_i time derivatives (Fig. 8) were compared with the simulations using a finite element model and the lumped-parameter equation (3). In the case of the B-dot, the magnetic field time derivative is the directly measured quantity so that the comparison between the measurement and the models is more accurate than using the integrated signal. Moreover, as it can be seen from Fig. 8, the magnetic field derivative inside the superconducting tube is more sensitive to the peculiarities of the B dynamics and shows a sharp spike with a higher amplitude than an unscreened external field at the moment when the magnetic field penetrates into the superconductor. The plateau region before the field starts to decrease is also better pronounced in the derivative of the field. At around 1.8 ms, a region where the derivative is zero can be seen, indicating that the sample remains superconducting, while it is hard to tell from the integrated signal (Fig. 6).

TABLE I. Values used to fit experimental data with the lumped-parameter model.

L	l_s	R	d	$j_c(B)$
2.62 μH	33 mm	2.25 mm	0.5 mm	Fig. 10

The best fit of the experimental curves was obtained at $n = 20$. This means that the flux creep is small in the sample and that the sample exhibits Bean-like behavior. The results presented in Figs. 5–7 show that the experimentally measured B_i dynamics are in good agreement with the calculations, which confirms the validity of the application of the power law and the isothermal simplification assumed in the case of the investigated superconducting tube. The simulation results also agree well with the experimental measurements when predicting the trapped flux. The measured remaining flux density fluctuated from 2.9 mT to 3.7 mT, while the simulations predicted 2.9 mT–3.3 mT for the short pulses and 1.5 mT–3 mT for the experimental and 2.6 mT–3.4 mT in the simulations for the longer ones, confirming that the lumped-parameter method is capable of predicting the persistent currents and in turn, the trapped field in dynamic conditions.

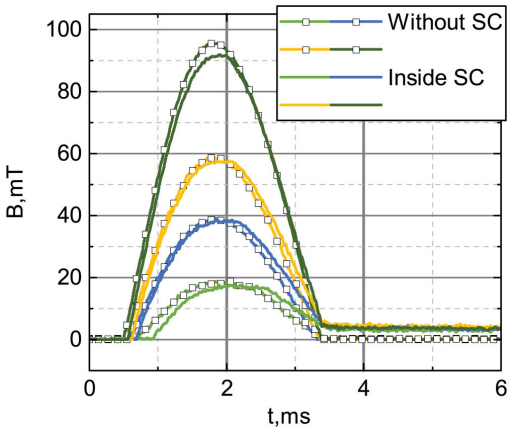

FIG. 7. The B_i dynamics measured using the CMR-B-scalar sensor when the B_a pulse duration was ≈3 ms. B_a is marked with symbols.

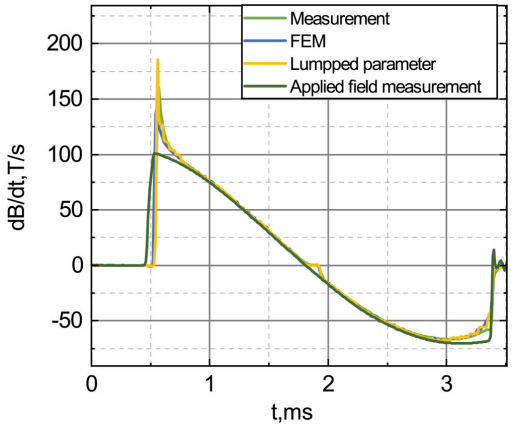

FIG. 8. The time derivatives of the applied magnetic flux density (B_a) and the density inside (B_i) the superconducting tube. Experimental data, the finite element, and lumped-parameter models are compared.

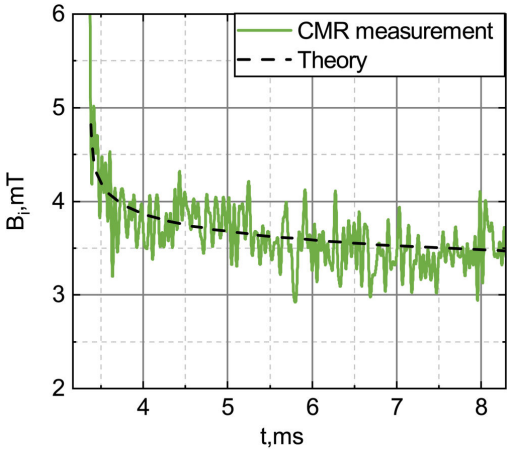

FIG. 9. The B_i decay after the applied magnetic field pulse. Comparison between the CMR-B-scalar sensor measurement and the analytical expression (5).

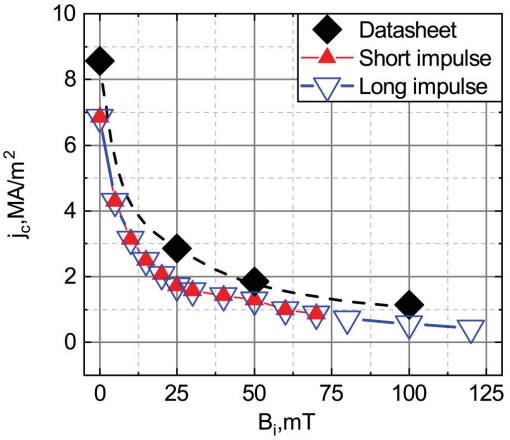

FIG. 10. The j_c vs B curves obtained from fitting the experimental data using the lumped-parameter equation. The square shaped dots show the $j_c(B)$ values presented in the datasheet of the superconducting tube manufacturer.

The third phase of the B_i dynamics, i.e., the B_i value decay over time after the end of applied magnetic field pulse, was investigated using the CMR-B-scalar sensor. Figure 9 shows the results of this decay measurement using an applied magnetic field pulse of 19 mT amplitude and 3 ms duration. The dashed line illustrates the decay behavior described by the equation (5). The analytical decay is in a good agreement with the measurement results. The values used for the curve are given in Table II. This confirms the validity of the assumptions made in order to get the analytical formula (5) for the B_i decay process.

These measurements and simulations make it possible to evaluate the power law index n and j_c vs B dependence. Figure 10 presents this dependence as triangles, which were obtained using two applied magnetic field pulses with different pulse durations and amplitudes (3 ms, 8 ms and 77.5 mT, 125 mT, respectively), when the power law index n was equal to 20. As can be seen for both pulses, the j_c vs B dependence value and the shape are the same and do not depend on the parameters of the magnetic pulse being used. Thus, in our case, the magnetic pulse parameters (derivative and amplitude) were not critical for the investigation of the properties of the thin-walled superconducting tube material. Figure 10 also shows a comparison of the results obtained from fitting the experimental results with simulations using the lumped-parameter equation and the datasheet of the tube manufacturer (diamonds).

TABLE II. Values used to draw the theoretical curve in Fig. 9.

B_0	n	j_c	β
4.82 mT	20	5.8 MA/m^2	2.5 mT/A

Our investigations showed very similar j_c vs B dependence behavior but about a 20% lower j_c value, which can be explained as the different magnetic field orientation to the electrical current flowing in the superconductor. This phenomenon was demonstrated in the Bi-2223 tubular current leads when the magnetic field was applied parallel and perpendicular to the tube axis.[30]

V. CONCLUSION

Experimental and theoretical investigations of the pulsed magnetic field penetration dynamics conducted on a thin-walled tube made from a type Bi-2223 superconductor have demonstrated that the lumped-parameter approach is capable of describing the magnetic field dynamics and the trapped flux inside this tube. It is possible to evaluate the j_c vs B dependence and the exponent n in power law of the tube material from a single measurement. With further development, this method could be used as a quick nondestructive way to check the quality and to characterize such superconducting tubular samples.

REFERENCES

[1]A. Morandi, E. Perini, G. Giunchi, and M. Fabbri, IEEE Trans. Appl. Supercond. **21**, 1460 (2010).
[2]A. Patel, G. Giunchi, A. F. Albisetti, Y. Shi, S. Hopkins, R. Palka, D. Cardwell, and B. Glowacki, Phys. Procedia **36**, 937 (2012).
[3]M. Alqadi, F. Alzoubi, S. Saadeh, H. Al-Khateeb, and N. Ayoub, J. Supercond. Nov. Magn. **25**, 1469 (2012).
[4]G. P. Lousberg, J.-F. Fagnard, M. Ausloos, P. Vanderbemden, and B. Vanderheyden, IEEE Trans. Appl. Supercond. **20**, 33 (2009).
[5]J. Rabbers, M. Oomen, E. Bassani, G. Ripamonti, and G. Giunchi, Supercond. Sci. Technol. **23**, 125003 (2010).

[6]J.-F. Fagnard, S. Elschner, A. Hobl, J. Bock, B. Vanderheyden, and P. Vanderbemden, Supercond. Sci. Technol. **25**, 104006 (2012).
[7]F. Sirois, J. R. Cave, and Y. Basile-Bellavance, IEEE Trans. Appl. Supercond. **17**, 3652 (2007).
[8]I. Vajda, A. Gyore, S. Semperger, A. Baker, E. Chong, F. Mumford, V. Meerovich, and V. Sokolovsky, IEEE Trans. Appl. Supercond. **17**, 1887 (2007).
[9]M. Dione, F. Sirois, F. Grilli, and J. Mahseredjian, IEEE Trans. Appl. Supercond. **19**, 1913 (2009).
[10]J. Bock, S. Elschner, and F. Breuer, "Compact superconducting current limiting component in coil configuration with low inductance," U.S. patent 7,706,110 (27 April 2010).
[11]G. Ciovati, J. Anderson, B. Coriton, J. Guo, F. Hannon, L. Holland, M. LeSher, F. Marhauser, J. Rathke, R. Rimmer *et al.*, Phys. Rev. Accel. Beams **21**, 091601 (2018).
[12]Y. Itoh and U. Mizutani, Jpn. J. Appl. Phys. **35**, 2114 (1996).
[13]U. Mizutani, T. Oka, Y. Itoh, Y. Yanagi, M. Yoshikawa, and H. Ikuta, Appl. Supercond. **6**, 235 (1998).
[14]T. Kono, M. Tomita, M. Murakami, and T. Takizawa, Supercond. Sci. Technol. **13**, 794 (2000).
[15]E. H. Brandt, Phys. Rev. B **55**, 14513 (1997).
[16]P. M. Grant, Ind. Phys. **7**(5), 22 (2001).
[17]P. Mikheenko and T. H. Johansen, Energy Procedia **58**, 73 (2014).
[18]P. Mikheenko, in *Journal of Physics: Conference Series* (IOP Publishing, 2011), Vol. 286, p. 012014.
[19]Y. Zhao, T. Qureishy, P. Mikheenko, and J.-C. Grivel, IEEE Trans. Appl. Supercond. **26**, 1 (2016).
[20]E. H. Brandt, Phys. Rev. B **58**, 6506 (1998).
[21]S. Denis, L. Dusoulier, M. Dirickx, P. Vanderbemden, R. Cloots, M. Ausloos, and B. Vanderheyden, Supercond. Sci. Technol. **20**, 192 (2007).
[22]J.-F. Fagnard, M. Dirickx, M. Ausloos, G. Lousberg, B. Vanderheyden, and P. Vanderbemden, Supercond. Sci. Technol. **22**, 105002 (2009).
[23]CAN, see https://www.can-superconductors.com/uploads/2/1/2/9/21298520/csl˙datasheetv2.pdf for "Superconducting Current Leads," Datasheetv2 (2015), cSL-5/70.2.
[24]J. Novickij, S. Balevičius, N. Žurauskienė, R. Kačianauskas, V. Stankevič, Č. Šimkevičius, S. Keršulis, and S. Bartkevičius, J. Low Temp. Phys. **159**, 406 (2010).
[25]N. Žurauskienė, S. Balevičius, D. Pavilonis, V. Stankevič, V. Plaušinaitienė, S. Zherlitsyn, T. Herrmannsdörfer, J. M. Law, and J. Wosnitza, IEEE Trans. Magn. **50**, 1 (2014).
[26]Y. Cha and T. Askew, Physica C **302**, 57 (1998).
[27]Q. Peng, S. McMurry, and J. Coey, J. Magn. Magn. Mater. **268**, 165 (2004).
[28]J. Zou, M. D. Ainslie, H. Fujishiro, A. Bhagurkar, T. Naito, N. H. Babu, J.-F. Fagnard, P. Vanderbemden, and A. Yamamoto, Supercond. Sci. Technol. **28**, 075009 (2015).
[29]K. Zmorayova, V. Antal, M. Radusovska, S. Piovarci, D. Volochova, and P. Diko, Acta Phys. Pol. A **126**, 366 (2014).
[30]V. Plechacek and J. Hejtmanek, Physica C **282**, 2577 (1997).

3rd publication / 3 publikacija

Superconducting protector against electromagnetic pulses based on YBCO film prepared on an Al_2O_3 substrate with a CeO_2 sublayer

V. Vertelis, T. Stankevic, S. Balevicius, V. Stankevic, N. Zurauskiene, V. Plausinaitiene, S. Tolvaisiene, M. Schneider, C. Simkevicius

Supercond. Sci. Technol., vol. **34**, no. 3, p. 035007 (2021)

DOI: 10.1088/1361-6668/abd459

IOP Publishing Superconductor Science and Technology
Supercond. Sci. Technol. 34 (2021) 035007 (10pp) https://doi.org/10.1088/1361-6668/abd459

Superconducting protector against electromagnetic pulses based on YBCO film prepared on an Al_2O_3 substrate with a CeO_2 sublayer

V Vertelis[1,2], T Stankevic[2], S Balevicius[2], V Stankevic[2,3], N Zurauskiene[2,3], V Plausinaitiene[2], S Tolvaisiene[3], M Schneider[1] and C Simkevicius[2,3]

[1] French-German Research Institute of Saint-Louis, 68300 Saint-Louis, France
[2] Center for Physical Sciences and Technology, 01108 Vilnius, Lithuania
[3] Faculty of Electronics, Vilnius Gediminas Technical University, 10223 Vilnius, Lithuania

E-mail: Vilius.VERTELIS@isl.eu

Received 24 September 2020, revised 23 November 2020
Accepted for publication 16 December 2020
Published 29 January 2021

Abstract

The electric and magnetic properties of microbridges made from 440 nm thick Y–Ba–Cu–O films prepared on Al_2O_3 substrates with CeO_2 sublayers by the pulsed injection metal organic chemical vapor deposition (MOCVD) method were studied in temperatures ranging from 20 K to 300 K in order to investigate the possibilities of using these microbridges as fast fault current limiters. The application of an external magnetic field (B_{ex}) causes the flux flow induced magneto-resistive effect, which is proportional to B_{ex} and to $B_{ex}{}^{1/2}$ at low and high temperatures, respectively. The experimentally obtained S-shaped *I–V* characteristic and the change of the microbridge resistance over time when affected by a step-like magnetic field can be well explained using a thermo-electrical model based on Joule heating and the flux flow nature of the resistive state (RS). The transition from the superconducting to the RS, studied using ns duration rectangular waveform electrical pulses able to create up to ≈2106 A cm^{-2} current densities without rises of microbridge temperatures, demonstrated that the *I–V* characteristics of the RSs consisting of an assembly of straight lines corresponding to the different pinning centers. At temperatures close to the critical temperature of superconductivity, the number of these lines increases, and the *I–V* characteristics can be described with high accuracy by a power law. It was concluded that microbridges made from these films can be used as protectors against complicated waveform electromagnetic pulses having short rise times, high voltage peak amplitudes and long low-value over-current 'tails'.

Keywords: superconductivity, thin films, EMP protector

(Some figures may appear in color only in the online journal)

1. Introduction

The search for means to mitigate electromagnetic pulses (EMPs) began in 1962 when a high-altitude nuclear explosion was initiated over the Johnston Island area of the Pacific Ocean [1]. The proliferation of manmade nuclear [2–5] and non-nuclear EMP devices [6–8] as well as intelligent electronic devices (IEDs), which are increasingly more sensitive to EMP effects has renewed the interest in the EMP threat and in technologies which would protect against it. Moreover, the protection of modern IEDs used in high-speed communication technologies against EMP produced by natural sources such as

lightning [9] is still particularly important. Various measures are used for the protection of these electronic devices such as surge protectors [10, 11], modular attachment kits using Faraday cages [12] or EMP shields [13]. 'Front door' protection is the most difficult, because this part of such communication systems is itself highly vulnerable to EMP attack.

To protect high frequency electronic circuits connected to receiving antennas against wide frequency band EMPs, protectors must be sufficiently fast, powerful and able to operate in the case of bipolar signals. Moreover, they also need to induce as low as possible an initial attenuation of the useful signal and to be ready to operate after each EMP event. In the case of a nuclear EMP or an EMP generated by lightning, the fault overvoltage pulse induced in the receiving antenna's output consists of powerful high frequency components (hundreds of megahertz to several gigahertz) [1, 14] and has relatively long (up to tens of milliseconds) low frequency 'tails'. Thus, protectors against this type of EMP have to react in subnanosecond times and to be able to withstand large energy absorption shocks during these EMP 'tail' periods. To satisfy both of these requirements in one and the same device is thus not an easy task, primarily because such high-speed electronic devices are usually of small dimensions [13], which can cause high current densities and irreversible damage of the protectors.

It has been demonstrated that thin, high-T_c superconducting films can be successfully used for the design of such high-speed fault current limiters [15–20]. An important requirement for these films is that their *V*–*I* characteristics need to exhibit a wide range of nonlinear dissipative states. It has been determined that in polycrystalline films, such states are induced by the motion of homogeneous magnetic flux vortices across the superconducting microstrips [21, 22] and can be controlled by temperature [23–25], magnetic fields [26–28] or by light irradiation [29–31].

Different material deposition technologies and substrates have been used for the preparation of these films. The most popular techniques are laser ablation and magnetron sputtering. The main advantages of laser ablation are: good repeatability of the chemical content, easy control of the layer thicknesses and the possibility of *in situ* film annealing in an oxygen atmosphere. Unfortunately, this method allows one to prepare films having only relatively small areas and their growth regimes are sensitive to the laser pulse parameters. Moreover, it is difficult to avoid leaving small drops and solid particles on the film surfaces [32]. Films prepared by magnetron sputtering can have larger areas and more uniform properties, but the deposition rates are slow and most of the energy acting on the target is transformed into heat energy, which must be removed. Magnetron-sputtered layers, deposited in an atmosphere of inert gas, are contaminated by the auxiliary gas itself. Moreover, the roughness of the substrate and the incidence angles of the atoms deposited on the cavity walls induce porosity of the film [33].

Since the discovery of high-T_c superconducting oxides, the metal organic chemical vapor deposition (MOCVD) technique has also been used for the deposition of thin films. The so-called pulsed injection MOCVD (PI-MOCVD) method provides digital deposition control by means of a high-speed injection of precursor microdroplets into an evaporator. This was used for the preparation of polycrystalline and epitaxial Y–Ba–Cu–O (YBCO) films [29, 34]. The main advantages of PI-MOCVD are: high reproducibility, flexible control of the growth rate, thicknesses and composition of the film [34]. This method enables covering large substrate areas and does not require a high vacuum.

$SrTiO_3$ (STO; dielectric constant $\varepsilon = 300$), $LaAlO_3$ (LAO; $\varepsilon = 23.7$) and $NdGaO_3$ (NGO; $\varepsilon = 20$) are the usual substrates for YBCO deposition. These materials are very compatible with thin cuprate films in terms of their lattice constants and thermal expansion coefficients. However, for high-speed microelectronic technologies, substrates with dielectric constants of about 10 are preferable. Among these, Al_2O_3, whose ε ranges between 9.164 and 9.424, appears to be quite attractive. In this case, its low dielectric constant is accompanied with high thermal conductivity ($\approx$20 W m^{-1} K^{-1} around liquid nitrogen temperature) [35]. This is very important for the design of superconducting high-speed protectors against EMPs with complicated waveforms that consist of fast rise times and long decay 'tails'. However, in order to grow this superconducting film, a special sublayer between this film and the substrate is necessary due to a large lattice mismatch [35].

In this paper, we present an investigation of the resistive states (RSs) of thin YBCO films prepared by the Pi-MOCVD technique on Al_2O_3 substrates with CeO_2 sublayers, when they are influenced by DC currents, magnetic fields and short high power electrical pulses. It has been demonstrated that these films can be used as protectors while operating simultaneously against low DC over-currents and fast high voltage electrical transients.

2. Sample preparation

The PI-MOCVD method was used for the preparation of both the CeO_2 sublayers and the YBaCuO films. The layers were deposited on a single crystal Al_2O_3 substrate. The deposition of the CeO_2 sublayer and the YBaCuO film was made *in situ* at 750 °C substrate temperature. The CeO_2 sublayer thickness (h) was 140 nm or 480 nm. For the preparation of the YBaCuO film, the metal organic precursors with Y:Ba:Cu = 1:1.6:1.6 and 1:2.0:1.6 content were used. After the deposition of the YBaCuO film, whose thickness (d) was 440 nm, it was annealed in an O_2 atmosphere for 30 min. The annealing temperature was the same as for the deposition (750 °C). The analysis of the YBaCuO film performed using the reflection high-energy electron diffraction (RHEED) method showed spot-like intensive diffraction patterns (see figure 1(a)), indicating that the films were of perfect structure and high surface roughness. An investigation of the film surfaces by an atomic force microscope (AFM) also demonstrated that the films consisted of microcrystallites oriented in mosaic-like morphologies, which were different for different thicknesses of the CeO_2 sublayers (see figures 1(b) and (c)).

After deposition, the samples were shaped by conventional photolithography as 3 mm length (l) and 60 μm or 100 μm

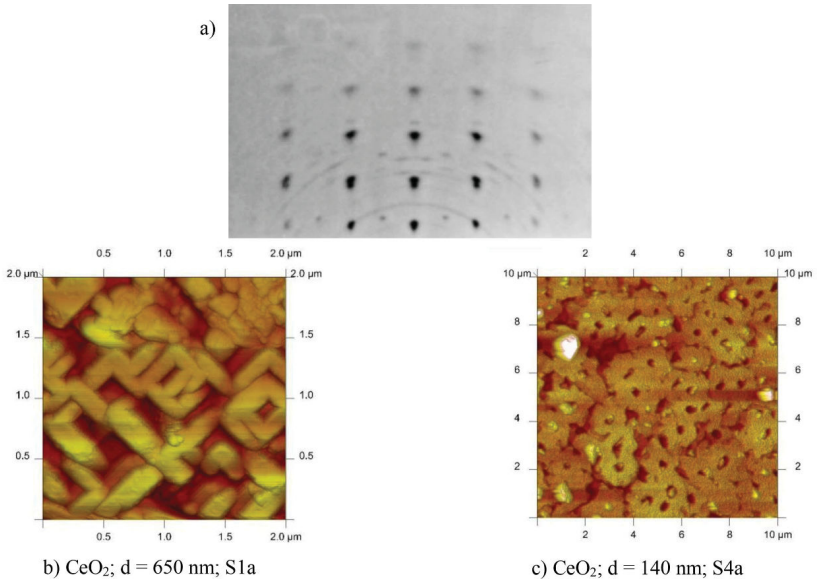

Figure 1. (a) A RHEED pattern obtained from a 440 nm thick YBCO film. It was prepared using 1:1.6:1.6 precursors on a 650 nm thickness CeO_2 sublayer. (b), (c) Show surface images obtained by AFM on YBCO film, when the height (h) of the CeO_2 sublayer was 480 nm and 140 nm for samples S1a and S4a, correspondingly.

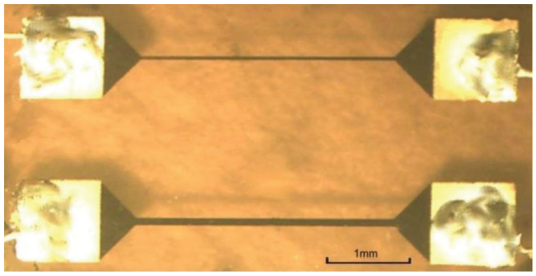

Figure 2. Top view of the YBCO strip-like microbridges used for the investigation of their electrical properties.

width (w) strip-like microbridges with contact sites at their ends (see figure 2). The contact sites (1×1 mm^2) were covered with a 2 μm thickness silver film deposited using thermal vacuum evaporation. After that, the samples were annealed for 20 min in an oxygen atmosphere at 420 °C–450 °C temperature.

3. Measurement technique

For the characterization of electric and magnetic properties of the YBaCuO films, the experimental setup presented in figure 3 was used. This setup consisted of two parts: one for the measurement of their I–V characteristics using DC current and a magnetic field and other that used high voltage nanosecond duration electrical pulses. In both these measurement regimes, the sample was mounted inside a closed cycle He cryocooler 'Janis' in order to perform the investigations at different temperatures, which could be varied from 4.2 K to 300 K.

The resistance (R) vs temperature (T) dependences in the DC case were investigated using a two-terminal method when the applied current was 0.1 mA in a temperature range from 40 K to 150 K. The voltage drops and current through the samples were recorded by means of a multimeter. The I–V characteristics were measured using a slow ramp signal generated using a digitally controlled power supply. For the investigation of magnetic field influence on the electrical conductivity of the films, the microbridges were placed inside an external magnetic field (B_{ex}), which was directed perpendicular to the microbridge plane and was changed from zero up to 0.7 T (see experimental setup in figure 3). During these measurements, the electrical current flowing through the samples was kept constant and was equal to 0.75 mA.

Strong pulsed electric field measurements were performed using rectangular shape pulses with durations of about 10 ns, 0.5 ns rise times and amplitudes up to 1 kV. These pulses were generated in a 50 Ohm coaxial transmission line by means of an electromechanical Hg relay. For I–V characteristic measurement, the samples were mounted in a special wide band ($\sim$10 GHz) coplanar holder and connected in series with the transmission line. Measurements were performed in a temperature range from 20 K to 80 K.

In order to measure the sample resistance, the amplitudes of incident U_{in} and transmitted U_{tr} pulses were measured using a signal splitter with a 1:80 ratio and two separate channels of a

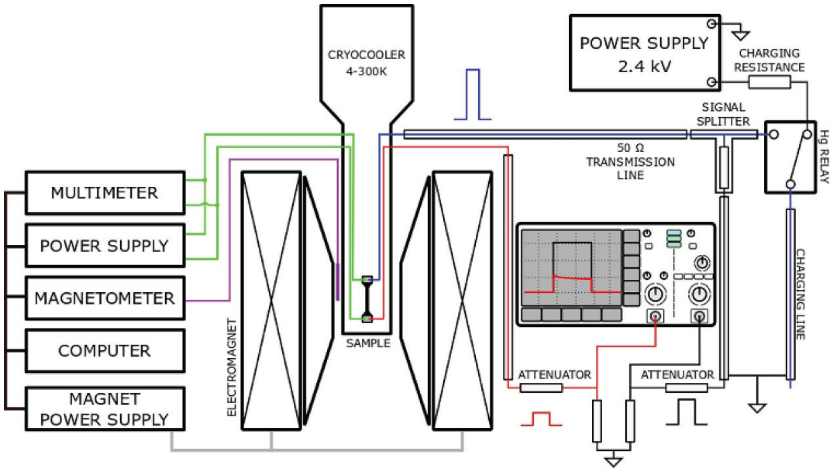

Figure 3. Schematic diagram of the setup used for the investigation of the YBCO strip-like microbridge *I–V* characteristics at different temperatures, low DC current, presence of a magnetic field and high voltage nanosecond duration pulses.

high-speed Tektronix DPO 70604 oscilloscope. The voltage drops (U_s) and current (I_s) in the samples were calculated using following formulas: $U_s = 2(U_{in} - U_{tr})$ and $I_s = U_{tr}/Z$. Here Z was the impedance of coaxial transmission waveguide and was equal to 50 Ω.

4. Electrical conductivity at DC electric current

4.1. Zero external magnetic field (bias current 0.1 mA)

The typical resistance (R) vs temperature (T) dependences measured for the investigated YBCO microbridges are presented in figure 4. The main parameters of the samples used for this investigation are shown in table 1. As it can be seen from figure 4, the $R = f(T)$ dependences exhibit three regions: the metallic normal state (NS) obtained at temperatures higher than T_{C1}, the transient state (TS), which covers temperature range from T_{C1} to T_{C2} and the superconducting state (SS) appearing below T_{C2}. The T_{C1} was determined as a temperature at which the linear decrease of the sample resistance with temperature in NS transforms to the abrupt decrease of this resistance down to the zero resistance SS state. The T_{C2} corresponded to the highest temperature where the sample resistance in the frame of measurement accuracy is zero.

According to the results shown in figure 4, the resistance and the corresponding resistivity of the films in NS was higher for films deposited on the larger thickness of the CeO_2 sublayers and prepared using 1:2.0:1.6 precursors content (samples S3a and S4a). The increase of Ba in the precursors content from 1:1.6:1.6 to 1:2.0:1.6 led to a decrease of NS resistivity by about two times, but it did not radically influence the T_{C1} and T_{C2} values. Meanwhile, films prepared on lesser (140 nm) thickness CeO_2 sublayers demonstrated

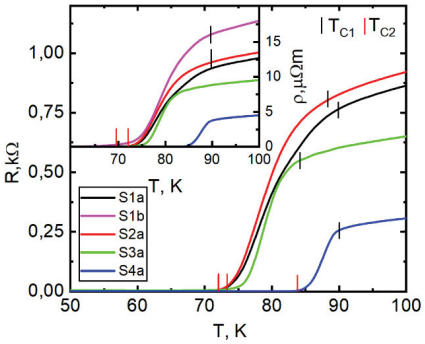

Figure 4. Electrical resistance (R) dependence on temperature (T) for various microbridges (parameters are presented in table 1) prepared on Al_2O_3 substrates with CeO_2 sublayers. The insert shows the dependence of the resistivity (ρ) on temperature (T) for the microbridges with different widths (S1a; $w^{\circ} = {}^{\circ}100$ μm, S1b; $w^{\circ} = {}^{\circ}60$ μm (pink)).

a significant increase of T_{C1} and T_{C2}. As it is can be seen from figure 4 and table 1, the temperature range of the TS state $\Delta(TS) = T_{C1} - T_{C2}$ is smaller for samples with lower NS resistance. It was obtained that in the case of S1 type films microbridges having 60 μm width exhibit higher resistivity in comparison to that of 100 μm wide microbridges. As this parameter is important for fault current limiter's attenuation value, it was decided to perform further investigations only on microbridges with a width equal to 100 μm. The insert in figure 4 shows how the resistivity (ρ) of the film depends on T for two superconducting samples having different widths when the thickness of the CeO_2 sublayer h was constant.

Table 1. Sample parameters for YBCO films with CeO_2 sublayer.

Sample name	Y:Ba:Cu	d (YBCO), nm	h (CeO_2), nm	w, μm	T_{C1}–T_{C2}, K	Δ(TS), K
S1a	1:1.6:1.6	440	650–700	100	89.8−72	17.8
S1b	1:1.6:1.6	440	650–700	60	89.7−69.5	20.2
S2a	1:1.6:1.6	440–480	650	100	88.3−72.1	16.2
S3a	1:2.0:1.6	440	650	100	84.2−73.3	10.9
S4a	1:1.6:1.6	440	140	100	90−83.8	6.2

4.2. DC external magnetic field (bias current 0.75 mA)

Figures 5(a) and (b) show the magneto-resistive effect of YBCO film manifesting as a change of microbridge resistance $\Delta R(B_{ex}) = R(B_{ex}) - R(0)$ (here $R(B)$ and $R(0)$ are the resistance of the microbridge at fixed and zero magnetic field, respectively) at external magnetic field (B_{ex}). The ΔR vs B_{ex} dependences for the superconducting microbridge S1a were measured at two different temperatures ranges: (I) $T < T_{C2}$ and (II) $T_{C2} < T < T_{C1}$. It was obtained (see figure 5(a)) that the ΔR vs B_{ex} dependences of the temperature range I are well expressed in the low resistivity region (close to zero in the frame of measurement method sensitivity (≈0.05 Ω)), which does not depend on the magnetic field values up to the critical magnetic field B_c. An increase of the temperature (T) led to a decrease of the B_c value as $B_c \approx B_{c0}\left[1-(T/T_c)^2\right]$ (see figure 5(c)). Here B_{c0} is a constant and T_c is the critical superconductor temperature. It is a fitting constant describing the thermal of B_c and should not be confused with T_{C1} or T_{C2}. At magnetic fields higher than B_c, the superconducting film was transformed into the RS, which starts as a linear ΔR dependence on B_{ex} and transforms at higher B_{ex} to nonlinear behavior. The increase of T produced a more abrupt ΔR vs B_{ex} dependence and larger range of ΔR in the linear part of ΔR vs B_{ex} curve. At $T \approx T_{C2}$, the ΔR as a function of B_{ex} is linear in the whole B_{ex} range. In the temperature range II, a further increase of temperature showed a decrease of the magneto-resistive effect (see figure 5(b)) and a change of the linear ΔR vs B_{ex} dependence to $\Delta R \propto {B_{ex}}^{1/2}$ behavior.

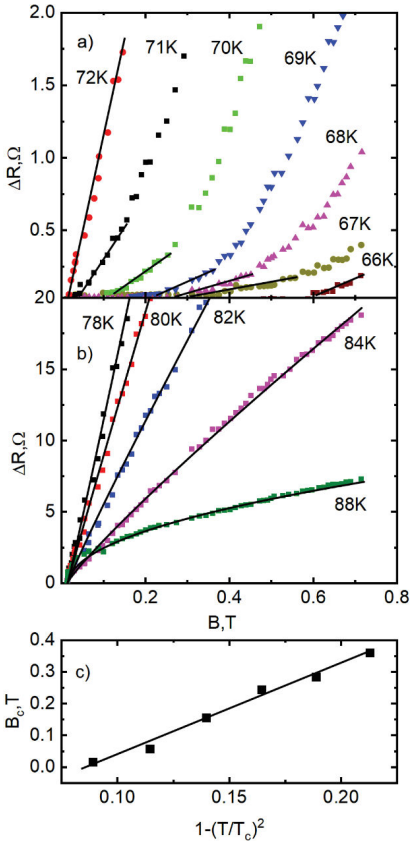

Figure 5. (a), (b) Resistance change (ΔR) dependence on the external magnetic field (B_{ex}) at different temperatures of a microbridge S1a. (c) Shows the critical magnetic field (B_c) dependence on temperature in a $1-(T/T_c)^2$ scale.

4.3. High current (up to 200 mA) regime

Figure 6 shows the voltage (V) vs current (I) characteristics of a microbridge S1a measured at different temperatures. These characteristics were measured in a stabilized voltage source regime in two cases: at zero external magnetic field and when B_{ex} was 0.7 T. As it can be seen from figure 6, they were S-shaped, having a branch with negative differential resistance. The critical current (I_{ci}) at which the negative differential resistance appeared decreased with an increase of temperature T and the B_{ex} value.

4.4. Kinetics of the microbridge resistance (triggered by a $B_{ex} = 0.75$ T field)

When a superconducting bridge, kept at a constant current I_a that is less than I_{ci}, was affected by an external magnetic field (B_{ex}), an instability was manifested as a resistance increase over time. This phenomenon is demonstrated in figure 7, which shows the time evolution of R when microbridge S1a was exposed to 0.75 T DC external magnetic field for 4.45 s. Below $I_a = 4$ mA, the increase of the R caused by the external magnetic field did not induce any R changes over time; however for higher I_a values, the B_{ex} induced a time dependent growth of R, which started at the beginning of the B_{ex} application. This growth tends to saturate when $I_a < I_{ci}$. However, at $I_a = I_{ci}$ (≈12 mA), after a relatively slow R increase at the beginning

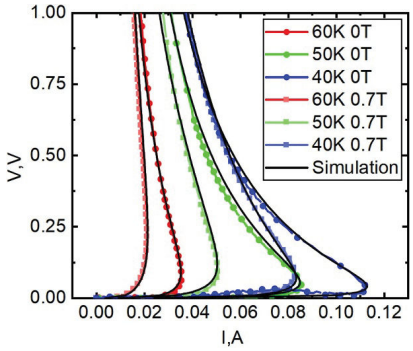

Figure 6. The *I–V* characteristics of a microbridge S1a at different substrate temperatures. The circles correspond to measurements performed at zero magnetic field, the squares at $B_{ex} = 0.7$ T. Solid lines are simulations obtained using isothermal *I–V* curves measured by nanosecond duration pulses.

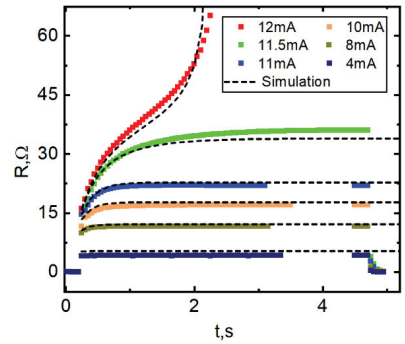

Figure 7. Time evolution of the superconducting YBCO microbridge S1a resistance when it was triggered by 0.75 T DC external magnetic field. Dashed lines are simulation results using *I–V* curves obtained with nanosecond electrical pulses.

of the magnetic field influence, the dynamics of the *R* time evolution drastically changes, demonstrating a fast growth of *R* over time.

5. RS induced by high voltage nanosecond duration electrical pulses

5.1. The dynamics of the microbridge resistance

Figure 8 demonstrates the typical waveforms of the incident and transmitted electrical pulses at low (figure 8(a)) and high (figure 8(b)) current regimes when the microbridge is cooled down to 60 K temperature. At $I \ll I_c$, there is no difference in the waveform of these pulses; however, the amplitude of the transmitted pulse is slightly lower than the incident pulse amplitude. It corresponds to an attenuation of about 0.2 dB being introduced by the superconducting microbridge in a 50 Ω impedance transmission line. This is the result of contact pad resistance and the small impedance change at the

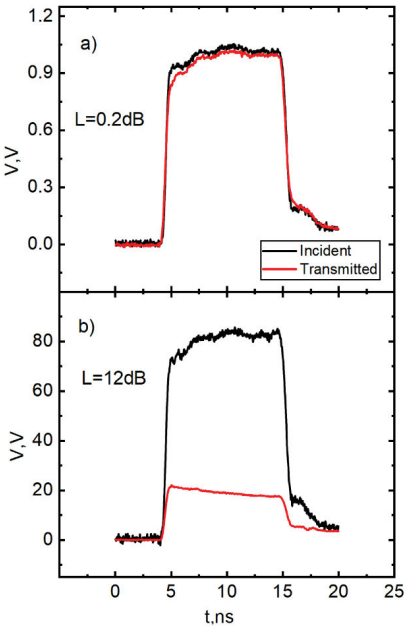

Figure 8. Waveforms of the incident and the transmitted pulse when microbridge S2a, cooled down to 60 K, was connected in series to a 50 Ohm impedance transmission line: (a) low current $I \ll I_c$ regime and (b) high current $I \gg I_c$ regime.

interconnection between coaxial cable and strip-like sample holder. When $I \gg I_c$, the difference between amplitudes of the incident and transmitted pulses strongly increases and a large attenuation (12 dB) is induced in the transmission line. Moreover, the waveform of the transmitted pulse demonstrates a slow voltage decrease over time.

In this case, the *I–V* characteristics are different when measured at different time instants from the beginning of the current pulse (see figure 9). It shows that thermal effects (Joule heating) play a significant role when the current density through the 100 μm width microbridge exceeds $\approx 4.5\ 10^5$ A cm^{-2} ($I \approx 200$ mA). Consequently, for the investigation of the *I–V* characteristics in which the influence of Joule heating is negligible, measurements performed shortly after ($\approx$1 ns) the start of the pulse are preferable.

Figure 10(a) shows the *I–V* characteristics measured for the S1a sample at different temperatures when the incident electrical pulse rise time is $\approx$1 ns. These characteristics were typical for all investigated samples and, as it can be seen from figure 10(a), consisted of an assembly of straight line segments whose number and angle to the current axis increased with an increase of the microbridge temperature. Such shapes of the *I–V* characteristics were obtained earlier in [21] for polycrystalline YBCO films prepared on NGO substrates and were explained by the motion of the vortices associated with various pinning centers having different pinning strengths, which were uniformly distributed in the superconducting film. The number

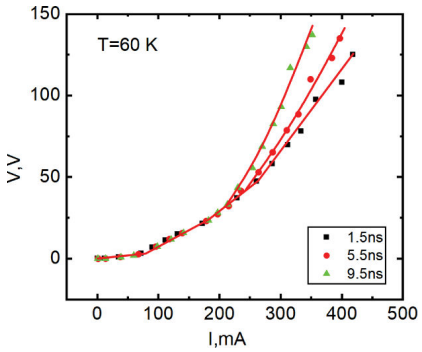

Figure 9. The *I–V* characteristics of microbridge S2a measured at different time instances.

of centers that can be depinned increases when the temperature of the film approaches T_c. For this reason, at temperatures near T_c, the total *I–V* characteristic becomes highly nonlinear and can be described with high enough accuracy by the power law $V \sim I^n$. This can be seen from the logarithmic plot of the *I–V* characteristics presented in figure 10(b). Moreover, this plot shows that the *I–V* characteristic consists of two straight lines: one, which manifests itself at the beginning of the *V–I* curves and does not depend on the temperature and corresponds to the Ohm's law ($n \approx 1$), the other corresponding to the power-law of type II superconductors. The Ohm's law part of the *I–V* characteristic shows initial attenuation (about 0.3–0.7 dB), which, as it was mentioned earlier, has to be associated with the microbridge's electrical contact areas and transmission line cable interconnections.

The analysis using this plot (see inclusion in figure 10(b)) showed that an increase of temperature (T) linearly decreases the power-law index n as:

$$n = n_0 - \alpha \times T \tag{1}$$

Here α and n_0 are constants. Meanwhile, the critical current (I_c) depends nonlinearly on temperature as:

$$I_c = I_{c0} \times \left[1 - \left(\frac{T}{T_c}\right)\right]^4 \tag{2}$$

The I_{c0} in formula (2) is a function of magnetic field induction (B).

The results presented in figures 8–10 show that YBCO films prepared on Al_2O_3 substrate with CeO_2 sublayer can be used as protectors against subnanosecond rise time electrical transients. Figure 11 demonstrates how microstrips prepared from different films are able to induce attenuation in a 50 Ohm transmission line when pulsed overcurrent is produced during subnanosecond time.

For comparison of the attenuation properties, microstrips S1a, S2a, and S4a were cooled down to 70 K. The attenuation using microstrip S3a is presented for two temperatures 70 K and 80 K. According to figure 11, larger attenuation was realized using microstrips, whose films exhibit a wider TS temperature range.

6. Discussion

This investigation demonstrated that thin submicron thick YBCO films prepared on Al_2O_3 substrates with CeO_2 sublayers exhibit superconducting properties below temperatures ranging from 72 K to 84 K for different content of metal organic precursors and CeO_2 thicknesses. The significantly wider temperature range of TS for films prepared on thicker (440 nm) CeO_2 sublayers in comparison to the films deposited on thinner (160 nm) CeO_2 layers show that these films contained large numbers of structural imperfections having different superconducting properties. In case of the 160 nm thick CeO_2 layer, better matching of the lattice constants between the YBCO films and this layer is thus achieved, which makes it possible to prepare more perfect films having higher critical temperatures and lower TS temperature ranges. Moreover, an insert in figure 4 shows that films have macroscopic inhomogeneity of the properties resulting in wider TS temperature range for lower w microbridges. Also, it has to be stated that the less perfect films are preferable for certain applications as they can provide larger protection of the electrical circuits due to their wider resistive *I–V* characteristic state and thus be triggered more easily by an external magnetic field.

The application of an external DC magnetic field (B_{ex}) induces the RS, whose appearance can be well explained in terms of magnetic flux flow. When B_{ex} is applied at temperatures below T_{C2}, the critical magnetic field (B_c) obtained from the ΔR vs B_{ex} dependences, fit the classic rule $B_c \approx B_{c0}\left[1-(T/T_c)^2\right]$. According to the data presented in the insert of figure 5 for sample S1a, the $T_C \approx T_{C2} = 72$ K. At $T < T_{C2}$, if B_{ex} was higher when B_c the linear increase of resistivity with B_{ex} would demonstrate the validity of the Bardeen-Stephen model typical for flux flow in dirty superconductors [36]. The nonlinear behavior of ΔR vs B_{ex} at higher B_{ex} was also obtained in [37] and explained by the interaction between some vortices, which start to move at the banks of the grain boundary and contribute to higher voltage along the sample. In our case, such boundaries could be related to the structural imperfections of wide TS range films.

In case when $T_{C2} < T < T_{C1}$, some part of the microstrip is in a NS and the contribution of the magneto-resistive effect to the total resistance of the microstrip decreases. This is a result of essentially different behavior of the magneto-resistive effect, i.e. a decrease of the ΔR value with the increase of microstrip temperature T. Moreover, because the other superconducting regions of the microstrip are close to the critical temperature of the superconducting to NS transition, the external magnetic field is sufficiently strong and nears the critical field H_{C2} of type II superconductors. In this case as it was shown in [38], the reduction of the number of the quasiparticles participating in the energy dissipation in the d-wave vortex state produces the flux flow resistivity $\sim B_{ex}^{1/2}$ behavior.

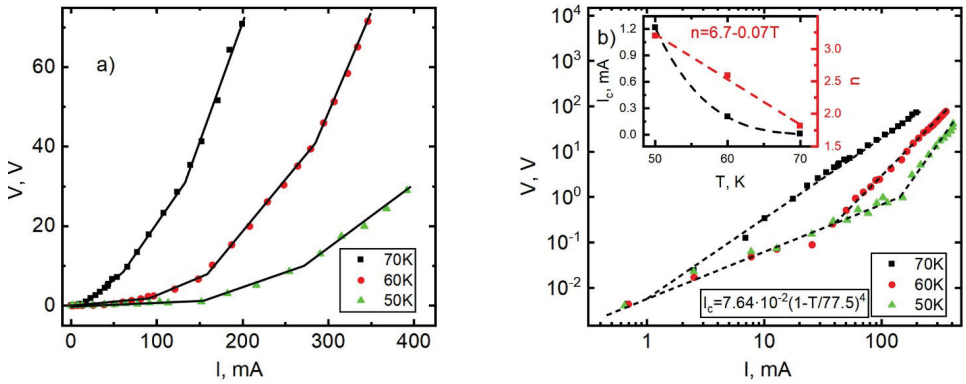

Figure 10. (a) *I–V* characteristics of S1a sample measured at the end of a square waveform electrical pulse rise time (≈1 ns). (b) The logarithmic plot of these *I–V* characteristics.

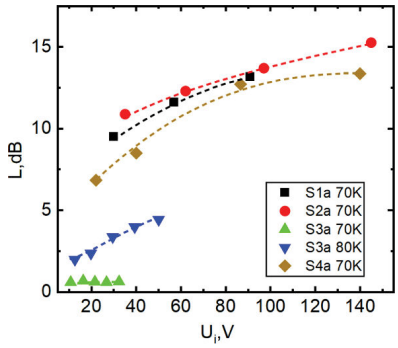

Figure 11. Attenuation of 50 Ohm transmission line (L) vs incident pulse voltage (U_i) for different microstrips prepared using films listed in table 1.

The electrical characteristics of the strip-like microbridges measured using DC bias exhibited strongly non-linear behaviors. We assume that the negative differential resistance region in the *V–I* curve (figure 6) as well as the resistance instability (figure 7) is the product of the current-induced flux flow RS and the thermal heating of the film, which is uniform along the whole microbridge length. Such model was successfully used to explain *I–V* characteristics of similar microbridges with widths ranging from 10 to 100 μm made from 0.15 μm thick epitaxial $YBa_2Cu_3O_{7-\delta}$ films grown on $SrTiO_3$ substrates [39, 40]. We also reject the 'hot spot' phenomenon during the thermo-electrical instability in our modeling, because, as it was shown in [41], there was no additional voltage jump in the *V–I* characteristics at the investigated temperature range.

For the numerical simulations of the microbridge behavior, we used the isothermal power-law relationship for type II superconductors obtained using nanosecond duration pulses (as suggested in [40]) with the experimental critical current I_c and the power-law index n dependences on temperature (see figure 10(b)):

$$I = I_c(T) \times \left(\frac{V}{V_c}\right)^{1/n(T)} \tag{3}$$

here V_c is the critical voltage ($E_c l = 0.3\ \mu$V) and I_c is the current at which V_c is reached. The resistance (R_t) of the microbridge obtained from Ohm's law is the following:

$$R_t(T) = V_c \times I^{n(T)-1} \times I_c^{-n(T)} \tag{4}$$

In order to simulate the *V–I* characteristic and the time evolution of the microbridge resistance, we calculated the temperature change of the microbridge when it was affected by the electrical current. This was done by using a heat balance equation where the increase in heat (dQ/dt) is equal to the difference between the Joule heating (VI) and Newtonian cooling ($k\Delta T$), assuming that the specific heat (C) of the YBCO material linearly increased with the temperature as:

$$C(T) = \gamma T + C_0 \tag{5}$$

where γ and C_0 are empirical constants. Taking formulas (1) and (2) into consideration and expressing V from equation (3), we obtained the following equation for the calculation of the temperature (T) vs time (t) dependence:

$$Dd_f \frac{dT(t)}{dt}(\gamma T(t) + C_0) = \frac{V_c I^{n(T)+1}}{lw} I_c(T)^{-n(T)} - k(T(t) - T_s) \tag{6}$$

here d_f is the microbridge thickness, D is the density of the YBCO material, k and T_s are the heat conductance and temperature of the substrate, correspondingly.

For simulation of the resistance dynamics when the microbridge was triggered by a pulsed magnetic field, the equation (6) was solved numerically. The solid line curves in

figure 7 show the modeling of the dynamic resistance response to the magnetic field pulse. At low currents ($I \leqslant 4$ mA), the value of the steady state resistance did not change with the applied magnetic field. At such times, the influence of the Joule heating induced temperature increase is negligible. However, at higher currents ranging approximately from 4 mA to 11.5 mA, the value of the steady state resistance reached after several seconds is the result of both the magnetic field and the increase of the microbridge temperature.

The essential change of resistance (R) vs time (t) dynamic behavior observed when under the influence of a 12 mA current can also be explained on the basis of the electro-thermal instability model. The solid line curve in figure 7 shows the simulation results using equations (4)–(6), demonstrating that the resistance grows relatively slowly at the beginning of magnetic field pulse and transforms into a rapid, avalanche-like increase of the resistance due to the heating of the tape. It has to be noted that both 'saturating' and 'unstable' types of R vs t dependences shown in figure 7 demonstrate qualitative agreement with microbridge temperature vs time dependences predicted in [40], which additionally confirms the electrothermal origin of the instability.

The I–V curves measured using DC were calculated by substituting the empirical $I_c(T)$ and $n(T)$ laws (equations (1) and (2)) into the power law equation (3). In the DC case, each point in the I–V dependence is stable because the YBCO microbridge is in thermal equilibrium. For this reason, the $\mathrm{d}T/\mathrm{d}t$ term in equation (6) is zero. This makes it possible to obtain a steady state temperature of the film (T_{fs}), which depends on the power ($P = I \times V$) dissipated in the film as $T_{fs} = IV/(wlk) + Ts$. The final equation for the current voltage relationship was obtained using (3) and replacing T in (1) and (2) by T_{fs}. This equation was solved numerically in respect to I for V values that ranged from 0 to 2 V, while looking for the smallest positive root. Experimental coefficient values were used for these calculations. The results are presented in figure 6 (black lines) and show good agreement with the measurements. This demonstrates that the I–V curve peculiarities in the DC mode can be well explained by Joules heating due to the induced flux flow resistance.

7. Conclusions

The properties of thin YBCO films prepared on Al_2O_3 substrates with CeO_2 layers by the PI-MOCVD method strongly depend on the content of the MOCVD precursors and the thicknesses of the CeO_2 sublayers. These factors influence the film's morphology, resistivity in their NS, the critical temperature of superconductivity and the temperature range of the transition from normal to the SS.

The exposure of a YBCO film cooled down to a SS to an external DC magnetic field slightly higher than the critical one causes the linear magneto-resistive effect, which is in accordance with the Bardeen–Stephen model typical for flux flow in dirty superconductors. If the film is in the temperature range of superconducting to NS transition, this corresponds to the condition where the external magnetic field is close to upper critical field of type II superconductors and the resistance change due to the magnetic field is proportional to the square root of this field. That is typical for d-wave vortices appearing due to the reduction of the number of the quasiparticles participating in the energy dissipation.

The current–voltage (I–V) characteristics of microbridges made from these films obtained using DC electrical current have demonstrated S-shaped behaviors, which can be triggered by an external magnetic field and be well explained by the thermo-electrical instability appearing as a result of the uniform Joule heating of the flux flow-induced RS of the superconducting film. Meanwhile, the resistive part of the I–V characteristics measured using high voltage nanosecond duration electrical pulses consists of several straight lines and is a result of the heating free flux flow. This RS is wider for films with large temperature ranges of superconducting to NS transition. These films are preferable for the design of fault current limiters as they exhibit low voltage thresholds and higher possibilities of transmission line attenuation.

The low dielectric constant and the high thermal conductivity of Al_2O_3 films with submicron thick CeO_2 layers make it possible to design multiuse superconducting protectors based on YBCO microbridges, which are able to protect high frequency 'front door' transmission lines against ultra-fast high voltage transients and low DC currents faults.

ORCID iDs

V Vertelis https://orcid.org/0000-0001-5298-5217
N Zurauskiene https://orcid.org/0000-0003-0912-4563

References

[1] Glasstone S *et al* 1977 *The Effects of Nuclear Weapons* (U.S. Department of Defense) (https://doi.org/10.2172/6852629)
[2] Friedman G and Orchard P 2018 The EMP threat: how it works and what it means for the Korean crisis *GeoPolitical Futures* (available at: https://geopoliticalfutures.com/emp-threat-works-means-korean-crisis) (Accessed 22 November 2020)
[3] Schneider M and Bartlett C R 2007 The emerging EMP threat to the United States (available at: www.nipp.org/wp-content/uploads/2014/12/EMP-Paper-Final-November07.pdf) (Accessed 22 November 2020)
[4] Oliveira D, Ghani N, Hayat M, Crichigno J and Bou-Harb E SDN testbed for evaluation of large exo-atmospheric EMP attacks 2019 *IEEE Commun. Mag.* **57** 88–97
[5] Coughlin C 2007 North Korea helping Iran with nuclear testing *The Telegraph UK* (available at: www.telegraph.co.uk/news/worldnews/1540429/N-Korea-helping-Iran-with-nuclear-testing.html) (Accessed 22 November 2020)
[6] Altgilbers L L *et al* 2000 Magnetocumulative generators *Magnetocumulative Generators* (Berlin: Springer) pp 57–123
[7] Barker R J and Schamiloglu E 2010 *High-Power Microwave Sources and Technologies* (New York: Wiley-IEEE Press)
[8] Drexler P and Fiala P Identifying of the special purpose generator pulses 2006 *PIERS Online* **2** 657–61
[9] Willett J C, Bailey J C and Krider E P 1989 A class of unusual lightning electric field waveforms with very strong high-frequency radiation *J. Geophys. Res.* **94** D13

[10] Meteolabor 2020 Lightning and EMP protection devices (available at: www.meteolabor.ch/fileadmin/user_upload/pdf/emc/All_Products_Catalog/Lightning_and_EMP_Protection_Devices_All_Products_e_2020.pdf) (Accessed 22 November 2020)

[11] Hao R, Zhang X, Gao H, Wu H, Cheng J and Li G-P A novel high-altitude electromagnetic pulse (HEMP) protection circuit for RF applications 2019 *Microelectron. J.* **84** 1–8

[12] Meteolabor MAK—modular attachment kit the complete EMC solution Meteolabor (available at: www.meteolabor.ch/fileadmin/user_upload/pdf/emc/MAK/System/ML_Fl_MAK_e_v1.pdf) (Accessed 22 November 2020)

[13] Wang K, Liu P, Qin Y, Huang J and Yi B 2017 A miniaturized self-actuated bandpass protection structure based on energy low-pass mechanism *2017 Int. Symp. Electromagn. Compat.—EMC Eur. 2017* pp 6–9

[14] Dong W, Wong J and Chen C 2002 Lightning electromagnetic radiation field spectra in the interval from 25 to 100 MHz *IEEE Int. Symp. Electromagn. Compat.* 2002 470–3

[15] Balevičius S, Anisimovas F, Balčiūnas V, Butkut R, Vengalis B and Flodström A S 1994 The electrical instabilities during ultra-fast SN switching in high-T_c thin film microstrip *Physica* C **235** 3377–8

[16] Altgilbers L L, Baleviciusa S, Zurauskiene N, Stankevic V, Cimmperman P and Anisimovas F 2003 Hybrid superconducting-magnetic fault current limiter *Digest Technical Papers-IEEE Int. Pulsed Power Conf.* 2 1040–3

[17] Liang L, Wang Y, Hu Y, Chen W and Yan Z 2019 Protection of electronic circuit based on YBCO superconducting thin film against the induced current interference *IEEE Trans. Appl. Supercond.* **29** 5000606

[18] Liang L, Wang Y, Yan Z, He Z, Wang P and Chen W 2019 Application of high-temperature superconducting small current limiting against over-current in low-noise amplifier electronic circuit *Physica* C **563** 28–32

[19] Belyaev B A, Govorun I V, Leksikov A A and Serzhantov A M 2012 Receiver protecting device based on microstrip structure with high-temperature superconductor film *Tech. Phys. Lett.* **38** 211–4

[20] Noe M and Steurer M 2007 High-temperature superconductor fault current limiters: concepts, applications, and development status *Supercond. Sci. Technol.* **20** R15

[21] Balevicius S *et al* 1993 Flux flow during high power nanosecond SN switching in thin high-T_c films *IEEE Trans. Magn.* **29** 3589–91

[22] Ricketts J, Vinen W F, Abell J S and Shields T C 1991 Flux flow and flux creep in thick films of YBCO *Physica* C **185** 2521–2

[23] Petrov M I, Balaev D A, Gokhfel'd D M, Shaikhutdinov K A and Aleksandrov K S 2002 Temperature evolution of the hysteresis in the current-voltage characteristic of a polycrystalline high-temperature superconductor with 1-2-3 structure *Phys. Solid State* **44** 1229–34

[24] Yurgens A 2011 Temperature distribution in a large $Bi_2Sr_2CaCu_2O_{8+\delta}$ mesa *Phys. Rev.* B **83** 2–7

[25] Bernstein P *et al* 2014 The role of a-axis grains in the transition to the normal state of $YBa_2Cu_3O_{7-\delta}$ films and of 2G-coated conductors when induced by high electrical current densities *J. Appl. Phys.* **115** 053910

[26] Rivera V A G, Stari C, Sergeenkov S, Marega E and Araújo-Moreira F M 2008 Manifestation of vortex depinning transition in nonlinear current-voltage characteristics of polycrystalline superconductor $Y_{1-x}Pr_xBa_2Cu_3O_{7-\delta}$ *Phys. Lett.* A **372** 5089–92

[27] Balchev N, Nenkov K, Mihova G, Pirov J and Kunev B 2010 Superconducting properties of Ca-doped $MoSr_2YCu_2O_{8-\delta}$ *Physica* C **470** 178–82

[28] Nazarova E, Zaleski A and Buchkov K 2010 Doping dependence of irreversibility line in Y1-xCaxBa2Cu3O7-δ *Physica* C **470** 421–7

[29] Balevičius S *et al* 1999 Fast high-voltage light triggered superconducting opening switch *J. Low Temp. Phys.* **117** 1561–5

[30] Kityk I V 2003 Photoinduced nonlinear optics methods as new methods of monitoring the superconducting films *Opt. Lasers Eng.* **40** 179–87

[31] Kazim S *et al* 2017 Light induced electron-phonon scattering mediated resistive switching in nanostructured Nb thin film superconductor *Sci. Rep.* **7** 1–10

[32] Morintale E, Constantinescu C and Dinescu M 2010 Thin films development by pulsed laser-assisted deposition *Phys. AUC* **20** 43–56 (http://cis01.central.ucv.ro/pauc/vol/2010_20_part1/2010_part1_43_56.pdf)

[33] Langner J *et al* 2006 Deposition of superconducting niobium films for RF cavities by means of UHV cathodic arc *Vacuum* **80** 1288–93

[34] Abrutis A *et al* 1998 High quality $YBa_2Cu_3O_7$ films grown on $LaAlO_3$ by single source pulsed metalorganic chemical vapor deposition *J. Cryst. Growth* **191** 79–83

[35] Suzuki S, Shimakage H, Kawakami A, Saito A and Takeda M 2013 Characteristics of MOD Bi-2212 thin films on r-cut sapphire with CeO_2 buffer layer *IEEE Trans. Appl. Supercond.* **23** 3–6

[36] Bardeen J and Stephen M J 1965 Theory of the motion of vortices in superconductors *Phys. Rev.* **140** A1197–207

[37] Diaz A, Mechin L, Berghuis P and Evetts J E 1998 Evidence for vortex pinning by dislocations in YBa_2Cu_3 $O_{7-\delta}$ low-angle grain boundaries *Phys. Rev. Lett.* **80** 3855

[38] Kambe S, Huxley A D, Rodière P and Flouquet J 1999 Low field scaling of the flux-flow resistivity in the unconventional superconductor UPt3 *Phys. Rev. Lett.* **83** 1842–5

[39] Maza J, Ferro G, Veira J A and Vidal F 2008 Transition to the normal state induced by high current densities in $YBa_2Cu_3O_{7-\delta}$ thin films: a thermal runaway account *Phys. Rev.* B **78** 94512

[40] Maza J, Ferro G, Osorio M R, Veira J A and Vidal F 2011 Analytical approach to the thermal instability of superconducting films under high current densities *Phys. Rev.* B **84** 214530

[41] Xiao Z, Andrei E and Ziemann P 1998 Coexistence of the hot-spot effect and flux-flow instability in high superconducting films *Phys. Rev.* B **58** 11185–8

4th publication / 4 publikacija

The Application of a CMR-B-Scalar Sensor for the Investigation of the Electromagnetic Acceleration of Type II Superconductors

V. Vertelis, S. Balevicius, V. Stankevic, N. Zurauskiene, and M. Schneider

Sensors, vol. **21**, no. 4, p. 1293 (2021)

DOI: 10.3390/s21041293

sensors

MDPI

Article

The Application of a CMR-B-Scalar Sensor for the Investigation of the Electromagnetic Acceleration of Type II Superconductors

Vilius Vertelis [1,2,*], Saulius Balevicius [2], Voitech Stankevic [2,3], Nerija Zurauskiene [2,3] and Markus Schneider [1]

[1] French-German Research Institute of Saint-Louis, 68300 Saint-Louis, France; MARKUS.SCHNEIDER@isl.eu
[2] Center for Physical Sciences and Technology, Department of Functional Materials and Electronics, LT-10257 Vilnius, Lithuania; saulius.balevicius@ftmc.lt (S.B.); voitech.stankevic@ftmc.lt (V.S.); nerija.zurauskiene@ftmc.lt (N.Z.)
[3] Faculty of Electronics, Vilnius Gediminas Technical University, LT-03227 Vilnius, Lithuania
* Correspondence: vilius.VERTELIS@isl.eu

Abstract: In this paper, we investigated the behavior of a type II superconducting armature when accelerated by a pulsed magnetic field generated by a single-stage pancake coil. While conducting this investigation, we performed a numerical finite element simulation and an experimental study of the magnetic field dynamics at the edge of the pancake coil when the payload was a superconducting disc made from $YBa_2Cu_3O_{7-x}$, cooled down to 77 K. The magnetic field measurements were performed using a CMR-B-scalar sensor, which was able to measure the absolute magnitude of the magnetic field and was specifically manufactured in order to increase the sensor's sensitivity up to 500 mT. It was obtained that type II superconducting armatures can outperform normal metals when the launch conditions are tailored to their electromagnetic properties.

Keywords: electromagnetic launch; type II superconductors; CMR-B-scalar sensor; magnetic field dynamics

Citation: Vertelis, V.; Balevicius, S.; Stankevic, V.; Zurauskiene, N.; Schneider, M. The Application of a CMR-B-Scalar Sensor for the Investigation of the Electromagnetic Acceleration of Type II Superconductors. *Sensors* **2021**, *21*, 1293. https://doi.org/10.3390/s21041293

Academic Editor: Cristina Gómez-Polo
Received: 19 January 2021
Accepted: 6 February 2021
Published: 11 February 2021

1. Introduction

Electromagnetic (EM) launch is a technology which produced a significant science-to-technology breakthrough in the field of solid body acceleration up to space velocities. The list of its possible applications includes space launch [1–3], transportation [4,5], material research [6–8] and even defense technologies [9–11]. A coil accelerator or coilgun, also known as a Gauss gun, is a type of electromagnetic (EM) launcher that accelerates ferromagnetic (reluctance coilgun) or conductive (induction coilgun) armatures to high velocities by employing magnetic fields. The lack of any physical contact between the barrel and the launch package as well as the absence of a propellant eliminates friction and reduces the mass of the launch package, while in turn reducing the amount of energy needed to reach the desired velocities. On the other hand, a complex modular power delivery system with high requirements for switches, real-time projectile tracking and control is required [9,12]. Joule heating, armature flux capture and structural integrity are the factors which limit the performance of metal armatures [13,14].

Type II superconductors are intriguing materials which behave very differently from normal conductors. These superconductors below their transition temperature T_c exhibit a near-zero resistivity when the currents through them are below a certain value called a critical current. The resistivity that emerges when the current approaches this critical value is not caused by electron scattering but rather by the motion of quantized magnetic field lines accelerated by the Lorentz force acting on them. Above the critical current, the resistivity of the superconductor increases rapidly, and the superconductor goes back into

its normal (resistive) state. This nonlinear behavior makes the electric and magnetic properties of these materials attractive for various applications [15–17], one of which is electromagnetic launching. The use of these materials as armatures for electromagnetic launchers can reduce some of the limitations imposed on normal conductors as well as cause some new unforeseen behavior.

At present, only a relatively small number of investigations of the electromagnetic launch of such superconducting armatures have been performed compared to those which investigated the launch of armatures made from normal metals. Calculations performed in [18] demonstrated that a pre-magnetized superconducting armature (using field-cooled magnetization (FCM)) can be accelerated more effectively by a pulsed magnetic field than an armature made from conventional metals. However, this method of acceleration is more complicated when compared to a non-magnetized (NM) superconducting armature, as it adds a preparation stage that requires energy. Another drawback when using a magnetized armature is that it can be necessary to move the armature to the optimal trigger position after the pre-magnetization process [18]. A simple NM armature acceleration method is thus preferable for space applications, such as active removal of space debris by a coilgun mechanism [19]. Unfortunately, up to now, incisive investigations of the electromagnetic launch of NM superconducting armatures have not been conducted.

In the past decade, due to developments in software and computing power, the modelling of the electrodynamic behavior of type II superconductors has become less restrictive, and good agreements between experiments and simulations have been achieved when investigating superconductor magnetization [20,21] and magnetic levitation [22–24]. Various eddy current problem formulations have been proposed, suited to handle different superconductor application scenarios or to improve computation times [25–29].

Experimental investigation of the magnetic field behavior when an armature is accelerated by a pulsed magnetic field is still problematic, regardless of the material used. In these setups, the magnetic field is highly inhomogeneous, and its magnitude changes rapidly as does its direction due to the movement of the armature. Thus, for high accuracy measurements, it is necessary to use an especially small, sensitive and fast sensor. These requirements are well met by the CMR-B-scalar sensor [30], which is able to measure the magnitude of the magnetic field independent of its orientation and has been successfully used in investigations of the EM acceleration of a metallic ring [31], cylindrical metallic armatures [32], as well as in studies of magnetic pulse welding of metals [33].

In this paper, we are presenting the results of both experimental and theoretical investigations of the electromagnetic acceleration of an NM armature made from a type II superconductor. For these studies, we used a disc-shaped superconducting armature made from bulk $YBa_2Cu_3O_{7-x}$ (YBCO) material, which was launched vertically by a magnetic field generated by a pancake coil. The investigation of the magnetic field dynamics was carried out by numerical finite element modelling (FEM) in combination with the experimental measurements obtained using a unique CMR-B-scalar sensor that was specifically adapted to the experimental conditions. The obtained results are compared with armatures made from high conductivity metals, such as copper and aluminum.

2. Experimental Setup

The electromagnetic acceleration of the superconducting armature was performed in a vertical arrangement. This allowed for easy cooling and did not require any mechanical guides for the armature. Moreover, by measuring the highest altitude reached by the armature and its time of flight, it was possible to easily evaluate the mechanical energy applied to the armature by the electromagnetic acceleration. The schematic diagram of the experimental setup used for these investigations is presented in Figure 1a. The magnetic field source used was a 13-turn pancake coil, made from an enameled copper wire (2 × 4 mm). The coil had an inner diameter of 1 cm, an outer diameter of 6.2 cm and was glued to a textolite housing, which was hollowed out to accommodate the pancake (the housing

is not shown in Figure 1a). The distance from the top of the pancake coil to the top of the housing was 2 mm. The isolation gap between coil windings was about 0.1 mm. The container for the liquid nitrogen, which served as a cryostat, was made from polystyrene and was mounted on top of the housing. The base of the cryostat on which the YBCO sample rested had a thickness of 5 mm; thus, the total distance between the surface of pancake coil and the superconducting armature was l_{cd} = 7 mm. The cryostat was closed with a lid, leaving an 8.5 cm distance for the projectile to travel vertically inside it.

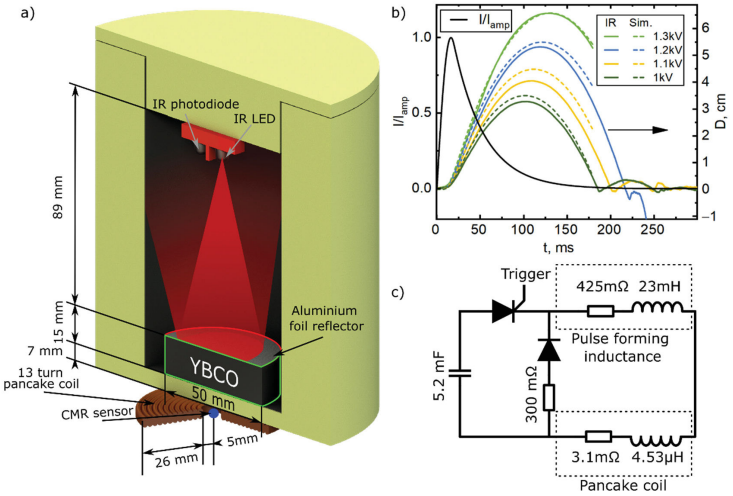

Figure 1. Experimental setup: schematic diagram and geometry of the coilgun (**a**), normalized current pulse produced by the pulse forming unit (black curve) and typical displacement measurements (**b**). An electrical diagram of the pulse forming unit is presented in (**c**).

For the superconductor launch experiments, a commercially available bulk single domain seed melt grown YBCO sample with a critical temperature of ~90 K [34] was used. The sample had a disc geometry with a diameter of d_D = 50 mm, a height of h_D = 15 mm and a mass (m) of 171 g. The disc was cooled down by slowly dripping liquid nitrogen onto it until the nitrogen began to wet the YBCO surface, after which the nitrogen was poured onto it until it was submerged. The experiments were performed once the nitrogen boiled off and was no longer visible at the bottom of the container in order to avoid any drag caused by the residual nitrogen.

Power to the pancake coil was delivered from a pulse forming unit (PFU). A schematic electrical circuit of the PFU is presented in Figure 1c. The PFU generated a single, tooth-shaped current pulse with a ~16 ms rise time and a ~150 ms decay ("tail") (see black curve in Figure 1b). The PFU capacitor bank was rated for 5 kV charging voltage and was able to produce about a 2.5 T amplitude magnetic field pulse at the center of the pancake coil. The PFU was equipped with a large (23 mH) pulse forming inductance (compared with the 4.53 μH of the pancake coil) in order to reduce the superconductor's influence on the total inductance of the circuit. This allowed the use of a standard pulse shape, regardless of the amplitude of the pulse or the presence of the superconducting armature. To

minimize the influence of the mechanical stress on the superconductor created by the transient magnetic field, the amplitude of the magnetic field pulse used for the EM acceleration was no more than 0.35 T. This magnetic pulse amplitude was able to launch the superconductor to the upper limits of our measuring range.

The CMR-B-scalar sensor used for the pulsed magnetic field measurements was made from a 0.4 μm thick La-Sr-Mn-O (LSMO) film grown onto a polycrystalline Al_2O_3 substrate by the pulsed injection metal–organic chemical vapor deposition technique [35]. For the relatively low magnetic field values (up to 0.3 T) used in our experiments, it was necessary to have an extremely sensitive sensor. This was achieved by using the special chemical content of the film, i.e., $La_{0.82}Sr_{0.18}Mn_{1.15}O_3$ with Mn excess. According to [36], the magnetoresistance of films with this content at room temperature is about 30% higher compared to films with stoichiometric Mn content. Another specific feature of our experiment was the highly inhomogeneous distribution of the magnetic field in the space between pancake coil and the superconducting armature where the sensor was placed. In such case, the accurate measurement of the local magnetic field requires a sensor with an extremely small active volume. For this reason, we used a CMR-B-scalar sensor with the following dimensions: 400 μm width, a 50 μm gap between electrodes and a 0.4 μm thickness. The effective volume of such sensor, estimated by using its highest dimension as its diameter, was $\approx 10^{-2}$ mm^3.

Manganites (LSMO) below the temperature of the transition from the paramagnetic to the ferromagnetic states (T_m) exhibit remnant magnetization [37]. Therefore, special procedures of calibration were required to avoid memory effects when the sensor was used at cryogenic temperatures [38]. This complicated the use of the CMR-B-scalar sensor in the vicinity of a superconductor cooled down to a liquid nitrogen temperature. To circumvent this, the CMR-B-scalar sensor was placed on the central axis of the pancake coil outside the cold zone, so that only the sensor's encapsulation touched the base of the cryostat. Thus, the active volume of the sensor was at a 7.5 mm distance from the bottom of the superconducting disc-shaped armature. As the temperature of the CMR-B-scalar sensor did not get much lower than room temperature, the sensor demonstrated no memory effects.

It should be noted that the magnetoresistance effect in such thin manganite films has a very low anisotropy (less than 2%) to the direction of the magnetic field when the value of this field is higher than 1T [39]. However, for lower fields, this anisotropy increases with the decreasing magnitude of the field, and in our case was about ±10%. In order to decrease the measurement error due to this anisotropy, we placed the sensor so that the thin film plane was perpendicular to the symmetry axis of the pancake coil. We estimated that a ten degree change in the field direction produces about a 0.3% measurement deviation from the real value.

For measurements of the vertical displacement of the superconducting armature, an analogue IR distance sensor was placed in the middle of the cryostat lid. This sensor measured the intensity of the reflected infrared light, which is a distance-dependent quantity. The bore of the cryostat was covered with an IR absorbing coating to reduce the background signal of the distance sensor. A reflector made from thin aluminum foil was mounted on the top surface of the YBCO disc to increase the reflectance and in turn, the signal at greater distances.

Our experiments began with the cooling procedure described above. Once the liquid nitrogen had mostly boiled off, the capacitor bank was charged to the desired voltage. After the liquid nitrogen was no longer visible at the bottom of the cryostat, the cryostat was carefully closed with the lid. The estimated disk temperature based on a measurement made using a resistive thermometer Pt-1000 placed at the bottom of the disk was ~76.6 K. Then, the capacitor bank was discharged through the pulse-forming inductance connected in series with the pancake coil. Typical disc trajectories can be seen in the top right of Figure 1b (colored solid curves). Artefacts seen in the trajectory after armature touchdown were caused by a physical rebound from the bottom of the container. After

the experiment, the sample was repositioned and resubmerged in nitrogen for a consecutive test

3. Experimental Results

Disk displacement (D) studies were performed in the free flight regime when the drag force caused by the surrounding nitrogen gas was negligible. To avoid any rotational motion of the disk-shaped superconducting armature that could lead to an unreliable signal from the IR sensor, the disk center, the pancake coil center and the magnetic field sensor were placed along the same axis. The experimental armature displacement vs. time curves are presented in the top right of Figure 1b. They consisted of several peaks, the first of which shows the armature movement due to the electromagnetic acceleration, while the others are the result of the disk bouncing from the bottom of the cryostat. As it can be seen, the front of the first peak exhibits two phases: a relatively slow (delay) altitude change that lasts approximately 15 ms after the beginning of the current pulse and corresponds to the current pulse rise time, and a fast phase, which lasts up to the time instant when the armature reaches its highest altitude. The displacement growth during the delay phase was more abrupt at higher capacitor bank charge voltages. The fast phase of the displacement curve can be well approximated by a parabolic law that is typical for free fall at the surface of the Earth.

Maximum displacements (D_m) in addition to direct readings of the IR sensor (labelled "Voltage" in Figure 2) were also estimated from the flight durations (labelled "Timing" in Figure 2) as the lift-off and touchdown events could be clearly identified from the displacement curves. The values of D_m for different capacitor charge voltages (from 1 to 1.3 kV) are presented in Figure 2. The experimentally used capacitor voltages corresponded to the 450, 490, 530 and 570 A current amplitudes I_{amp} flowing through the pancake coil. At higher charging voltages, the armature rose past the distance sensor calibration range, which covered nearly the whole cryostat. For voltages below 1 kV, the displacement readings were too small to be reliable, and no displacement was observed for voltages below 700 V when the Lorentz force was smaller than the weight of the YBCO disc. "Timing" and "Voltage" approaches gave similar results. D_m appeared to follow a nearly linear trend with increasing capacitor voltage within the investigated voltage range.

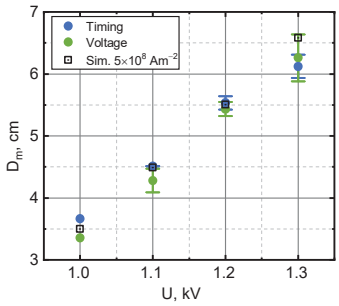

Figure 2. Maximum displacement (D_m) reached by the superconductor for different capacitor voltages. The height calculated from the flight duration is labelled "Timing". "Voltage" corresponds to the height measured by the sensor, and "Simulation" shows the results obtained from modelling with $j_C = 5 \times 10^8$ Am^{-2}.

Figure 3 shows the results of the magnetic field measurements using a CMR sensor placed, as shown in Figure 1a, during experiments with and without the superconductor. In the case of the empty cryostat experiments (labelled "Without SC"), the magnetic field

pulses had the same waveforms as the current pulses flowing through the pancake coil. Introducing the superconductor significantly changed the magnetic pulse waveforms coming from the empty cryostat case. The superconducting disk caused a decrease in the magnetic field magnitude. This decrease was strongly expressed in the beginning of the magnetic field pulse and partially covered the pulse decay period. The difference between the reference field magnitude ("Without SC") and the one during launch ("With SC") gradually disappeared as the superconducting armature moved away from the pancake coil and its influence on the field in the sensor position diminished. The time until the magnetic field value for "Without SC" and "With SC" became the same, decreased with the increasing capacitor bank charging voltage and was approximately equal to the delay time visible in the displacement vs. time curve (see Figure 1b). This shows that the electromagnetic interaction between coil and superconducting disk mainly took place during this time period.

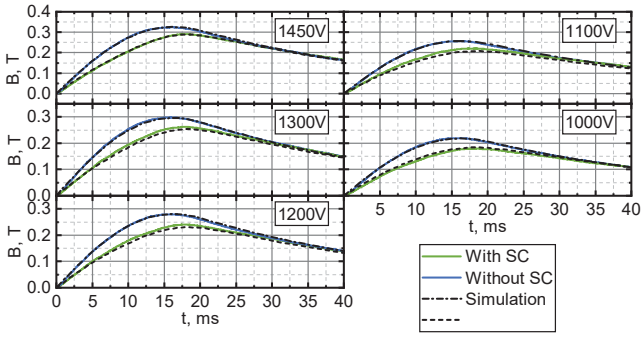

Figure 3. Magnetic field dynamics: the blue curves show the measured field with the empty cryostat. The green curves represent the measurements during the acceleration of the superconductor. The dashed lines are the simulation results of the reference field and the field during superconductor acceleration ($j_C = 5 \times 10^8$ Am^{-2}) for the corresponding capacitor charge voltages.

4. Simulation Background

The behavior of our experimental setup was also investigated numerically. Figure 4 shows the principal geometry used in our modelling. The dimensions of the superconducting domain used for simulation were the same as that of the sample's used in the experiments. The nonlinear eddy current problem was solved in the armature's frame of reference using Maxwell's equations in their H-formulation (H-form) in 2D axis-symmetric form using Comsol Multiphysics commercial software:

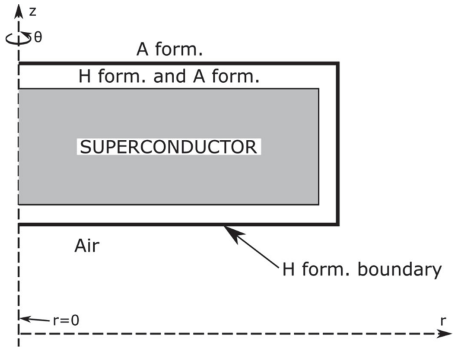

Figure 4. Model geometry: the superconductor domain is represented by the grey square, and the air domain is left white.

$$\nabla \times \boldsymbol{E} + \mu \frac{\partial \boldsymbol{H}(t)}{\partial t} = 0, \tag{1}$$

$$\nabla \times \boldsymbol{H} = \boldsymbol{j}. \tag{2}$$

Here, $\boldsymbol{E}$ is the electric field (bold symbols represent vectors), μ—the magnetic permeability, $\boldsymbol{H}$—the magnetic field and $\boldsymbol{j}$—the current density. Different $\boldsymbol{E}$ substitution laws were used for the air and superconductor domains. The air was described as having linear resistivity $\boldsymbol{E} = \rho \boldsymbol{j}$, while a power–law relationship was used for the superconducting domain.

$$\boldsymbol{E} = E_C \left(\frac{|\boldsymbol{j}|}{j_C} \right)^n \frac{\boldsymbol{j}}{|\boldsymbol{j}|} \tag{3}$$

Here, E_C is the critical electric field (by convention 1 μV/cm), j_C is the current density at which the critical electric field is reached and n is a parameter that describes the "hardness" of the superconductor and models the "steepness" of the superconducting-normal transition. Generally, j_C depends on the magnetic field and the temperature. These dependencies were neglected in our model, and a constant j_C was assumed. This is physically accurate when the sample does not heat up, and a slowly varying region of the $j_C - H$ curve is reached.

The H-form problem is a boundary value problem with a boundary condition [22]:

$$\boldsymbol{H}(r, z, t) = \boldsymbol{H}_{SC} + \boldsymbol{H}_{PC}. \tag{4}$$

Here, $\boldsymbol{H}_{SC}$ is the magnetic field generated by the eddy currents inside the superconductor and $\boldsymbol{H}_{PC}$ is the field generated by the pancake coil. $\boldsymbol{H}_{PC}$ is the product of the current pulse $I_{amp} \cdot G(d \cdot t)$ (I_{amp} is the amplitude of the pulse, G represents the pulse waveform seen in Figure 1b, t is the time and d is the pulse duration multiplier. $d = 1$ corresponds to the experimental pulse). The magnetic field generated by the coil thus was:

$$\boldsymbol{H}_{PC} = \boldsymbol{F}(r, z + l_{cd} + D(t)) \cdot I_{amp} G(d \cdot t). \tag{5}$$

Here, the $\boldsymbol{F}(r, z)$ is the spatial magnetic field map of the pancake coil, which was calculated separately. $\boldsymbol{H}_{SC}$ was calculated in a separate A formulation module (magnetic fields in AC/DC module) using the current density calculated in the H-form module as an input and treating the entire model domain as air to avoid a secondary generation of eddy currents.

The electrodynamic problem was solved in the superconductor's frame of reference, offsetting the magnetic field map by the solution of the mechanical problem $D(t)$ for each time step. The displacement, velocity and acceleration were calculated from the Lorentz force, taking gravity into account. Since the problem is axially symmetric, the dynamic equation for the vertical displacement (D) was:

$$m\frac{d^2D(t)}{dt^2} = \int (j_\theta \cdot \mu H_r)dV \; - mg. \tag{6}$$

Here, m is the disk mass (in our calculations 171 g), and j_θ and H_r are current density and magnetic field components in θ and r directions. V is the disk volume, and g is the standard gravity (9.8 m/s²).

5. Simulation Results and Discussion

For the analysis of the experimental results presented in Figures 1–3 (D vs. t, D_m vs. capacitor bank voltage U and B vs. t at sensors position), we performed calculations using the mathematical procedures presented in Section 4. In our model, the superconductor was described by two parameters: j_C and n. The value of the parameter n was chosen to be 20, because at that value, it describes a hard super-conductor with a flux-creep regime [40], which is the most common kind supported by the literature [18,21,41]. The dashed curves in Figure 1b show the modelling results of the D vs. t dependence. As it can be seen, it well demonstrates all the features of the disc movement obtained experimentally (delay and parabolic phases). Good quantitative agreement (in the frame of experimental error) between the experiments and the calculations was achieved using $j_C = 5 \times 10^8$ A/m^2. In order to estimate how reasonable this value was, we calculated the j_C using the trapped magnetic field ($B_t = 1.2 - 1.3$ T) measured at 77 K temperature 1 mm above the superconductor's surface, which was included in the data sheet provided by the disk manufacturer [34]. This estimation was performed using an analytical formula (7) derived from the Biot–Savart law by its direct integration over a cylindrical domain populated by a constant current density directed azimuthally:

$$j_C = \frac{2B_t}{\mu}\left((z-d)\ln\left|\frac{\sqrt{a^2+(z-d)^2}+a}{(z-d)}\right| - (z+d)\ln\left|\frac{\sqrt{a^2+(z+d)^2}+a}{(z+d)}\right|\right)^{-1}. \tag{7}$$

Here, B_t is the trapped field, a is the radius of the disk, d is its half height and z is the distance between the center of the disk and the point at which the trapped field was measured (on the central axis of the disk). A j_C in the range 1.2–1.3× 10^8 A/m² was obtained. A four times higher j_C value that was satisfactory to match our modelling with the experiments can be easily explained by the significantly lower magnetic field (0.35 T) in our experiments than the one generated by the magnetized sample according to the datasheet. Such bulk superconductor j_C behavior was provided by the disc manufacturers in [42].

Using fixed j_C and n values (5×10^8 A/m^2 and 20, respectively), the obtained simulations were in good agreement with the experimental data (maximal displacement D_m for different U) that is presented in Figure 2. D_m was evaluated from the calculated D vs. t curves, taking the peak value. Modelling based on equations presented in Section 4 allowed the simulation of the magnetic field dynamics measured by a CMR-B-scalar sensor (see Figure3) in both the "Without SC" (dashed–dotted curves) and "With SC" (dashed curves) cases. As it can be seen from Figure 3, the B vs. t dependences measured during the launch of the superconducting disk can be well described by simulations using the same j_C and n parameters that were used for the simulation of D vs. t and D_m vs. U.

Good agreement between the simulation and the experimental results demonstrated that the modelling method in the armature's frame of reference, neglecting Joule heating, is suitable for the study of the behavior of type II superconductors during an electromagnetic launch. In the following sections, we present theoretical studies of this configuration, which were outside the limits of our experimental capabilities. We investigated different

scenarios with different pancake current waveforms: "step-like" (1 ms rise time) and "experimental" (Figure1b). In addition, we investigated the effects of critical current density, the armature starting distance from the driving coil and the pulse duration using the experimental current pulse waveform. The performance of the superconducting armatures was compared with Cu and Al armatures of the same geometry, cooled to 77 K.

5.1. Influence of j_C on Energy Conversion

In a vertical acceleration arrangement, the total mechanical energy is the sum of its kinetic energy and potential energy. During acceleration, this energy evolves over time until a steady value W_{tot} is reached. This energy value depends on the electromagnetic energy generated in the pancake coil and the electromagnetic interaction between the superconducting armature and the coil. With a fixed coil current pulse waveform, the amplitude I_{amp} and the armature geometry W_{tot} depends only on the magnitude of j_C. Calculations of the j_C influence on W_{tot} transferred to the armature at different coil current amplitudes were performed using experimental armature geometry at two starting distances from the surface of the pancake coil and the superconducting armature: 7 (our experimental condition) and 5 mm, presented in Figure 5. Initially, as can be seen in Figure 5, an increase in the j_C leads to an increase in W_{tot} transferred to the superconductor, but with sufficiently high j_C, this transfer tends to saturate. This can be explained by the decrease of the magnetic field penetration depth, which becomes shallower and approaches a surface field limit due to the increase in the j_C. This depth then again increases with the field amplitude and the surface current limit is pushed to higher j_C values. As can be seen in Figure 5, under otherwise identical launch conditions (pulse waveform and amplitude), a decrease in the distance between the pancake coil and the superconducting armature l_{cd} increases the W_{tot} value. Lowering the l_{cd} by 2 mm causes increases in the W_{tot} of about 40%, 27% and 22% for pulse amplitudes of 0.53, 1 and 1.5 kA, respectively. These results indicate a way of making more economical launch systems. Relatively high launch efficiency can be reached using a superconductor with a relatively low j_C. Thus expensive, high j_C armature material could be replaced by materials with a lower j_C without a significant decrease in the launch efficiency.

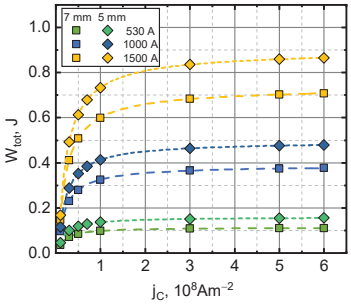

Figure 5. The influence of the critical current density on the total mechanical energy transferred to the superconductor for different current pulse amplitudes and starting heights. The symbols represent the simulation data. The lines are the logistic function fits $(y(x) = (c_1 - c_2)/(1 + (x/x_0)^p) + c_2)$.

5.2. Effects of Pulse Amplitude

To investigate the behavior of an electromagnetic superconductor launch in a broader range, we performed numerical calculations outside the current amplitude range that our experimental setup could withstand. Two sets of l_{cd} and j_C were investigated

(7 mm with 5×10^8 A/m^2 and 5 mm with 3.55×10^7 A/m^2). The first one corresponded to the experimental conditions. The second set produced values of W_{tot}, which were close to those obtained in the experimentally investigated scenarios, only with a 2 mm shorter starting distance l_{cd}. This set illustrates the worst case that could be justified by experimental error. The performance of the superconductors was also compared with armatures of the same geometry, which were made from copper and aluminum, the materials most commonly used today. We assumed the temperature of liquid nitrogen for all of the materials to make the comparisons fair. Masses and resistivities of the armatures used in the simulations were $m = 264$ g and $\rho = 2.65 \times 10^{-9}$ Ωm for copper and $m = 79.5$ g and $\rho = 4.44 \times 10^{-9}$ Ωm for aluminum. The results obtained from the simulations are presented in Figure 6 (points up to 600 A correspond to the experimental values). As can be seen, an increase in the current amplitude resulted in a higher energy being transferred to all the armatures. For the superconducting armatures, this increase is larger in the lower amplitude range ($W_{tot} \propto I_{amp}^{\sim 2}$) and reduces to a nearly linear relationship for the first parameter set and a sublinear one for the second set. Superconducting armatures performed better than the normal metal ones at these lower current pulse amplitudes in both cases. This advantage decreased with the current pulse amplitude, and in the second parameter set case, copper overtook the superconductor at $I_{amp} \approx 3.7$ kA. By extrapolating the data, copper is expected to overcome the superconductor at 43 kA in the first parameter set case.

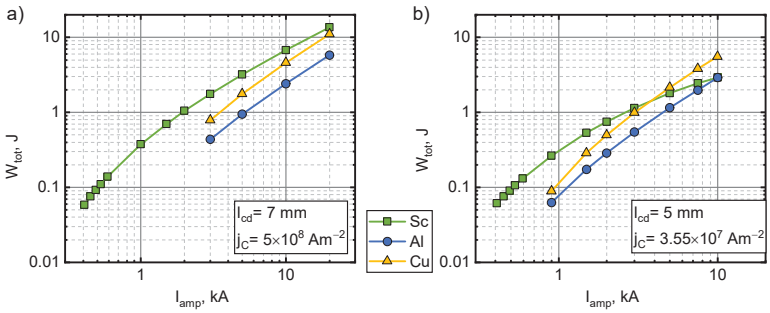

Figure 6. The influence of the current pulse amplitude on the total mechanical energy transferred to an armature made from a type II superconductor, copper or aluminum for the experimental pulse shape and duration. $l_{cd} = 7$ mm, $j_C = 5 \times 10^8$ A/m^2 (**a**) and $l_{cd} = 5$ mm, $j_C = 3.55 \times 10^7$ A/m^2 (**b**).

5.3. The Influence of Pulse Duration

The energy obtained by the superconducting armature due to electromagnetic acceleration depends on the duration of the coil current pulse. In addition, the launch process is complicated by the large magnetic field gradient through which the armature passes during acceleration. To investigate how W_{tot} depends on pulse duration (d), we performed calculations using pulses with a fixed current pulse amplitude (1.5 kA) and the waveform shown in Figure 1b, scaled in time by a factor of d. d is the relative pulse time duration, and its value represents how many times the pulse duration is shorter. The experimental pulse duration was taken to be $d = 1$.

Figure 7 illustrates the effects of the d value on W_{tot} in each of the parameter sets. In the case of the first parameter set, the superconductor outperformed the metal armatures within the entire investigated duration range. However, this advantage of the superconducting armature was lower in the case of the second set of values and disappeared when the pulse duration was four times shorter. The metal armatures also showed improvement when brought close to the field source due to the increased magnetic coupling.

All of the materials exhibited a peak in their W_{tot} vs. d dependence. The superconductor peaked at a ~2 times shorter pulse for the first set and ~1.5 times shorter for the second one and was ~3 and ~1.5 times more effective than the Cu armature at the same pulse length. Such behavior can be explained by examining both the very long and the very short pulses. At the very short magnetic field pulses, the armature can be considered stationary throughout the pulse. In such cases, the force applied to the armature is proportional to the amplitude of the field for both the metal and superconducting armatures. When the pulse amplitude is kept constant, an increase in the pulse duration acts only by increasing the interaction time between coil and armature, which increases the energy transferred to the armature. However, under the action of a long pulse, the position of the armature cannot be considered static. At a certain moment, the driving force overcomes gravity, and the armature starts to move away from the coil. As it does so, the coupling to the coil decreases and the utilization of the remaining part of the magnetic field pulse for the energy transfer becomes smaller. In the metal armature cases, this increase in the pulse duration also reduces the driving force as the eddy currents decay over time and the field penetrates deeply into the armatures. This explains why metal armatures peaked at higher values of d. The results obtained show that the superconductor can be effectively accelerated using slower magnetic pulses. This opens up possibilities of using cheaper power sources, which do not require fast, high power switching to drive the coil.

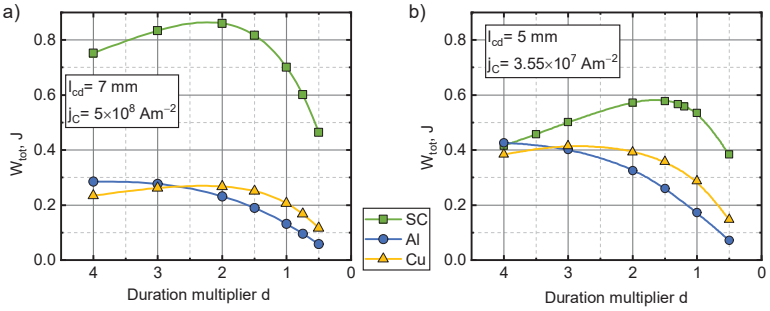

Figure 7. The influence of pulse duration on the total mechanical energy transferred to armatures made from type II superconductor, copper or aluminum. The pulse amplitude was 1. 5 kA. $l_{cd} = 7$ mm, $j_C = 5 \times 10^8$ A/m^2 (**a**) and $l_{cd} =$ 5 mm, $j_C = 3.55 \times 10^7$ A/m^2 (**b**).

5.4. Step-Like Field Pulses

The effects of pulse duration showed that the superconducting armature is better than the metal ones at longer pulses. For this reason, we investigated the effects of step-like (rise time of 1 ms) current pulses and their amplitude. This pulse shape has both a high magnetic field transient in the beginning of the pulse and a constant field afterwards. The results for this scenario can be seen in Figure 8. Initially, the energy transferred to the armature increased with the increasing magnitude of the applied field. For the first set of parameters, W_{tot} for the superconductor increased with I_{amp} by a power of 1.7, while for the metals, this power was 2.3. In case of the second set of parameters, the power index of this relationship for metals did not change much and stayed at about 2.5. For the superconducting armature, the initial growth power of ~1.5 decreased with I_{amp} and W_{tot} and began to decrease for the higher values of I_{amp}. The superconductor outperformed the metals until the amplitude of the step reached ~7.5 and ~1.15 kA for the first and second parameter sets, respectively. This relatively low current crossover point was in part caused by the strong braking of the superconducting armature (see analysis presented in the next section).

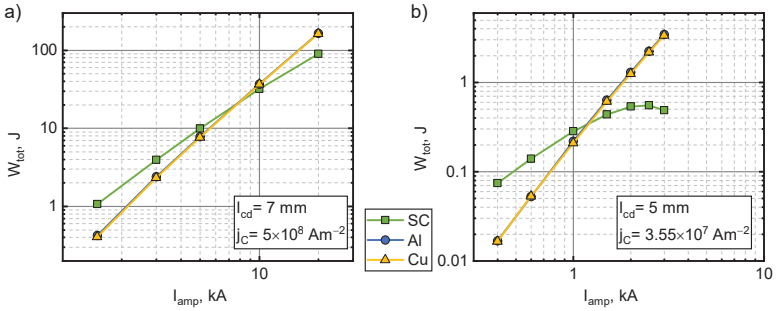

Figure 8. The influence of step-like current pulse amplitude on the total mechanical energy transferred to an armature made from type II superconductor, copper or aluminum. $l_{cd} = 7$ mm, $j_C = 5 \times 10^8$ A/m^2 (**a**) and $l_{cd} = 5$ mm, $j_C = 3.55 \times 10^7$ A/m^2 (**b**).

5.5. Magnetic Braking

The magnetic braking phenomenon is important for the operation effectiveness of inductive electromagnetic launchers. It is caused by the interaction between an armature and the magnetic field source when the flux that has already penetrated the armature begins to decrease. Magnetic field penetration into the armature is called armature capture [43]. At a certain acceleration stage, it decreases the armature driving force and consequently the efficiency of the synchronous wave induction coilguns, which use metal as the material for the projectile. During electromagnetic acceleration, the flux through an armature can decrease due to the decrease in the external field when the driving current begins to fall or due to its motion in a large magnetic field gradient. When this flux starts to decrease, a counter current is induced. This current then flows in the same direction as the current in the coil, and an attractive force component is introduced. In some cases, this attractive force can overcome the propelling force, and the armature is decelerated.

We obtained that this breaking phenomenon in the case of the superconducting armature is well expressed in the case of step-like pulses. Figure 9 illustrates the evolution of the mechanical energy ($W_{me}(t) = W_{kinetic}(t) + W_{potential}(t)$) over time when a superconducting armature is being accelerated by a step-like pulse, using the second set of parameters. It depicts the transition between no braking and the considerable braking regimes. For low current amplitudes, the W_{me} steadily approaches a constant value (W_{tot}). The W_{me} vs. t dependences at higher current amplitudes have a maximum (W_{max}) that is reached in the beginning of the acceleration, after which they decay to a steady value of W_{tot}, which we consider to be the total energy transferred to the armature. The energy lost to magnetic braking or the braking energy is the difference between the W_{max} and W_{tot}.

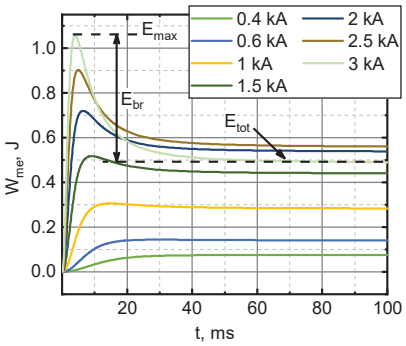

Figure 9. Evolution of the mechanical energy of the superconducting armature over time when the armature was accelerated by a step-like driving current pulse. l_{cd} = 5 mm, $j_C = 3.55 \times 10^7$ A/m^2.

No magnetic braking was observed in the critical current density parametric sweep. The values of W_{br} for all the other investigated scenarios can be seen in Figure 10. The strongest braking was observed using step-like pulses when W_{br} increased with I_{amp} by the power of ~3.5 and ~3 for the first and second sets, respectively, for the superconducting armature. This strong dependence was the reason why W_{tot} started to decrease with the higher values of I_{amp} when using the second set. Meanwhile, metals showed a nearly linear behaviour. It needs to be noted that even though the power of the relationship was higher for the superconducting armatures, they lost less energy than the metals along a wide range of I_{amp}. Magnetic braking could be minimized by rapidly switching the driving current off when the acceleration of the superconducting armature approached zero.

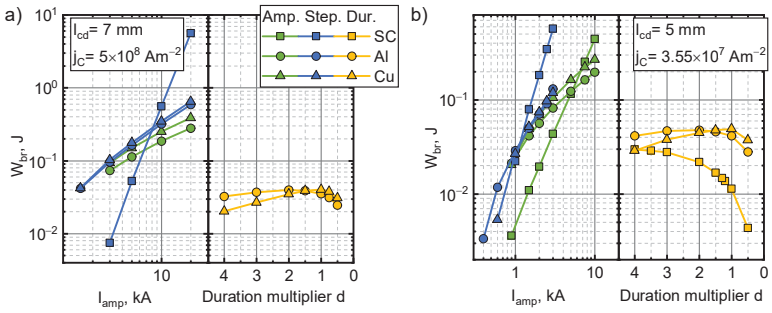

Figure 10. Total mechanical energy lost to magnetic braking. The green line (left) illustrates the effect of the experimental pulse shape amplitude, the blue line, the step-like current pulse amplitude. The yellow line(right) depicts the effects of the pulse duration. l_{cd} = 7 mm, $j_C = 5 \times 10^8$ A/m^2 (**a**) and l_{cd} = 5 mm, $j_C = 3.55 \times 10^7$ A/m^2 (**b**).

No braking occurred using the first set of j_C and l_{cd} for the superconducting armature when the simulations were performed using the experimental pulse waveform. It was, however, observed when using the second set of parameters. In this case, the W_{br} followed a parabolic behaviour ($\propto I_{amp}^{\sim 2}$). Meanwhile, the braking energy for the metals again satisfied a nearly linear trend.

For the pulse duration sweep, the W_{br} of the metal armatures was similar for both starting distances. The superconductor did not show braking with the first set of parameters. The W_{br} seemed to approach a maximum for high d and decreased as d approached 0 with the second set. This behaviour of W_{br} can be explained in the same manner as in the case of W_{tot}. At short pulses, the braking energy is mainly dependant on the interaction time and increases with the increasing pulse length. For long pulses, the armature moves away from the coil, thus reducing the magnetic coupling and thereby reducing the energy transfer between the coil and the armature.

Figure 11 shows the induced current density distributions along a vertical line at r = 1 cm at different time instances when armatures were accelerated by an experimental pulse with an amplitude of 3 kA. The current density in the Cu armature (as well as in all other normal conductors) decays both in time and along the line, going deeper into the sample. This results in the current density being strongest near the bottom of the sample, where the magnetic coupling to the driving coil is the strongest. In the superconducting armature case, the current density distribution is rectangular and close to j_C in magnitude. A high dB/dt induces an overcritical current density that is highest near the driving coil. This current also decays in time, but the decay rate is negligible below j_C. The result of this is the generation of two opposite currents circulating within the superconductor, which are located near the surface when the magnetic pulse begins to decrease. For this reason, there is always a non-negligible accelerating force component that mitigates the braking, and superconductors lose less W_{br} than the metals. It follows that larger W_{br} should be expected in situations where the magnetic field penetration depth is large, as the accelerating current would then be situated further away from the coil. This argument agrees well with the braking results discussed earlier (note W_{br} vs. I_{amp} dependences for experimental and step-like current pulses).

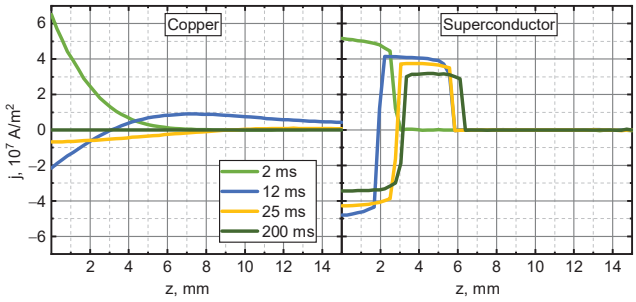

Figure 11. Current density distributions in the copper and superconducting armatures (second set of parameters) along a vertical line 1 cm from the center at different times when accelerated by an experimental current pulse of 3 kA amplitude. $l_{cd} = 5$ mm, $j_C = 3.55 \times 10^7$ A/m^2.

Overcritical current densities have to produce substantial Joule heating in the superconductors due to the power-law $E - j$ relationship. For this reason, rapidly changing the magnetic field pulses should be avoided, as it increases the armature temperature and lowers the j_C. This could damage the armature due to thermal shock. A reasonably slow magnetic field ramp-up to a constant value would mitigate this problem. This field should move synchronously with the superconductor to produce constant acceleration.

The nonhomogeneous current distribution in the armature is important not only for the magnetic braking phenomenon but also for the optimal armature geometry design. Figure 12 shows the current density distribution within a superconducting armature (j_C

= 3.55×10^7 A/m^2) 200 ms after a 3 kA experimental pulse. The regions carrying no current only contribute to the total mass of the projectile and are not utilized for its acceleration. The magnetic field did not fully penetrate the superconductor in any of the regimes tested. This suggests that an armature geometry optimization is required to achieve efficient and cost-effective launch setups. The optimized shape will depend on the magnetic field distribution, its amplitude as well as the critical current density of the superconductor.

The examples discussed in this paper illustrate the main differences between normal metals and type II superconductors in coil accelerator applications. When normal metals are used, the induced current density is proportional to the magnetic field derivative and the resistivity of the material. Due to resistive losses, the field diffuses into the normal metals. When superconductors are used, the eddy currents are limited near the value of j_C by the highly nonlinear $E - j$ relationship (Equation (3)). For these reasons, these two kinds of materials behave differently in coilgun scenarios. Normal metals require the transient magnetic field to be accelerated, while superconductors can be accelerated by a time constant field (provided it has a gradient). This modifies the requirements for coilgun design and the design of its power supply. A slow field ramp-up is desired to avoid armature heating. A magnetic field wave of a constant amplitude travelling synchronously with the superconducting armature would provide constant acceleration without a time limit in contrast to normal metals where the acceleration decreases due to the armature capture.

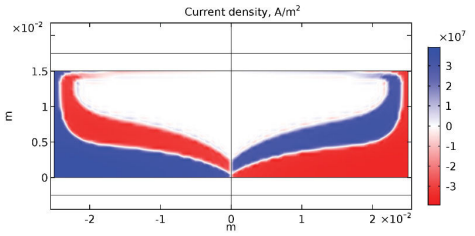

Figure 12. Current density distribution within the superconducting armature for an experimental current pulse with an amplitude $I_{\text{amp}} = 1.5$ kA, $j_C = 3.55 \times 10^7$A/m^2, $l_{cd} = 5$ mm at $t = 0.2$ s after the beginning of the pulse.

6. Conclusions

In this paper, we investigated the behavior of an electromagnetically accelerated disk-shaped superconducting YBCO armature cooled to 77 K. The acceleration was performed in a vertical arrangement using a single-stage pancake coil. The vertical displacement of the disk was measured using an IR distance sensor, and the magnetic field was measured using a CMR-B-Scalar sensor with small dimensions, which was able to measure the local magnitude of the magnetic field independent of its direction. It was observed that the motion and the magnetic field dynamics agreed well with the numerical simulations based on Maxwell's equations in their H-formulation, assuming that the superconductor is a nonlinear conductor with a power-law $E - j$ relationship using realistic values of j_C. The numerical investigations showed that a higher critical current density of the superconductor increased the mechanical energy transferred to the superconducting armature. This energy, however, had a limit for a given accelerating coil current pulse and armature starting position. The performance of the superconducting armature was numerically compared to normal metal armatures, cooled to liquid nitrogen temperature. This comparison showed that an increase in the current amplitude resulted in higher energy being transferred to all these armatures. For the superconducting armature, this increase was larger in the lower amplitude range and then was reduced to a nearly linear or

sublinear relationship depending on the parameter set used for the calculations. Thus, the use of superconducting armatures was advantageous in the lower pulse amplitude range. Investigations of the influence of the pulse duration performed using pulses with a fixed current pulse amplitude and an experimental waveform demonstrated that the superconductor outperforms normal metals when accelerated by magnetic pulses with smaller time derivatives. Simulations using a step-like driving current pulse also revealed that superconductors again outperform normal metals using lower current amplitudes. The range in which they did so was, however, reduced by the strong magnetic braking caused by persistent currents. The mechanical energy lost to the magnetic braking had the strongest dependence on the pulse amplitude for step-like pulses, where the interaction was not mitigated by the reduction in the driving current. As eddy currents in type II superconductors do not decay past the critical current density, the use of superconducting armatures reduces the armature capture limitation and can increase the effectiveness of synchronous induction coilgun launchers.

Author Contributions: V.V. designed and performed the experiment, analyzed the results, built the FEM model and obtained the numerical results, and wrote the manuscript. V.S. and N.Z. developed the CMR-B-scalar sensor. S.B. and M.S. supervised the process and revised the manuscript. All authors have read and agreed to the published version of the manuscript.

Funding: This research received no external funding.

Conflicts of Interest: The authors declare no conflict of interest.

References

1. Hundertmark, S. Applying railgun technology to small satellite launch. In Proceedings of the 5th International Conference on Recent Advances in Space Technologies—RAST2011, Istanbul, Turkey, 9–11 June 2011; pp. 747–751, doi:10.1109/RAST.2011.5966941.
2. McNab, I.R. Progress on hypervelocity railgun research for launch to space. *IEEE Trans. Magn.* **2009**, *45*, 381–388, doi:10.1109/TMAG.2008.2008601.
3. Lehmann, P.; Reck, B.; Vo, M.D.; Behrens, J. Acceleration of a suborbital payload using an electromagnetic railgun. *IEEE Trans. Magn.* **2007**, *43*, 480–485, doi:10.1109/TMAG.2006.887666.
4. Kaye, R.J.; Turman, B.N.; Shope, S.L. Applications of coilgun electromagnetic propulsion technology. In Proceedings of the Conference Record of the Twenty-Fifth International Power Modulator Symposium, 2002 and 2002 High-Voltage Workshop, Hollywood, CA, USA, 30 June–3 July 2002; pp. 703–707, doi:10.1109/modsym.2002.1189573.
5. Bertola, L.; Cox, T.; Wheeler, P.; Garvey, S. Superconducting and conventional electromagnetic launch system for civil aircraft assisted take-off. In Proceedings of the ECCE 2016—IEEE Energy Conversion Congress & Expo, Milwaukee, WI, USA, 18–22 September 2016; Volume 26, doi:10.1109/ECCE.2016.7855477.
6. Gores, P.A.; Vincent, G.; Schneider, M.; Spray, J.G. Appraisal of Rapid-Fire Electromagnetic Launch Effects on Ceramic Targets. *IEEE Trans. Plasma Sci.* **2019**, *47*, 4175–4180, doi:10.1109/TPS.2019.2921731.
7. Schneider, M.; Vincent, G.; Hogan, J.; Spray, J. The use of a railgun facility for dynamic fracture of brittle materials. In Proceedings of the 2014 17th IEEE International Symposium on Electromagnetic Launch Technology, La Jolla, CA, USA, 7–11 July 2014; pp. 1–5.
8. Vricella, A.; Delfini, A.; Pacciani, A.; Pastore, R.; Micheli, D.; Rubini, G.; Marchetti, M.; Santoni, F. A new advanced railgun system for debris impact study. *Procedia Struct. Integr.* **2017**, *3*, 545–552, doi:10.1016/j.prostr.2017.04.044.
9. Kaye, R.; Turman, B.; Aubuchon, M.; Lamppa, D.; Mann, G.; Van Reuth, E.; Fulton, K.; Malejko, G.; Magnotti, P.; Nguyen, D.; et al. Induction coilgun for EM mortar. In Proceedings of the PPPS-2007—IEEE International Pulsed Power Conference, Albuquerque, NM, USA, 17–22 June 2007; Volume 2, pp. 1810–1813, doi:10.1109/PPPS.2007.4652542.
10. Hundertmark, S.; Schneider, M.; Vincent, G. Payload acceleration using a 10-MJ des railgun. *IEEE Trans. Plasma Sci.* **2013**, *41*, 1455–1459, doi:10.1109/TPS.2013.2242904.
11. Lockner, T.R.; Kaye, R.J.; Turman, B.N. Coilgun technology, status, applications, and future directions at Sandia National Laboratories. In Proceedings of the Conference Record of the Twenty-Sixth International Power Modulator Symposium, 2004 and 2004 High-Voltage Workshop, San Francisco, CA, USA, 23–26 May 2004; pp. 119–121, doi:10.1109/modsym.2004.1433521.
12. Kaye, R.J. Operational requirements and issues for coilgun EM launchers. In Proceedings of the 2004 12th Symposium on Electromagnetic Launch Technology, Snowbird, UT, USA, 25–28 May 2004; Volume 41, pp. 59–64, doi:10.1109/elt.2004.1398047.
13. Williamson, S. Pulsed coilgun limits. *IEEE Trans. Magn.* **1997**, *33*, 201–207, doi:10.1109/20.559951.
14. Zhang, T.; Guo, W.; Lin, F.; Cao, B.; Dong, Z.; Ren, R.; Huang, K.; Su, Z. Experimental results from a 4-stage synchronous induction coilgun. *IEEE Trans. Plasma Sci.* **2013**, *41*, 1084–1088, doi:10.1109/TPS.2013.2249116.

15. Deng, Z.; Zhang, W.; Zheng, J.; Wang, B.; Ren, Y.; Zheng, X.; Zhang, J. A High-Temperature Superconducting Maglev-Evacuated Tube Transport (HTS Maglev-ETT) Test System. *IEEE Trans. Appl. Supercond.* **2017**, *27*, 1–8, doi:10.1109/TASC.2017.2716842.
16. Durrell, J.H.; Ainslie, M.D.; Zhou, D.; Vanderbemden, P.; Bradshaw, T.; Speller, S.; Filipenko, M.; Cardwell, D.A. Bulk superconductors: A roadmap to applications. *Supercond. Sci. Technol.* **2018**, *31*, doi:10.1088/1361-6668/aad7ce.
17. Wera, L.; Fagnard, J.F.; Hogan, K.; Vanderheyden, B.; Namburi, D.K.; Shi, Y.; Cardwell, D.A.; Vanderbemden, P. Magnetic shielding of open and semi-closed bulk superconductor tubes: The role of a cap. *IEEE Trans. Appl. Supercond.* **2019**, *29*, doi:10.1109/TASC.2019.2891897.
18. Yang, W.; Yao, L.; Fu, Z. Simulation of Dynamic and Electromagnetic Characteristics of a Superconductor Bulk in a Single-Stage Induction Coilgun. *IEEE Trans. Plasma Sci.* **2019**, *47*, 821–827, doi:10.1109/TPS.2018.2865011.
19. Sadasivam, L.; Sriram, A.; Subendran, R.V. Active Space Debris Removal by Using Coil Gun Mechanism. In Proceedings of the International Conference on Advances in Engineering and Technology (ICAET'2014), Singapore, 29–30 March 2014; pp. 464–467.
20. Ainslie, M.D.; Fujishiro, H. Modelling of bulk superconductor magnetization. *Supercond. Sci. Technol.* **2015**, *28*, doi:10.1088/0953-2048/28/5/053002.
21. Zou, J.; Ainslie, M.D.; Fujishiro, H.; Bhagurkar, A.G.; Naito, T.; Hari Babu, N.; Fagnard, J.F.; Vanderbemden, P.; Yamamoto, A. Numerical modelling and comparison of MgB2 bulks fabricated by HIP and infiltration growth. *Supercond. Sci. Technol.* **2015**, *28*, doi:10.1088/0953-2048/28/7/075009.
22. Sass, F.; Sotelo, G.G.; De Andrade, R.; Sirois, F. H-formulation for simulating levitation forces acting on HTS bulks and stacks of 2G coated conductors. *Supercond. Sci. Technol.* **2015**, *28*, 125012, doi:10.1088/0953-2048/28/12/125012.
23. Quéval, L.; Liu, K.; Yang, W.; Zermeño, V.M.R.; Ma, G. Superconducting magnetic bearings simulation using an H-formulation finite element model. *Supercond. Sci. Technol.* **2018**, *31*, 084001, doi:10.1088/1361-6668/aac55d.
24. Sass, F.; Dias, D.H.N.; Sotelo, G.G.; De Andrade Junior, R. Superconducting magnetic bearings with bulks and 2G HTS stacks: Comparison between simulations using H and A-V formulations with measurements. *Supercond. Sci. Technol.* **2018**, *31*, 025006, doi:10.1088/1361-6668/aa9dc1.
25. Ainslie, M.; Grilli, F.; Quéval, L.; Pardo, E.; Perez-Mendez, F.; Mataira, R.; Morandi, A.; Ghabeli, A.; Bumby, C.; Brambilla, R. A new benchmark problem for electromagnetic modelling of superconductors: The high-T c superconducting dynamo. *Supercond. Sci. Technol.* **2020**, *33*, 105009, doi:10.1088/1361-6668/abae04.
26. Grilli, F.; Stavrev, S.; LeFloch, Y.; Costa-Bouzo, M.; Vinot, E.; Klutsch, I.; Meunier, G.; Tixador, P.; Dutoit, B. Finite-Element Method Modeling of Superconductors: From 2-D to 3-D. *IEEE Trans. Appl. Supercond.* **2005**, *15*, 17–25, doi:10.1109/TASC.2004.839774.
27. Liang, F.; Venuturumilli, S.; Zhang, H.; Zhang, M.; Kvitkovic, J.; Pamidi, S.; Wang, Y.; Yuan, W. A finite element model for simulating second generation high temperature superconducting coils/stacks with large number of turns. *J. Appl. Phys.* **2017**, *122*, 043903, doi:10.1063/1.4995802.
28. Berrospe-Juarez, E.; Zermeño, V.M.R.; Trillaud, F.; Grilli, F. Real-time simulation of large-scale HTS systems: Multi-scale and homogeneous models using the T–A formulation. *Supercond. Sci. Technol.* **2019**, *32*, 065003, doi:10.1088/1361-6668/ab0d66.
29. Berrospe-Juarez, E.; Trillaud, F.; Zermeno, V.M.R.; Grilli, F.; Weijers, H.W.; Bird, M.D. Screening Currents and Hysteresis Losses in the REBCO Insert of the 32 T All-Superconducting Magnet Using T-A Homogenous Model. *IEEE Trans. Appl. Supercond.* **2020**, *30*, 1–5, doi:10.1109/TASC.2020.2969865.
30. Stankevič, T.; Medišauskas, L.; Stankevič, V.; Balevičius, S.; Žurauskienė, N.; Liebfried, O.; Schneider, M. Pulsed magnetic field measurement system based on colossal magnetoresistance-B-scalar sensors for railgun investigation. *Rev. Sci. Instrum.* **2014**, *85*, 044704, doi:10.1063/1.4870280.
31. Liebfried, O.; Loffler, M.; Schneider, M.; Balevicius, S.; Stankevic, V.; Zurauskiene, N.; Abrutis, A.; Plausinaitiene, V. B-scalar measurements by CMR-based sensors of highly inhomogeneous transient magnetic fields. *IEEE Trans. Magn.* **2009**, *45*, 5301–5306.
32. Vertelis, V.; Vincent, G.; Schneider, M.; Balevičius, S.; Stankevič, V.; Žurauskiene, N. Magnetic Field Expulsion from a Conducting Projectile in a Pulsed Serial Augmented Railgun. *IEEE Trans. Plasma Sci.* **2020**, *48*, 727–732, doi:10.1109/TPS.2020.2970764.
33. Stankevic, V.; Lueg-Althoff, J.; Hahn, M.; Tekkaya, A.E.; Zurauskiene, N.; Dilys, J.; Klimantavicius, J.; Kersulis, S.; Simkevicius, C.; Balevicius, S. Magnetic Field Measurements during Magnetic Pulse Welding Using CMR-B-Scalar Sensors. *Sensors* **2020**, *20*, 5925, doi:10.3390/s20205925.
34. Can Superconductors s.r.o. Superconducting YBCO Levitation Bulk. Available online: https://www.can-superconductors.com/levitation-bulk.html (accessed on 16 December 2020).
35. Lukose, R.; Plausinaitiene, V.; Vagner, M.; Zurauskiene, N.; Kersulis, S.; Kubilius, V.; Motiejuitis, K.; Knasiene, B.; Stankevic, V.; Saltyte, Z.; et al. Relation between thickness, crystallite size and magnetoresistance of nanostructured $La_{1-x}Sr_xMn_yO_{3\pm\delta}$ films for magnetic field sensors. *Beilstein J. Nanotechnol.* **2019**, *10*, 256–261, doi:10.3762/bjnano.10.24.
36. Žurauskienė, N.; Stankevič, V.; Keršulis, S.; Klimantavičius, J.; Šimkevičius, Č.; Plaušinaitienė, V.; Vagner, M.; Balevičius, S. Increase of Operating Temperature of Magnetic Field Sensors Based on La–Sr–Mn–O Films With Mn Excess. *IEEE Trans. Plasma Sci.* **2019**, *47*, 4530–4535, doi:10.1109/TPS.2019.2911545.

37. Žurauskiene, N.; Balevičius, S.; Pavilonis, D.; Stankevič, V.; Plaušinaitiene, V.; Zherlitsyn, S.; Herrmannsdörfer, T.; Law, J.M.; Wosnitza, J. Magnetoresistance and resistance relaxation of nanostructured La-Ca-MnO films in pulsed magnetic fields. *IEEE Trans. Magn.* **2014**, *50*, 18–21, doi:10.1109/TMAG.2014.2324895.
38. Vertelis, V.; Balevicius, S.; Stankevic, V.; Zurauskiene, N.; Schneider, M. Pulsed magnetic flux penetration dynamics inside a thin-walled superconducting tube. *J. Appl. Phys.* **2020**, *127*, 113901, doi:10.1063/1.5145370.
39. Balevicius, S.; Zurauskiene, N.; Stankevic, V.; Kersulis, S.; Baskys, A.; Bleizgys, V.; Dilys, J.; Lucinskis, A.; Tyshko, A.; Brazil, S. Hand-Held Magnetic Field Meter Based on Colossal Magnetoresistance-B-Scalar Sensor. *IEEE Trans. Instrum. Meas.* **2020**, *69*, 2808–2816, doi:10.1109/TIM.2019.2925411.
40. Brandt, E.H. Superconductors of finite thickness in a perpendicular magnetic field: Strips and slabs. *Phys. Rev. B Condens. Matter Mater. Phys.* **1996**, *54*, 4246–4264, doi:10.1103/PhysRevB.54.4246.
41. Yamasaki, H.; Mawatari, Y. Current-voltage characteristics and flux creep in melt-textured $YBa_2Cu_3O_{7-\delta}$. *Supercond. Sci. Technol.* **2000**, *13*, 202–208, doi:10.1088/0953-2048/13/2/315.
42. Plechacek, V.; Jirsa, M.; Rames, M.; Muralidhar, M. Batch Production of YBCO Disks for Levitation Applications. *Phys. Procedia* **2012**, *36*, 538–543, doi:10.1016/j.phpro.2012.06.080.
43. Su, Z.; Zhang, T.; Guo, W.; Yue, J.; Zhang, H.; Fan, W.; Sun, X.; Huang, K. Investigation of armature capture effect on synchronous induction coilgun. *IEEE Trans. Plasma Sci.* **2015**, *43*, 1215–1219, doi:10.1109/TPS.2015.2410302.

NOTES

Vilnius University Press
9 Saulėtekio Ave., Building III, LT-10222 Vilnius
Email: info@leidykla.vu.lt, www.leidykla.vu.lt
Print run copies 20